

DIBRIS, University of Genoa

PhD Program in Computer Science
and Systems Engineering

CIMA Research Foundation



Enhancing Operational Flood Detection Solutions through an Integrated Use of Satellite Earth Observations and Numerical Models

by
Mauro Arcorace

Thesis submitted for the degree of Doctor of Philosophy (XXXIII cycle)

May 2021

DIBRIS, Università di Genova
Via Opera Pia, 13 16145 Genova, Italia

www.dibris.unige.it

Fondazione CIMA
Via Armando Magliotto, 2, 17100 Savona, Italia

www.cimafoundation.org

Università degli Studi di Genova

**Dipartimento di Informatica, Bioingegneria,
Robotica ed Ingegneria dei Sistemi**

**Ph.D. Thesis in Computer Science and Systems Engineering
Systems Engineering Curriculum**

**Enhancing Operational Flood Detection Solutions
through an Integrated Use of
Satellite Earth Observations and Numerical Models**

by

Mauro Arcorace

May 2021

This page intentionally left blank

Dottorato di Ricerca in Informatica ed Ingegneria dei Sistemi
Indirizzo Ingegneria dei Sistemi
Dipartimento di Informatica, Bioingegneria, Robotica ed Ingegneria dei Sistemi
Università degli Studi di Genova

DIBRIS, Università degli studi di Genova
Via Opera Pia, 13
I-16145 Genova, Italia
<http://www.dibris.unige.it/>

Ph.D. Thesis in Computer Science and Systems Engineering
Systems Engineering Curriculum
(S.S.D. ICAR/02)

Submitted by Mauro Arcorace
DIBRIS, University of Genoa, Genoa

. . .

Date of submission: May 2021

Title:

*Enhancing Operational Flood Detection Solutions
through an Integrated Use of
Satellite Earth Observations and Numerical Models*

Advisors:

Prof. Giorgio Boni, DICCA, University of Genoa, Italy
Dr. Simone Gabellani, CIMA Research Foundation, Italy

. . .

Ext. Reviewers:

Prof. Salvatore Manfreda, University of Naples "Federico II", Italy
Dr. Luz Adriana Cuartas, National Center for Monitoring and Early Warning of Natural Disasters, Brazil

This page intentionally left blank

I dedicate this thesis to Valentina

This page intentionally left blank

Abstract

Among natural disasters floods are the most common and widespread hazards worldwide (CRED and UNISDR, 2018). Thus, making communities more resilient to flood is a priority, particularly in large flood-prone areas located in emerging countries, because the effects of extreme events severely setback the development process (Wright, 2013).

In this context, operational flood preparedness requires novel modeling approaches for a fast delineation of flooding in riverine environments. Starting from a review of advances in the flood modeling domain and a selection of the more suitable open toolsets available in the literature, a new method for the Rapid Estimation of FLOOD EXtent (REFLEX) at multiple scales (Arcorace et al., 2019) is proposed.

The simplified hydraulic modeling adopted in this method consists of a hydro-geomorphological approach based on the Height Above the Nearest Drainage (HAND) model (Nobre et al., 2015). The hydraulic component of this method employs a simplified version of fluid mechanic equations for natural river channels. The input runoff volume is distributed from channel to hillslope cells of the DEM by using an iterative flood volume optimization based on Manning's equation. The model also includes a GIS-based method to expand HAND contours across neighbor watersheds in flat areas, particularly useful in flood modeling expansion over coastal zones.

REFLEX's flood modeling has been applied in multiple case studies in both surveyed and ungauged river basins. The development and the implementation of the whole modeling chain have enabled a rapid estimation of flood extent over multiple basins at different scales. When possible, flood modeling results are compared with reference flood hazard maps or with detailed flood simulations.

Despite the limitations of the method due to the employed simplified hydraulic modeling approach, obtained results are promising in terms of flood extent and water depth. Given the geomorphological nature of the method, it does not require initial and boundary conditions as it is in traditional 1D/2D hydraulic modeling. Therefore, its usage fits better in data-poor environments or large-scale flood modeling. An extensive employment of this slim method has been adopted by CIMA Research Foundation researchers for flood hazard mapping purposes over multiple African countries.

As collateral research, multiple types of Earth observation (EO) data have been employed in the REFLEX modeling chain. Remotely sensed data from the satellites, in fact, are not only a source to obtain input digital terrain models but also to map flooded areas. Thus, in this work, different EO data exploitation methods are used for estimating water extent and surface height. Preliminary results by using Copernicus's Sentinel-1 SAR and Sentinel-3 radar altimetry data highlighted their potential mainly for model calibration and validation.

In conclusion, REFLEX combines the advantages of geomorphological models with the ones of traditional hydraulic modeling to ensure a simplified steady flow computation of flooding in open channels. This work highlights the pros and cons of the method and indicates the way forward for future research in the hydro-geomorphological domain.

This page intentionally left blank

Table of Contents

List of figures	VI
List of tables.....	XII
Acronyms.....	XIII
Introduction.....	1
Context	2
Background.....	2
Problem statement.....	3
Thesis outline.....	4
Chapter 1 - Material	7
1.1 Introduction.....	8
1.2 Different ways to acquire water depth and surface extent observations	8
1.2.1 Estimating water level and discharge along the river	8
1.2.2 Inland waters mapping using remotely sensed data.....	10
1.3 The estimation of surface terrain elevation and its hydrologically conditioning.....	11
1.3.1 Multiple sources data for different Digital Elevation Models	11
1.3.2 DEM conditioning	12
1.3.3 Examples of multi-source DEM datasets.....	14
1.4 Extract hydrological derivatives and basin characteristics from the DEM.....	15
1.4.1 Drainage modeling	15
1.4.2 Hydrological derivatives	19
1.5 Low-complexity flood models	21
1.5.1 Simplified 2D hydrodynamic models.....	21
1.5.2 LISFLOOD-FP	23
1.5.3 AutoRoute.....	23
1.5.4 Hydrogeomorphic approaches	23
1.6 Discussion	27
1.6.1 About input datasets	27
1.6.2 Critical analysis of drainage methods.....	27
1.6.3 Critical analysis of low complexity flood model	28

Chapter 2 - Method	29
2.1 Introduction	30
2.2 A simplified 2D hydro-morphological modeling approach: REFLEX	30
2.3 Collecting and pre-processing of REFLEX inputs	31
2.3.1 Input discharge values	31
2.3.2 DEM conditioning in REFLEX	31
2.3.3 Define flowlines	35
2.4 Module 1: Extracting Hydrological Derivatives from Conditioned DEM	35
2.4.1 Drainage modeling and extraction of derivatives	35
2.5 Module 2: Streams Hierarchy and Surface Runoff Estimation	36
2.5.1 Stream network and watersheds delineation	36
2.5.2 Stream hierarchy	37
2.5.3 Morphologic parameters from the DEM	41
2.5.4 Computation and distribution of runoff volume across the network	42
2.5.5 Discussion	44
2.6 Module 3: HAND Mapping and Coastal Expansion	45
2.6.1 HAND mapping for each sub-basin	45
2.6.2 Coastal expansion	46
2.7 Module 4: Flood Inundation	49
2.7.1 Static volume optimization	50
2.7.2 Estimating transit time via a simplified version of the Manning equation	53
2.7.3 Creating output flood map	55
2.7.4 Binary classification in REFLEX flood extent validation	56
2.8 The integration of external satellite-based observation	58
2.8.1 EO-based water mask	58
2.8.2 Water level surface height from radar altimetry	58
2.8.3 Flood impact assessment using SAR data	60
Chapter 3 - Results	61
3.1 Introduction	62
3.2 The implementation of the REFLEX modeling chain	63
3.2.1 The REFLEX development	63
3.2.2 The REFLEX modeling chain	63

3.2.3	The REFLEX dependencies	65
3.2.4	REFLEX parameters.....	66
3.2.5	The REFLEX GIT repository.....	69
3.3	REFLEX Case study – The Magra river basin in Northern Italy	70
3.3.1	Case study description.....	70
3.3.2	Input data	71
3.3.3	Modeling.....	73
3.3.4	Results	83
3.4	REFLEX Case study – The Entella river basin in Northern Italy.....	101
3.4.1	Case study description.....	101
3.4.2	Input data	102
3.4.3	Modeling.....	103
3.4.4	Results	109
3.5	REFLEX Case study – The Secchia river basin in Northern Italy.....	124
3.5.1	Case study description.....	124
3.5.2	Input data	125
3.5.3	Modeling and results.....	125
3.5.4	Discussion	126
3.6	REFLEX Case study – Hazard Mapping in southern African countries.....	127
3.6.1	Case study description.....	127
3.6.2	Input data	127
3.6.3	Modeling.....	127
3.6.4	Results	128
3.6.5	Discussion	137
3.7	Earth Observation data integration case studies	138
3.7.1	An approach to detect water level from satellite altimetry.....	138
3.7.2	HAND maps to reduce false alarms in SAR-based unsupervised flood mapping	146
3.7.3	Discussion	152
Conclusions.....		153
Acknowledgments.....		159
Bibliography.....		160

List of figures

Chapter 1

Figure 1 - typology of features in DEM flow enforcement (Source: Lindsay, 2016).	13
Figure 2 – ArcGIS D8 Flow Direction encoding	17
Figure 3 - Schema of D-inf flow direction (Image credits: TauDEM)	18
Figure 4 - GRASS GIS drainage encoding for D8 and MFD algorithms	18
Figure 5 – Example of derivatives from hydrologically conditioned DEM (Arcorace et al., 2015).	20
Figure 6 - Concept of “relative elevation”. The surface elevation of a generic Hillslope Cell (HC), such as 15m above a vertical datum (e.g., MSL), can be expressed as relative elevation by calculating the vertical distance from the nearest Channel Cell (CC) of drainage, having an elevation of 10m (figure a). As a result, in the HAND map the hillslope cell of interest has a relative elevation of 5m, and its nearest channel cell, being a vertical reference, a value of 0m (figure b).	25

Chapter 2

Figure 7 - REFLEX model flowchart.	30
Figure 8 - Schema of the stream elevation filtering	32
Figure 9 - Schema of SRD incremental stream burning.	33
Figure 10 - Schema of constant SRD stream burning.	34
Figure 11 - The usage of constant and incremental stream burning scenarios over a simple basin. Figure (a) shows a sample classification of the river network between the inlet, connector, and outlet branches. Figure(b) presents an application of the method with sample SRD at nodes. SRD is constant only for connector branches while it is incremental for all the others.	34
Figure 12 - Flow directions obtained by using D8 (a), Holmgren’s MFD (b), and D-infinity (c) flow directions over the Lake Maga in Chad. Flatwater surface highlights the increasing level of flow direction dispersion of the three methods respectively from (a) to (b) and to (c). Flow directions are obtained by using hydrologically conditioned SRTM data from the SRTM-FM dataset (source: UNOSAT).	36
Figure 13 - Hack stream order for the Magra river basin. The thickest blue line, having Hack order equal to one, identifies the main stem.	37
Figure 14 - Strahler stream hierarchy for the Magra river basin. All headwaters can be identified with Strahler order equal to one. The thickest blue line represents the downstream part of the river network that collects the flow of all upstream tributaries and that drains to the river mouth.	38
Figure 15 - Pfafstetter stream order for the Magra river basin. Interbasins 1, 3, 5, 9 are the ones along the main stem (having HACK order equal to one). Even orders 2-8 are used for basins of main stem tributaries. Coding of sub-basins, as shown for Basin 4, follows again an upstream incremental 1-10 ordering at multiple levels from outlet to divide (e.g., from 4100 to 4930).	39
Figure 16 - Drainage area, headwater, and downstream masks for a generic sub-basin derived by identifying 6 headwater branches and 2 downstream river branches from the entire Pfafstetter coded river network.	40
Figure 17 - Backwater effect in REFLEX.	40
Figure 18 - Schema of a temporal evolution of the flow for a generic cross-section of a river (flood hydrograph). The flood volume is defined as the time integral of the surface runoff component of the hydrograph above the bankfull discharge (QP).	42

Figure 19 - Hydrograph shapes for dimensionless time and discharge.	43
Figure 20 - Schema of the HAND map for the sub-basin of a generic branch of the input river network. All channel cells have values equal to zero. Pixel values for Hillslope cells are elevation differences from the nearest drainage expressed in meters.	45
Figure 21 - Schema of a watershed having funnel-like shape. Flood extent is constrained within watershed boundary only.....	46
Figure 22 – Schema of the coastal expansion in REFLEX.....	48
Figure 23 - high-level description of the REFLEX Flood module.....	49
Figure 24 - REFLEX's static volume optimization.....	50
Figure 25 - Schema of the REFLEX computation of water depth raster for a generic sub-basin.	52
Figure 26 - Planar view of a cross-section along a river branch of length L (figure a). Principal hydraulic variables are shown in the sample cross-section A-A' (figure b): the river stage (h), the cross-sectional area of the flow (A_w), and the wetted perimeter (P_w).....	53
Figure 27 - Rectangular approximation of river geometry with river stage (h) rescaled to the average water depth (h) derived from the ratio between the flood volume and the flooded area.	54
Figure 28 - Runoff volume as a function of the transit time	55
Figure 29 – Schema for the linear binary classification of flood-prone areas.....	56
Figure 30 - Workflow for water level estimation using Sentinel-3 SAR altimeter.....	58
Figure 31 – A general workflow for the computation and the validation of water level estimations from radar altimetry and its exploitation in hydrology for flood modeling purposes.	59

Chapter 3

Figure 32 – Organization and upload of all REFLEX source codes and their setup into a GIT repository. All related documentation is also given together with a reference result to better explain REFLEX installation and usage to the end-user.....	69
Figure 33 – The Magra river basin in Northern Italy.	70
Figure 34 – Coverage of MATTM LiDAR data for the Magra river basin. Hill shaded DEM from mosaicking of all available tiles is shown in graded grayscale.	72
Figure 35 – Streamlines used in the stream burning of the 10m DEM in the Lower Magra valley. Labeled numbers indicate the artificial depression in meters used in the stream burning of the river branches.	74
Figure 36 – Result of Epsilon filling over the lower Magra river basin. The Artificial gradient ensures a hydrologically consistent drainage of the area, also visually highlighted by estimated HAND contours only overfilled terrain elevation.....	75
Figure 37 – Before and after the DEM Conditioning of the multi-source digital elevation model for Magra at 10m spatial resolution obtained with the REFLEX model.	76
Figure 38 – A comparison of multiple elevation profiles for a river branch in the Magra river basin derived from resampled LiDAR high-resolution DEM. The dotted black line shows the input raw DEM, the blue line the filtered one, and the red line the burned one using incremental SRD values.....	77
Figure 39 - A comparison of multiple elevation profiles for a river branch in the Magra river basin derived from resampled LiDAR high-resolution DEM. The dotted black line shows the input raw DEM, the blue line the filtered one, and the red line the burned one using constant SRD values.	77
Figure 40 - A comparison between the DEM-based flowlines (lines in purple) derived from burned, on the left, and filled, on the right, LiDAR DEM over the Magra river basin. Artificial depressions introduced into the	

DEM along real river paths, allow the extraction of more realistic flowlines which are necessary as input for the REFLEX flood modeling.....	78
Figure 41 – Evaluation of HAND contours using multiple drainage algorithms for the Magra river basin, near the junction between Magra and Vara rivers. Only pixels having a height above the nearest drainage values below 10 m are considered. HAND contours are derived from the Filled resampled LIDAR data at 5m from MATTM. Input flowlines are derived from the burned DEM. The vertical distance from flowlines is shown in a blue graded color scale for D8, Holmgren’s MFD, and D-infinity drainage methods. Input flowlines are shown in purple. HAND maps are derived from the Filled DEM and not from the burned one to avoid artifacts caused by the burning of streams into the DEM. From an overall perspective, the DINF method shows a continuous delineation of relative vertical distances. Areas of discontinuity encountered in the other methods are highlighted with circles in yellow.	81
Figure 42 – Flood hazard map for the Magra river basin from “Piano di Gestione del Rischio Alluvioni” of the Northern Apennine Interregional River Basin Authority. Areas in red show flood extent at the 30-year return period used as a reference in this case study.	83
Figure 43 – Flood hazard map for the Magra river basin from “Piano di Gestione del Rischio Alluvioni” of the Northern Apennine Interregional River Basin Authority. Areas in red show flood extent at the 200-year return period used as a reference in this case study.	84
Figure 44 -A comparison between the validation of REFLEX flood extents against the reference flood hazard map (PGRA) for the same flood return period (RP 30 years) using MERIT DEM over the Magra river basin. Areas of exclusions are shown in red, areas of omissions in green, and the matched areas in blue. On the left and the right are shown REFLEX modeling results respectively without and with the volume optimization routine based on Manning’s formula.	85
Figure 45 – Water depth at 10 spatial resolution from the REFLEX flood modeling at 30-year return period for the Magra basin.....	86
Figure 46 – Water depth at 10 spatial resolution from the REFLEX flood modeling at 200-year return period for the Magra basin.	87
Figure 47 –The figure shows a comparison between the flood extent delineation from the REFLEX model at the 30-year return period and the PGRA Flood Hazard map at the same return period for the Magra river basin in Northern Italy. Areas in blue, green, and red show respectively agreement (TP), error of inclusion (FP), and error of exclusion (FN).....	88
Figure 48 – Detail of binary classification at 30-year return period in the low Magra valley.	89
Figure 49 – Detail of binary classification at 30-year return period at the junction between Vara and Magra rivers.	90
Figure 50 – Detail of binary classification at 30-year return period in the Vara Magra river.	91
Figure 51 – Detail of binary classification at 30-year return period in the Lower Magra river.....	92
Figure 52 – Bar chart showing accuracy, Cohen's kappa coefficient, and index, and Matthews Correlation Coefficient of the binary classification of the 30-year return period flood map from REFLEX at different scales.	93
Figure 53 – The figure shows a comparison between the flood extent delineation from the REFLEX model at the 200-year return period and the PGRA Flood Hazard map at the same return period for the Magra river basin in Northern Italy. Areas in blue, green, and red show respectively agreement (TP), error of inclusion (FP), and error of exclusion (FN).....	94
Figure 54 – Detail of binary classification at 200-year return period in the low Magra valley.	95
Figure 55 – Detail of binary classification at 200-year return period at the junction between Vara and Magra rivers.	96
Figure 56 – Detail of binary classification at 200-year return period in the Vara Magra river.	97

Figure 57 – Detail of binary classification at 200-year return period in the Lower Magra river.....	98
Figure 58 – Bar chart showing accuracy, Cohen's kappa coefficient, and index, and Matthews Correlation Coefficient of the binary classification of the 200-year return period flood map from REFLEX at different scales.	99
Figure 59 – The Entella river basin in Northern Italy investigated in this REFLEX case study.....	101
Figure 60 - streamlines employed in REFLEX modeling of the Entella river basin.	102
Figure 61 – Watershed, sub-outlet, not expanded HAND map, and search areas (b and dmax) for the Entella river branch.	104
Figure 62 – Planar view in shaded gray and cross-section of expanded HAND in Entella's floodplain using a head loss of 20cm per pixel.	105
Figure 63 – Planar view in shaded gray and cross-section of expanded HAND in Entella's floodplain using a head loss of 5cm per pixel.	105
Figure 64 – Planar view in shaded gray and cross-section of expanded HAND in the Entella floodplain using a head loss of 1cm per pixel.	106
Figure 65 – Iterative Evolution of water extent for a sample Entella subbasin in the REFLEX Manning-based volume optimization.....	107
Figure 66 – Flood hazard map for the Entella river basin from “Piano di Gestione del Rischio Alluvioni” of the Northern Apennine Interregional River Basin Authority. Areas in light red, red, and dark red show flood extent at 50-, 200- and 500-year return periods, respectively.....	109
Figure 67 – Flood hazard map at 500-year return period for the Entella river basin from CIMA Research Foundation.	110
Figure 68 – Water extent over the Entella river basin derived from the REFLEX flood model at different flood magnitudes. Hill shaded LiDAR data from MATTM is shown in graded grayscale. Reflex flood extent at 5m resolution for 50, 150, 200, and 500 years return periods are shown in dark blue, blue, light blue, and very light blue respectively.....	111
Figure 69 – Water depth over the Entella river basin derived from the REFLEX flood model at 50 years return periods. Water depths in meters are shown in a blue scale graded color bar.	112
Figure 70 – Water depth over the Entella river basin derived from the REFLEX flood model at 150 years return periods. Water depths in meters are shown in a blue scale graded color bar.	113
Figure 71 – Water depth over the Entella river basin derived from the REFLEX flood model at 200 years return periods. Water depths in meters are shown in a blue scale graded color bar.	114
Figure 72 – Water depth over the Entella river basin derived from the REFLEX flood model at 500 years return periods. Water depths in meters are shown in a blue scale graded color bar.	115
Figure 73 - Comparison between the flood extent delineation from the REFLEX model at the 50-year return period and the PGRA Flood Hazard map at the same return period for the Entella river basin in Northern Italy. Areas in blue, green, and red show respectively agreement (TP), error of inclusion (FP), and error of exclusion (FN).	116
Figure 74 - Comparison between the flood extent delineation from the REFLEX model at the 200-year return period and the PGRA Flood Hazard map at the same return period for the Entella river basin in Northern Italy. Areas in blue, green, and red show respectively agreement (TP), error of inclusion (FP), and error of exclusion (FN).	117
Figure 75 - Comparison between the flood extent delineation from the REFLEX model at the 500-year return period and the PGRA Flood Hazard map at the same return period for the Entella river basin in Northern Italy. Areas in blue, green, and red show respectively agreement (TP), error of inclusion (FP), and error of exclusion (FN).	118

Figure 76 - Bar chart showing accuracy, Cohen's kappa coefficient, and index, and Matthews Correlation Coefficient of REFLEX binary classification in the Entella at multiple return periods using the PGRA flood hazard map as a benchmark.....	119
Figure 77 - Comparison between the flood extent delineation from the REFLEX model at the 500-year return period and the CIMA Flood Hazard map at the same return period for the Entella river basin in Northern Italy. Areas in blue, green, and red show respectively agreement (TP), error of inclusion (FP), and error of exclusion (FN).	120
Figure 78 – Water depth difference in meters between the REFLEX water depth map at the 500-year return period and the one from the CIMA water depth map at the same return period for the Entella river basin in Northern Italy. Areas in red, yellow, and blue show respectively underestimate ($0 < \text{WD difference} < -5$), match ($\text{WD difference} = 0$), and overestimate ($5 < \text{WD difference} < 0$).....	121
Figure 79 - Distribution of Water depth differences between the REFLEX water depth and the benchmark one derived by CIMA Foundation using TELEMAT 2D model.	122
Figure 80 – A portion of the Secchia river basin in Northern Italy investigated in this REFLEX case study (Image credits: Ferrari, Protezione Civile Modena, Aeroclub Marzaglia).	124
Figure 81 - Flood scenario from a 2D hydraulic model used as benchmarking (Source CIMA Foundation).	125
Figure 82 – HAND contours from REFLEX over the Secchia case study area.	126
Figure 83 – An example of REFLEX flood mapping applied for the Zanzibar Island.	127
Figure 84 – Flood scenario 50 years Return Period derived from REFLEX over the Tanzania islands.....	128
Figure 85 – Flood scenario 50 years Return Period derived from REFLEX in Northern Zambia near Lakes Kampolombo and Kangwena.....	129
Figure 86 – Maximum Water Extent (1984-2020) from the Global Surface Water dataset (Pekel et al., 2016) in Northern Zambia near Lakes Kampolombo and Kangwena. This satellite-based water extent is derived from 37 years of Landsat observations (Source: EC JRC/Google).	130
Figure 87 – Flood scenario 50 years Return Period derived from REFLEX in the south-west of Zambia along the Zambezi River in the Caprivi region near Katima Mulilo.....	131
Figure 88 – Maximum Water Extent (1984-2020) from the Global Surface Water dataset (Pekel et al., 2016) in the southwest of Zambia along the Zambezi River in the Caprivi region near Katima Mulilo. This satellite-based water extent is derived from 37 years of Landsat observations (Source: EC JRC/Google).	132
Figure 89 – Flood scenario 50 years Return Period derived from REFLEX in western Zambia along the Zambezi river in the Mongu region.....	133
Figure 90 – Maximum Water Extent (1984-2020) from the Global Surface Water dataset (Pekel et al., 2016) in western Zambia along the Zambezi river in the Mongu region. This satellite-based water extent is derived from 37 years of Landsat observations (Source: EC JRC/Google).	134
Figure 91 – Flood scenario 50 years Return Period derived from REFLEX in eastern Angola and north-west of Zambia in the Higher Zambezi.	135
Figure 92 – Maximum Water Extent (1984-2020) from the Global Surface Water dataset (Pekel et al., 2016) in eastern Angola and north-west of Zambia in the Higher Zambezi. This satellite-based water extent is derived from 37 years of Landsat observations (Source: EC JRC/Google).	136
Figure 93 - The portion of the Chad basin in Southern Chad along the Logone and the Chari rivers investigated in this radar altimetry case study.	139
Figure 94 - Map of gauging station including an example of instrumentation and collected water level time series (Credits: Ministry of Environment, Water, and Fisheries Chad, Google).	140
Figure 95 - The identified workflow to derive water level estimation from Sentinel-3 radar altimeter	141

Figure 96 - Preliminary results about the validation of altimetry-based water estimations at Lai gauge, Logone River, Chad. Contains modified Copernicus sentinel-3 data (2016, 2017) accessed via the ESA G-POD (Credits: ESA, Google).	142
Figure 97 - Preliminary results about the validation of altimetry-based water estimations at Moundou gauge, Logone River, Chad. Contains modified Copernicus sentinel-3 data (2016, 2017) accessed via the ESA G-POD (Credits: ESA, Google).....	143
Figure 98 – Observed, estimated, and forecast discharge values at Lai station for 2017 in the Logone river (Credits: UNOSAT).	144
Figure 99 - Stream gauges, Sentinel-3 A and B ground tracks, and the identification of additional virtual stations, highlighted with circles in green, for the Chari and Logone river basins (Credits: ESA, Google). ..	145
Figure 100 – A portion of the Karun river basin in the Khuzestan province in Iran investigated in this SAR flood mapping case study. Image footprints are also shown of SAR Ground Range Detected data acquired in March and April 2019 from Copernicus Sentinel-1 A and B satellites in Interferometric Wide mode and VV polarization.....	146
Figure 101 - HASARD flood map from Copernicus Sentinel-1B data acquired on 26 March 2019 over the southwest of the Khuzestan province, Iran. Contains modified Copernicus Sentinel-1 data (2019) accessed and processed in ESA G-POD (Credits: ESA, LIST).....	147
Figure 102 - HASARD flood map from Copernicus Sentinel-1 A data acquired on 2 April 2019 over the southwest of the Khuzestan province in Iran. Contains modified Copernicus Sentinel-1 data (2019) accessed and processed in ESA G-POD (Credits: ESA, LIST).....	148
Figure 103 - HASARD Flood binary mask from Sentinel-1 data for the 2 nd of April 2019 in the lower Karun river basin in Iran.	149
Figure 104 - Water Occurrence (1984-2020) from the Global Surface Water dataset (Pekel et al., 2016) over the lower Karun river basin in Iran. This satellite-based water extent is derived from 37 years of Landsat observations (Source: EC JRC/Google).	150
Figure 105 – Before (top) and after (bottom) the HAND-based filtering of HASARD flood binary mask with HAND from MERIT Hydro.	151

List of tables

Chapter 1

Table 1 – Characteristics of a selection of Global Digital Elevation Models (Source: NASA, USGS, DLR, JAXA, Copernicus).....	12
Table 2 – Examples of Multi-source Digital Elevation Models products.	15
Table 3 - A review of hydrodynamic models for river modeling available in the literature.	22

Chapter 2

Table 4 – The multi-purpose usage of different flow direction models in REFLEX.	35
Table 5 – List of empirical methods integrated into REFLEX to estimate the time of concentration. All formulas are expressed with an output time of concentration in hours.	41
Table 6 – Schema of confusion matrix employed to test the performance of the REFLEX model.	56

Chapter 3

Table 7 – Overview of REFLEX dependencies.	65
Table 8 – Overview of all GRASS GIS Add-ons employed in REFLEX.....	66
Table 9 – Overview of all REFLEX parameters.	68
Table 10 - Discharge values for the Magra river basin at 30 years RP (AdB Magra, 2016).	73
Table 11 - Discharge values for the Magra river basin at 200 years RP (AdB Magra, 2016).	73
Table 12 – List of parameters used in the application of REFLEX in the Magra river basin at 30- and 200-year return periods.....	82
Table 13 – Results from the binary classification of flood extent at 30-year return period.	93
Table 14 – Results from the binary classification of flood extent at 200-year return period.	99
Table 15 - Discharge values for the Entella river basin at 50-, 200-, and 500-year RP (Regione Liguria, 2020b).	103
Table 16 – List of parameters used in the application of REFLEX in the Magra river basin at 30- and 200-year return periods.....	108
Table 17 - Results from the binary classification of flood extent in the Entella at 50-, 200-, and 500-year return periods using the PGRA flood hazard map as a benchmark.....	119
Table 18 – Metrics from the binary classification of flood extent in the Entella at 500-years using the CIMA flood hazard maps.	121
Table 19 - Input satellite imagery employed in this case study	147

Acronyms

ADCP	Acoustic Doppler Current Profiler
ALOS	Advanced Land Observing Satellite
ASTER	Advanced Spaceborne Thermal Emission and Reflection Radiometer
AW3D	ALOS World 3D DEM
CC	Channel Cell
CERN	European Organization for Nuclear Research
CGIAR	Consultative Group for International Agricultural Research
CIMA	International Centre on Environmental Monitoring
CNES	French Space Agency
CREST	Coupled Routing and Excess Storage
CRISTAL	Copernicus Polar Ice and Snow Topography Altimeter
CSI	Consortium for Spatial Information (CGIAR)
CSV	Comma Separated Value
D8	Deterministic Eight-Node
DAHITI	Database for Hydrological Time Series of Inland Waters
DEM	Digital Elevation Model
DIAS	Data and Information Access Services (Copernicus)
DIBRIS	Department of Informatics Bioengineering Robotics and Systems Engineering
DFO	Dartmouth Flood Observatories
DINF	D-INfinity
DLR	German Aerospace Center
DSM	Digital Surface Model
DTM	Digital Terrain Model
EEA	European Environment Agency
EGM	Earth Gravitational Model
EM	Electro Magnetic
EMS	Emergency Management Service (Copernicus)
EO	Earth Observation
EPSG	European Petroleum Survey Group
ESA	European Space Agency
CCI	Climate Change Initiative (ESA)
ETUH	Equivalent Triangular Unit Hydrograph
EUMETSAT	European Organisation for the Exploitation of Meteorological Satellites

EWS	Early Warning System
FDM	Finite Difference Method
FEM	Finite Element Method
FN	False Negative
FP	False Positive
FVM	Finite Volume Method
GAR	Global Assessment Report on Disaster Risk Reduction (UNISDR)
GDAL	Geospatial Data Abstraction Library
GeoTIFF	Geospatial Tagged Image File Format
GFI	Geomorphic Flood Index
GFMS	Global Flood Monitoring System
GFT	USGS GIS Flood Tool
GIS	Geographic Information System
GIT	Geospatial Information Technology
GloFAS	Global Flood Awareness System
GMTED	Global Multi-resolution Terrain Elevation Data
G-POD	Grid Processing On-Demand (ESA)
GRASS	Geographic Resources Analysis Support System
GRD	Ground Range Detected
GRDC	Global Runoff Data Centre (WMO)
GRRATS	Global River Radar Altimetry Time Series
GSW	Global Surface Water
GUI	Graphical User Interface
HAND	Height Above the Nearest Drainage
HC	Hillslope Cell
HDA	Height-Driven Approach
HDMA	Hydrologic Derivatives for Modeling and Applications
HR	High Resolution
HSBA	Hierarchical Split Based Algorithm
HydroSHEDS	HYDROlogical data and maps based on SHuttle Elevation Derivatives at multiple Scales
IDW	Inverse Distance Weighting
IW	Interferometric Wide swath mode (Sentinel-1)
JAXA	Japan Aerospace Exploration Agency
JRC	Joint Research Center
L1	Level 1
L2	Level 2

LEGOS	Laboratory Studies in Geophysics and Space Oceanography
LiDAR	Light Detection And Ranging
LIST	Luxembourg Institute of Science and Technology
MATTM	Ministry for Environment, Land and Sea Protection of Italy
MCC	Matthews Correlation Coefficient
MERIT	Multi-Error-Removed Improved-Terrain dataset
MFD	Multiple Flow Direction
MPI	Message Passing Interface
NASA	National Aeronautics and Space Administration
NGO	Non-Governmental Organization
NHD	National Hydrological Departments
NOAA	National Oceanic and Atmospheric Administration
NRT	Near Real Time
NWM	National Weather Model (NOAA)
OS	Operating System
OSGEO	Open-Source Geospatial Foundation
PDF	Portable Document Format
PGRA	Flood Risk Management Plan
PPV	Positive predictive value (or Precision)
PRISM	Panchromatic Remote-sensing Instrument for Stereo Mapping
QGIS	Quantum GIS
RADAR	RAdio Detection And Ranging
REFLEX	Rapid Estimation of FLood EXtent
RivDIS	Global River DIScharge (NASA DAAC)
RP	Return Period
RSS	Research and Service Support (ESA)
S1	Sentinel-1
S2	Sentinel-2
S3	Sentinel-3
SAR	Synthetic Aperture Radar
SARvatore	SAR Versatile Altimetric Toolkit for Ocean Research and Exploitation
SCA	Specific Catchment Area
SFD	Single Flow Direction
SHP	Shapefile
SMASH	SMAll Altimetry Satellites for Hydrology
SONAR	SOund Navigation And Ranging

SRAL	Synthetic Aperture Radar Altimeter (Sentinel-3)
SRD	Simulated River Depth
SRTM	Shuttle Radar Topography Mission
SWOT	Surface Water and Ocean Topography
TauDEM	Terrain Analysis Using Digital Elevation Models
TFN	Triangular Face Network
TIN	Triangular Irregular Network
TOC	Top Of Canopy
TN	True Negative
TP	True Positive
TPR	True Positive Rate (or Sensitivity)
TUM	Technical University of Munich
UH	Unit Hydrograph
UNEP	United Nations Environment Programme
UNISDR	United Nations Office for Disaster Risk Reduction
UNITAR	United Nations Institute for Training and Research
UNOSAT	UNITAR Operational Satellite Applications Programme
US	United States
USACE	United States Army Corps of Engineers
USGS	United States Geological Survey
UTM	Universal Transverse Mercator
VDA	Volume-Driven Approach
VHR	Very High Resolution
WD	Water Depth
WGS	World Geodetic System
WMO	World Meteorological Organization
WWF	World Wildlife Fund

Introduction

An introduction to the topics investigated in this Ph.D. research.

Context

Flooding is the most common and widespread hazard worldwide. Every year, floods cause colossal loss of lives and properties, especially in developing states, in which accumulated impacts from multiple events delay the development and growth (Wright, 2013). In addition to that, most flood-prone areas in the globe are mainly located in emergent countries, where making communities more flood resilient is a priority. A priority that has been also clearly highlighted in the Sendai Framework for Disaster Risk Reduction 2015-2030 (UNISDR, 2015a) where technology is playing a special role.

Concerning flood crises, satellite-based analysis plays a central role in the enhancement of national strategies for disaster risk management and the support of disaster relief operations (ESA, 2015; UNISDR, 2015b). During a major disaster, satellite-based flood impact assessments can be estimated by exploiting multi-sensor medium and high-resolution images in a Geographic Information System (GIS). This activity is normally conducted by rapid mapping services as requested by local authorities or humanitarian actors involved in the field (UNOSAT, 2011). When a particular flood event is not represented by any type of analysis, algorithms able to extract flood water from both commercial and open EO data (e.g., Sentinel-1, Pleiades, or TerraSAR-X) can be used to overcome this lack of information.

However, Earth Observation (EO) based services of flood mapping in rush mode generally suffer from delays caused by the time required for their activation, programming acquisitions, and image processing. This produces often excessive delays in delivering the first information on flood extent, which arrives several days after the events have occurred, while it would be extremely useful to have it in the early stages.

The use of meteorological, hydrological, and hydraulic models can fill this gap, ensuring data availability and information delivery in time. Early Warning Systems (EWS) provides useful information identifying potential extreme events even days in advance (Alfieri et al., 2013, 2014a). This helps local authorities to take precautions and to better manage the emergency.

Flood modeling is also crucial for preparedness. As an example, flood hazard modeling provides useful delineations of potential water depth in flood-prone areas for multiple magnitudes of the event. Flood hazard maps represent strategic assets for civil protection and disaster management because they allow the identification of the most vulnerable zones in a river basin and most risky areas through an accurate knowledge of exposure.

Therefore, flood modeling represents a key instrument for both early warning and preparedness. A synergy between numerical flood modeling and EO data is crucial. Flood models can complement the limitations of flood monitoring based only on satellite imagery and, at the same time, EO-based flood records can be used for the calibration and validation of the hydraulics models.

Background

Satellite-based flood monitoring services and early warning systems are consolidated practices, however, in different developing nations the use of such technologies is often not possible due to a lack of financial support. In such scenarios, it arises the need for an open integrated system able to couple the accuracy of satellite imagery with the usefulness of forecasting models. Even though different flood forecasting initiatives are now available from academia and research centers, such as the *GloFAS* (Alfieri et al., 2013), the *GFMS* (Wu et al., 2014), or the *CREST* (Wang et al., 2011) models, what is often missing is the connection between the timely hazard detection and the community response to warnings. To bridge the gap between science

and decision-makers, UN agencies play a key role in the dissemination of information in the field and capacity-building for local governments.

For these reasons since 2012 UNITAR-UNOSAT has been actively involved with partners (USGS, UNEP, CIMA Foundation, CERN) in the development of new flood prevention and flood response capacities to boost its emergency response in support to developing countries (Arcorace et al., 2015). This intent turned into practice through the “Flood Finder” initiative (Arcorace et al., 2016) which aimed to create an integrated flood forecasting routine to enable Early Warning services at the country level and support UNOSAT’s Emergency mapping service. This initiative was meant to effectively respond to the increasing demand for timely and accurate flood information needed by Government agencies, UN entities, NGOs, and vulnerable communities.

For this scope, a complex modeling system has been conceived to improve national, regional, and international coordination before and during major flood events through timely access to flood records, modeled flood hazard maps, early warning, as well as situation monitoring with remote and in situ observations. The Flood Finder system essentially integrates satellite observations, numerical weather prediction outputs, and in-situ data and consists of a hydro-meteorological forecasting chain for the estimation of modeled inundation scenarios based on streamflow forecasts. Results from pilot cases in Thailand, Mozambique, and the Horn of Africa demonstrated the feasibility and the usefulness of this system to enable early monitoring of flooded areas for emergency response and rush mapping. This system has been used and it is currently adopted by UNOSAT for multiple and slightly different implementations of flood forecasting/monitoring applications at the country level in Chad, Yemen, and Guyana.

Concerning the hydraulic modeling in the Flood Finder system, a simplified 1D model has been employed in the prototype, the USGS’s *GIS Flood Tool - GFT* (Verdin et al., 2016). The GFT model is based on Manning’s equations and it estimates water depth by combining the Height Above the Nearest Drainage (Nobre et al., 2015) and water stages calculated at given cross-sections. Such a tool has been also employed by UNEP and CIMA Foundation for the Flood Hazard Mapping of the UNISDR Global Assessment Report (GAR) of 2013 and 2015 (Herold and Rudari, 2013). This simplified hydraulic model has been improved to consider, for example, also backwater effects through the development of an ad-hoc version. The GAR2015 global flood hazard map version represents one of the major reference datasets for flood preparedness, given its simplicity and consistency at a regional scale.

Problem statement

In the context of the above-described flood monitoring, flood forecasting, and flood hazard mapping activities, in which CIMA Research Foundation is directly involved, this Ph.D. research aims to enhance the existing configuration of operational flood hazard mapping and EWS chains through an assessment of limitations and the proposition of new modeling solutions. The choice of this area of research is strategic due to its degree of innovation in this domain and its potential application in the field of Disaster Management.

This Ph.D. research aims to overcome some of the needs collected by the user community (local authorities, UN, NGOs, stakeholders, etc.). As an example, there is a need for accurate flood hazard maps, timely flood forecasts, and effective EO-based mapping over flood-prone areas of least developed countries. This is a priority for different ungauged basins across the world. In addition to that, a slim flood modeling tool could be also useful over gauged river basins for a fast delineation of floodplains during preliminary analysis and/or emergencies. Many hydraulic models are available in the literature with different numerical implementations of fluid mechanics in 1D or 2D approaches. However, it is difficult to find a modeling solution that is both slim

to reduce computation time and versatile to allow a rapid flood delineation at multiple scales. A possible solution is to combine EO data with simplified flood models, as investigated in this dissertation.

Therefore, the objective of this Ph.D. research is to integrate remote sensing and numerical modeling to enhance rapid flood modeling for flood hazard mapping and EWS. This research aims to:

1. identify limitations into existing flood modeling chains for flood hazard mapping and EWS and propose new solutions,
2. analyze the model connections between hydrological and hydraulic models and develop new methodologies,
3. design a robust and slim configuration of the hydro-modeling chain to be used for applications at multiple scales,
4. indicate and assess multi-source satellite-based methodologies to improve and calibrate/validate flood modeled results over poor data environments.

This thesis describes in detail the research carried out into this Ph.D. with a focus on these four objectives.

Thesis outline

The thesis is structured into 3 chapters: Chapter1 illustrates the material and methodologies needed for this research, Chapter 2 describes the method adopted for the fulfillment of the main research objectives, and Chapter 3 presents the application of this method over multiple case studies and compares achieved results with model benchmarks or in-situ observations. Finally, the last part of the thesis presents the conclusions from this research and provides discussion and closing remarks.

The **first chapter** includes a detailed review of the state of the art for both data and methods which are directly linked to this Ph.D. research. It begins with a description of one of the inputs required for flood modeling, which is the temporal evolution of streamflow across the basin. An overview of principal modeling and observation techniques is given to estimate water level and discharge from both stream gauges and remotely sensed data. This first section ends by presenting inland water mapping techniques using remotely sensed data.

The second section of this chapter presents the second input required for flood modeling, the digital elevation model. This second data source, in fact, represents the basis for DEM-based hydro geomorphological models, and thus this part of the thesis aims to present the state of the art of the estimation of surface terrain elevation and its hydrologically conditioning. After a panorama of the most referenced multi-source DEMs, the different techniques for the conditioning, such as filling, filtering, and flow enforcement, are shown.

Once these two essential inputs are effectively introduced, the third section explains the available techniques to extract hydrological derivatives and basin characteristics from the DEM. After a classification of multiple drainage models among dispersive and non-dispersive methods, an overview of drainage modeling of regular gridded elevation data using multiple GIS-hydro tools is given. Later, the traditional hydrological derivatives which are commonly derived from the DEM are also listed. Once input DEM and its hydrological derivatives are effectively presented, a wide variety of flood models available in the literature is analyzed.

In the last section of this chapter, after an in-depth overview and classification of hydraulic models, a critical analysis of low complexity flood models is presented by focusing on simplified methods built on different hydro-geomorphological approaches. Here it is highlighted the role of the Height Above the Nearest Drainage

(HAND) in multiple hydro geomorphological models developed in the last few years. The first chapter ends with a critical analysis of low complexity flood models and suggests a possible classification of HAND-based hydro geomorphological models between level and volume-driven approaches.

The **second chapter** of this thesis illustrates the method identified and adopted in this Ph.D. research, developed by employing a selection of the datasets, methodologies, or tools described in the first chapter. This chapter begins by presenting the novel modeling chain developed in this research for a rapid conversion of input discharge into an output flood map. The here presented *Rapid Estimation of Flood EXtent - REFLEX* model consists of a simplified 2D hydro morphological method in which a driven volume approach is employed to derive water depth maps from the HAND model.

After an overview of the whole REFLEX modeling chain, the chapter illustrates in detail all its components. The description of the REFLEX method begins by explaining how to collect and preprocess the inputs which are DEM, streamlines, and streamflow. After a brief explanation on how to properly gather and prepare input discharges, the chapter presents an in-depth overview of the DEM conditioning in REFLEX. The hydrologically conditioning in REFLEX is described by detailing the sequential workflow of filtering, filling, and the burning of streams into the DEM. Particular attention is reserved to the ad-hoc stream burning methodology developed in this Ph.D., which essentially relies on a slope-based filtering of the watercourse elevation profile by removing points having significant absolute local difference into river slope. Later, it is explained how to prepare the input flow lines required for the modeling in REFLEX.

After this introductory section, the chapter moves to the description of the core of this model. Thus, the first REFLEX module dedicated to the extraction of multiple hydrological derivatives from the hydrologically conditioned DEM is presented. Here, it is explained the employed drainage modeling schema and extracted derivatives in REFLEX.

Later, the second REFLEX module is essentially dedicated to the delineation of stream and watersheds, the classification of stream branches using multiple hierarchy schemas, the estimation of morphological parameters from the DEM for each sub-basin, and the computation of surface runoff volumes from input hydrographs across the entire river network.

Then, the third REFLEX module shows the extraction of HAND contours in the whole basin explaining how the HAND mapping is performed for each sub-basin. It is also detailed the novel model approach developed in this research for the artificial expansion of HAND contours to adjacent basins in flat areas, particularly designed for its application in coastal floodplains.

After that, the chapter illustrates the last REFLEX module, dedicated to flood modeling through a volume-driven inundation of HAND contours. At first, it is explained the static volume optimization algorithm, then it is shown how the transit time is estimated using a simplified version of the Manning formula, and, finally, how output flood maps are created. This portion of the chapter dedicated to REFLEX ends by explaining how the binary classification of predicted and observed flood extents is performed in the validation of flood modeling results.

The last section of this chapter describes the integration of external satellite-based observations to gather REFLEX auxiliary data. After the explanation of the intended usage in REFLEX of multiple EO-based water masks, it is proposed a method to derive water level surface height from radar satellite altimetry and useful methodologies for flood impact assessment using SAR data.

The third chapter summarizes the major outcomes of this Ph.D. research. The first section shows the results from the implementation work of the REFLEX model, which represents a synergy of different open Hydro-GIS toolsets, software, and codes from multiple sources. This section describes how to launch the REFLEX code, lists all the parameters included in the configuration file, and indicates the software dependencies.

After this first section dedicated to the REFLEX software, the third chapter includes all major results collected under multiple case studies spread among different geographical locations. Such results are obtained by using methods described in the second chapter of the thesis and are presented and discussed in the following five sections.

Sections from 3.2 to 3.5 are dedicated to the application of REFLEX using real data (DEM, Hydrographs) at multiple scales over different regions of the world. Case studies here described are the following: Magra, Entella, Secchia river basins in Italy at medium and local scales, and the one in Southern Africa at a regional scale. For each of these REFLEX case studies, the chapter provides a description of the context and the area of interest, explains the modeling approach employed, illustrates the flood modeled results obtained, and provides a validation of results. In such case studies, the REFLEX validation is performed by comparing predicted water extent and water depth with the ones from benchmark hydraulic models (e.g., flood hazard maps or flood scenarios from 2D models) using the binary classification metrics explained in the second chapter. When this has not been possible due to the scarce data environment or a larger modeling scale, such as in the Southern Africa case study, a qualitative assessment of REFLEX results has been made by using surface water extents derived from multi-temporal satellite imagery.

After the analysis of REFLEX results over gauged river basins in Italy and poorly gauged river basins in Southern Africa, the last section includes major outcomes from the complementary research activity about the integration of secondary data from Earth Observation. Preliminary results from the evaluation of radar altimetry and SAR data are shown in two separate case studies. The first one presents water level estimations using Copernicus's Sentinel-3 SRAL altimetry data in the Lake Chad Basin. The second one is about the combination of two different sources of information, the Copernicus Sentinel-1 SAR multi-temporal acquisitions and the HAND contours from filtered SRTM data to map water surfaces in Iran.

Chapter 1 - Material

The first chapter describes the material used in this Ph.D. research.

1.1 Introduction

This chapter provides basics and generalities, state of the art, main contributions, and last novelties in this area of research including available toolsets and data used either as input of the modeling or as reference for calibration and validation purposes.

1.2 Different ways to acquire water depth and surface extent observations

This first section introduces the first input required for the hydraulic modeling, which is the streamflow across the basin. An overview of principal modeling and observation techniques is given to estimate the water level and mapping the water extent.

1.2.1 Estimating water level and discharge along the river

Hereinafter is given a brief overview of multiple techniques commonly used in hydrology to measure or estimate water level and discharge along a river.

1.2.1.1 Field observation at stream gauges

River water level measurements at gauging stations are used in surveyed basins to monitor the evolution of the water stage over the years and to provide near real-time observations of the river over emergencies. In-situ data are not only essential for Near Real-Time (NRT) monitoring but are also an important source of information for calibrating and validating hydrological and hydraulics models. In situ data are also used by hydrologists to derive statistical information (e.g., flood river stage for a return period of 25 years) but also to calibrate hydrological models by comparing modeled discharges with the ones derived at gauges.

Field observations of river flow are usually collected by using stream gauges based on the optic, acoustic, floating, or radar measuring principles, current meters, and Acoustic Doppler Current Profiler (ADCP). Acoustic and radar gauging stations are the most employed techniques in surveying river basins. Most river gauging stations are designed to collect NRT measurements with high frequency and at high accuracy for flood prevention purposes. Stream gauges are normally installed over strategic points along the river network in which the river morphology is likely to remain constant across the years and cross-section geometry can be regularly surveyed (e.g., at bridges) also in the aftermath of a flooding event. This ideal configuration allows to locally convert river stage measurements into discharges via a calibrated rating curve.

Streamflow field observations are generally managed, collected, stored, and distributed by National Hydrological Departments (NHD). However, thanks to the joint effort of NHDs, international organizations, and research institutes, few global repositories of river flow measurements and statistics are also available to the public. Examples are the *“Long-Term Statistics and Annual Characteristics of GRDC Timeseries Data”* of WMO, the NASA DAAC’s *“Global River Discharge (RivDIS)”* that includes monthly averaged discharge observations over the 1807-1991 period, and the *“Monthly Flow Rates of World Rivers”* dataset from NCAR UCAR.

1.2.1.2 Modeled discharge from Hydrological Routines

Field observations from rain and stream gauges are essential information to employ hydrological routine over a surveyed river basin to translate rainfall information into a modeled discharge values over the entire river network. In absence of distributed field observations from rain gauges, hydrological modeling can also be carried out using satellite-based rainfall estimations. In fact, the forcing of hydrological models with satellite-derived precipitation products often represents the only possibility to model streamflow due to the lack of

near real-time in situ measurements in regions where those infrastructures are not available. Satellite observations coupled with meteorological models are capable to provides estimations of multiple physical quantities, such as precipitation, temperature, wind, and relative humidity, which are all needed inputs for the hydrological model to derive modeled surface runoff volumes.

An example of a hydrological routine is the Continuum model (Silvestro et al., 2013) developed by CIMA Research Foundation. This model is particularly suitable to be used with satellite-derived precipitation products, given its flexible applicability at multiple catchment scales and the good level of parameterization shown in past studies over data-scarce environments (Silvestro et al., 2015). The main outputs produced by the computational system are probabilistic and deterministic discharges in a defined number of outlet sections of the regional catchments. Such estimates represent key discharge estimations for flood modeling.

1.2.1.3 *Water surface height and discharge estimation from radar altimetry*

Where in-situ observations are not available, a remote sensing technique can be used to detect the height of large inland rivers by using information from satellite altimeters. In remote sensing, the time delay of the echoes of the microwave signal emitted from radar altimetry onboard a satellite is used to derive the height of the satellite above the earth's surface, and thus to estimate the height of a target point of the earth surface from the reference ellipsoid. Historically, this technique has been widely employed to derive sea surface height at a global scale, but over the last years, it has shown its potential also in the hydrological application for satellite-based monitoring of inland waters and estuaries (Vignudelli et al., 2019). Radar altimetry data is now widely employed across different hydrological applications (Créaux et al., 2018; Abileah et al., 2017). As an example, the data acquired from radar altimeters can be used to estimate the level of water bodies such as rivers, lakes, reservoirs, and flood plains, which is essential for environmental monitoring and natural resource management. The benefit of this remote sensing technique represents a key asset in data-scarce environments to track natural phenomena and to derive critical information economically and sustainably (Bogning et al., 2018).

Water surface elevation over large inland rivers can be currently measured by employing different radar altimeters onboard multiple satellites:

- Sentinel-3 A and B (Copernicus, ESA, EUMETSAT),
- CryoSat-2 (ESA),
- Sentinel-6 A (Copernicus, ESA, EUMETSAT),
- Jason-2 and Jason-3 (NASA, CNES, NOAA, EUMETSAT).

This amount of satellite-based information will be further enriched in the future with new missions partially or dedicated to inland water monitoring from space such as:

- “SWOT” (Surface Water and Ocean Topography) mission of NASA-CNES,
- “SMASH” (SMall Altimetry Satellites for Hydrology) mission of CNES,
- “CRISTAL” (Copernicus Polar Ice and Snow Topography Altimeter) mission of Copernicus, ESA.

The estimation of water surface elevation is generally not provided by the space agencies and an ad-hoc preprocessing of radar altimetry data (Level 1) is needed to derive this physical quantity. For this scope, multiple processors and tools are now available and open to the public to simplify the exploitation of radar altimetry data also to users not experts in remote sensing.

An example is the web processing service of the *SAR Versatile Altimetric Toolkit for Ocean Research and Exploitation* (SARvatore) Processor Prototype (Dinardo, 2020; ESA 2021b) available from ESA's Grid-Processing On-Demand (G-POD) distributed computing platform (<https://gpod.eo.esa.int/>). The SARvatore service enables simple on-demand processing of Copernicus's Sentinel-3, or ESA's Cryosat-2 altimetry data, and allows to obtain in output the physical quantities (Level 2 products) necessary to derive surface height over inland waters.

In addition to that, web platforms are also available for a direct visualization in the browser of satellite-based time series of water levels (Level 2 products) of rivers and lakes around the globe. Examples are the "Hydroweb" platform provided by Theia, LEGOS, and CNES, the "Database for Hydrological Time Series of Inland Waters - DAHITI" from Technical University of Munich (TUM), and the "Global River Radar Altimetry Time Series - GRRATS" from Ohio State University.

Over the last few years, particular attention has been reserved to estimate discharge from water surface heights derived from satellite altimetry. The methods available in the literature employ different modeling techniques by combining data fusion of multi-sensor EO data (Kebede et al., 2020; Tarpanelli et al., 2013, 2019). A particular interest is given to this application due to its potential in estimating discharge globally from multiple radar satellite missions, particularly over data-scarce environments.

1.2.2 Inland waters mapping using remotely sensed data

Earth Observation data not only allow to estimate the time evolution of rainfall and river water level but also to map the extent of water bodies.

Spaceborne or aerial optical imagery represents the most intuitive way to monitor a river from above for both flooding and water resource management purposes. However, the ground information derivable from optical EO data directly depends on the cloud coverage. Cloud coverage can extremely affect the result of EO-based inland water mapping in tropical regions or during a flooding event due to a tropical storm. EO imagery from Synthetic Aperture Radar (SAR) sensors instead, given their all-weather capabilities, are not affected by this limitation. As a result, SAR data are widely employed under multiple flood mapping algorithms such as the "Hierarchical Split Based Algorithm" (Chini et al., 2017) of the HASARD on-demand flood mapping processing service developed by the Luxembourg Institute of Science and Technology (LIST), available in the ESA's G-POD (ESA, 2021a).

The exploitation of multi-temporal and multi-source optical EO data is also used to derive from multiple satellite imagery a binary classification of land and water, also referred to as water masks. Such masks indicate a probability to find permanent water bodies over a given pixel. Examples of global water masks are the: 100% Water Occurrence from the Global Surface Water dataset (Pekel et al., 2016; JRC, 2021), and the waterbody class from the ESA CCI Land Cover product. In most cases, water masks are derived from the classification of multiple mid-resolution optical images acquired over a specific period (e.g., Landsat mission). As an example, more than 30 years of observations from Landsat missions have been used in the production of the GSW dataset (Pekel et al., 2016).

Furthermore, in addition to the mapping of permanent water bodies, also river geometry can be derived from satellite imagery. Landsat imagery has been also employed in the creation of the "Global River Bankfull Width and Depth Database" (Andreadis et al., 2013), also based on the widely employed USGS's HydroSHEDS (USGS, 2008) river delineation from SRTM elevation data, which provides a distribution of the river bankfull width and depth for major basins of the globe.

1.3 The estimation of surface terrain elevation and its hydrologically conditioning

This section provides state-of-the-art for the second remotely sensed input for the hydraulic modeling, the digital elevation model. This source data represents the basis for DEM-based hydrological modeling.

1.3.1 Multiple sources data for different Digital Elevation Models

A Digital Elevation Model (DEM) is a geometric representation of the land surface in a digital format. For a specific surveyed area, the DEM is conceived using either regular grids or meshes and the elevation values are geolocated using a projected or geographic coordinate system. In a Raster, or a Triangular Irregular Network (TIN) DEM, the pixel, or the triangular facet, represents an elevation to a reference surface or vertical datum (e.g., above the local mean sea level).

A DEM can be derived from multiple passive or active sensors onboard either satellite or airborne platforms. As an example, concerning active sensors, acoustic waves (SONAR) or radio waves (RADAR) measurements are used to derive respectively bathymetries over the sea and DEM over the land. Also, passive sensors, that measure the Electro-Magnetic (EM) radiation reflected by the Earth's surface, allow deriving a DEM. Examples of remotely sensed topography from passive measurements are the 3D terrain models derived from stereo pairs of optical images and photogrammetry (e.g., using Very High-Resolution images acquired from UAV or airborne topographic survey). Another example is the *Light Detection And Ranging* (LiDAR) sensor which represents one of the most accurate methods for creating high-quality and high-resolution DEMs.

Such remote sensing techniques have been applied to derived multiple global DEMs at different scales. As an example, the phase of the radar signal acquired in 2000 from a Synthetic Aperture Radar (SAR) sensor on board a space shuttle has been used to derive, using an interferometric SAR (InSAR) technique, a global DEM from NASA's Shuttle Radar Topography Mission (SRTM) data. The USGS's *SRTM DEM* is one of the most known and employed global DEM (homogeneous near-global coverage from 56°S to 60°N) available at both 1 -arc-second (~30m) and 3 arc-second (~90m) spatial resolution. Other examples of medium-high resolution global DEM are NASA's *Advanced Spaceborne Thermal Emission and Reflection Radiometer (ASTER) Global DEM (ASTER GDEM)*, the *ALOS World 3D DEM (AW3D DEM)* from the Japan Aerospace Exploration Agency (JAXA), and the *WorldDEM* from the TanDEM-X mission of the German Aerospace Center (DLR).

Dataset	<i>SRTM DEM</i>	<i>ASTER GDEM</i>	<i>AW3D DEM</i>	<i>WorldDEM</i>
Mission	SRTM	Terra	ALOS	TanDEM-X
Sensor	SIR-C/X-SAR	ASTER	PRISM	SAR-X
Agency	NASA-JPL	NASA METI	JAXA	DLR
Method	InSAR	Stereo-pair photogrammetry	Stereo-pair photogrammetry	InSAR
Acquired	2000	Since 1999	2006-2011	2011-2015
Released	2002, 2014 outside US for the 1 arc sec data	2009	2016	2016

Coverage	60°N - 56°S	Global	Global	Global
Spatial Resolution	3" ~90m or 1" ~30m	1" ~30m	1" ~30m or 0.15" ~5m	0.4" ~12.4m or 3" ~90m
Vertical accuracy	6-9m LE90	15-20m LE90	7m LE90	<4m LE90
Access	Open	Open	Commercial and Open (AWD30)	Commercial and Restricted

Table 1 – Characteristics of a selection of Global Digital Elevation Models (Source: NASA, USGS, DLR, JAXA, Copernicus).

These sources of global elevation data differ in terms of accessibility, acquisition time, spatial resolution, coverage, vertical accuracy, and access (see Table 1). Thus, the employment of one of these datasets as input raw DEM for the hydrological modeling requires a complete evaluation of all these characteristics. As an example, the SRTM 1 arc-second and the AW3D30 datasets are valuable options for hydrological and hydraulic modeling at a regional/local scale given their spatial resolution, and vertical accuracy. Instead, LiDAR data represents the optimal option for flood modeling at a local scale because of the high-quality data at the 1-meter spatial resolution, which is needed to represent in detail the geometry of the river and infrastructures.

Often the DEM is used as a general term to represents two different types of digital surfaces, the Digital Surface Model (DSM) and the Digital Terrain Model (DTM). A DSM represents the elevation of the surface as seen from above by the sensor and thus includes the elevation of Top Of Canopy (TOC), building roofs, bridges. Instead, the DTM represents the elevation of the bare land surface and is the one often employed in hydrology for surface runoff modeling. In most of the remote sensing techniques, the product is a DSM and the DTM is derived after processing the elevation data using different conditioning and filtering methods.

1.3.2 DEM conditioning

A pre-processing of the input elevation grid is necessary while handling raw DEM. Hereinafter are described some of the techniques often employed in this domain.

1.3.2.1 Filtering

The problem of filtering noisy DEM can be addressed by using multiple interpolations and filtering procedures (Sithole and Vosselman, 2003; Wang et al., 2019; Meng et al., 2010). Vosselman (2000), Roggero (2001), Sithole (2003), and Wang and Tseng (2010) used slope-based filters to identify ground elevation. To remove non-ground measurement from High Resolution (HR) elevation data Zhang et al. (2003) and Pingel et al. (2013) employed morphological filters. Other methods adopt linear regression, cluster/segmentation, or iterative interpolating techniques. However, for hydrological applications, the DEM filter must maintain small drainage features in the output ground elevation which is not often possible in most of these methods. Thus, the methods often employed for the filtering of DEM in slope-sensitive applications are the feature-preserving denoising algorithms (Sun et al., 2007; Gallant, 2011; Lindsay et al., 2019; Chen et al., 2019). As an example, Stevenson et al. (2010) employed a feature-preserving denoising algorithm (Sun et al., 2007) to remove speckle noise from medium resolution interferometric SRTM data. The adaptive smoothing filter for speckle noise removal proposed by Gallant (2011) has been used instead to smooth SRTM data over the entire Australian continent in the *DEM-S* (Geoscience Australia, 2021) and the entire globe in the *Multi-Error-Removed Improved-Terrain (MERIT)* DEM (Yamazaki et al., 2017).

Concerning the filtering of HR elevation data, Lindsay et al. published in 2019 a method that can be efficiently used to denoise high-resolution DEM such as the LiDAR data. Some of them are directly integrated into GIS software such as the “*MDenoise*” program (Sun et al., 2007) available in both GRASS GIS and SAGA GIS. *MDenoise* is the one chosen for this research. Despite its limitations in processing LiDAR data (Lindsay et al., 2019), it is a valuable solution for filtering InSAR-derived DEM which are often the only ones available at global or regional scales. Limitations in the application of the smoothing method proposed by Sun et al. with large DEM, such as the LiDAR ones, have been highlighted due to a not efficient triangular-based iterative algorithm (Lindsay et al., 2019).

1.3.2.2 Filling

The “Filling” of the DEM is another necessary technique to remove depressions from the filtered elevation grid. A depression, also commonly referred to as pit or sink, is a cell that is surrounded by higher terrain. This happens to a cell when all the eight neighbor cells have higher elevation. Thus, a drainage direction cannot be computed since it is not possible to identify a surrounding cell having lower elevation, and consecutively the modeled flow path is interrupted. A detailed mapping of the principal typologies of features to be considered in the DEM flow enforcement (Figure 1), such as pits, depressions, flats, and sinks, is the one proposed by Lindsay (Lindsay, 2016).

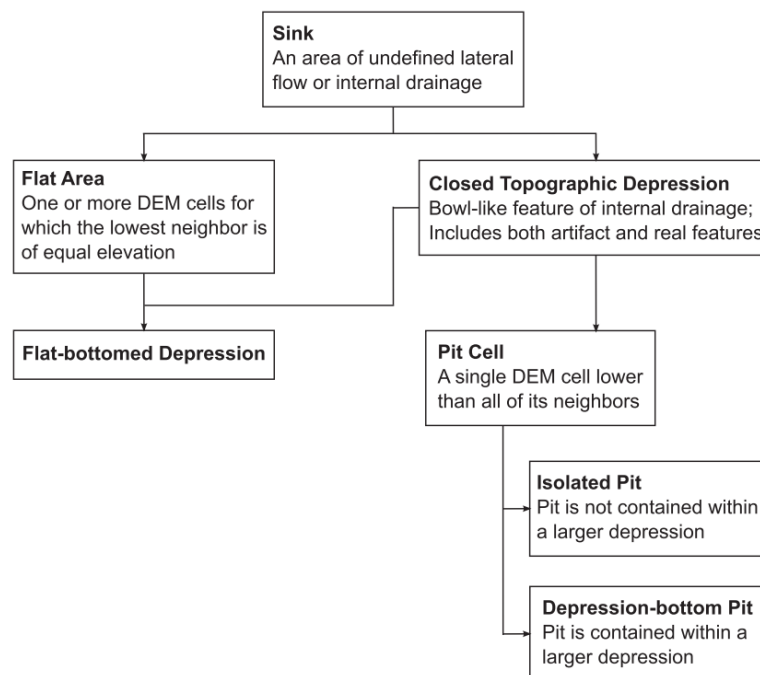


Figure 1 - typology of features in DEM flow enforcement (Source: Lindsay, 2016).

Not all the sinks, that can be derived from topography, need to be processed during the hydrological conditioning of a DEM. A depression can either represent a natural sink or a spurious topographic error. Thus, the drainage enforcement of the DEM should be focused only on such spurious errors. Natural sinks must be preserved in the DEM (Verdin and Jenson, 1996) because they characterize watersheds with no outlet, also referred to as endorheic basins.

The creation of a depression-less DEM is an iterative process in which each of the identified sinks is filled to its pour point elevation. In the upslope contributing area of a sink, the pour point is the cell having the lowest elevation of the ones that belong to the border of the watershed. An iterative filling process is needed because, once the first depression is filled, new sinks may result at the boundary of the filled area which then

needs to be processed again in the following iteration. Therefore, this process can be as time-consuming as the spatial resolution, the coverage, or the level of bias of the DEM is increasing.

Multiple methods to deal with sinks are available in the literature (Wang et al., 2019). Some of them, named *depression-filling*, solve the problem by raising the elevation of the depressed area (Jenson and Domingue, 1988; Planchon and Darboux, 2002; Wang and Liu, 2006). In other methods, also referred to as *depression-breaching*, the removal of the downstream obstacle that creates the sink is overpassed by carving a descending path from the identified depression (Soille P. et al., 2003). Some others employ a *hybrid* approach that combines filling with carving (Soille P., 2004; Barnes et al., 2014).

Particular attention should be deserved while employing a pit removal method in the hydrological conditioning of High-Resolution DEM. As an example, *depression-filling* methods in some cases can destroy all traces of the original DEM by filling large areas of the river environment. Alternatively, the *depression-breaching* approach can sensitively change local hydraulics due to an artificial change into infrastructure topography, with effects like a breach into the dykes or the opening of a culvert in a dam. Hybrid approaches represent a good compromise for this application due to a balance of these two effects.

Concerning applications, numerical implementations of the above-mentioned filling methods are available via GIS software, hydrological specialized software, or GIT repositories. Examples of such tools are the “*r.hydrodem*” add-on of GRASS GIS (Lindsay and Creed, 2005; GRASS Development Team, 2021j), the “*Fill*” tool from the Spatial Analyst extension of ArcGIS (Planchon and Darboux, 2002), the module “*Fill Sinks*” of SAGA GIS (Wang and Liu, 2006) the “*Pit Removal*” tool in TauDEM software (Tarboton, 1997; Tesfa et al., 2011), and the “*richdem*” software (Barnes et al., 2014; Zhou et al., 2016).

If plateaus are produced because of the complete filling of depressions, artificial flat areas need to be solved while computing flow direction. This problem can be solved by filling with a not flat surface driven by a small artificial gradient or by employing ad-hoc iterative procedures to resolve flats. In *richdem*, both these approaches are implemented using respectively the *epsilon filling* and the *flat resolution* tools (Barnes, 2016).

1.3.2.3 Flow enforcement for hydrologically adjusted elevation

Flow enforcement is necessary to correct misleading flow paths derived from DEM flow directions. This is often caused by flow obstacles due to residual artifacts not properly removed from the DEM after the filtering and the filling steps. Furthermore, a wrong delineation of streams from the DEM often occurs in very low elevation gradient water tables such as lakes and major rivers. In such areas, the flow enforcement is often employed by “burning streamlines into the DEM”. This technique aims to overcome the problems described above by artificially deepening the DEM elevation along a line and, thus, forcing flowlines to follow real streams derived from field observations, water masks, or visual interpretation of high-resolution imagery.

1.3.3 Examples of multi-source DEM datasets.

Examples of semi-global hydrologically conditioned DEM are the *HYDROlogical data and maps based on Shuttle Elevation Derivatives at multiple Scales - HydroSHEDS* (USGS, 2008; Lehner et al., 2008), and the *SRTM-FM* (Arcorace et al., 2015). Instead, concerning global hydrologically adjusted elevation datasets, an example is the Hydrologically Adjusted Elevation of the *Multi Error Removed Improved Terrain - MERIT-hydro* (Yamazaki et al., 2017) datasets at 3 Arc-Seconds derived from different iterative correction process of SRTM3 and AW3D-30m data. Another global hydrologically conditioned DEM is the one available within the *Hydrologic Derivatives for Modeling and Analysis - HDMA* database (Verdin, 2017) which combines elevation data from the HydroSHEDS (Lehner et al., 2008), *Global multi-resolution terrain elevation data - GMTED2010*

(Danielson and Gesch, 2011) and the CGIAR-CSI *Void Filled SRTM data* (CIAT-CSI, 2004; Reuter et al., 2007; Jarvis et al., 2008).

The DEM of HydroSHEDS, the GMTED2010, and the MERIT-hydro DEM from the University of Tokyo are freely available to the public. Instead, the SRTM-FM, made by UNITAR-UNOSAT from SRTM data using the ANUDEM method (Hutchinson, 1989, 2011), has restricted access. Both HydroSHEDS and SRTM-FM have been derived from filtered SRTM data which has been then conditioned by burning the streams into the DEM. In all these conditioned DEMs the original elevation of terrain is artificially altered to be used for extracting coherent hydrological derivatives for flood mapping purposes. DEM-based hydrological derivatives are further described in the following sections of this chapter.

Finally, an overview of multi-source DEM products that provide void-filled, filtered, and hydrologically conditioned elevations is shown in Table 2.

Dataset	Type	Source	Producer	Horizontal resolution
HydroSHEDS	DSM-hydro	SRTM3	WWF	90m
CGIAR-CSI DEM	DSM	SRTM3	CGIAR-CSI	90m
SRTM-FM	DSM-hydro	SRTM3	UNOSAT, USGS	90m
MERIT DEM	DSM-hydro	SRTM3, AW3D30	IIS University of Tokyo	90m
HDMA	DSM-hydro	SRTM3, GMTED2010	USGS, NASA GSFC	3 arc-sec for SRTM3 coverage, 7.5 arc-sec for areas north to 60°, and 20 arc-sec for Antarctica.
EU-DEM	DSM	SRTM, ASTER, ICESat	EEA/Copernicus	25m
COP-DEM	DSM	Tandem-X, ASTER, SRTM, AW3D30, and others	Copernicus	10m (EEA-10), 30m (GLO-30), and 90m (GLO-90)
NASADEM	DSM	SRTM, ASTER, and other sources	NASA	30m

Table 2 – Examples of Multi-source Digital Elevation Models products.

SRTM data is widely employed in most of these products given its consolidated usage over the last 20 years and the multiple reviews and enhancements made to this data across the years (Jarvis et al., 2008).

1.4 Extract hydrological derivatives and basin characteristics from the DEM

This section explains what are the derivatives that can be extracted from a conditioned DEM to be used for hydrology by illustrating the state-of-the-art methods retrieved from the literature.

1.4.1 Drainage modeling

Most of the drainage direction methods available in the literature for a grid-based DEM can be classified into two groups: Single Flow Direction (SFD), or non-dispersive algorithms, and Multiple Flow Direction (MFD), or dispersive algorithms. The differences among these methods can be summarized by the following statement extracted from the paper of Wolock and McCabe: “An SFD algorithm assumes that subsurface flow occurs only in the steepest downslope direction from any given point; an MFD algorithm assumes that subsurface flow occurs in all downslope directions from any given point” (Wolock and McCabe, 1995). Hereinafter a

review of the state of the art is given by including a critical analysis of the most referenced methods to define local drain directions at the surface available in the literature.

1.4.1.1 *Single Flow Direction (SFD) – Non-dispersive methods*

A list of *local non-dispersive* or SFD methods are reported below:

- Deterministic Eight-Node (D8) (O’Callaghan and Mark, 1984),
- Rho4 and Rho8 (Fairfield and Leymarie, 1991),
- Lea’s Method (Lea, 1992).

An example of the Path-Based non-dispersive method is the *Deterministic Eight-Node Least Transversal Deviation -D8-LTD* (Orlandini et al., 2003; Orlandini and Moretti, 2009).

Many SFD methods discretize drainage directions into eight cardinal points of the compass (Fairfield and Leymarie, 1991; Lea, 1992; O’Callaghan and Mark, 1984; Orlandini et al., 2003). The Deterministic Eight-Node (D8) method is a classic example of a non-dispersive method. While applying this SFD method over divergent hillslope, the surface flow does not diverge but converge by flowing on a single flow path. The D8 developed by O’Callaghan and Mark in 1984 has been widely employed in multiple following studies and applications (Jenson and Domingue, 1988; Mark, 1984; Martz and Garbrecht, 1992). Other alternatives to the D8 method have been also proposed a few years later (Fairfield and Leymarie, 1991; Lea, 1992), however, a significant extension to the D8 algorithm has been only introduced in the early 2000s with the publication of a path-based non-dispersive D8-LTD method (Orlandini et al., 2003).

1.4.1.2 *Multiple Flow Direction (MFD) – Non-dispersive methods*

SFD algorithms have shown intrinsic modeling limitations, particularly over flat areas, because water does not drain only in eight directions. Attempts to overcome the limits of SFD algorithms resulted in the identification of multiple flow directions (MFD) drainage models. Therefore, different MFD algorithms have been developed across the years by following different approaches. The most referenced MFD algorithms are listed below:

- Freeman Multiple Flow Direction (FMFD) (Freeman, 1991),
- Holmgren Multiple Flow Direction (Holmgren, 1994),
- Quinn Multiple Flow Direction (QMFD) (Quinn et al., 1991),
- DEMON (Costa-Cabral and Burges, 1994),
- Pilesjö/Zhou algorithm (Pilesjö and Zhou, 1996),
- Deterministic Infinite-Node (DINF) (Tarboton, 1997),
- MFD based on maximum downslope gradient (MFD-md) (Qin et al., 2007),
- Triangular Multiple Flow Direction (TMFD) (Seibert and McGlynn, 2007),
- Triangular Facet Network (TFN) (Zhou et al., 2011).

Some methods estimate flow directions in each direction by looking at slope gradients (Freeman, 1991; Holmgren, 1994; Quinn et al., 1991; Wolock and McCabe, 1995) and with improvements in letting drainage converging over concave surfaces (Pilesjö and Zhou, 1996). In later studies, other authors revisited the concept of centroid-based modeling flow movement within a DEM by following a vector-based approach derived from a partition of cells into triangular facets. The aim was to reduce the impact of a grid data structure into derived flow patterns. Examples of such MFD based on triangular facets are the *D-infinity* drainage method (Tarboton, 1997), the *Triangular Multiple Flow Direction* (Seibert and McGlynn, 2007), and the *Triangular Facet Network* algorithm (Zhou et al., 2011).

1.4.1.3 Drainage modeling using GIS-hydro tools

Most of the drainage methods described in the previous section have been implemented within a various range of GIS-Hydro software such as:

- 1) ArcGIS (ArcINFO; ArcMap, ArcGIS Pro),
- 2) Geographic Resources Analysis Support System (GRASS),
- 3) Terrain Analysis Using Digital Elevation Models (TauDEM),
- 4) System for Automated GeoScientific Analysis (SAGA),
- 5) RichDEM Terrain Analysis Software.

Hereinafter an overview of widely used GIS/Hydrological software is presented to highlight the pro and cons of each tool and to identify the more suitable solution for a flood modeling chain based on open-source software and deployable into Linux OS.

1.4.1.3.1 ArcGIS

“ArcGIS” is a licensed GIS software developed by ESRI, the Environmental System Research Institute, (ESRI, 2021a). ArcGIS is Windows-only compatible program. The ARC/INFO hydrological modeling functions are retrievable from the Hydrology section of the Spatial Analyst extension (ESRI, 2021b). In particular, the ArcGIS’s Flow Direction tool offers to the users three different drainage methods:

- 1) D8,
- 2) MFD,
- 3) DINF.

Such drainage methods have been included in the “Flow direction”, “Flow Accumulation”, and “Flow Distance” toolsets. The implementation of the D8 algorithm (ESRI, 2021b; O’Callaghan and Mark, 1984) follows the approach presented by Jenson and Domingue (Jenson and Domingue, 1988) and the encoding of topological surrounds presented by Greenlee (Greenlee, 1987). In addition to the D8, other two dispersive methods are available in this toolset: the MFD-md algorithm (Qin et al., 2007) and the D-infinity one (Tarboton, 1997).

While using the D8 in ArcGIS, the resulting Flow Direction raster is an integer raster in which values follow a pre-defined direction coding for each of the eight directions from the center cell. Such codes (Figure 2) are defined in a clockwise rotation with a 2 power N geometrical progression from 1 (east) to 128 (north-east).

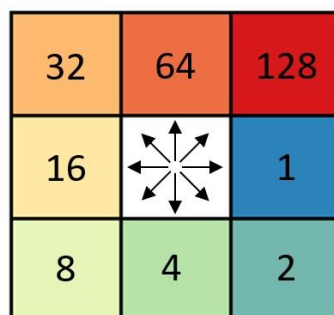


Figure 2 – ArcGIS D8 Flow Direction encoding

The output of the Flow direction tool using the D-infinity algorithm is a floating-point raster which represents the distribution of flow direction angles in degrees across the domain by following a counterclockwise rotation from 0 (due east) to 360 (again due east).

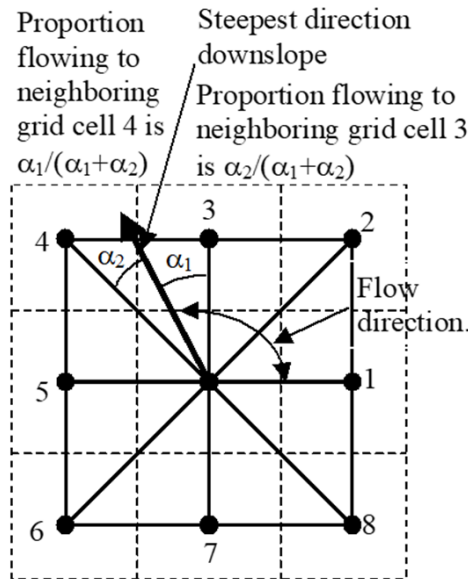


Figure 3 - Schema of D-inf flow direction (Image credits: TauDEM)

1.4.1.3.2 GRASS

The “*Geographic Resources Analysis Support System - GRASS*” software (GRASS Development Team, 2021a) is part of the Software Projects of the Open Source Geospatial Foundation (OSGeo). GRASS GIS is free and open-source software licensed by GNU General Public License. GRASS supports multiple Operating Systems (OS) such as Mac OSX, Microsoft Windows, and GNU/Linux. In GRASS the estimation of flow direction raster can be addressed by using different add-ons repositories such as:

1. MFD and D8 in “*r.watershed*” (GRASS Development Team, 2021b),
2. MFD and D8 in “*r.terraflo*” (GRASS Development Team, 2021c),
3. SFD in “*r.flow*” (GRASS Development Team, 2021d).

The *r.watershed* add-on (Ehlschlaeger, 1989; Metz et al., 2011) adopts a MFD algorithm (Holmgren, 1994) as default drainage method. However, the D8 algorithm is also integrated into this repository and can be employed by using a dedicated flag. A MFD method (D-inf) and an SFD one (D8) are also available in GRASS through the *r.terraflo* add-on (Toma et al., 2001) from Duke University. Finally, another similar toolset is the one provided by the *r.flow* add-on (Mitasova et al., 1995) which employs a vector-driven SFD.

GRASS drainage encoding is different from the one adopted by ArcGIS and ranges from 1 (north-east) to 8 (east) in a counterclockwise rotation (Figure 4). Negative values in output flow direction obtained with GRASS GIS indicates that the flow from the cell is leaving domain boundaries.

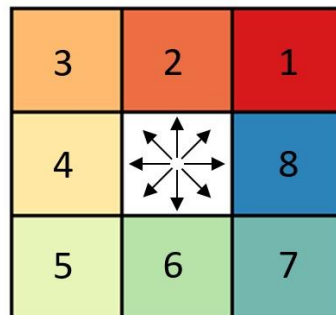


Figure 4 - GRASS GIS drainage encoding for D8 and MFD algorithms

1.4.1.3.3 TAUDDEM

The “*Terrain Analysis Using Digital Elevation Models - TauDEM*” software from the Utah State University Hydrology Research Group (Tarboton, 2021) provides a wide range of tools (a total of 34 executables from Basic, Stream Network, and Specialized Analysis algorithms) for the extraction of hydrological information from the DEM (Tarboton, 1997; Tarboton and Baker, 2008; Tesfa et al., 2011). TauDEM represents an evolution of its predecessor *TARboton Digital Elevation Models - TARDEM*. This software is meant to be used on Windows OS and it can be integrated into both QGIS (QGIS Development Team, 2021) and ArcGIS via a dedicated QGIS add-on and ArcGIS toolbox. For Linux OS, the source code available in GitHub must be compiled through the given UNIX make files. Concerning flow direction algorithms, TauDEM offers:

- 1) D8,
- 2) DINF.

Such methods can be used to derive drainage grids using the “D8 Flow Direction” (O’Callaghan and Mark, 1984) and the “D-infinity Flow Direction” tools (Tarboton, 1997). In the implementation of the D8 algorithm, TauDEM employs the method presented by Garbrecht and Martz for assigning flow directions over flat areas (Garbrecht and Martz, 1997). While estimating drainage from a not hydrologically conditioned DEM, the execution of “Pit remove” from TauDEM is essential before deriving the flow directions raster. Flow accumulation raster can be derived using the “D8 Contributing Area” or the “D-infinity Contributing Area” tools. A grid containing the distance to stream can also be derived from the DEM by using the “D8 Distance to Streams” or the “D-infinity Distance Down” tools. Algorithm performance in TauDEM is achieved through parallel processing of domain partitions by using the Message Passing Interface (MPI).

1.4.1.3.4 RichDEM

The “*RichDEM High-Performance Terrain Analysis*” software (Barnes, 2020) allows to pre-process DEM (e.g. depressions filling and breaching) and to derive its hydrological derivatives using a range of eight different drainage methods: D8, D4, Rho8, Rho4, Quinn, Freeman, Holmgren, and D-inf. To have an aesthetically pleasing drainage pattern over flats the Barnes Flat Resolution algorithm or the Epsilon Filling methods are available (Barnes, 2016; Barnes et al., 2014a, 2014b). This toolset has been developed by Richard Barnes from Energy and Resources Group, Berkeley, USA.

1.4.2 Hydrological derivatives

Multiple hydrological derivatives can be extracted from a conditioned DEM:

- DEM slope,
- Flow direction grid,
- Flow accumulation grid (number of cells),
- Sink points,
- Drainage area (square km),
- Streamlines,
- Watershed of the whole basin,
- Watersheds divide for each sub-basin,
- Sub-outlets for each branch of the river network.

All these products can be derived by using various GIS software like the ones mentioned in section 1.4.1.3.

An example of the hydrological derivatives of the UNOSAT's SRTM-FM dataset (Arcorace et al., 2015) for an entire African Hydrologic Region (Zambezi river basin) is shown in Figure 5. Similar derivatives are also provided into the WWF's HydroSHEDS and the USGS's HDMA datasets.

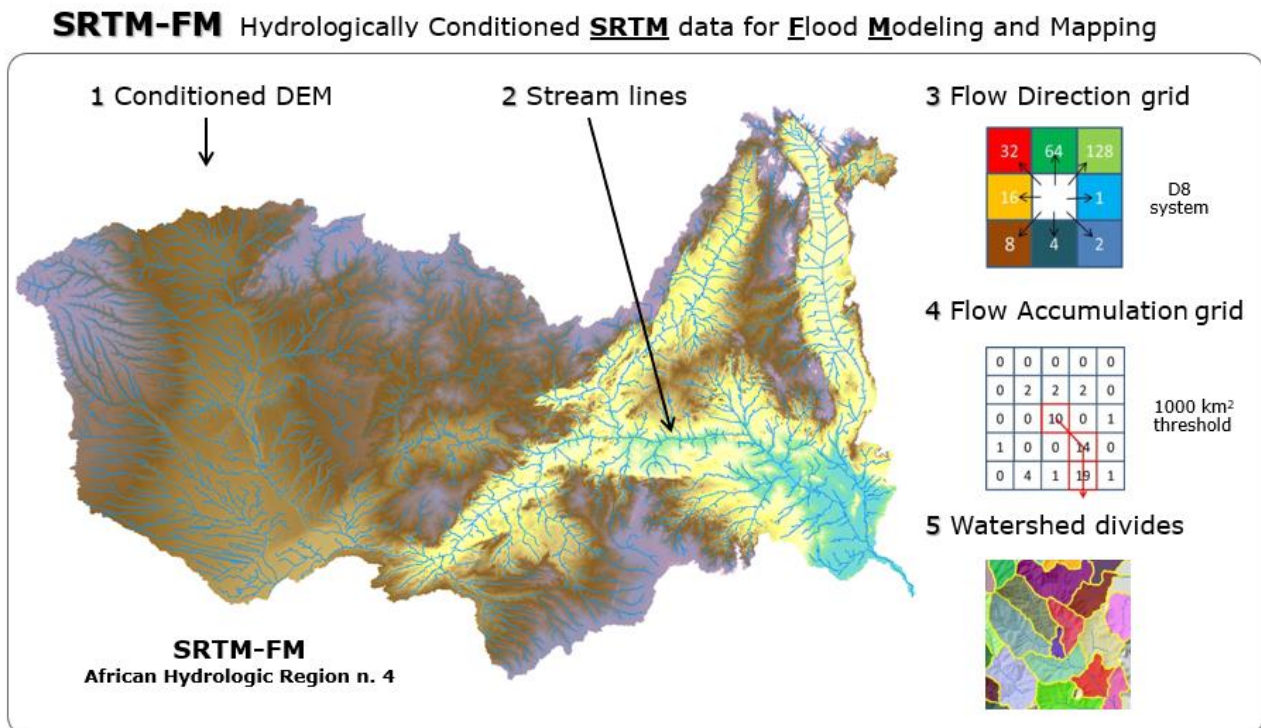


Figure 5 – Example of derivatives from hydrologically conditioned DEM (Arcorace et al., 2015).

Concerning the delineation of flowlines, the streamlines derived from the DEM are often classified by assigning a different order to each branch of the network. In geomorphology, a topological ordering is, in fact, necessary to define the hierarchical position of each branch within the river network. Multiple methods are available in the literature for the computation of stream hierarchy:

- Horton (1945),
- Strahler (1952),
- Hack (1957),
- Pfafstetter (1989),
- Shreve (1996).

All these stream coding systems can be directly derived from input streamlines by using various GIS toolsets dedicated to hydrology.

Finally, the hydrologically conditioned DEM can also be used to derive some essential geomorphic characteristics of the basin such as the length and the slope of each river branch, the slope of the main stem, as well as the time of concentration for each watershed.

1.5 Low-complexity flood models

This section provides a panorama of existing 1D/2D hydraulic models and geomorphological ones. It aims to introduce the state of the art concerning the numerical modeling topic of this Ph.D. thesis.

1.5.1 Simplified 2D hydrodynamic models

Multiple hydraulic models are available in the literature (Afshari et al., 2017) which are essentially based on different numerical implementations of mathematical simplification taken from basic fluid mechanics such as the backwater and Navier-Stokes equations.

Most of these tools rely on a one-dimensional (1D) hydraulic modeling approach based on the momentum equation of Saint-Venant equations (differential conservation equations of mass and momentum of flow).

In particular, the various 1D hydraulic modeling approaches, such as the one adopted in HEC-RAS or MIKE11, are based on finite-difference solutions of the full Saint-Venant equations. These models represent river floodplains as a sequence of cross-sections along the Thalweg and perpendicular to the direction of flow. Consequently, 1D modeling is widely employed with the combination of traditional field surveying in which cross-sections are derived in the field during the dry season. One of the challenges in using this approach is the choice of appropriate cross-section locations along the river.

The cross-section domain discretization of the 1D models does not allow a continuous representation of topography. The output flood inundation extent in a 1D model is approximated by interpolating the water depths calculated at each cross-section.

More advanced models, such as the ones based on two-dimensional (2D) hydrodynamic modeling approaches allow a better representation of real river hydrodynamics by solving Navier-Stokes equations and the depth-averaged continuity using finite difference (FDM), finite-volume (FVM), or finite-element (FEM) methods.

The adoption of a high-resolution DEM coupled with a 2D hydraulic model can overcome these limitations through more consistent modeling of river hydraulics. However, 2D models are employed for floodplain modeling only under certain conditions. Most of these 2D hydraulic models require, in fact, a high number of initial tide heights and inflow/outflow boundary conditions which are not easy to determine in data-poor environments. Furthermore, the computational effort to run these models remains an important parameter to be taken while integrating a 2D model in an operational modeling system. As a result, traditional 2D hydraulic models are often replaced with simplified DEM-based hydrodynamic approaches for flood hazard assessments at medium-large scales.

Model	Developer	Type	Method	Reference	License
<i>HEC-RAS 1D</i>	United States Army Corps of Engineers (USACE)	1D	Cross-section FDM	Brunner, 2016	Public domain
<i>MIKE 11</i>	Danish Hydraulic Institute (DHI)	1D	Cross-section FDM	DHI, 2017	Commercial
<i>SOBEK 1D</i>	TU-Delft Deltares	1D	Cross-section FDM	Deltares, 2019	Commercial
<i>AutoRoute</i>	United States Army Corps of Engineers (USACE)	1D/2D	Cross-section FDM	Follum et al., 2012	Public domain
<i>LISFLOOD-FP</i>	Bristol University	1D/2D	Simplified FVM	Bates and De Roo, 2000	Free (non-comm. use)

<i>MIKE Flood</i>	Danish Hydraulic Institute (DHI)	1D/2D	Cross-section and Regular/nested grid FDM	DHI, 2017	Commercial
<i>TUFLOW</i>	BMT WBM	1D/2D	Structured grid FDM	Syme, 2001, GS	Commercial
<i>ANUGA</i>	Australian National University (ANU)	2D	Triangular mesh FVM	Mungkasi and Roberts, 2012, DOI	Open Source
<i>BASEMENT</i>	ETH Zurich	2D	Flexible mesh FVM	Vetsch et al., 2005	Free
<i>FESWMS-2DH</i>	USGS	2D	Irregular mesh FEM	Froehlich (1989)	Free
<i>FLO-2D</i>	FLO-2D Software Inc	2D	Structured grid FDM and FVM	FLO-2D Software Inc, 2020	Commercial
<i>HEC-RAS 2D</i>	United States Army Corps of Engineers (USACE)	2D	hybrid discretization of FDM and FVM	Brunner, 2016	Public domain
<i>IBER</i>	Universitat Politècnica de Catalunya (UPC), Universidade da Coruña (UdC)	2D	Structured and not structured mesh FVM	Bladè et al., 2014, DOI	Public domain
<i>iRIC Nays2DFlood</i>	Hokkaido University	2D	Regular grid FVM	Shokory et al., 2016, DOI	Public domain
<i>JFLOW</i>	JBA Consulting	2D	Regular grid FDM	Bradbrook et al., 2004, DOI	Commercial
<i>CCHE2D-Flow</i>	National Center for Computational Hydroscience and Engineering (NCCHE)	2D	Irregular mesh FEM	Jia and Wang, 1999, DOI	Public domain
<i>MIKE 21</i>	Danish Hydraulic Institute (DHI)	2D	Regular/nested grid FDM or flexible mesh FVM	DHI, 2017	Commercial
<i>RiverFlow2D</i>	Hydronia	2D	Flexible mesh FVM	Hydronia LLC, 2018	Commercial
<i>SOBEK 2D</i>	TU-Delft Deltares	1D/2D	Structured grid FDM	Deltares, 2019	Commercial
<i>SRH-2D</i>	US Bureau of Reclamation (USBR)	2d	Flexible mesh FVM	Lai, 2008, 2009, DOI	Public domain
<i>TELEMAC-2D</i>	Electricite De France (EDF)	2D	Grids of prismatic elements FEM	Hervouet, 2000	Open-source
<i>TUFLOW-FV</i>	BMT WBM	2D	Flexible mesh FVM	BMT, 2019	Commercial

Table 3 - A review of hydrodynamic models for river modeling available in the literature.

From the list of models shown in Table 3, only AutoRoute, JFLOW, LISFLOOD-FP, and a few commercial software with GPU processing enabled can be considered as candidates for large-scale modeling. Some of the capabilities of most of these hydraulic models, such as solving the Saint-Venant equations as well as modeling hydraulic structures bridges, are not a priority in the rapid estimation of flood extent required by large-scale flood hazard or in early warning applications. Furthermore, while considering only tools with no commercial license to be used under a regular grid DEM, the LISFLOOD-FP and the AutoRoute models become valuable solutions. Below a brief description for each of the two selected models is given.

1.5.2 LISFLOOD-FP

An example of a robust and slim 2D numerical flood model is the raster-based 2D hydrodynamic modeling approach of the LISFLOOD-FP model. This model relies on a 2D numerical implementation of the hydrodynamic equations (Bates and De Roo, 2000; Horritt and Bates 2001). In particular, the kinematic routing model of LISFLOOD-FP is based on an approximation of full Saint-Venant equations which is applied at each channel cell. The 2D wave representation of floodplain flow is triggered at the inflow channel cell and therefore it requires as input only an upstream inflow hydrograph. The flood modeling is based on a storage cell approach in which the flow rate from a given channel cell into its four adjacent cells is calculated using uniform flow formula. In this model, the continuity equation is solved by evaluating the volume stored in each channel cell. Given the simplicity of the numerical method, LISFLOOD-FP has been applied in multiple flood forecasting and hazard assessment scenarios at multiple scales (Neal et al., 2012; Schumann et al., 2013; Alfieri et al., 2013, 2014b).

1.5.3 AutoRoute

The AutoRoute model of USACE (Follum, 2012) creates a raster-based flow depth by estimating flow depth raster at multiple cross-sections using Manning's equation for a given discharge value. This approach faces the problem of having not flooded patches, being not perpendicular to the stream, between cross-sections. In later studies, the orientation of each cross-section along each cell of the streams is made by averaging upstream and downstream flow directions. Furthermore, the adoption of multiple cross-sections per stream cell has shown a better representation of the floodplain domain as shown in the Mississippi case study (Follum et al., 2017). The approach is suitable for massive flooding with the channelized flow not affected by backwater, however, it shows limitations for events with low magnitude or in flat areas and urban environments. Some of these limitations have been partly solved by simulating riverbed with artificial depressions of river cross-sections with exponential shape areas, and by considering the role of topography in the post-processing of resulted flood extent through IDW interpolation of water depths over stream cell surroundings (Follum et al., 2020).

1.5.4 Hydrogeomorphic approaches

In hydrology, hydrogeomorphic approaches rely on the gradient of potential energy derived from topography as the main physical driver for the spatialization of surface runoff within a 2D domain. Given this strong relationship with the input elevation grid, those approaches, in hydrology, are also referred to as DEM-based methods (Samela et al., 2017). The concept of the relative gradient of potential energy along a watercourse is one of the easiest approaches to identify the relationship between the channel and its surrounding floodplain. One of the most adopted methods for the delineation of relative elevation contours from regular grid topography of rivers is the Height Above the Nearest Drainage (HAND) method (Nobre et al., 2015).

1.5.4.1 *Scaling relations geomorphic models*

Most immediate approaches to estimate flood-prone areas from the geomorphic analysis are based on empirical laws. Since the publishing of the work about hydraulic geometry for stream channel of Leopold and Maddock in 1953 and their recent generalization in 2004 (Dodov and Foufoula-Georgiou, 2004), the hydrogeomorphic analysis at cross-section level became a reference in the field. In such analysis, multiple empirical relationships between the discharge and the hydraulic characteristics of a stream channel, such as the river depth, width, water velocity, or suspended load are used (Leopold and Maddock, 1953). In this way, water depth at a given channel cell can be expressed as a power of the contributing area at the cell via ad-hoc calibration of expression coefficients.

Therefore, many empirical models become available in the literature. In some, the water depth is expressed as a function of the power of the contributing area via a parameterization of downstream river geometry. This is the case of the contributing area models, also referred to as “scaling relations”, in which power-law exponents and coefficients are derived via a linear regression of the expression by knowing the water stage and contributing area at multiple gauges.

Examples of contributing areas hydro-geomorphic models are the *Variable Contributing Area Model* presented by Beven and Kirkby in 1979, the hydro-geomorphic delineation method proposed by Nardi et al. in 2006, or the *Geomorphic Flood Index -GFI* published by Samela et al. in 2017.

1.5.4.2 *Geomorphic Flood Index*

Manfreda and Samela proposed a DEM-based method to estimate flood extent and water depth based on the Geomorphic Flood Index (GFI) (Samela et al., 2017). This geomorphic approach performs a binary classification of the DEM to depict flood-prone areas by looking at multiple geomorphological descriptors such as the upslope drainage area, surface curvature, slope, flow distance, and elevation difference from nearest drainage. This is accomplished by estimating the river depth along the drainage using an exponential scaling relationship with the local contributing area. The GFI geomorphic index is then computed as the logarithm of the ratio between the river depth and the elevation difference to the nearest drainage. Once the flood extent is defined as binary classification, the water depth is then derived from geomorphic analysis of the elevation difference of areas near the river.

This approach is based only on topography and the estimation of water depth relies on the upslope contributing area. Thus, the method is not capable to simulate flood wave propagation (Manfreda and Samela, 2019). However, given the simplicity and the geomorphic nature of this method, it is suitable for large-scale flood risk mapping in data-scarce environments (Manfreda and Samela, 2019). The Geomorphic Flood Area tool (GFA tool) is available as a QGIS plugin as open-source software (Samela et al., 2018).

1.5.4.3 *HAND-based hydrogeomorphic models*

1.5.4.3.1 *Height Above the Nearest Drainage*

The *Height Above the Nearest Drainage - HAND* model (Rennó et al., 2008; Nobre et al., 2011; Nobre et al., 2015) allows deriving from the DEM a map of river-based relative elevations from a given river network. In the HAND model, the absolute height of a hillslope cell is then re-classified by considering as its new vertical reference the elevation of the closest channel cell. For a general pixel, the nearest channel cell is identified by looking at the relative vertical flow path distances derived from the flow direction grid (Nobre et al., 2011). As a result, in the HAND map, all cells do not represent anymore the absolute elevation height of the DEM but are set to zero for channel cells and to differences in elevation heights above the nearest drainage for all channel cells (Figure 6).

The concept of elevation above streams of the HAND approach has been extensively adopted under multiple DEM-based flood mapping tools. In such systems, the derived HAND maps become key products to be extracted from the DEM. For this reason, many mapping initiatives using multisource DEMs have been undertaken after the publication of the HAND method to create reference relative elevation maps at a global or continental scale to be employed in multiple hydrological applications.

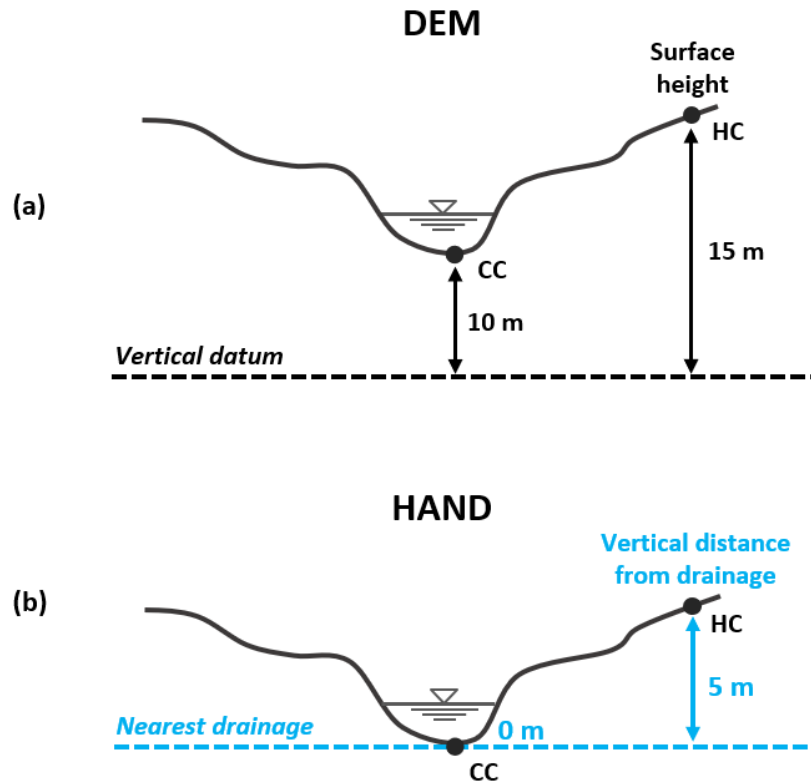


Figure 6 - Concept of “relative elevation”. The surface elevation of a generic Hillslope Cell (HC), such as 15m above a vertical datum (e.g., MSL), can be expressed as relative elevation by calculating the vertical distance from the nearest Channel Cell (CC) of drainage, having an elevation of 10m (figure a). As a result, in the HAND map the hillslope cell of interest has a relative elevation of 5m, and its nearest channel cell, being a vertical reference, a value of 0m (figure b).

Examples of these datasets are the HAND maps for the continental US at 10m resolution (Liu et al., 2016) and the global HAND maps at 90m resolution (Yamazaki et al., 2019) derived from the MERIT-DEM dataset (Yamazaki et al., 2017). In most of these HAND mapping efforts, the D8 (O’Callaghan and Mark, 1984) or the D-infinity (Tarboton, 1997), via its parallelized implementation in the TauDEM software (Tarboton, 2021; Tesfa et al., 2011), drainage methods are often employed.

1.5.4.3.2 An expansion of HAND for flood delineation

An extension of the HAND approach is possible with the combination of river stages derived from simplified hydraulic modeling. Thus, a water depth map can be derived by filling a HAND map. This static filling is made by imposing a column of water along the entire flow line having a vertical distance equal to zero. In this way, all the neighbor pixels along the flowline are “flooded” in case the elevation above the drainage is minor or equal to the imposed water column.

The static inundation of a HAND map can be accomplished in two possible ways by following a:

1. “height-driven approach” (HDA),
2. or a “volume-driven approach” (VDA).

The first HDA method can model the water stage closer to the 1D hydraulic modeling only near the cross-section. In this first modeling approach, it is necessary to dynamically update the stage-discharge rating curve along the watercourse or to assume a synthetic stage-discharge rating curve for the entire river branch. An alternative to HDA is the volume-driven approach. In VDA the driver of the forcing for the static inundation

of HAND contours is not the river stage derived from input discharge using a local rating curve, but the runoff volume, obtained via the time integral of the discharge. Such volume is then used to derive a flood extent that can store the same mass of water for each river branch.

Hereinafter are presented brief descriptions of the most referenced models that extend the HAND approach.

1.5.4.3.3 GIS Flood Tool

A first example of a hydro-geomorphological method is the one developed by USGS, the “*GIS Flood Tool – GFT*” (Verdin et al., 2016). The GFT model is based on Manning’s equations to estimate the water stage at a given cross-section and on the HAND model to spread over the 2D domain the resulting water depth calculated at each cross-section via the relative heights to the watercourse. This method automatically extracts a river cross-section centered at the centroid of each river branch and oriented perpendicularly to the flow using the input D8 flow direction grid. The river stage at each DEM-based cross-section is derived from the rating curve using the input discharge given by the user. This GIS-based model is built with ESRI’s ArcPy libraries and it is meant to be primarily used via the ArcMap GUI. This method relies on the user’s sensitivity and experience in defining reaches and in placing a well-located cross-section for each reach (Verdin et al., 2016). A validation of the method is presented in Verdin et al 2016 by comparing GFT flood maps near gauges with national flood hazard/scenarios benchmarks made with HEC-RAS. A similar methodology presented by Verdin et al. in 2016 has been also employed by the United Nations Environmental Program (UNEP-GRID) and the CIMA Research Foundation for the development of the global flood hazard maps of the GAR (Herold and Rudari, 2013). In this context, the authors presented an extension of this DEM-based method via ad-hoc modeling solutions to increase the number of cross-sections and to simulate the backwater effect.

1.5.4.3.4 Continental Flood Inundation Mapping

Another example of low complexity flood model is the one presented by Liu et al. in 2018, within the *Continental Flood Inundation Mapping - CFIM*. This work presented a “CyberGIS” workflow that has been applied at a continental scale over the entire territory of the United States via high-performance computing. In such a method, the HAND dataset for the US at 10m is coupled with streamflow values from the NOAA National Weather Model (NWM). Flood maps are then derived through a “static mapping solution” by inundating HAND maps using stage height at multiple river stations (Liu et al., 2018).

1.5.4.3.5 GeoFlood

The “*GeoFlood*” model (Zheng et al., 2018b) is another hydro-geomorphological method that extends the HAND model with simplified 1D modeling to estimate flood extent and water depth along the watercourse. River stages for multiple river segments are computed from input discharges using synthetic channel hydraulic parameters and synthetic rating curves derived from the DEM (Zheng et al., 2018b). In such computation, the authors subdivided each river branch of the network into segments having a length of 1.5 Km. Inundation maps are then derived for each river segment using an expression of Manning’s formula tailored for the HAND relative topography (Zheng et al., 2018a). The strength of this method lies in its innovative high-fidelity river network extraction routine, named “*GeoNet*”, which is designed to handle high-resolution DEM (e.g., LiDAR data). The authors have already shown the potential application of GeoFlood for flood modeling using either approximated or calibrated roughness coefficients into Manning’s formula. Despite the key role of the Manning coefficient in water depth calculation, modeled results using raw Manning coefficients have shown acceptable estimation of the flood extent (Zheng et al., 2018b). The *GeoFlood* software is distributed via a dedicated GitHub repository.

1.5.4.3.6 NWM-HAND Flood Mapping

In a similar manner to the already presented models, also the *NWM-HAND Flood Mapping model* (Johnson et al., 2019) extends the HAND model using Manning's formula over averaged geometry of river channel. Water depth is calculated at each river branch by adopting the approach proposed by Zheng et al. in 2018 for the estimation of the synthetic rating curve (Zheng et al., 2018a). Validation of the model is performed nearby water gauges using observed water levels and EO-based flood maps (Landsat 5, 7, 8, and Sentinel 1). According to the authors, the application of the NWM-HAND model at catchment scale using a default Manning's coefficient tends to underestimate flooding areas in lower-order reaches and to overestimate at higher-order reaches (Johnson et al., 2019). To mitigate this unbalance in flood extent prediction, the authors suggest a systematic increase and decrease of the Manning coefficient respectively in low and high order reaches (Johnson et al., 2019). The software developed from NWM-HAND is available at the *FloodMapping* repository in GitHub.

1.6 Discussion

In this last section of the chapter, it is given a summary of remarks and recommendations of best practices identified in this research. The following outcomes and assumptions are the ones used for building the method described in the next chapter.

1.6.1 About input datasets

Concerning the input DEM, hydrologically conditioned SRTM data at medium scale and LiDAR data at local scale are considered as reference sources for terrain elevation. Input streamflow estimations are either taken from local stream gauges, published hydrological studies or eventually modeled values derived from the Continuum model by CIMA Foundation. Finally concerning the multiple types of remote sensing products, only open access products derived from freely available EO data, such as the ones from NASA and Copernicus missions (Landsat-8 for optical imagery, Sentinel 1 for SAR, and Sentinel-3 for altimetry data), are considered for this research.

1.6.2 Critical analysis of drainage methods

Different qualitative and quantitative algorithm analyses as well as inter-comparison of several drainage methods can be found in the literature. The D8 drainage algorithm represents the most simple and slim flow direction method available. For this reason, it is widely employed in many applications, particularly for river network extraction. However, the assumption of the one-dimensional flow routing shows its limit in the D8 drainage modeling for planar convergent and divergent topography (Costa-Cabral and Burges, 1994). Furthermore, while comparing MFD with SFD over the same topography most of the authors have shown a more realistic output drainage grid with a reasonable estimation of stream network (Pilesjö and Zhou, 1996).

The innovation given by the introduction of the vector-based approach raised new questions on drainage modeling and offered a significant alternative to consolidated grid-based methodologies. As an example in 1997 Tarboton, while comparing D-infinity with other MFD methods, highlighted an over-dispersion of drainage in such methods given by their distribution of flow which is proportioned to the slope (Tarboton, 1997). Furthermore resulting flow directions appear to be too coarsely described in centroid-based drainage modeling given the introduction of grid bias into drainage estimation (Tarboton, 1997).

The introduction of dispersive methods based on triangular facets has been recognized to solve some of the issues of non-dispersive methods. In 2011 Zhou et al. also presented a qualitative and quantitative comparison between its own TFN algorithm and seven selected methods (D8, D8-LTD, DINF, MDINF, FMFD,

QMFD, and DEMON) by comparing the error with respect to theoretical Specific Catchment Area (SCA) values (Costa-Cabral and Burges, 1994) over mathematical surfaces and real digital elevation models. The accuracy assessment of this vector-based approach has shown advantages to the other methods. However, the TFN algorithm still must be parallelized before any applications over large DEMs (Zhou et al., 2011).

Based on the above considerations and the state of the art of their numerical implementation in open source software the drainage models adopted in this research are: the Deterministic Eight-Node - D8 (O'Callaghan and Mark, 1984), Holmgren's MFD (Holmgren, 1994), and the D-Infinity (Tarboton, 1997, 2021). All these methods are employed in this research by using only open-source toolsets to simplify the sharing of the method.

1.6.3 Critical analysis of low complexity flood model

The review of the literature has shown the advantages and disadvantages of multiple numerical methods for flood modeling. Simplified 1D/2D hydraulic models still require an effort to be automatized and to be easily deployed in an unsupervised manner and at multiple scales. On the other hand, geomorphic methods do not often satisfy some of the basic principles of fluid mechanics. In this research, it has been chosen to employ a different expansion of the HAND geomorphic model and to build a novel hydro-geomorphic modeling chain for a quick estimation of flood extent with the inclusion of simplified hydraulics.

As explained in section 1.5.4.3.2 the expansion of HAND maps can be performed by using either a height-driven (HDA) or a volume-driven (VDA) approach.

In HDA a synthetic stage-discharge rating curve is derived to convert input discharge into a water stage. However, it must be effectively representative of the entire portion of the river. This may be not immediate for irregular topography, man-made river environments, and river branches having rapid changes in river slope. Furthermore, while extracting the water depth map by filling the HAND map with a calculated river stage it is not always possible to fulfill the conservation of mass requirement at nodes. As an example, if we consider a simple "Y" confluence, a false loss of mass may occur due to an underestimation of the water stage after the junction derived from a synthetic stage-discharge rating curve which is not representative of the downstream river environment. On the contrary, a false increase of mass at the confluence may happen if tributaries are not properly modeled, with an underestimation of flood extent due to low river stage values. In general, a not-representative synthetic rating curve causes an inaccurate estimation of flood extent. Moreover, intrinsic limitations of the method persist on the river stage estimation at cross-sections in floodplains with small relief.

In VDA the expansion of HAND contours is not driven by the river water stage but directly by the source, the input discharge. In this way, no further errors are introduced into the VDA by using as forcing a derived variable of the discharge, the river stage. Furthermore, the adoption of multiple input runoff volumes for each river branch aims to fulfill the conservation of mass at nodes. As an example, this is possible if all input runoff volumes are derived from a distributed hydrological simulation of the entire basin. Alternatively, in case of flood hydrographs not available from hydrological simulations, the runoff volume can be also approximated via simplified hydrographs built from the statistical peak of historical discharges. The resulting water depth map is the one obtained by filling the HAND map with an unknown water stage that identifies an underlying water volume that is close to the input runoff one.

The above analysis led to adopt a Volume-Driven Approach in this research, also to propose an alternative method to the different multiple HDA recently published over the last 4 years.

Chapter 2 - Method

The second chapter illustrates the method identified and adopted in this Ph.D. research.

2.1 Introduction

This chapter aims to illustrate a novel modeling chain developed for quickly converting input discharge into output flood map. This method employs data and methodology described in Chapter 1. Hereinafter is described in detail the whole modeling chain and how each component has been implemented.

2.2 A simplified 2D hydro-morphological modeling approach: REFLEX

The *Rapid Estimation of Flood Extent - REFLEX* model (Arcorace et al., 2019) is an expansion of the Height Above the Nearest Drainage (HAND) approach (Nobre et al., 2015), designed as a slim tool able to provide rapid inundation mapping, constraining the possible geo-morphological flood extent with the available flood volume. A high-level schema of the entire REFLEX modeling chain is shown in Figure 7. This workflow also highlights the connections between the four modules.

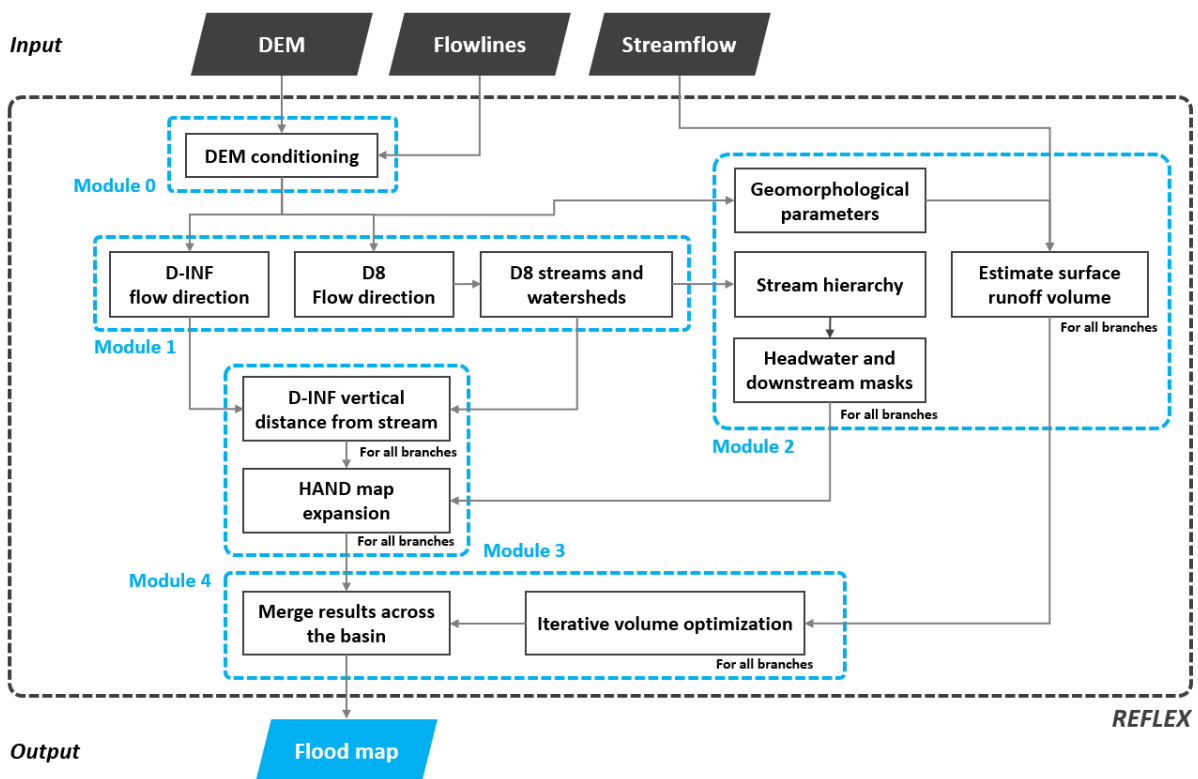


Figure 7 - REFLEX model flowchart.

Inputs of the REFLEX modeling chains are a Digital Elevation Model (DEM), flowlines, and the streamflow or surface runoff (given as discharge value). The output is a flood map that includes water extent and depth. The representation of terrain elevation is based on a hydrologically conditioned Digital Elevation Model (DEM). Output hydrological derivatives extracted from the input DEM are obtained following the D-infinity approach to increase the level of dispersion of flow direction over flat areas. Concerning the floodplain delineation, the HAND methodology is adopted to derive from topography the relative soil gravitational potentials. Stream hierarchy is computed using multiple stream ordering methods, which are necessary for an organized combination of DEM derivatives under the multiple REFLEX modules. Therefore, a different HAND map is created for each river order, starting from headwaters. Finally, flood extent and depth information are derived for each sub-basin by sequentially “filling” the HAND maps using input runoff volumes. An optimum flood map is derived from a water balance between the volume underlying the HAND map and the observed one. A detailed description of each sub-component is given in the following sections.

2.3 Collecting and pre-processing of REFLEX inputs

This section describes all necessary pre-processing of the inputs required in the REFLEX modeling chain.

2.3.1 Input discharge values

The hydro-geomorphic method identified and developed in this research to build REFLEX relies on a Volume Driven Approach to expand the HAND delineation and obtain a flood scenario. Thus, the input runoff volume is an essential source of information. This quantity is derived from the time integration of an input hydrograph over each branch of the river network (more details in section 2.5).

Input flood hydrograph can be either derived from hydrological models or in-situ observations. In REFLEX, the collection of the input discharge values requires a pre-processing of this data. This is often needed to ensure that a discharge value is properly assigned for each branch of the input flowlines. Moreover, in this process, it is important to use the same grid of the source hydrologically conditioned DEM to avoid data shifting. In this research, this pre-processing has been performed case by case using GIS software and has not been fully automated for REFLEX.

2.3.2 DEM conditioning in REFLEX

The representation of terrain elevation is based on a hydrologically conditioned DEM. Given the nature of REFLEX as a hydro-geomorphological model, good quality conditioned DEM needs to be chosen as input. For this purpose, the role of filtering and conditioning of raw DEM is essential.

The employment of already pre-processed global DEM datasets, such as the ones from the SRTM-FM, the HDMA, or the MERIT datasets (Arcorace et al., 2015; Yamazaki et al., 2017; Verdin, 2017), represents a valuable input for this method at medium scales. When available and for application of the method at local scales, conditioned LiDAR data is advisable given its resolution and spatial and vertical accuracy.

In case a raw DEM needs to be used as input for this hydro-geomorphic model, a DEM conditioning chain has been developed in REFLEX to handle this type of source elevation data. The identified workflow for the hydrologically conditioning of the DEM in REFLEX can be summarized in the following steps:

- 1) Filtering,
- 2) Filling,
- 3) and burning streams into DEM.

2.3.2.1 DEM noise filtering

The first step, filtering, is necessary to remove noise from input raw DEM such as absolute bias, stripe and speckle noise, and canopy height bias (Yamazaki et al., 2017). This is mandatory if input raw DEM is affected by elevation artifacts. If required, in REFLEX it is possible to perform a filtering of this input by employing the filtering routine of the “*MDenoise*” program (Sun et al., 2007).

2.3.2.2 DEM filling

Once the DEM is efficiently smoothed and the four different types of bias are filtered out, it is possible to begin the hydrologically part of the conditioning of the DEM. The second step of the DEM conditioning in REFLEX consists of “Filling” the DEM to remove depressions from the filtered elevation grid. In REFLEX the filling of the DEM is made using the epsilon filling approach (Barnes, 2016). This approach has been chosen due to its simplicity and effectiveness in filling depressions with a not flat surface having a small artificial elevation gradient.

This choice has been crucial to boost the iterative procedures to resolve flats in the computation of flow directions in REFLEX (more details in section 2.4). As an example, while employing the D-infinity flow direction method of TauDEM (Tarboton, 1997) over LiDAR data, the implementation of the epsilon filling approach in REFLEX has shown a drastic reduction of the computation time required to resolve the flats.

2.3.2.3 Stream burning

After the filtering and the filling of the raw DEM, an artificial depression of the elevation along the input flowlines, and the surrounding cells, is often required to artificially force the drainage over the desired path and to ensure a coherent decreasing of terrain elevation along the watercourse. In REFLEX the flow enforcement of filtered and filled data is made possible by burning input streamlines into the DEM. The stream burning methodology adopted in this research essentially relies on a slope-based filtering of the watercourse elevation profile by removing points having significant absolute local difference into river slope. In particular, the filtering of raw elevation along the flowline is performed using the formula:

$$\left| \left(\frac{z_{i+1} - z_i}{d} - \frac{z_i - z_{i-1}}{d} \right) \right| < \frac{\hat{i}_s}{C} \quad (1)$$

where $\hat{i}_s = (z_{inlet} - z_{outlet})/d_{stream}$, d_{stream} is the stream length in pixels, C is a scalar representing the filtering magnitude ($c < 1$ for a light and $c > 1$ for heavy filtering), and d is the distance in pixels ($d = 1$). The equation (1) is applied to each elevation of the channel cell of the river branch by looking at the closest upstream and downstream channel cell elevations. A stream point having elevation that does not satisfy the equation (1) is deleted from the river profile (Figure 8).

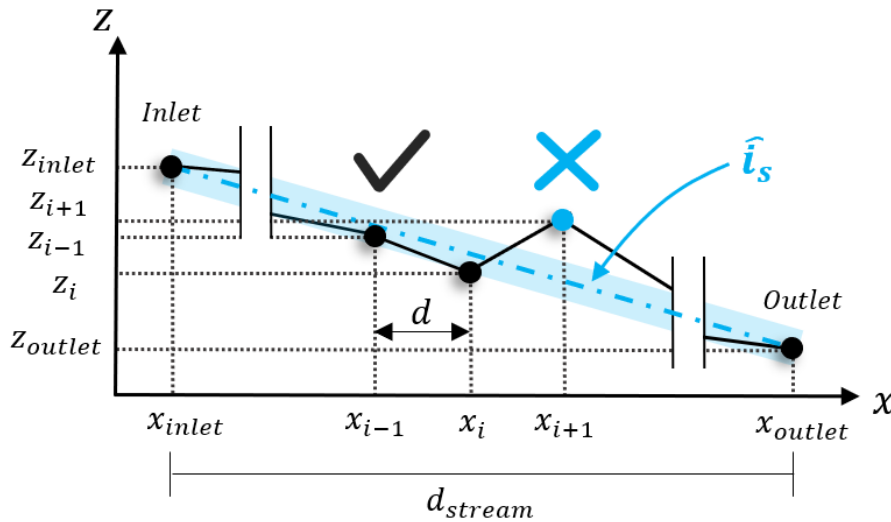


Figure 8 - Schema of the stream elevation filtering

In a later stage, all river point elevations deleted by the filter are then replaced with artificial elevations computed from linear interpolation of the elevations in the remaining upstream and the downstream points.

Once the entire river profile is filtered, an artificial depression of the bed of the river is employed by deepening the DEM along the flowline with a certain which represents the Simulated River Depth (*SRD*). In particular, the DEM is carved by lowering the elevation of the channel cell of the scalar *SRD* and the closest right and left hillslope cells with half of *SRD*. In this way, the stream burning for a generic channel cell is accomplished by deepening the water table with an elementary triangle having a height equal to the simulated river depth and a base equal to five times the DEM spacing resolution.

In this method, for each branch of the river network, the stream burning is employed by following two possible scenarios in which SRD is defined as either **incremental** or **constant** along the branch.

In the first scenario, the DEM is incrementally carved from zero to the chosen SRD scalar for the river branch. The min-max normalization is employed to normalize elevations $z_{FCC,adim}$ over channel cells from the filtered river profile using the equation (2),

$$z_{FCC,adim} = (z_{FCC} - z_{outlet}) / (z_{inlet} - z_{outlet}) \quad (2)$$

in which z_{FCC} is the filtered elevation at the channel cell, z_{inlet} and z_{outlet} are respectively filtered elevation at inlet and outlet cells. The conditioned elevation after stream burning is then derived by incrementally lowering z_{FCC} using the equation,

$$z_{FCC,burned} = z_{FCC} - (SRD \cdot (1 - z_{FCC,adim})) \quad (3)$$

in which $z_{FCC,burned}$ ranges from 0 at the inlet to SRD at the outlet. A schema for this scenario is shown in Figure 9.

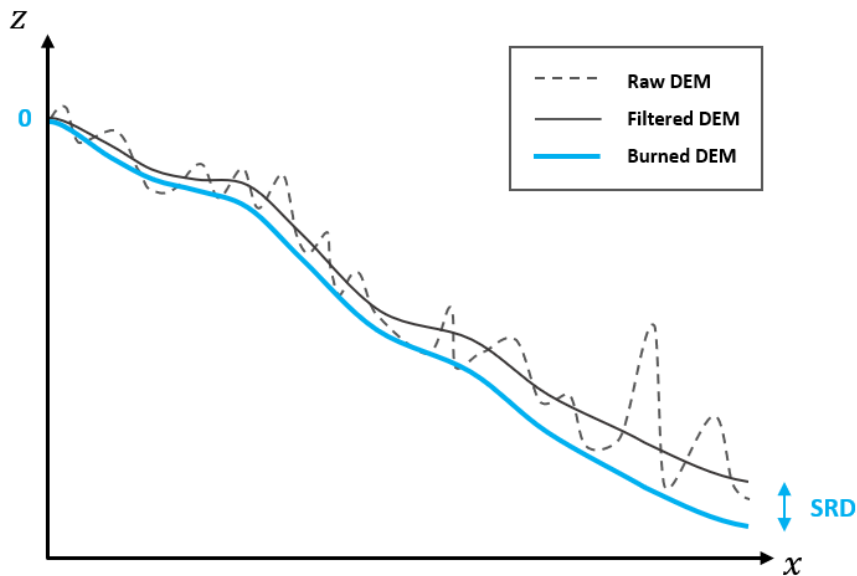


Figure 9 - Schema of SRD incremental stream burning.

In the second scenario, the elevation of the output conditioned DEM is equally deepened along the branch using:

$$z_{FCC,burned} = z_{FCC} - SRD \quad (4)$$

The result of the second scenario is a vertical translation of the river profile as shown in Figure 10.

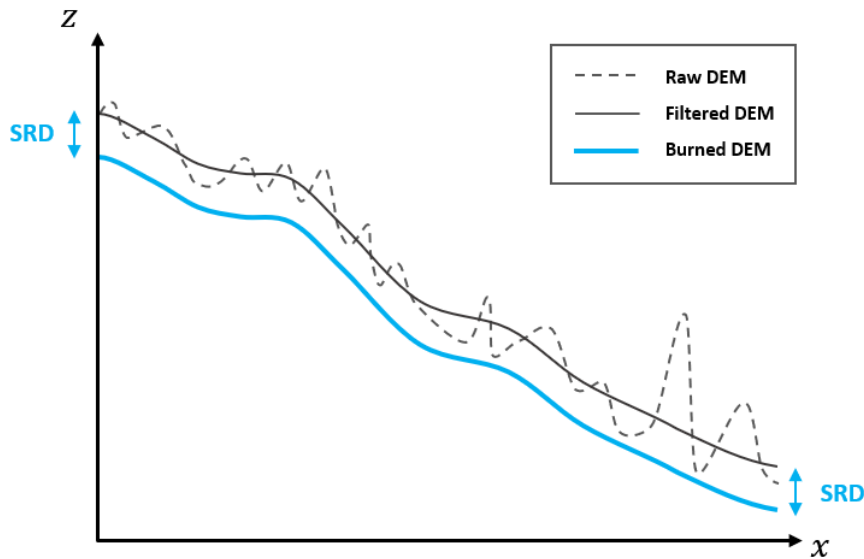


Figure 10 - Schema of constant SRD stream burning.

The choice of having two different carving scenarios is meant to condition the filtered DEM in REFLEX differently according to the hierarchy of the river network. In particular, the incremental stream burning of filtered DEM elevation (first scenario) is employed for all river branches having no tributaries (e.g., headwaters) and for the ending branch of the network connected to the basin outlet. Instead, the constant stream burning (second scenario) is employed for all other connected branches.

The application of this method is automated via a simple GIS-based classification of each segment of the river network using “-1” for the outlet branch, “0” for inlet branches, and “1” for the connector ones (Figure 11).

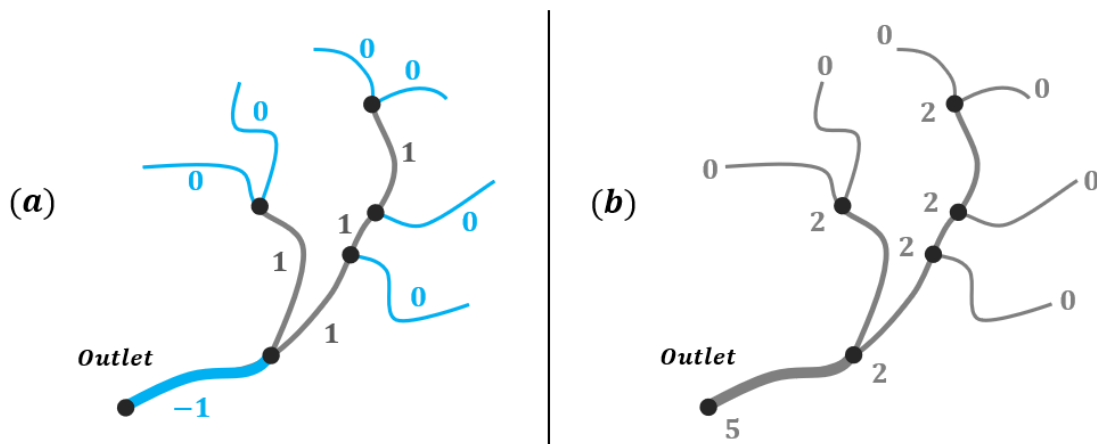


Figure 11 - The usage of constant and incremental stream burning scenarios over a simple basin. Figure (a) shows a sample classification of the river network between the inlet, connector, and outlet branches. Figure(b) presents an application of the method with sample SRD at nodes. SRD is constant only for connector branches while it is incremental for all the others.

The combination of the above-mentioned scenarios allows the creation of a map of values to be used for digging the DEM over the entire river network of the basin (Figure 11). Caution needs to be taken at nodes in which the conditioning of multiple tributaries must not create scaling effects at the confluence. This condition can be guaranteed by imposing the same SRD at the outlets of all the tributaries of a generic node.

After the conditioning of the entire river network, the SRD map is calculated by merging all obtained SRD values along the channel cells. The SRD map is then extended by adding half of the SRD values over all the hillslope cells included in the buffer zone of the river having a radius equal to the dimension of a cell grid. At the end of this process, the output conditioned DEM is obtained by subtracting the elevation of the filled DEM with the SRD map. If observed river networks are used as input of this process, the hydrologically conditioned DEM contains the corrections along real river paths. This is crucial for the extraction of more realistic flowlines from the conditioned DEM in REFLEX's flood modeling.

The entire DEM conditioning approach described in this section has been implemented in the REFLEX Module 0 by using multiple Python libraries, such as *geopandas*, *rasterio*, *numpy*, *scipy*, *pysheds*, and by integrating the following software: GDAL, GRASS GIS, TauDEM, *richdem*, and *mdenoise*. Not all the three steps of the DEM conditioning are mandatory in REFLEX. In case the source DEM is already noise filtered and the stream burning is not necessary, the only mandatory step of this workflow is the filling one.

2.3.3 Define flowlines

The third input of REFLEX is represented by the reference flowlines. Input flowlines or streamlines are meant to describe the river network of the basin and are composed of the cells of the DEM classified as a channel. Such cells identify where surface runoff is collected from hillslope cells. Channel cells are often represented by centerlines of permanent water bodies and can be derived from river delineation datasets or EO-based water masks. Flowlines can be also derived from thresholding of the flow accumulation extracted from the hydrologically conditioned DEM. The widely employed HydroSHEDS streamlines are an example dataset often used for this scope. This input static river network is needed to define and spatially assign the input discharge values over the entire basin. Thus, each branch of this input river network will be used in the REFLEX modeling to assign a discharge value and distribute a potential flood surface runoff over the sub-basin.

2.4 Module 1: Extracting Hydrological Derivatives from Conditioned DEM

The first REFLEX module aims to extract all necessary hydrological derivatives from the conditioned DEM. This module requires the hydrologically conditioned DEM as input. Outputs are hill-shaded DEM, flow direction, flow accumulation and sinks raster files.

2.4.1 Drainage modeling and extraction of derivatives

The review of drainage models allowed the design of this first REFLEX module which is needed to extract hydrological derivatives from the DEM. In this process, the first and most important step is the computation of the flow direction raster from the Conditioned DEM. This step is crucial because it sets the ground for the two following steps: the delineation of the stream network and the extraction of relative HAND maps. In particular, the flow direction grid is meant to be used in REFLEX for two distinct purposes (see Table 4).

Purpose	Drainage model	Hydrological Derivatives
Basin delineation	D8	Contributing Area, Streams, Sinks, Watersheds.
HAND mapping	MFD, DINF	HAND

Table 4 – The multi-purpose usage of different flow direction models in REFLEX.

The first one is required to extract all necessary hydrological derivatives which are needed as input in all following REFLEX modules. In the second usage, the flow direction is derived from the DEM and stored as a raster for the computation, in the third REFLEX module, of multiple HAND maps across the entire basin.

Modeled streams are efficiently derived in this module with thresholding on the contributing area (e.g., 1000 cells) using the D8 drainage model. Also, watershed and sub-watershed raster files are derived by using the conditioned DEM, and D8 flow direction and of the flow accumulation grids. The extracted river network and associated watersheds depend on the flow accumulation threshold (area or number of pixels) specified at this stage of the modeling. As an example, a low value of threshold drainage area implies a dense delineation of the network with multiple ramifications. Such threshold in REFLEX is defined as a parameter to allow tailored applications under multiple contexts.

Also, in the REFLEX Module 1, Holmgren's MFD or the D-infinity models are employed to derive flow direction and flow accumulated grids. Such products are needed in REFLEX's Module 3 to extract relative elevation contours to the D8 streams using the HAND approach. The adoption of the MFD and the D-infinity approaches to compute flow direction from the DEM is meant to increase the level of dispersion of drainage over flat areas, as shown in Figure 12.

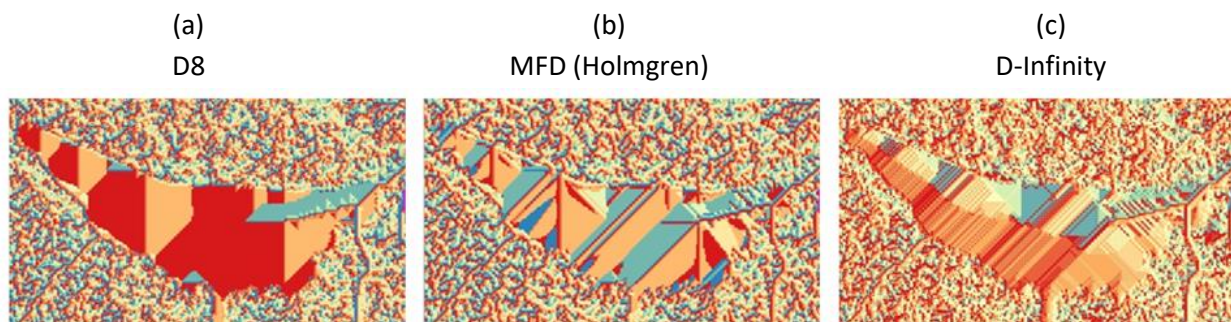


Figure 12 - Flow directions obtained by using D8 (a), Holmgren's MFD (b), and D-infinity (c) flow directions over the Lake Maga in Chad. Flatwater surface highlights the increasing level of flow direction dispersion of the three methods respectively from (a) to (b) and to (c). Flow directions are obtained by using hydrologically conditioned SRTM data from the SRTM-FM dataset (source: UNOSAT).

The computation of flow directions in REFLEX is achieved using the "*r.watershed*" function of GRASS (Ehlschlaeger, 1989; GRASS Development Team, 2021e; Metz et al., 2011) and the *D-infinity Flow Direction* tool of TauDEM (Tarboton, 1997, 2021). Flow accumulation, Sink, Stream, Catchment, and Sub-catchments are then derived as raster files from the D8 flow direction raster using and the GRASS GIS's "*r.accumulate*" (GRASS Development Team, 2021f) and "*r.stream.basins*" (GRASS Development Team, 2021g) add-ons.

2.5 Module 2: Streams Hierarchy and Surface Runoff Estimation

The second REFLEX module aims to extract and classify streams with multiple hierarchy methods using hydrological derivatives obtained at the precedent steps. Later, all necessary morphologic parameters are derived from the conditioned DEM, and the surface runoff volume is estimated from input discharge values collected from observations or hydrological models. This module requires input discharge values for the entire river network, the Filled DEM, and its hydrological derivatives from the first REFLEX module. Outputs are hierarchically ordered streams, and surface runoff volumes distributed at the nodes of the network.

2.5.1 Stream network and watersheds delineation

In the REFLEX Module 1 streams, watershed and sub-watersheds are derived from the DEM as raster files. Therefore, in this second module, obtained streams, basin, and sub-basins raster files are firstly converted to polylines and polygons. Streamline vectors are essential hydrological derivatives in REFLEX which are employed for multiple purposes in the modeling chain, such as: assigning single feature ID while relating rivers and watersheds vectors, distributing the runoff volume at nodes, and storing essential hydrological and morphological attributes of each sub-basin. On the other hand, watershed vectors are primarily used in

REFLEX to mask out the DEM and its derivatives over a sub-basin or its neighbor pixels. As an example, watershed vectors are used to derive morphological parameters and HAND contours for each sub-catchment. Furthermore, the same polygons are used to build buffered drainage area masks required in REFLEX's flood modeling to simulate backwater effects at confluences and the expansion of HAND maps near the coast.

2.5.2 Stream hierarchy

Once the stream network is derived, all branches are then classified using hierarchical methods. Multiple stream hierarchy methods are employed in REFLEX for the modeling of the whole basin. Hereinafter are listed the chosen methods, including a description of their different applications in the REFLEX modeling chain.

The first one is the Hack stream order (Hack, 1957) which is a bottom-up stream hierarchy method where the main watercourse is identified with the value 1 and higher orders are assigned to all the tributaries. This method is employed in REFLEX to easily identify and compute the length of the longest watercourse also referred to as “main stem” (Figure 13).

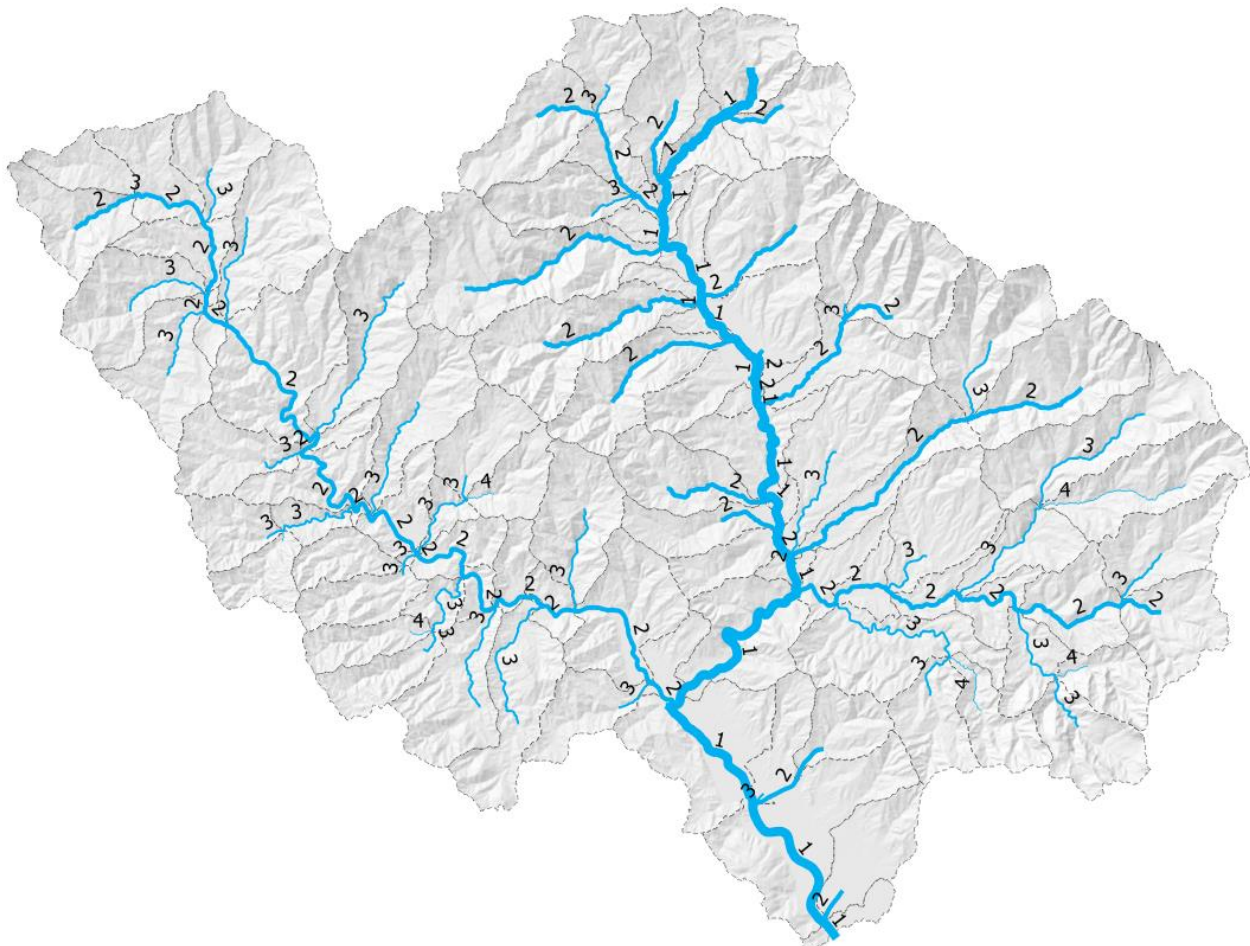


Figure 13 - Hack stream order for the Magra river basin. The thickest blue line, having Hack order equal to one, identifies the main stem.

Another method to assign stream hierarchy in REFLEX is the “top-down” method proposed by Strahler (Strahler, 1954) which allows the classification of streams from the source to the outlet (Figure 14). Headwaters are the first-order river branches in the Strahler hierarchy. A higher order is then assigned downstream at each confluence until the mouth of the basin is reached where river branches have the highest values.

The network encoding with Strahler stream order is used in REFLEX to differentiate and organize the creation of the HAND map library for the whole basin. Thus, the delineation of HAND contours in REFLEX begins from all headwaters which are identified by selecting the branches having the lowest order. On the other hand, the highest Strahler orders intersect the portion of the basin near the mouth where floodplains are often located. The calculation of both Hack and Strahler's streams hierarchy is performed in REFLEX using the GRASS GIS "*r.stream.order*" (GRASS Development Team, 2021h) add-on.

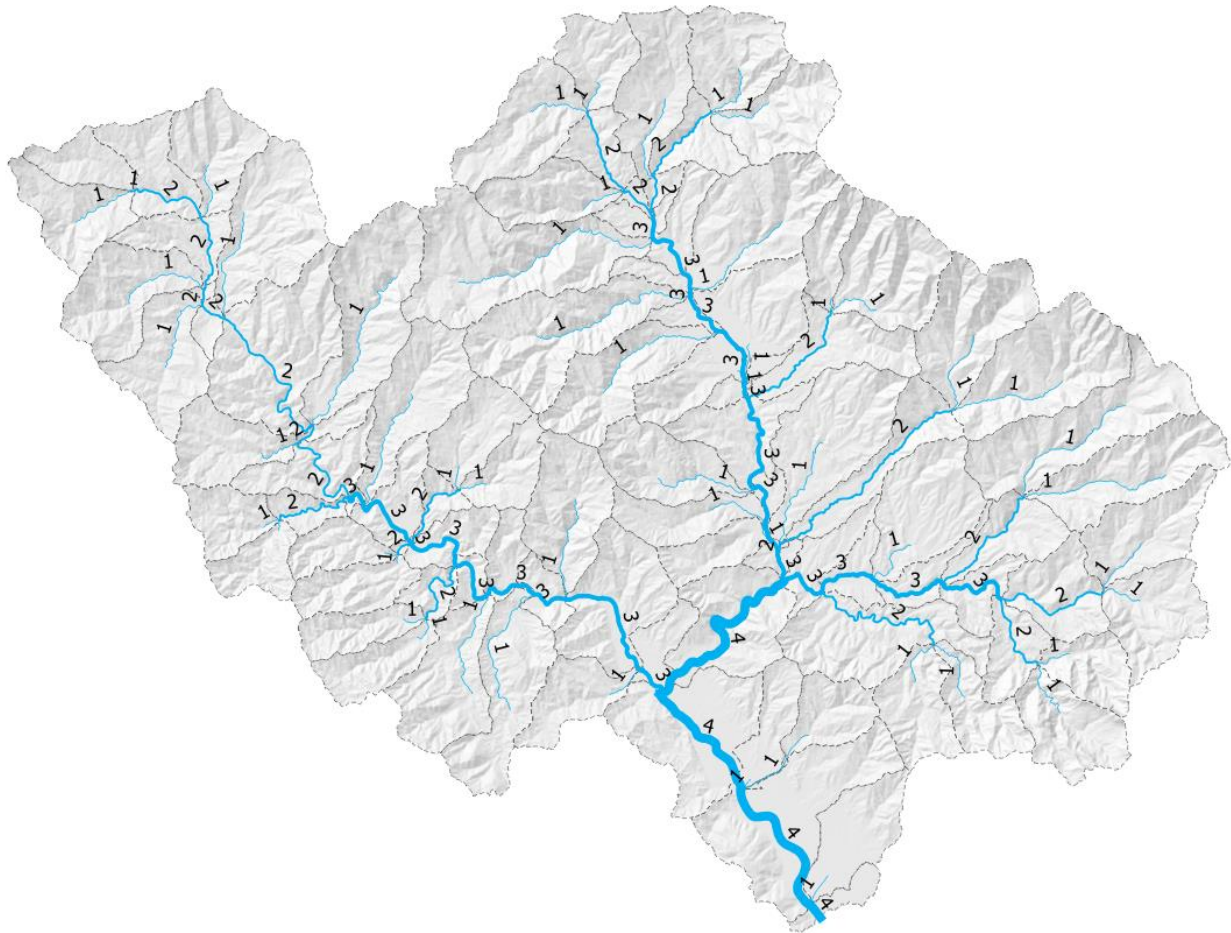


Figure 14 - Strahler stream hierarchy for the Magra river basin. All headwaters can be identified with Strahler order equal to one. The thickest blue line represents the downstream part of the river network that collects the flow of all upstream tributaries and that drains to the river mouth.

The last stream hierarchy method included in REFLEX is the Pfafstetter coding system proposed by Otto Pfafstetter (Pfafstetter, 1989). This system relies on the topology of the river network and on considerations on the drainage area to classify sub-basins and consecutively river branches. In this coding system, ordinal values from 1 to 10 are assigned from the mouth upstream by using even numbers for “basins” and odd digits for “interbasins” (Verdin and Verdin, 1999).

In this system, intervening areas that drain to the main stem are classified with odd values, from 1 (outlet) to 9 (source) and their tributaries are classified with even numbers in four basins, from 2 to 8 (Figure 15).

This approach is suitable for the coding of large river networks at continental and global scales. As an example, this method has been applied at multiple continental scales for the classification of the river network in all hydrological regions of the entire globe (Verdin and Verdin, 1999). Extended and modified Pfafstetter stream hierarchy has been also recently applied over the whole Australian continent with enhancements in ordering distributaries drainage networks and endorheic basins (Stein, 2018).

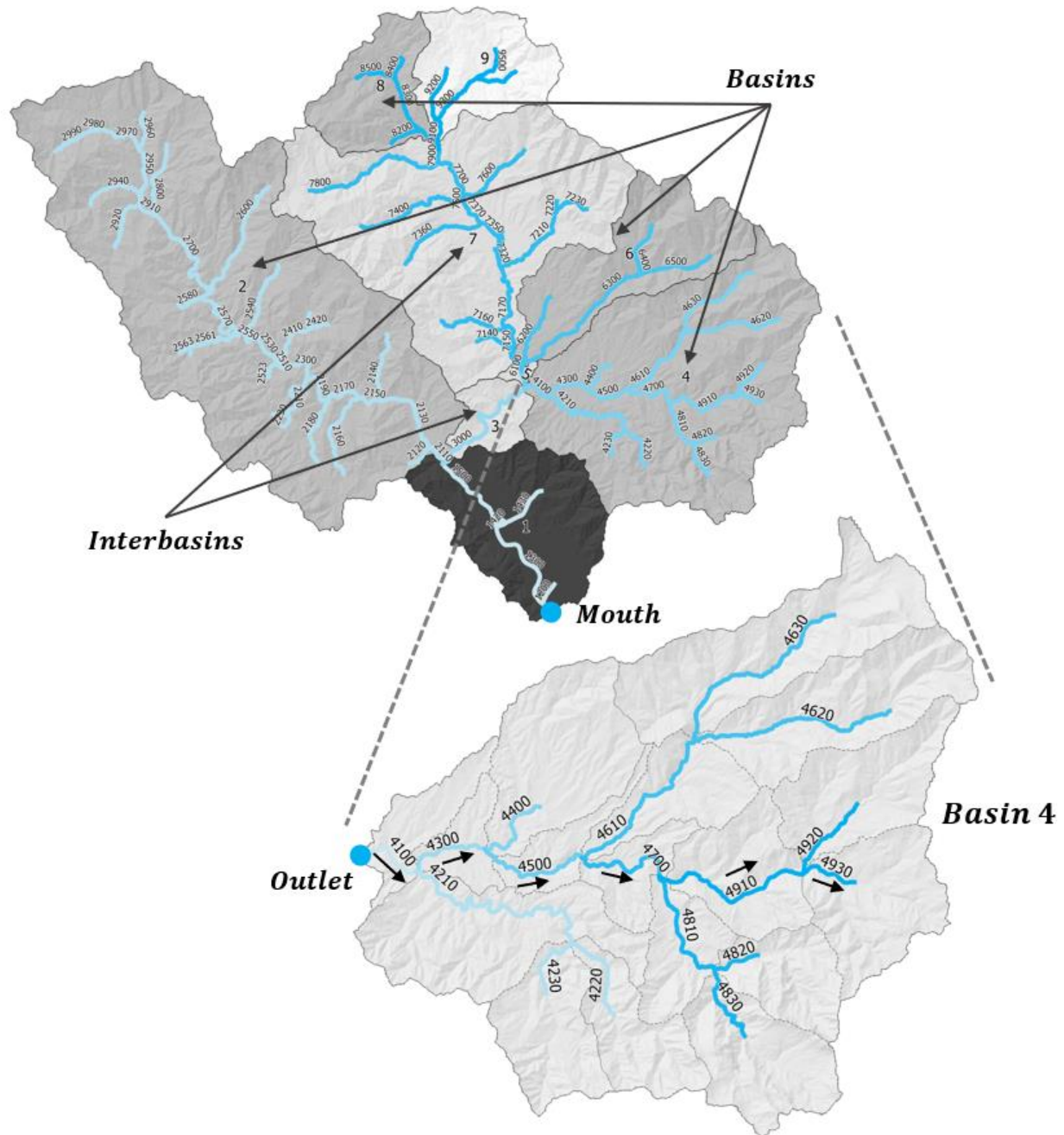


Figure 15 - Pfafstetter stream order for the Magra river basin. Interbasins 1, 3, 5, 9 are the ones along the main stem (having HACK order equal to one). Even orders 2-8 are used for basins of main stem tributaries. Coding of sub-basins, as shown for Basin 4, follows again an upstream incremental 1-10 ordering at multiple levels from outlet to divide (e.g., from 4100 to 4930).

Pfafstetter stream hierarchy is computed in REFLEX using a dedicated chain developed in Python and the obtained orders are tagged with additional attributes to the ones already included in the stream vector obtained after Hack and Strahler stream classification in GRASS.

The Pfafstetter coded river network is used in REFLEX to build multiple vector masks (Figure 16):

1. Sub-basin mask: obtained by selecting the current sub-basin.
2. Drainage area mask: obtained by computing drainage area at the outlet of the sub-basin.
3. Headwater mask: obtained by merging the current sub-basin with its six headwater ones.
4. Downstream mask: obtained by merging headwater mask with two downstream sub-basins.

The downstream mask is also buffered of a distance to be used for HAND expansion in coastal areas.

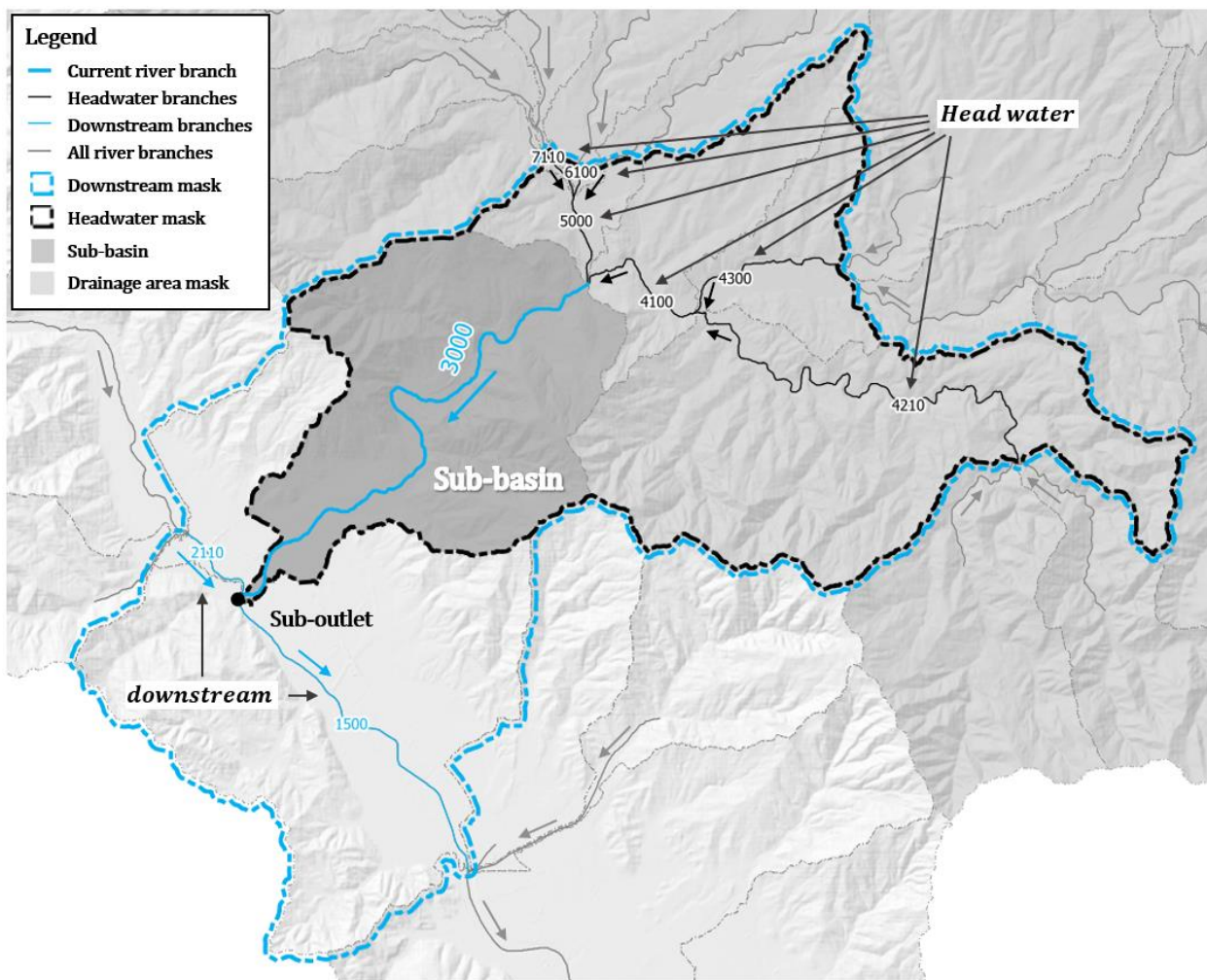


Figure 16 - Drainage area, headwater, and downstream masks for a generic sub-basin derived by identifying 6 headwater branches and 2 downstream river branches from the entire Pfafstetter coded river network.

The headwater mask is needed to consider the backwater effect in REFLEX (Figure 17). Six above Pfafstetter orders have been chosen to effectively simulate backwaters also in large and flat basins with low values in headwaters riverbed slopes. This is important while employing this method at continental scales.

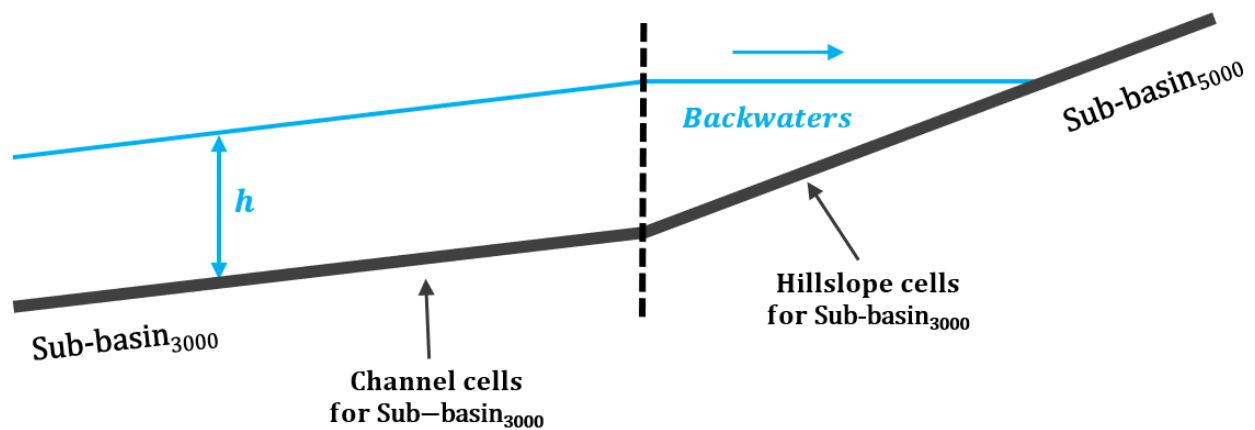


Figure 17 - Backwater effect in REFLEX.

Downstream mask instead is configured in this manner to expand HAND downstream from the outlet of the sub-basin (see coastal expansion in section 2.6).

2.5.3 Morphologic parameters from the DEM

After the delineation of both watersheds and streamlines, morphological parameters are then derived from the DEM. This is required to estimate the *time of concentration* (t_c) for each sub-basin of the region. The time of concentration (t_c) can be derived from various empirical methods (Almeida et al., 2016; Salimi et al., 2017) that are based on multiple morphologic parameters such as: divide (H_{max}), average (\bar{H}), and outlet (H_{min}) elevations, basin area (A), length (L), average basin slope (S_b), and average slope (S) of the longest watercourse.

Model	Formula	Notes	Application	Reference
Kirpich	$t_{c,K} = k \cdot L^{0.77} \cdot S^{-0.385}$	$k = 0.000325$, length of the longest watercourse (L) in [m], dimensionless average slope of the longest hydraulic way (S) in [m/m].	Small basins in Tennessee and Pennsylvania with A within $0.004 \div 0.453 \text{ km}^2$.	Kirpich (1940)
California Culvert Practice	$t_{c,CCP} = \left(\frac{k \cdot L^3}{H_{max} - H_{min}} \right)^{0.385}$	$k = 11.9$, length of the longest watercourse (L) in [mi], elevation difference between divide (H_{max}) and outlet (H_{min}) in [ft].	Small mountainous basins	California Culvert Practice (1955)
Giandotti	$t_{c,Gi} = \frac{k_1 \cdot \sqrt{A} + k_2 \cdot L}{k_3 \cdot \sqrt{\bar{H}} - H_{min}}$	$k_1 = 4, k_2 = 1.5, k_3 = 0.8$, basin area (A) in [km^2], length of longest watercourse (L) in [mi], mean basin elevation (\bar{H}) and outlet elevation (H_{min}) in [m].	Medium-large basins in central-north Italy with A within $170 \div 70000 \text{ km}^2$	Giandotti (1934)
Pasini	$t_{c,Pa} = k \cdot \frac{(A \cdot L)^{0.333}}{\sqrt{S}}$	$k = 0.108$, length of the longest watercourse (L) in [m], basin area (A) in [km^2], dimensionless average slope of the longest hydraulic way (S) in [m/m].	Developed for rural catchments	Pasini (1914)
Pezzoli	$t_{c,Pe} = k \cdot \frac{L}{\sqrt{S}}$	$k = 0.055$, length of the longest watercourse (L) in [km], dimensionless average slope of the longest hydraulic way (S) in [m/m].	Small alpine drainage basins with A within $5 \div 50 \text{ km}^2$	Pezzoli (1970)
Siccardi	$t_{c,Si} = k_1 \cdot \sqrt{A} + k_2$	$k_1 = 0.27, k_2 = 0.25$, basin area (A) in [km^2].	Small basins with A within $2 \div 10 \text{ km}^2$	CIMA (1999)
Tournon	$t_{c,T} = k \cdot \frac{L}{\sqrt{S}} \cdot \left(\frac{A}{L^2} \cdot \sqrt{\frac{S}{S_b}} \right)^{0.72}$	$k = 0.396$, basin area (A) in [km^2], length of the longest watercourse (L) in [m], dimensionless average slope of the longest hydraulic way (S) in [m/m], and average basin slope (S_b) in [m/m].	Small alpine basins with A within $30 \div 170 \text{ km}^2$	Merlo (1973)
Ventura	$t_{c,V} = k \cdot \left(\frac{A}{S} \right)^{0.5}$	$k = 0.1272$, basin area (A) in [km^2], dimensionless average slope of the longest hydraulic way (S) in [m/m].	Developed for rural catchments	Ventura (1905)

Table 5 – List of empirical methods integrated into REFLEX to estimate the time of concentration. All formulas are expressed with an output time of concentration in hours.

For this purpose, the area of the basin in square km (A) is derived from the projected polygon of the drainage area. Basin slope (S_b) is derived as the mean slope of the elevation grid, length (L), and average slope (S) of the main stem are derived by dissolving the Hack stream hierarchy at the first order. Finally, the elevation of divide (\bar{H}) and outlet (H_{min}) are derived from the DEM respectively as 98th and 2nd percentiles. Once all the above morphologic parameters are collected the time of concentration is computed in REFLEX by using all the methods listed in Table 5. Finally, obtained t_c values are converted from hours to seconds.

2.5.4 Computation and distribution of runoff volume across the network

The last step of the second module of REFLEX consists of assigning a surface runoff flood volume across the identified river network.

The flood component of the surface runoff volume for a generic river branch can be either derived from overtopping outflow (e.g., estimated via hydrological modeling of the basin) or from the time integral of the observed flood hydrograph. In the first case, an appropriate linkage with the hydrological chain (e.g., CIMA's Continuum model) is needed to associate the multi-temporal modeled river flow with the DEM grid and thus the river network used in REFLEX. In the second case input flood hydrographs, derived from either time series of observations at gauges or regionalization techniques for discharge quantiles estimation, are simply assigned to the closest river branch that intersects the gauge location.

Once modeled or observed discharge values along the river network are collected, an analysis of input hydrograms is required before their use in flood modeling.

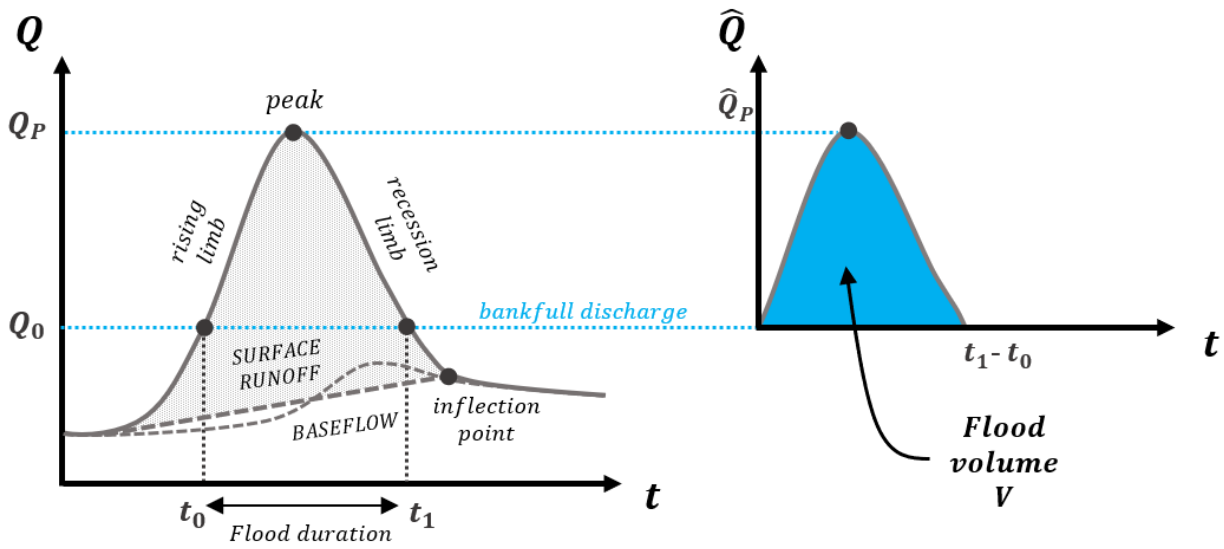


Figure 18 - Schema of a temporal evolution of the flow for a generic cross-section of a river (flood hydrograph). The flood volume is defined as the time integral of the surface runoff component of the hydrograph above the bankfull discharge (\hat{Q}_P).

The surface runoff flood volume is derived by removing baseflow and the portion of surface runoff below the bankfull discharge (Q_0) from the time integral of the hydrograph (Figure 18). Thus, flood volume can be derived as follows,

$$V_{flood} = \int_0^{t_f} \hat{Q}_P dt \quad (5)$$

where, $\hat{Q}_P = Q_P - Q_0$, and $\Delta t_f = t_1 - t_0$ is the duration of the event for which $\hat{Q}_P \geq 0$.

A distributed temporal evolution of flood discharge is not always available across the river network except for basins with a dense stream gauging system coupled with a hydrological model.

In most cases, only peak discharges derived from historical observations are available over few point locations. In this context, the shape of the hydrograph is unknown and is constructed with an artificial one having the same peak discharge. In hydrology, the surface runoff component of a hydrograph is generally approximated with triangular shapes equivalent to the surface runoff hydrograph.

The standard isosceles triangle with height equal to the peak discharge and centered at the time of concentration t_c is generally assumed in hydrology for the Rational Method. Thus, the equation (5) in first approximation can be simplified as follows:

$$V_{surface\ runoff} = \frac{1}{2} \cdot Q_p \cdot t_b \quad (6)$$

where the time base t_b represent the base of the isosceles triangle and is equal to the double of t_c .

Another example is the *Equivalent Triangular Unit Hydrograph - ETUH* derived from the dimensionless *Unit Hydrograph - UH* of the US Soil Conservation Service (Mockus, 1972). In this second example, the triangle maintains the same height, but the base is different (Figure 19).

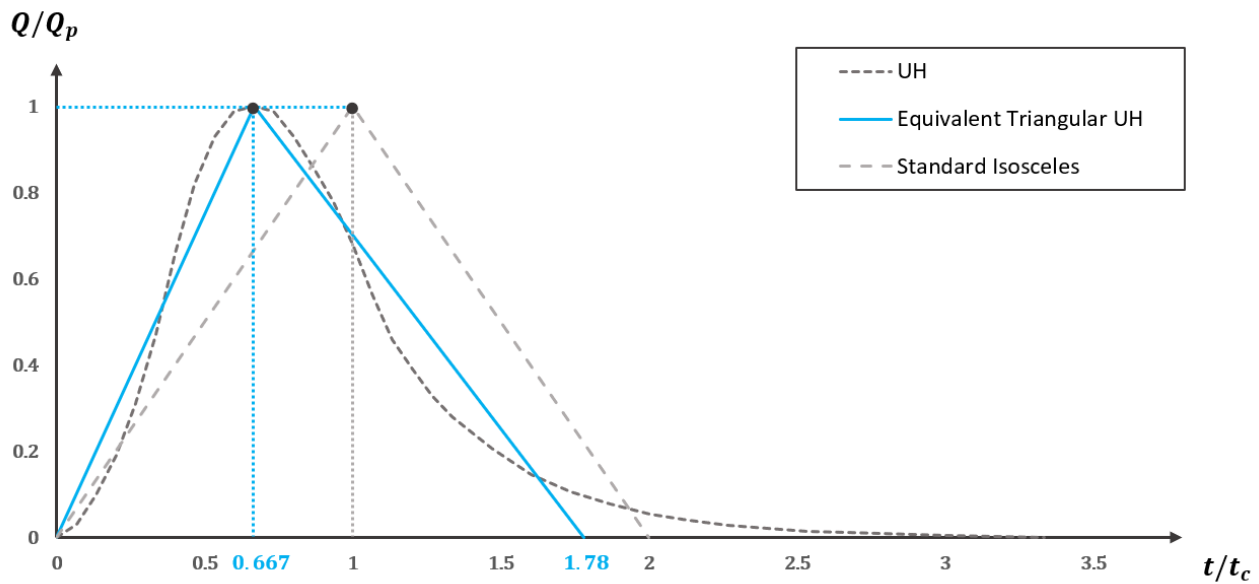


Figure 19 - Hydrograph shapes for dimensionless time and discharge.

In ETUH, the time base t_b is expressed as the sum of time of the peak discharge (t_p) and the recession time (t_{rec}) and can be calculated with

$$t_b = t_p + t_{rec} = 2.67 \cdot t_p = 1.78 \cdot t_c, \quad (7)$$

in which t_p is approximated with the following empirical formula,

$$t_p = \frac{(0.133 \cdot t_c)}{2} + 0.6 \cdot t_c = 0.667 \cdot t_c, \quad (8)$$

and the recession time is estimated as,

$$t_{rec} = 1.67 \cdot t_p. \quad (9)$$

In both these ways of defining the time base t_b , triangular hydrographs can be easily constructed in REFLEX by knowing only t_c and Q_p and the surface runoff volume is derived using equation (6).

Later, assuming the flood hydrograph is either gathered or reconstructed, the surface runoff (V_{flood}) is derived in REFLEX from the $V_{surface\ runoff}$ using a numerical approximation of equation (5). Once this step is accomplished, flood surface runoff volume, drainage area, stream ID, Strahler order of each sub-basins are then stored into a tabular and vector file at the location of each sub-outlet.

2.5.5 Discussion

Artificial triangular shapes hydrographs allow REFLEX to estimate surface runoff volume where only peak discharge values of different return periods are available. This is crucial while employing REFLEX in regional-scale modeling, in which input discharge information is often derived from regional hydrological studies based on a statistical analysis of historical extreme events. In this context, the estimation of the time of concentration is not straightforward, being often large basins having not homogenous topography. To tackle this issue, in REFLEX it is possible to either choose a single time of concentration method (e.g., where an empirical formula fits with the geomorphic characteristics of the basin of interest) or to use a statistic value (\bar{t}_c) derived from all formulas reported in Table 5,

$$\bar{t}_c = f(t_{c,K}, t_{c,CCP}, t_{c,Pa}, t_{c,Pe}, t_{c,Si}, t_{c,T}, t_{c,V}), \quad (10)$$

where the function f stands for average, maximum, or minimum.

Furthermore, while comparing the two triangular shapes available in REFLEX, the dimensionless volume from ETUH is 89% less than the one of Standard Isosceles hydrograph. Despite the simplicity of the Standard Isosceles approach, the difference in the triangular area led to assume the ETUH as the default method in REFLEX also in large-scale deployments given its better approximation of the hydrograph.

2.6 Module 3: HAND Mapping and Coastal Expansion

In the third REFLEX module, a GIS-based methodology is employed to derive all HAND maps from the filled DEM over the domain of interest. This module also includes an extension of the HAND method dedicated to coastal areas by using artificial expansion of the relative contours near the mouth of the river. This module requires as input the Filled DEM, the hydrological derivatives from module 1, and the hierarchically ordered streams from REFLEX Module 2. The output of this module is a library of multiple raster files of HAND maps and river binary masks.

2.6.1 HAND mapping for each sub-basin

Concerning the potential floodplain delineation, the geomorphic HAND method (Nobre et al., 2015) is adopted in REFLEX to derive from topography the relative soil gravitational potentials for each sub-basin (Figure 20). This method is coupled with Strahler's stream hierarchy which is necessary for a different and organized combination of HAND maps. Therefore, a different HAND map is created for each sub-basin, starting from headwaters having the lowest Strahler order.

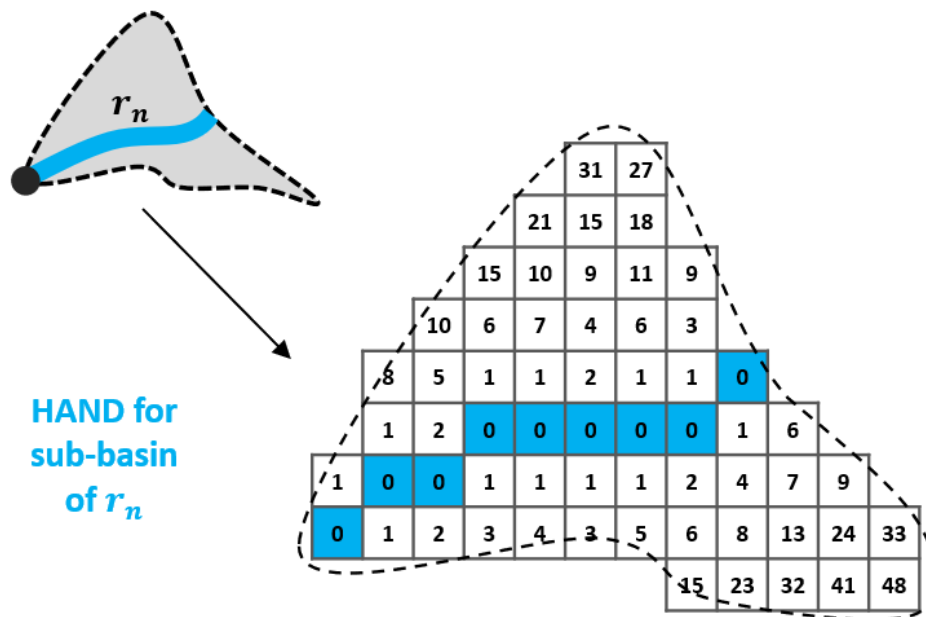


Figure 20 - Schema of the HAND map for the sub-basin of a generic branch of the input river network. All channel cells have values equal to zero. Pixel values for Hillslope cells are elevation differences from the nearest drainage expressed in meters.

The calculation of elevation difference above near drainage grids is performed in REFLEX, in case the MFD is employed, with the GRASS GIS “*r.streams.distance*” toolset (GRASS Development Team, 2021e), or in case the D-infinity is chosen, with the “*D-Infinity Distance Down*” function of TauDEM (Tarboton, 2021; Tesfa et al., 2011). Hand maps for each sub-basin are derived using the sub-basins mask derived in the REFLEX Module 2 as described in section 2.5.2.

2.6.2 Coastal expansion

This method consists of a novel GIS-based procedure which aims to solve a typical intrinsic problem of the HAND-based hydrogeomorphic models which is the constraint of the divide in the delineation of HAND contours near the mouth of the river.

2.6.2.1 A need to expand HAND contours

Watershed delineation near the coast depends on the way ridges are identified from the drainage modeling of input DEM. Ridges represent divides between a basin of interest from its adjacent ones. While delineating watershed downstream from the highest to the lowest elevation of the basin, it is important to consider that its boundaries are sensitive to the resolution, spatial and vertical accuracy of the DEM. Thus, a low level of accuracy in the delineation of watershed divides generally occurs near the mouth due to the flat terrain.

However, once a watershed is derived from the drainage modeling of the DEM, the resulting shape of the downstream part of the watershed near the mouth may change from one basin to another one. The case limit is when this shape is like a long bottom of a funnel when only a few hillslope cells are draining water from the left and right sides of the channel.

Both these aspects represent a limit for a hydro-geomorphological model since the HAND map can be computed only within watershed boundaries. As a result, flood water depth derived from such HAND contours often shows extent having a similar bottom-funnel shape in coastal environments (Figure 21).

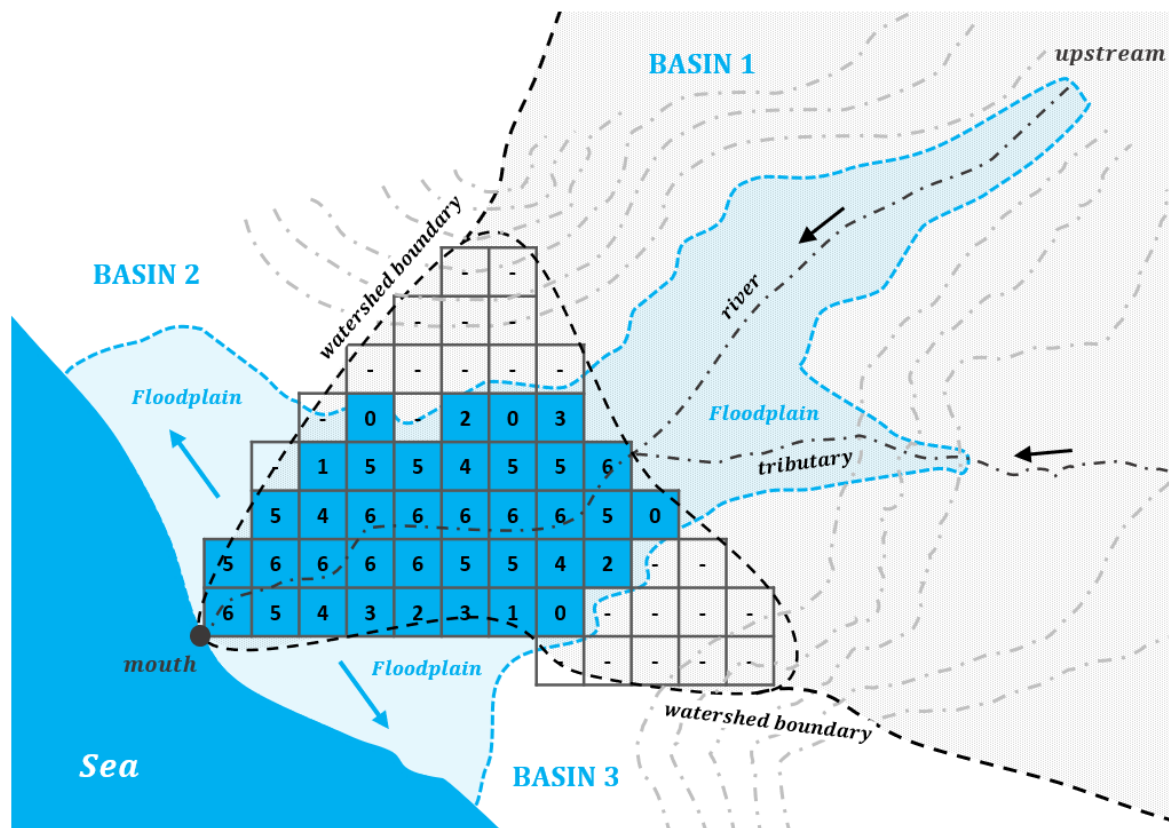


Figure 21 - Schema of a watershed having funnel-like shape. Flood extent is constrained within watershed boundary only.

In addition to that, a water wall effect along the divide often occurs since flood extent is constrained within watershed boundary only. These border effects in modeled flood depth maps are due to the impossibility to expand flood surface runoff volume from the boundary to the adjacent basins.

2.6.2.2 A general method to expand a HAND map to adjacent basins

The above-described limitations can be mitigated for a watershed (basin 1 in Figure 21) through an artificial expansion near the coast of the HAND contours from the divide towards the terrain of the adjacent ones (basins 2 and 3 in Figure 21). In REFLEX a “coastal expansion” GIS-based methodology has been developed for this purpose. The method is based on a cumulative cost of moving between a generic channel cell (CC) of the river and the neighbor’s hillslope cells (HC) of the DEM.

First, the domain of calculus for the generic river branch r_n is defined by considering the subset of the whole DEM, called “domain” matrix D . This domain matrix represents a wider portion of the DEM to the one covered by only the watershed of the river branch r_n , and it is required for the HAND expansion from the divide to the neighbor watersheds. D is defined in REFLEX by considering the minimum between a pre-defined distance from the divide b and a maximum distance from the stream d_{max} ,

$$D(r_n) = \min(b, d_{max}) . \quad (11)$$

where b is defined as the number of cells outside the watershed of river branch r_n , and d_{max} is the lateral distance from the stream in meters. In REFLEX b is constant and is defined a priori, while d_{max} is obtained for a generic river branch by using the following empirical formula:

$$d_{max} = \min(15000, 2000 + 0.13 \cdot A) \quad (12)$$

where A is the drainage area in square km of the river branch sub-basin. This empirical expression has been derived with CIMA Research Foundation during the application of this method over multiple types of basins in the African Continent.

The subdomain D is then used to derive the “price” matrix P , which is a binary mask with values equal to one, for CC and HC within the river buffered zone D , or equal to zero, for HC outside this buffer.

$$P = 1 \quad \text{if } HC, CC \in D, \quad \text{else} \quad P = 0 \quad (13)$$

Later, the “cost” matrix C , which is equal to pixel distance from the stream, is derived from P using the “*r.cost*” toolset available in GRASS GIS software (GRASS Development Team, 2021i). A “loss” matrix L is then derived by multiplying an a-priori negative dimensionless hydraulic gradient with the cost matrix:

$$L = J \cdot C \quad (14)$$

where the hydraulic gradient in the x-direction J is expressed as follows

$$J = -\frac{dh}{dx} \quad (15)$$

in which $-dh$ is the head loss and dx is the unit distance (pixel spacing). The loss matrix is meant to represent a distribution within the DEM grid equal to the pixel distance from the stream.

Once L is computed, the expansion of the HAND map is obtained by using the following expression:

$$HAND_{extended} = DEM - z_{25} + L \quad (16)$$

where z_{25} is the first quartile (or 25th percentile) of DEM elevation derived by using only elevation values extracted from channel cells of the river branch.

The above-described method has been also tailored for the flat topography of the coastal zone employing the buffered downstream mask (Figure 16) and by masking out the sea. An example of the application of this method near the mouth of a river basin is shown in Figure 22.

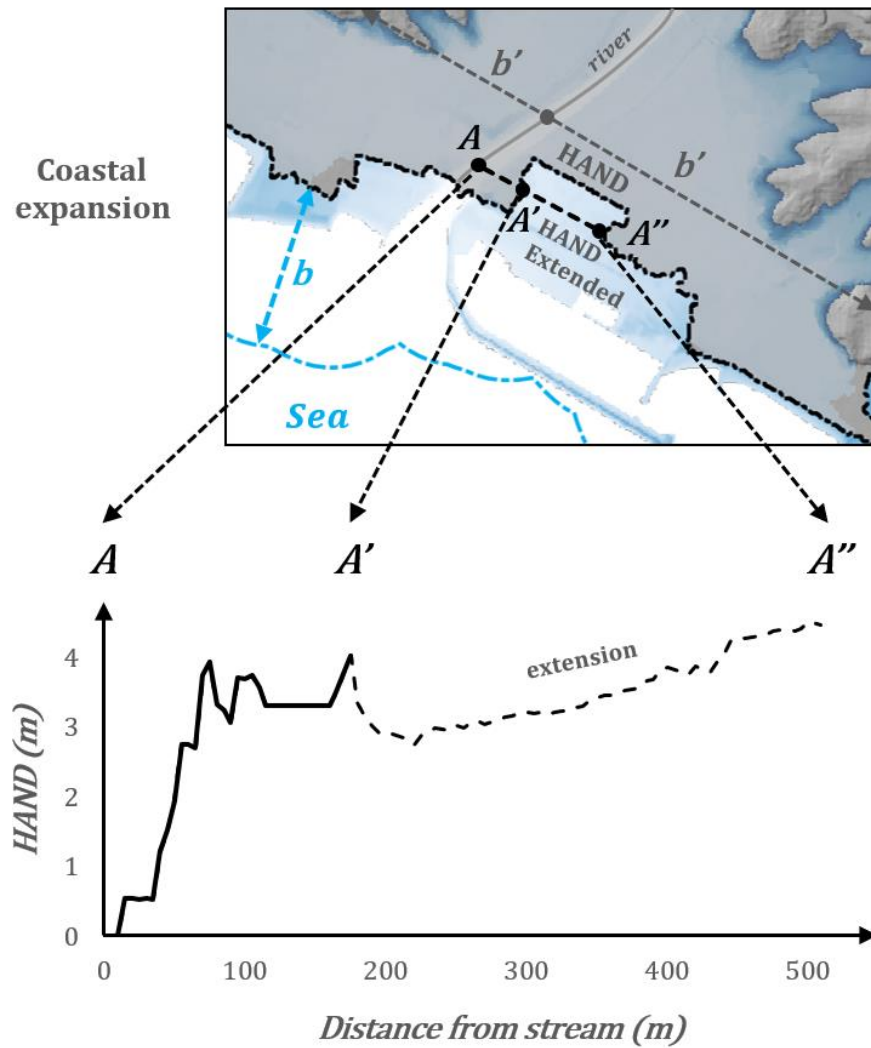


Figure 22 – Schema of the coastal expansion in REFLEX.

2.7 Module 4: Flood Inundation

The fourth module in REFLEX is about flood inundation. In this module, the library of HAND maps, obtained in the third module for each catchment of the whole basin, is combined with input runoff volumes, distributed across the river network, to estimate flood scenarios as water depth and extent maps (Figure 23).

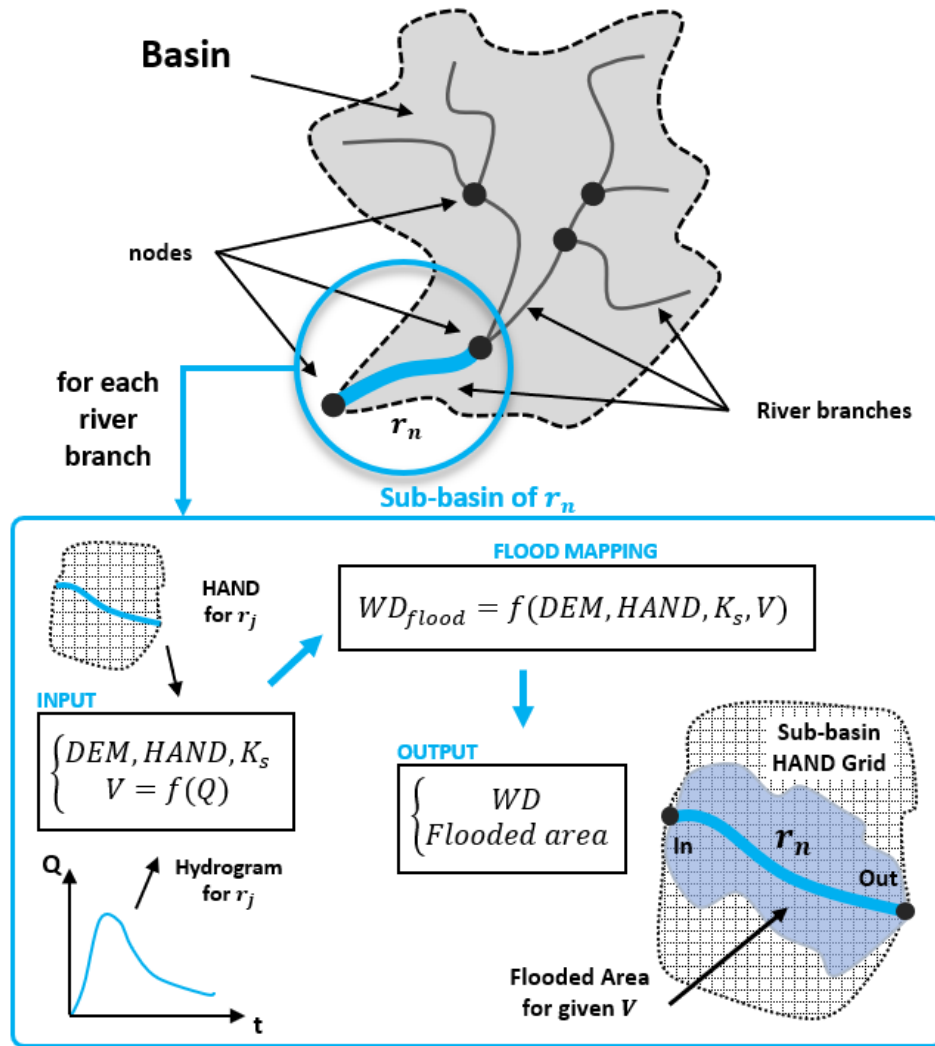


Figure 23 - high-level description of the REFLEX Flood module.

In this REFLEX Flood Module, the output water depth array WD_{flood} is derived by filling the HAND maps with a certain volume of water at each river branch. In particular, the hydro-geomorphic method here implemented follows a volume-driven approach that employs an iterative static volume optimization. In this iteration, the runoff volume is updated by using a simplified version of Manning's equation. Thus, the output water depth array WD_{flood} of this simplified flood model can be expressed as a function of the DEM, the HAND contours, the Manning roughness coefficient, and the runoff volume:

$$WD_{flood} = f(DEM, HAND, K_s, V) \quad (17)$$

At the first step of this iteration, the input runoff volume V_{obj} is taken from the time integral of the flood hydrograph as derived from Module 2 and explained in section 2.5.4. Assuming a triangular flood hydrograph the initial value of V_{obj} is the total surface runoff volume for a duration equal to the time base, as derived from equation (6). The obtained value is then used to trigger a static volume optimization.

2.7.1 Static volume optimization

A water depth map WD_{flood} , can be derived via a static distribution of this input volume V_{obj} over the input $HAND$ map of the correspondent catchment. This static distribution of the volume can be expressed with a simplified version of the function (17) expressed as:

$$WD_{flood} = f(HAND, V_{opt}) \quad (18)$$

where $V_{opt} = V_{obj} \pm \Delta V$ represents the unknown volume included between the surface elevation and the flooded area resulted from the water level h over the river centerline.

The unknown V_{opt} correspond to a numerical approximation of the input V_{obj} and $\Delta V = V_{opt} \pm V_{obj}$ represents the volume difference that needs to be minimized. To solve this function a numerical method for its optimization is necessary. For this scope, a volume optimization routine has been developed for the REFLEX Flood Module, as shown in Figure 24.

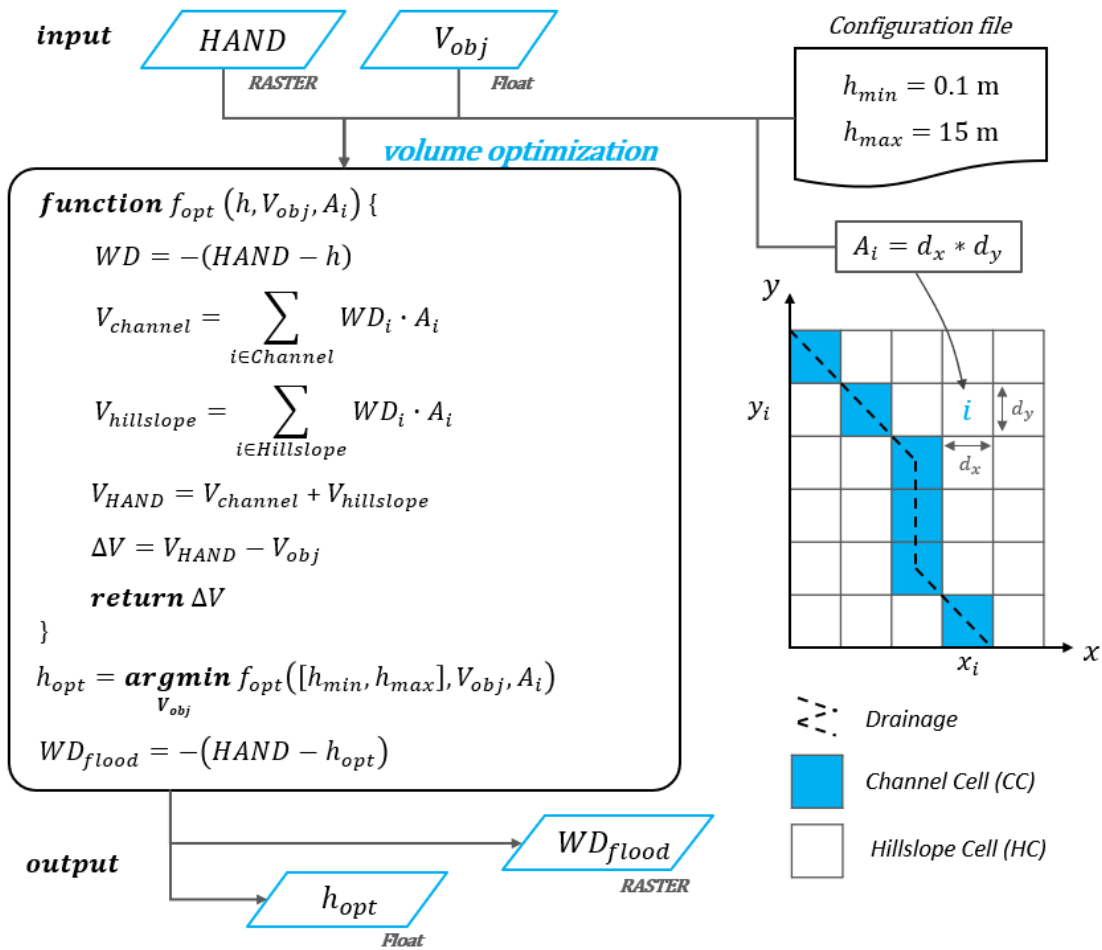


Figure 24 - REFLEX's static volume optimization.

Inputs of this volume optimization routine are the *HAND* raster file and four scalars which are:

- the runoff volume V_{obj} in cubic meters,
- the area of the pixel A_i in square meters,
- and minimum h_{min} and maximum h_{max} admissible values for channel cells of the water stage h which is unknown.

The outputs of the volume optimization routine are the optimized water stage h_{opt} and the WD_{flood} raster.

This volume optimization routine of REFLEX has been developed in R language (R Core Team, 2021a) and has been integrated into the entire modeling chain as a single module callable with Python. This optimization module relies on the *One-dimensional Optimization* package of the R software available via the “*optimize*” command (R Core Team, 2021b). This command allows the optimization of a given function by searching for its minimum or maximum in the range between the lower and the upper value of a specified interval.

In REFLEX, the *optimize* algorithm is used to minimize the function f_{opt} by passing its arguments, which are the input runoff volume V_{obj} , the area of the pixel A_i and a searching interval of river water stage $[h_{min}, h_{max}]$, in which $h_{min} = 0.1$ m and $h_{max} = 15$ m. Such interval values have been defined thanks to the experience acquired in the large-scale modeling of REFLEX in Africa (see section 3.6). However, h_{min} , h_{max} can be tailored to the specific application by simply editing the default values in REFLEX’s configuration file.

As a result, the optimization process can be defined as follow:

$$h_{opt} = \underset{V_{obj}}{\operatorname{argmin}} f_{opt}([h_{min}, h_{max}], V_{obj}, A_i) \quad (19)$$

The water depth array $WD(h)$ can be derived from the *HAND* map by filling the relative elevation with a value h along the flowline:

$$WD(h) = -(HAND - h) \quad (20)$$

The corresponding static volume of water in the catchment, derived by filling the DEM with a value h over its flowline, can be then calculated as follow:

$$V_{HAND}(h) = V_{channel}(h) + V_{hillslope}(h) . \quad (21)$$

In which $V_{channel}(h)$ is the standing water volume over the channel and $V_{hillslope}(h)$ the analog component over flooded hillslope areas. The first term is the result of the sum of all elementary volumes over all the channel cells,

$$V_{channel}(h) = \sum_{i \in Channel} WD(h)_i \cdot A_i , \quad (22)$$

2.7.2 Estimating transit time via a simplified version of the Manning equation

Water depth and extent derived from the first step of this iterative Manning-based volume optimization are then used in REFLEX to estimate the transit time using an average stream water velocity derived from Manning's formula:

$$v = k_S R^{\frac{2}{3}} \sqrt{S} \quad (26)$$

where k_S is the Manning roughness coefficient, R is the hydraulic radius, which is a function of the cross-sectional area of the flow and the wetted perimeter, and S is the linear hydraulic head loss. This formula allows estimating cross-sectional average water velocity for uniform open channel flow. River geometry for a generic cross-section A-A' of the river is shown in Figure 26.

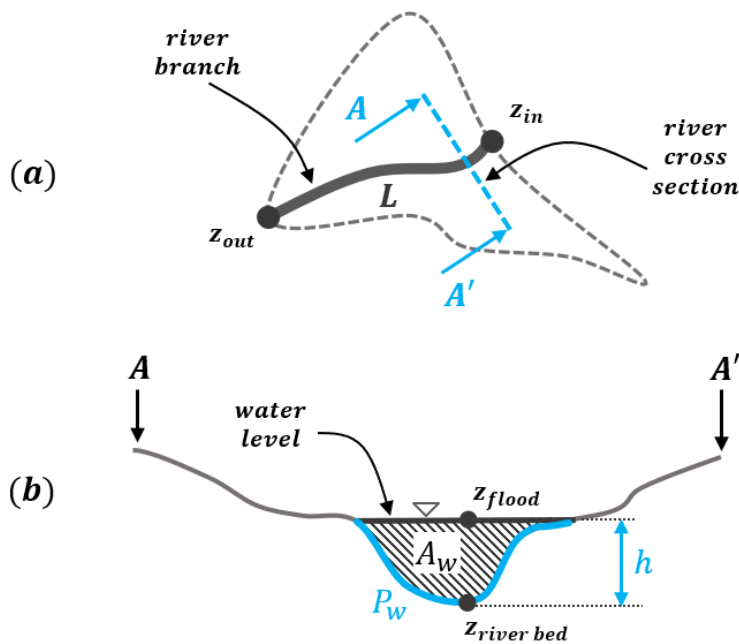


Figure 26 - Planar view of a cross-section along a river branch of length L (figure a). Principal hydraulic variables are shown in the sample cross-section A-A' (figure b): the river stage (h), the cross-sectional area of the flow (A_w), and the wetted perimeter (P_w).

In this hydraulic simplification, the river cross-section is considered large and rectangular (Figure 27). As a result, the hydraulic radius R can be approximated with the water stage h :

$$R \approx \frac{b \cdot h}{b + 2h} \approx h \quad (2h \approx 0 \text{ if } b \gg h). \quad (27)$$

Furthermore, the water stage h is assumed to be constant along the river branch. Thus, the hydraulic grade line can be approximated with the slope of the riverbed $S \cong i_f$. Thus, equation (26) is simplified as follows:

$$v = k_S h^{\frac{2}{3}} \sqrt{i_f} \quad (28)$$

which is employed in REFLEX to estimate the average flow velocity as a function of the water stage h .

Riverbed slope i_f is known for each branch of the river network, as calculated in REFLEX Module 3, and the roughness coefficient is defined a priori by employing nominal values available in the literature (e.g., 0.045 for natural channels).

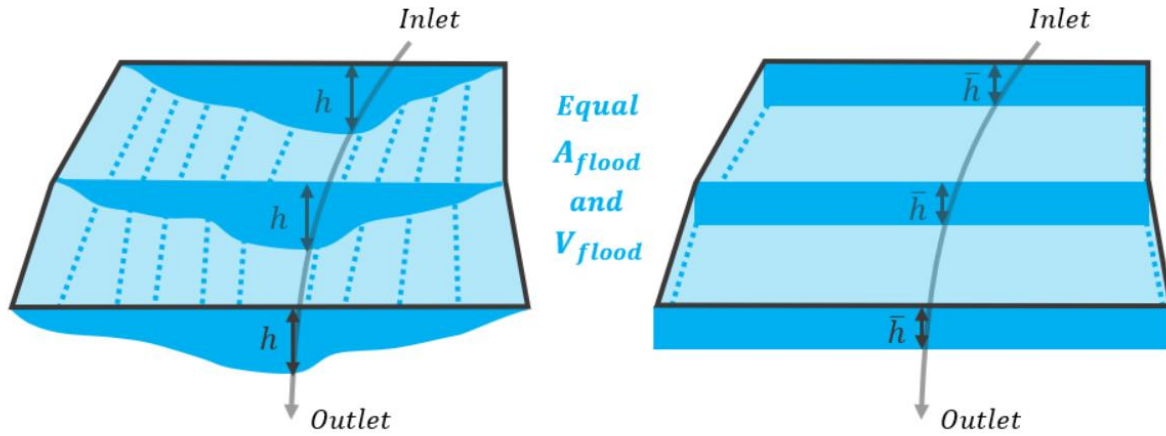


Figure 27 - Rectangular approximation of river geometry with river stage (h) rescaled to the average water depth (\bar{h}) derived from the ratio between the flood volume and the flooded area.

These assumptions enable estimating an average water stage \bar{h} for the generic river branch (Figure 27), which is computed by dividing the optimized runoff volume V_E^* with the water extent A derived at the first step of this iterative Manning-based volume optimization:

$$\bar{h} = \frac{V_E^*}{A} \quad (29)$$

The obtained average water stage \bar{h} is then used with Equation (28) to estimate an average velocity v_T and the transit time t_T is computed as follows:

$$t_T = \frac{L}{v_T} \quad (30)$$

where L is the length of the river branch.

Once the transit time is known, the runoff volume is computed again in REFLEX via the time integral of the flood hydrograph up to the transit time.

Assuming a triangular surface runoff hydrograph the updated runoff volume V_E^* is derived from:

$$V_E^* = \frac{\left(\hat{Q}_P + \left(\hat{Q}_P - t_T \tan(\beta) \right) \right) t_T}{2} \quad (31)$$

where $\beta = \arctan(\hat{Q}_P/t_C)$ and $\hat{Q}_P = Q_P - Q_0$.

Being the transit time lower than the time of concentration, this update will result in a reduction of the runoff volume. As a result, also a reduction will happen in the resulted updated water extent A^* and water depth WD^*_{flood} as shown in Figure 28.

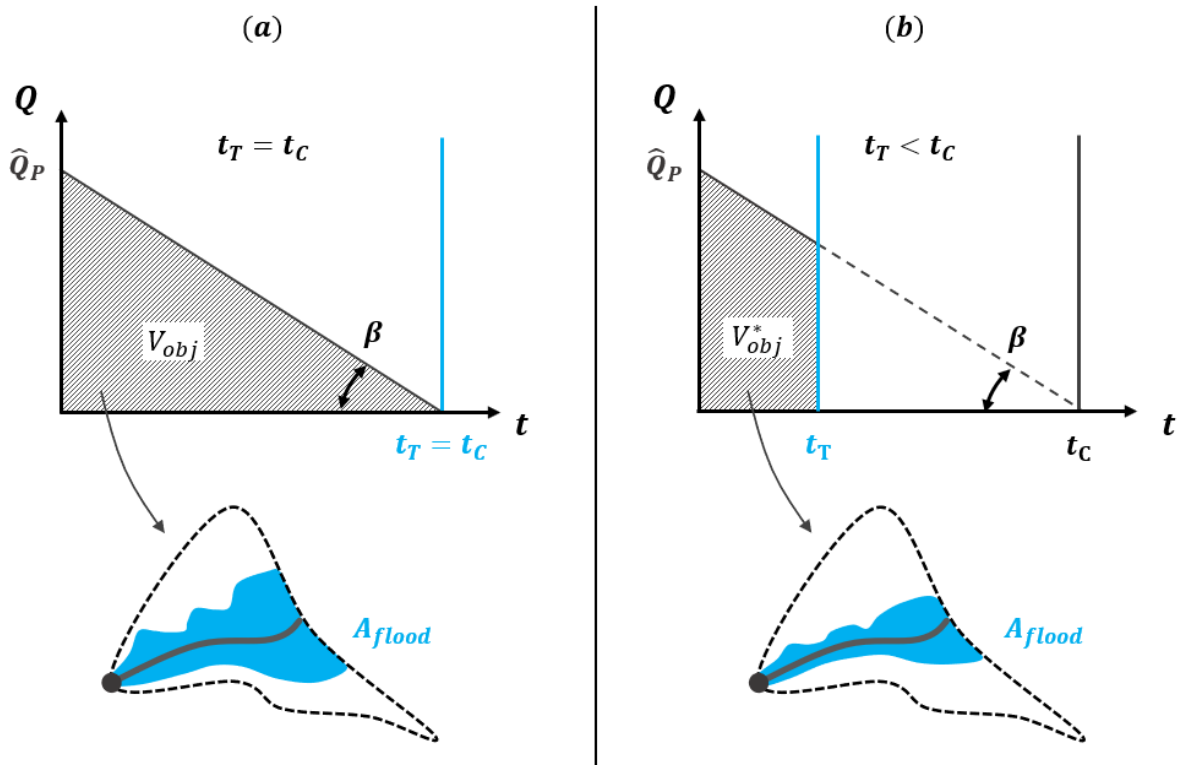


Figure 28 - Runoff volume as a function of the transit time

This process is repeated for multiple iterations by triggering the static volume optimization at each cycle and updating the transit time, A^* , and WD^*_{flood} until it converges.

2.7.3 Creating output flood map

The whole method, described in sections 2.7.1 and 2.7.2, is applied for each branch of the river network and the flood maps are merged into one for the entire basin. Following a precautionary approach, the maximum of overlapping values is taken while merging the water depth of multiple sub-basins near the confluences.

The outputs of this REFLEX module are water depth and flood binary mask raster files given in GeoTIFF formats.

2.7.4 Binary classification in REFLEX flood extent validation

To assess the performance of flood modeling results of REFLEX, multiple indexes are employed to assess the accuracy of the flood extent predicted by the model. The indexes are derived from the usual binary classification of predicted and reference flood maps, which allow the construction of a confusion matrix like the one described in Table 6.

Total pixels		Predicted (REFLEX)	
		P (predicted positive)	N (predicted negative)
Reference (benchmark flood map)	P (real positive cases)	TP	FN
	N (real negative cases)	FP	TN

Table 6 – Schema of confusion matrix employed to test the performance of the REFLEX model.

The comparison between predicted and reference flood extents performed within a given simulation domain allows the classification of all pixels of the grid in the following four classes: True Positive (TP), False Negative (FN), False Positive (FP), and True Negative (TN) as shown in Figure 29.

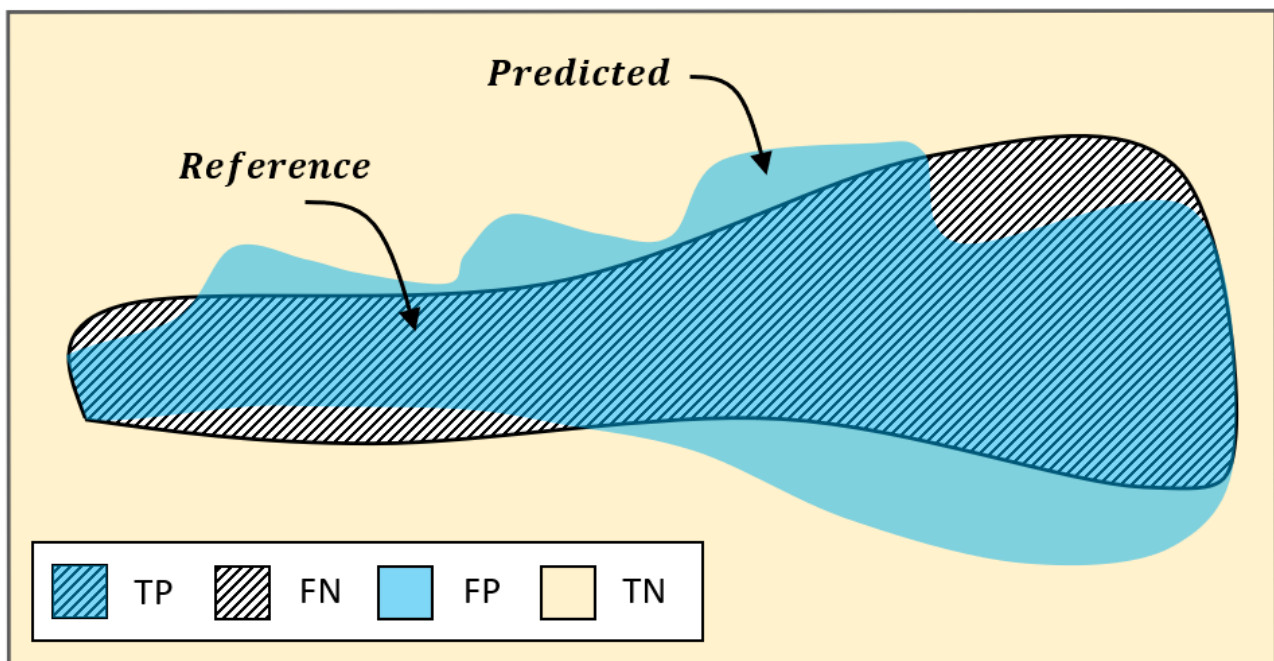


Figure 29 – Schema for the linear binary classification of flood-prone areas.

Once the number of pixels is derived for all the four classes, a selection of popular indexes, widely employed in assessing the performance of model-based predictions (Santos et al., 2019; Rahmati et al., 2020; Albano et al., 2020; Esfandiari et al., 2020), are then computed: Overall accuracy (ACC), True Positive Rate (TPR), Positive Predicted Value (PPV), Matthews Correlation Coefficient (MCC) and Cohen's kappa coefficient (K).

The first of these statistics, the overall accuracy (ACC), is defined as:

$$ACC = \frac{TP + TN}{TP + TN + FP + FN}. \quad (32)$$

The True Positive Rate (TPR), or sensitivity, which indicates the probability of correctly predicted flooded pixels into the domain, is then computed as follows:

$$TPR = \frac{TP}{TP + FN}. \quad (33)$$

Instead, the Positive Predicted Value (PPV), which indicates the probability that a pixel classified as positive is true, is chosen to indicate the precision of the model prediction. Thus, PPV is derived with:

$$PPV = \frac{TP}{TP + FP}. \quad (34)$$

In addition to that, two additional statistics are here employed to estimate the correlation rate between observed and predicted flood extent values. Therefore, the chance agreement probability is computed by using the Matthews Correlation Coefficient (Matthew, 1975), defined as:

$$MCC = \frac{(TP \cdot TN) - (FP \cdot FN)}{\sqrt{(TP + FP) \cdot (TP + FN) \cdot (TN + FP) \cdot (TN + FN)}}, \quad (35)$$

and by using the Cohen's kappa coefficient (Cohen, 1960), which also provide a measurement of agreement and that is derived using the expression:

$$K = \frac{p_a - p_e}{1 - p_e} \quad (36)$$

where p_a is the proportion of observations in agreement, and p_e is equal to the hypothetical probability of chance agreement.

Concerning MCC and K measures of agreement, these statistics can be interpreted by using the interpretation scales and scores available in the literature. The MCC coefficient ranges from -1 (complete disagreement $TP=TN=0$) to 1 (total agreement $FP=FN=0$). Instead, the K index ranges from 0 to 1 and its score can be evaluated as follows: None ($K<0.20$), Minimal ($K<0.4$), Weak ($K<0.6$), Moderate ($K<0.8$), Strong ($K<0.9$) and Almost Perfect ($K>0.9$).

2.8 The integration of external satellite-based observation

This section illustrates different earth observations data exploitation methods identified in this research to enhance the REFLEX modeling by collecting additional observations for calibration and validation purposes.

2.8.1 EO-based water mask

EO-based water masks and other derived products from optical images can be used to better define input flowlines for REFLEX. If streamlines are derived from an unsupervised extraction from the DEM, a post-processing of this hydrological derivative is often needed to remove some of the not representative branches. As an example, the 100% of Water Occurrence from the Global Surface Water dataset (Pekel et al., 2016; JRC, 2021) can be used to identify suitable flow accumulation threshold by feature matching or to exclude dry stream branches from the source dataset. Furthermore, an additional dataset, also based on the Landsat mission, can also indicate the river width and depth which can be useful for DEM conditioning (Andreadis et al., 2013).

2.8.2 Water level surface height from radar altimetry

In this Ph.D. research, an application of a remote sensing technique has been identified for the water surface height detection of large inland rivers by using Sentinel-3 Synthetic Aperture Radar Altimeter (SRAL) data. This proposed approach enables the use of Radar Altimetry data to enable a systematic ingestion of satellite-based river level estimations also in data-scarce environments or ungauged river basins.

Obtained products from the SARvatore for Sentinel-3 service can then be post-processed to extract the time series of relative water levels from the seasonal average as well as to estimate discharge.

The extraction of surface water height estimations by radar altimetry is accomplished starting from the identification, based on Sentinel-3A ground tracks, of virtual stations along the river network (see Figure 30).

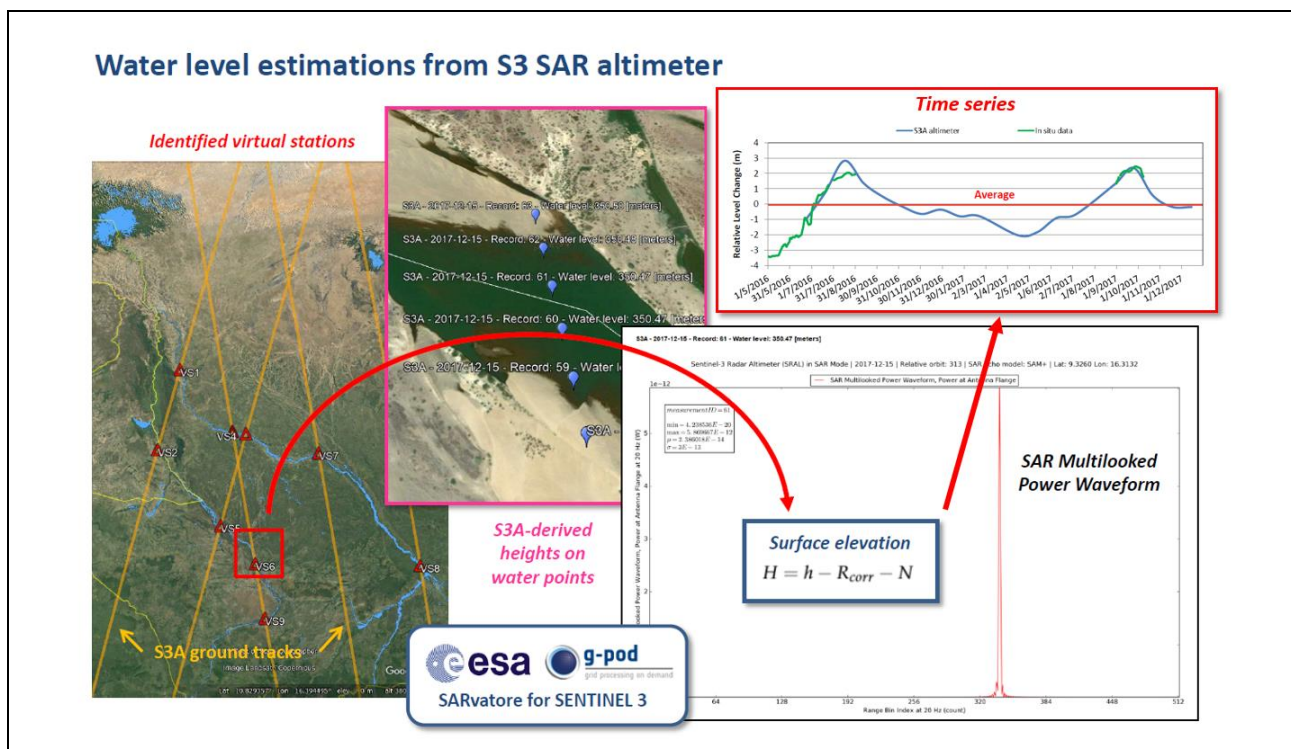


Figure 30 - Workflow for water level estimation using Sentinel-3 SAR altimeter

Once the virtual stations are identified all required Sentinel-3 SRAL L1A data products available over the desired period need to be harvested from the catalog (via Copernicus Open Access Hub or the DIAS).

Later, the gathered radar altimetry observations need to be processed to obtain the L2 products which are necessary to extract power echoes waveforms and along-track surface height profiles (see Figure 31).

Remote sensing

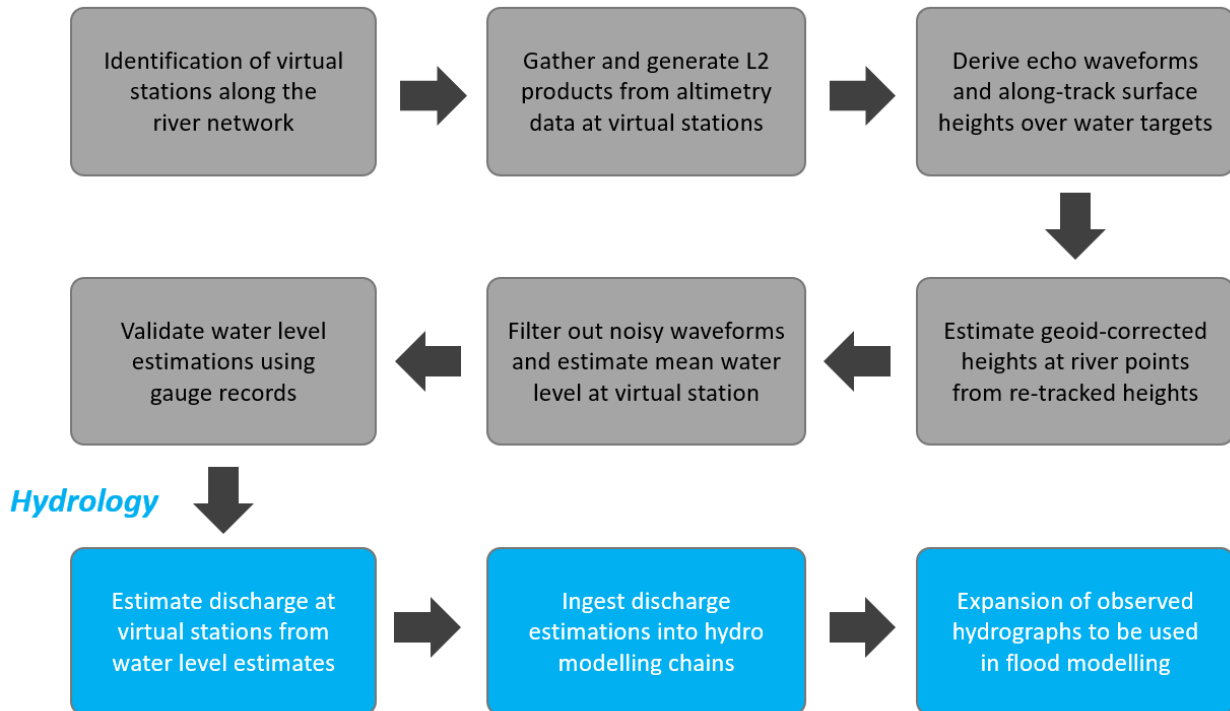


Figure 31 – A general workflow for the computation and the validation of water level estimations from radar altimetry and its exploitation in hydrology for flood modeling purposes.

For this scope, the on-demand exploitation of Sentinel-3 SRAL L1A data products in SAR mode (high-resolution) over these targets is achieved using a web processing service, based on the SARvatore (SAR Versatile Altimetric Toolkit for Ocean Research and Exploitation) processor, available within ESA's G-POD (Grid-Processing On-Demand) computing platform.

After that, SAR echoes from the obtained L2 products needs to be evaluated to derive consistent water surface elevation for the entire river and to avoid the inclusion of “polluted” estimations.

Once noisy waveforms are filtered, it is then possible to compute the absolute and relative height of water surface relative to EGM2008 geoid at virtual stations. Such water height estimates are then spatially densified via a spatial interpolation based on mean river level slope.

Finally, the validation of satellite-based estimates to in-situ stage records is made by comparing relative water level changes from the average over the observed period.

This information can be exploited to derive discharge estimation using one of the methods available in the literature (Kebede et al., 2020; Tarpanelli et al., 2013, 2019) or to be used as complementary data in hydrological modeling at a basin scale.

2.8.3 Flood impact assessment using SAR data

SAR missions are the reference for the mapping of water from space due to their advantages to detect standing water in all weather conditions. Satellite-based flood impact assessments derived from freely available mid-resolution SAR data, such as the one of Copernicus Sentinel-1 data, which can be used to validate REFLEX flood modeled extents where no field observations are available.

Flood map products available from the Copernicus Emergency Management Service (EMS), UNITAR-UNOSAT's Flood Portal and cartographic products (UNOSAT, 2011), and Dartmouth Flood Observatory (DFO) are key sources of flood extent records globally, which are obtained under major disasters using both optical and SAR data. This flood record repository can be expanded by using unsupervised flood change detection methods over new locations.

Different types of flood mapping algorithms are available in the literature. However, most of them are only accessible to a restricted group of users or are provided via a semi-automatic procedure. A valuable tool for flood mapping is the HASARD processing service developed by LIST which is open to the scientific community. Such service is built on the *Hierarchical Split-Based Approach - HSBA* algorithm (Chini et al., 2017) and is accessible within the ESA's grid processing on-demand (G-POD) environment. The current version of the HASARD service enables the user to obtain EO-based flood maps from ENVISAT and Sentinel-1 SAR images. In this Ph.D. research, the LIST's HASARD service in ESA G-POD (ESA, 2021a) has been chosen for the on-demand processing of Sentinel-1 GRD data.

Chapter 3 - Results

The third chapter summarized major results obtained by using the method identified under this Ph.D. research, including a general discussion.

3.1 Introduction

The third chapter of this thesis summarizes major results from the research carried out in this Ph.D. research. This chapter begins with the description of the complex modeling system, named REFLEX, which represents a synergy of multiple open tools and codes.

After a detailed description of the developed tool, the chapter presents the application of REFLEX using real data (DEM, Hydrographs) at multiple scales over different regions of the world. Case studies here described are the following: Magra, Entella, Secchia, and Southern Africa. Each REFLEX case study describes the area of interest, the modeling approach employed, obtained flood modeled results, and a validation of REFLEX by comparing its water extent and depth estimations with the ones retrieved from reference Flood Hazard maps, flood scenarios from benchmark hydraulic models, or satellite detected waters.

The last part of this chapter also includes major outcomes from the complementary research activity about the integration of secondary data from Earth Observation. Preliminary results from the evaluation of radar altimetry and SAR data are shown respectively for a case study in Chad and another one in Iran.

3.2 The implementation of the REFLEX modeling chain

This section aims to provide all related details about the numerical implementation of the REFLEX method, described in Chapter 2 of this Ph.D. thesis, into an automated chain. It includes an overview of the REFLEX modules, the list of employed tools (e.g., software dependencies and source code libraries), the description of the configuration file, and a quick presentation of the GIT repository.

3.2.1 The REFLEX development

Hereinafter is described how the entire method described in Chapter 2 about the REFLEX flood modeling approach has turned into software. This development activity has been crucial to implement the entire chain and to test if all the necessary components to build REFLEX can be merged into a single modeling system.

This applied research work represents one of the major outcomes of this Ph.D. research, given the complexity in building the REFLEX modeling chain. Such a result has been obtained from a synergy of multiple software, tools, and different methods available in the literature, as presented in Chapter 1 of this Ph.D. thesis.

With the goal to build a robust and stable repository for the REFLEX prototype, multiple research activities have been conducted to:

- harmonize the chain by linking multiple open-source software,
- develop code under modules to facilitate future modifications,
- contain computation time by using parallelized routines.

After a preliminary development phase conducted in the first year of the Ph.D., the tool has continuously improved with the inclusion, when possible, of parallel or optimized versions of external tools (e.g., the TauDEM D-infinity). In particular, the REFLEX code has been consolidated during the third year of the Ph.D. In this period, the entire code has been restructured to ensure a harmonized modeling chain that is able to respect in a Linux OS (Ubuntu or Centos7 OS) all dependencies of different software, such as GRASS, GDAL, TauDEM, MPICH, and R. As an example, the inclusion of most recent TauDEM GitHub version of the code, developed from the team of Prof. Tarboton, has allowed the estimation of HAND maps based on the D-infinity drainage approach (Tarboton, 1997) also in medium high-resolution DEMs, given its stable and parallelized implementation of the C++ code. All this reengineering work on the REFLEX code has also included the development of an ad-hoc setup script to ensure portability (e.g., to set up the code in CIMA and ESA servers) as well as the preparation of a setup script for the installation of REFLEX and the configuration of Linux OS.

The applied research behind the development of the REFLEX chain has been challenging and time-consuming. However, this activity was necessary to allow a simple, stable, and automatic deployment of the REFLEX under multiple case studies.

3.2.2 The REFLEX modeling chain

The entire REFLEX chain is built using Python 3 and is subdivided into five modules:

- REFLEX Module 0 - The “DEM conditioning”,
- REFLEX Module 1 - “The drainage module,
- REFLEX Module 2 - “The streams module”,
- REFLEX Module 3 - “The HAND module”,
- REFLEX Module 4 - “The Flood Inundation module.

A wrapper code in bash allows the activation of the *Anaconda* environment and the submission of the module in sequence.

REFLEX input files are:

- A configuration text file that contains all REFLEX parameters,
- A DEM raster in GeoTIFF format,
- Average discharge raster in GeoTIFF format,
- Flood discharge raster in GeoTIFF format,
- Reflex output directory path,
- Stream vector for burning streams into DEM in shapefile format (OPTIONAL).

REFLEX output files are:

- multiple hydrological derivatives (e.g., drainage, watershed, Pfafstetter streams, subbasins characteristics),
- water depth raster for the given flood return period,
- water extent raster for the given flood return period.

The first module (REFLEX Module 0) allows the “hydrologically conditioning” of the source DEM. It implements the method explained in Chapter 2 (see section 2.3.2). This step is particularly important if source DEM is given as raw elevation data. In case the input DEM is already hydrologically conditioned, this module simply employs the filling of the DEM using the epsilon filling algorithm of RichDEM. Outputs of this module are a Conditioned and Filled DEM given as GeoTIFF files.

The REFLEX Module 1, the “DEM Conditioning Module”, extracts all necessary hydro derivatives from the filled DEM by employing multiple drainage methods (D8, MFD, DINF). Outputs are multiple derivatives (flow direction, flow accumulation, streams, watersheds) provided as raster files in GeoTIFF format and vector files in Shapefile format.

The following REFLEX Module 2, the “Streams Module”, extracts essential geomorphic information from the Conditioned DEM, calculates streams hierarchy (Hack, Strahler, Pfafstetter), produces multiple masks (Sub-basin mask, Drainage area mask, Headwater mask, Downstream mask), and derives runoff volumes from input discharge values. Outputs are multiple files given as raster, in GeoTIFF format, vector files (classified streamlines and dissolved watersheds), in Shapefile format, and tabular files in CSV format (table with a summary of geomorphic information and runoff volume at each sub-outlet of the river network).

In REFLEX Module 3, “The HAND module”, a python code collects different output from the previous steps (e.g., the Filled DEM and the flow directions grids) to derive HAND maps with gradient-based extension for flat areas (e.g., to deal with the coastal zone). Outputs of this module are stream and HAND maps given as raster files in GeoTIFF format.

Finally, in the last and fourth “Flood Inundation module” (REFLEX Module 4) flood maps are derived by combining all the HAND maps into a 2D Flood scenario using the runoff volumes derived at step 2. Output files are water extent and water depth flood maps given as raster file given in GeoTIFF format.

3.2.3 The REFLEX dependencies

REFLEX is built by integrating multiple software and its dependencies are shown in Table 7.







Name	Type	Version	Release	Distribution
	IT	4.8.2	<i>Miniconda</i>	anaconda
	IT	3.8.2	-	conda-forge
CMAKE	IT	-	-	-
GCC	IT	7	-	-
MPICH	IT	3.2.1	21/01/2020	mpich.org
	Geospatial	3.0.4	28/01/2020	OSGEO
	Statistical computing	3.6.3	29/02/2020	bionic-cran35
	GIS	7.8.2	12/12/2019	ubuntugis-unstable
pysheds	Terrain analysis software	0.2.7	01/11/2020	conda-forge
	Terrain analysis software	5	TauDEM "update-version" repository	GitHub
RichDEM	Terrain analysis software	0.3.4	13/07/2018	pypi anaconda
mdenoise	Terrain analysis software	-	mdsource	www.cs.cf.ac.uk

Table 7 – Overview of REFLEX dependencies.

Concerning the GRASS GIS software, the default set of tools has been enriched in this research by installing multiple Add-ons, available from the GRASS OSGEO community. This was needed to satisfy a need of particular terrain analysis processing (e.g. Hack and Strahler stream hierarchy through the “r.stream.order” Add-on) required in the REFLEX modules. The full list of these Add-ons together with their usage in REFLEX is reported in Table 8.

Name	Usage in REFLEX	Manual webpage
<i>r.stream.basins</i>	Used to delineate basins from input stream raster	https://grass.osgeo.org/grass78/manuals/addons/r.stream.basins.html
<i>r.stream.order</i>	Used to compute Strahler, and Hack streams hierarchy.	https://grass.osgeo.org/grass78/manuals/addons/r.stream.order.html

<i>r.stream.distance</i>	Used to compute elevation above streams from a flow direction map	https://grass.osgeo.org/grass78/manuals/addons/r.stream.distance.html
<i>r.accumulate</i>	Used to compute weighted flow accumulation and other derivatives from a flow direction map	https://grass.osgeo.org/grass78/manuals/addons/r.accumulate.html
<i>r.stream.extract</i>	Used to extract stream network.	https://grass.osgeo.org/grass78/manuals/r.stream.extract.html
<i>r.clip</i>	Used to clip raster	https://grass.osgeo.org/grass78/manuals/addons/r.clip.html
<i>r.hydrodem</i>	Used in the DEM conditioning to remove spurious sinks from raw DEM	https://grass.osgeo.org/grass78/manuals/addons/r.hydrodem.html

Table 8 – Overview of all GRASS GIS Add-ons employed in REFLEX.

3.2.4 REFLEX parameters

All the necessary information about the parameters of the REFLEX modeling chain is reported in Table 9. This information is included within the REFLEX configuration file, which is meant to be edited by the user to deploy REFLEX under multiple applications at different scales by tuning all essential parameters.

Parameter Name	Description	REFLEX module	Usage	Default value
<i>CONDADIR</i>	Path to the Anaconda directory	All	String	/PATH/Reflex_model/bin/anaconda/miniconda3
<i>TAUDEM_BUILD_PATH</i>	Path to the TauDEM directory	All	String	/PATH/Reflex_model/bin/taudem/TauDEM-update-version/src/build
<i>RSCRIPT_VOL_OPT_PATH</i>	/path/filename.extension of the static volume optimization R code	All	String	/PATH/Reflex_model/reflex/src/optimize_volume.R
<i>CONDAENV</i>	Name of python environment in Anaconda	All	String	reflex_py38
<i>GRASSBIN</i>	Name of GRASS executable	All	String	grass78
<i>SVER</i>	Version of the REFLEX code	All	String	v15
<i>ST0OUTDIRN</i>	Name of step 0 output directory	All	String	DEM_conditioning
<i>ST1OUTDIRN</i>	Name of step 1 output directory	All	String	hydro_derivatives
<i>ST2OUTDIRN</i>	Name of step 2 output directory	All	String	streams
<i>ST3OUTDIRN</i>	Name of step 3 output directory	All	String	hand
<i>ST4OUTDIRN</i>	Name of step 4 output directory	All	String	flood
<i>ACPX</i>	Name of hydrological region	All	String	APP_SETT
<i>DOMAIN</i>	Name of domain	All	String	magra
<i>RRS_M</i>	DEM spatial resolution in m	All	Integer	90

<i>RRS_DD</i>	DEM spatial resolution in decimal degrees	All	Float	0.00083333333
<i>NANDEMVAL</i>	Value defined as not a number in the source DEM	All	Signed float	-9999
<i>EPSG_CRS</i>	Geographic coordinate system EPSG code	All	Integer	4326
<i>EPSG_PRJ</i>	Projected coordinate system EPSG code	All	Integer. Set local projection or UTM zone	32632
<i>STR_BURNING_ENABLED</i>	Flag to enable stream burning in REFLEX	Step 0	True or False	False
<i>TARGET_EPSG</i>	EPSG of output conditioned DEM.	Step 0	Integer	4326
<i>DCOND_BUFFER_CELLS</i>	Buffer zone along a branch as the number of cells used as input domain for stream burning.	Step 0	Integer	20
<i>DCOND_FILTERING_MAGNITUDE</i>	Magnitude of filtering used in the stream burning. See §3.3.2. Ref. scalar C in equation 1 of Chapter 2.	Step 0	Float number (<1 for light and >1 for heavy filtering).	1
<i>REMOVE_SINK_ENABLED</i>	Flag to enable removing of sinks ('hydrodem' GRASS Add-on) in REFLEX.	Step 0	True or False	False
<i>PIT_REMOVAL_ENABLED</i>	Flag to enable DEM pit removal (TauDEM) in REFLEX.	Step 0	It generates filled areas with a small artificial gradient. True or False.	False
<i>EPS_FILLING_ENABLED</i>	Flag to enable DEM epsilon filling (richdem) (Barnes, 2016) in REFLEX.	Step 0	It generates filled flats. True or False	True
<i>SOLVE_FLATS_ENABLED</i>	Flag to enable DEM flat resolving ('pysheds', Matt Bartos, UT Austin) in REFLEX.	Step 0	True or False	False
<i>FD_METHOD_STREAMS</i>	Drainage method to be used for extracting flowlines and watersheds from the DEM.	Step 1	String. Set 'D8' for the D8 (O'Callaghan and Mark, 1984), or 'MFD' for the Holmgren MFD (Holmgren, 1994).	D8
<i>FD_METHOD_HAND</i>	Drainage method to be used for deriving HAND contours from the DEM.	Step 1	String. Set 'D8' for the D8 (O'Callaghan and Mark, 1984), 'MFD' for the Holmgren MFD (Holmgren, 1994), or 'DINF' for D-infinity (Tarboton, 1997).	DINF
<i>DRAINAGE_THRSLD</i>	Threshold as the number of cells used to extract multiple hydrological derivatives and to define the level of detail in the	Step 1	Integer	3000

	output stream raster map (from D8 or MFD) in the GRASS 'r.watershed' tool.			
<i>BUFFER_DISTANCE_CELL</i>	Buffered distance is the number of cells to be used for creating a downstream mask for the REFLEX downstream expansion of HAND maps.	Step 2	Integer	50
<i>COASTEXP</i>	Flag to enable coastal expansion in REFLEX.	Step 3	Flag 0 (disabled) or 1 (enabled)	1
<i>HAND_TRSHLD_ELEV</i>	The maximum value of Height Above the Nearest Drainage I of REFLEX's HAND maps.	Step 3	Integer	2000
<i>HAND_MASK_BUFF_DIST_M</i>	Distance in meters used for buffer HAND map masked.	Step 3	Integer	300
<i>GRADIENT_LIMIT</i>	Gradient limit (m/m) to identify flat river branches.	Step 3	Float	0.0003
<i>STR_ELEV_PERCENTILE</i>	Define percentile (e.g., 25th) of the population for stream elevation of a branch where HAND expansion is triggered. Ref. z_{25} in equation 16 of Chapter 2.	Step 3	Integer	25
<i>HEAD_LOSS</i>	Head loss per pixel distance in cm (-JL). E.g., if equal to 1 cm and pixel spacing of 5 m, Hydraulic gradient ($-J=dh/dx$) is equal to $-J=dh/dx = 0.2\%$. Ref. J in equation 15 of Chapter 2.	Step 3	Float	20
<i>VOLMIN</i>	Minimum runoff volume in cubic meters of a river branch for which the Flood Inundation is triggered.	Step 4	Integer	1000
<i>WDMIN</i>	Minimum water depth in meters to be used for initializing static volume optimization. Ref. h_{min} in equation 19 of Chapter 2.	Step 4	Float	0.1
<i>WDMAX</i>	Maximum water depth in meters to be used for initializing static volume optimization. Ref. h_{max} in equation 19 of Chapter 2.	Step 4	Integer	15
<i>ITERATIONS_MAX_VOL_OPT</i>	The maximum number of iterations in Manning-based volume optimization.	Step 4	Integer	5
<i>ROUGHNESS_COEFF</i>	Value of roughness coefficient N in Manning Formula (e.g., 0.045 for natural channels). Ref. k_s in equation 26 of Chapter 2.	Step 4	Float	0.045
<i>TOLERANCE_VOL_OPT_M</i>	Tolerance in volume difference, used under the Manning-based volume optimization iteration.	Step 4	Float	0.1
<i>RP</i>	Flood Return Period in years of input peak discharge	Step 4	Integer	50

Table 9 – Overview of all REFLEX parameters.

3.2.5 The REFLEX GIT repository

The REFLEX code has been organized into a GitHub repository to take advantage of versioning and other tools. A GIT documentation is crucial to have a reliable, slim, and robust model that can be easily shared also with not IT expert end-users.

The screenshot displays the GitHub repository interface for 'mauroarcorace / Reflex_model'. The repository is private and has 1 star and 0 forks. The main branch is 'master' with 1 branch and 0 tags. The repository contains 172 commits and 11 days ago. The file structure is as follows:

File	Commit Message	Time Ago
config	Update reflex_entella.config	12 days ago
info	Delete test2.shx	4 months ago
log	Add files via upload	12 days ago
reflex	Add files via upload	11 days ago
setup	Update reflex_setup.sh	6 months ago
test/output_20210124_164403	Delete entella_streams_conditioning.dbf	12 days ago
README.md	Update README.md	12 days ago

The README.md file contains the following content:

About REFLEX (Rapid Estimate of FLOOD EXtent)

Description: An innovative 2D hydro-morphological model developed for a rapid identification of flooded areas of major rivers

The algorithm is subdivided into 4 modules:

1. REFLEX STEP 0 - DEM conditioning.
2. REFLEX STEP 1 - Extract hydroderivatives from DEM using multiple drainage methods (D8, MFD, DINF).
3. REFLEX STEP 2 - Extract basin information, calculate streams hierarchy (Strahler, Pfafstetter) and derive runoff volumes
4. REFLEX STEP 3 - Derive HAND plus maps with gradient-based extension for flat areas.
5. REFLEX STEP 4 - Combine HAND maps into 2D Flood scenarion using runoff volumes derived at step 2.

The right sidebar shows the repository's statistics: 1 star, 0 forks, and 0 releases. The 'Languages' section shows the following distribution: Python 91.2%, Shell 8.0%, and R 0.8%.

Figure 32 – Organization and upload of all REFLEX source codes and their setup into a GIT repository. All related documentation is also given together with a reference result to better explain REFLEX installation and usage to the end-user.

The development of this GIT repository (https://github.com/mauroarcorace/Reflex_model) has been necessary to maintain the master version of the REFLEX code (e.g. in sharing with CIMA hydrologists for systematic computation over multiple African basins) as well as to ensure effective usage and installation documentation to future REFLEX users.

The REFLEX model will be open to the research community. A stable version of the code is also foreseen to be published in the GitHub repository of the CIMA Research Foundation Department of Hydrology and Hydraulics (<https://github.com/c-hydro>).

3.3 REFLEX Case study – The Magra river basin in Northern Italy

This section described the results obtained from the application of REFLEX over a surveyed river basin in northern Italy.

3.3.1 Case study description

The area of interest for this REFLEX case study is the Magra river basin, which is part of the Northern Apennines District in northern Italy. The Magra river basin is in the eastern part of this hydrological region, and it covers the territory between the regions Liguria and Tuscany. The Magra river basin has an extension of about 1715 square kilometers and comprises mainly mountain and hilly areas. A map of the Magra river basin is shown in Figure 33.

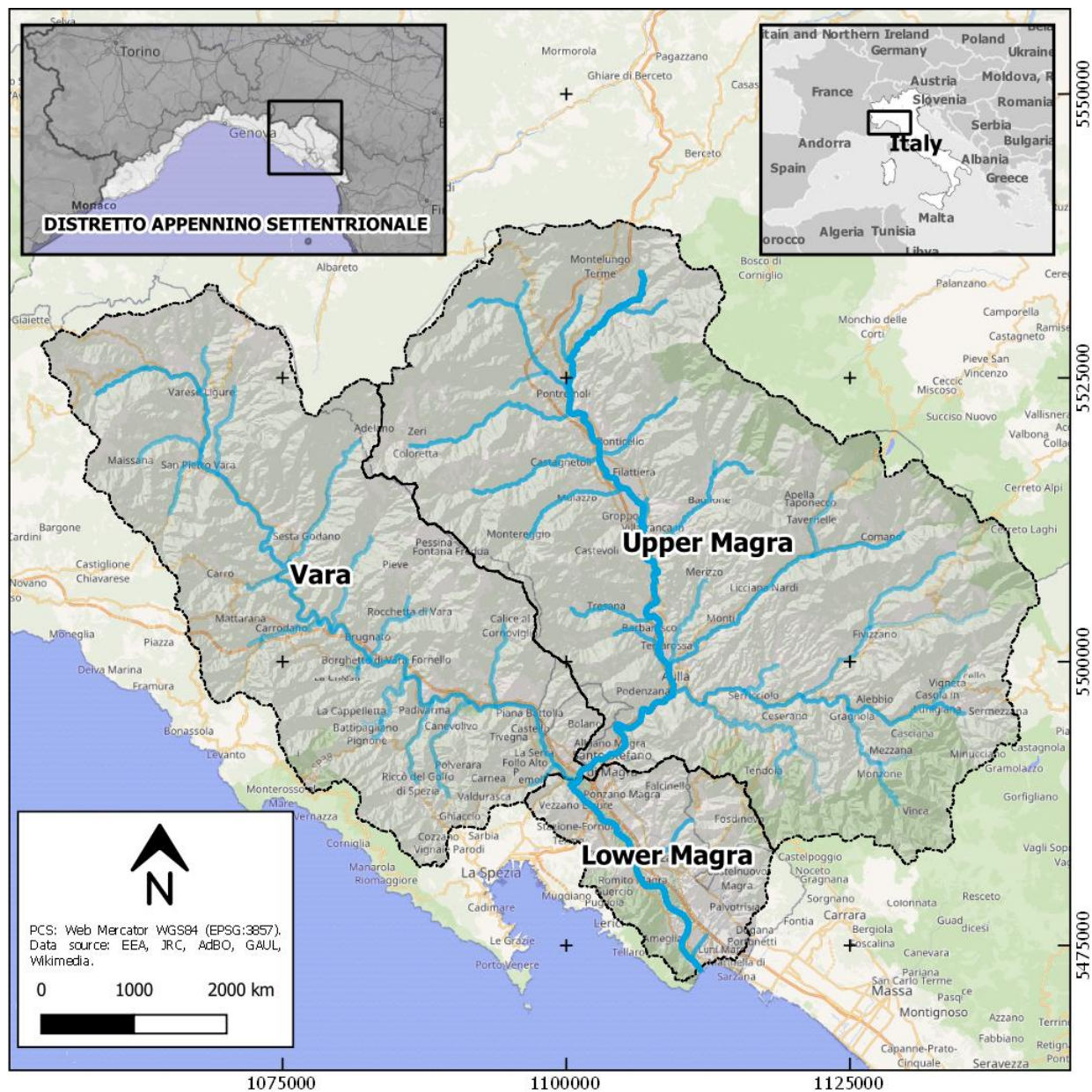


Figure 33 – The Magra river basin in Northern Italy.

The watershed of the Magra river can be subdivided into three principal sub-basins, the Vara, the Upper, and the Lower Magra catchments. The Vara river is the principal tributary of the Magra main stem. The Vara catchment essentially covers the Ligurian part of the whole Magra river basin. The Upper Magra catchment

collects the waters from the divide, in the northwestern part of the entire basin, and drains them until the confluence with the Vara. After the confluence, the Magra river basin is then composed of a third catchment, located in the south near the mouth in the Ligurian Sea. This downstream part of the basin is characterized by the presence of a coastal floodplain, the lower Magra River valley. This floodplain is part of an urban context and is characterized by the presence of multiple infrastructures (motorways, railways bridges). Thus, in this area, the Magra river environment, and the streamflow as well, are artificially confined within only a portion of the entire floodplain which is defended by embankments and floodwalls from the confluence until the mouth of the river. In addition to these intersections, local hydraulics is also characterized by the presence of multiple minor streams and channels that drain water from the hillslope parts of the lower Magra river valley. The ending part of the main stem of Magra near the mouth presents a channel-like morphology. In this area, the mouth is constrained on the right by steep riverbanks due to the presence of Monte Marcello and on the left by levee dikes. Thus, in case of flood events due to overflow of the existing embankment system, the resulting flood extent can interest only a portion of the Ligurian-Tuscan coastal plateau between the Magra mouth and the Parmignola stream catchment in the territory of Carrara, in Tuscany.

3.3.2 Input data

To employ REFLEX over the Magra river basin a preliminary data collection activity has been performed, tailored to the specific application of the method for flood hazard mapping purposes.

3.3.2.1 Digital Elevation Model

Input elevation data for this case study are represented by two different DEMs at 90 and 10m spatial resolution that covers the entire territory of the Magra river basin. The first DEM is derived from the MERIT DEM dataset (Yamazaki et al., 2017). The second one at higher resolution is obtained by data fusion of multi-resolution DEMs derived from multiple sources. This second DEM merges elevation data from the LiDAR DTM at 1m spatial resolution from the Italian Ministry for the Environment Land and Sea (MATTM), the “*DTM Liguria ed. 2016*” at 5m spatial resolution from the Liguria Region (Regione Liguria, 2021a), and the “*DTM 10m Idrologico*” from the Tuscany Region (Regione Toscana, 2021). LiDAR data has been retrieved under a collection of tiles that cover only a portion of the whole basin, along the Magra main stem and its principal tributaries. This data has been accessed via the CIMA foundation repository for the Ligurian tiles and from the “*GEOscopio*” web portal of the Tuscany Region for the Tuscan ones (Regione Toscana, 2021). The harvesting of MATTM LiDAR DTM resulted in a collection of about 600 tiles, mainly obtained from the MATTM’s DEM dataset of 2008 and complemented in only a few cases with LiDAR data derived from MATTM’s campaigns of 2010 and 2012 (see Figure 34). More information about this LiDAR data can be retrieved from the *MATTM Geoportale Nazionale* (<http://www.pcn.minambiente.it/mattm/tag/dati-lidar/>).

This dataset at 1m resolution can cover most of the valleys and flood-prone areas of the basins, but it cannot fully cover the plateau near the coast between the Magra mouth and the Parmignola stream.

It is worth noticing that MATTM’s LiDAR 2008 1m is provided by Liguria Region as tiles in Monte Mario (Italy Zone 1) projected coordinate system (EPSG: 3003), while the same LiDAR data for Tuscany obtained from the GEOscopio portal is given in WGS 84 geographic coordinate system (EPSG: 4326). Thus, a projection of half of this dataset has been necessary to merge this data into a single mosaic. Tiles have been projected in their native resolution using bilinear interpolation in GIS. Later, all these tiles have been merged using a GDAL-based virtual mosaic and resampled at 10m resolution. Finally, this dataset has been extended in hillslope regions by merging it with the *DTM Liguria ed. 2016* resampled at 10m from the Liguria Region and the *DTM 10m Idrologico* from the Tuscany Region.

As a result, the final DEM includes surface elevation for hillslope areas from medium-high quality DEM combined with resampled LiDAR data with higher accuracy over most of the floodplain areas.

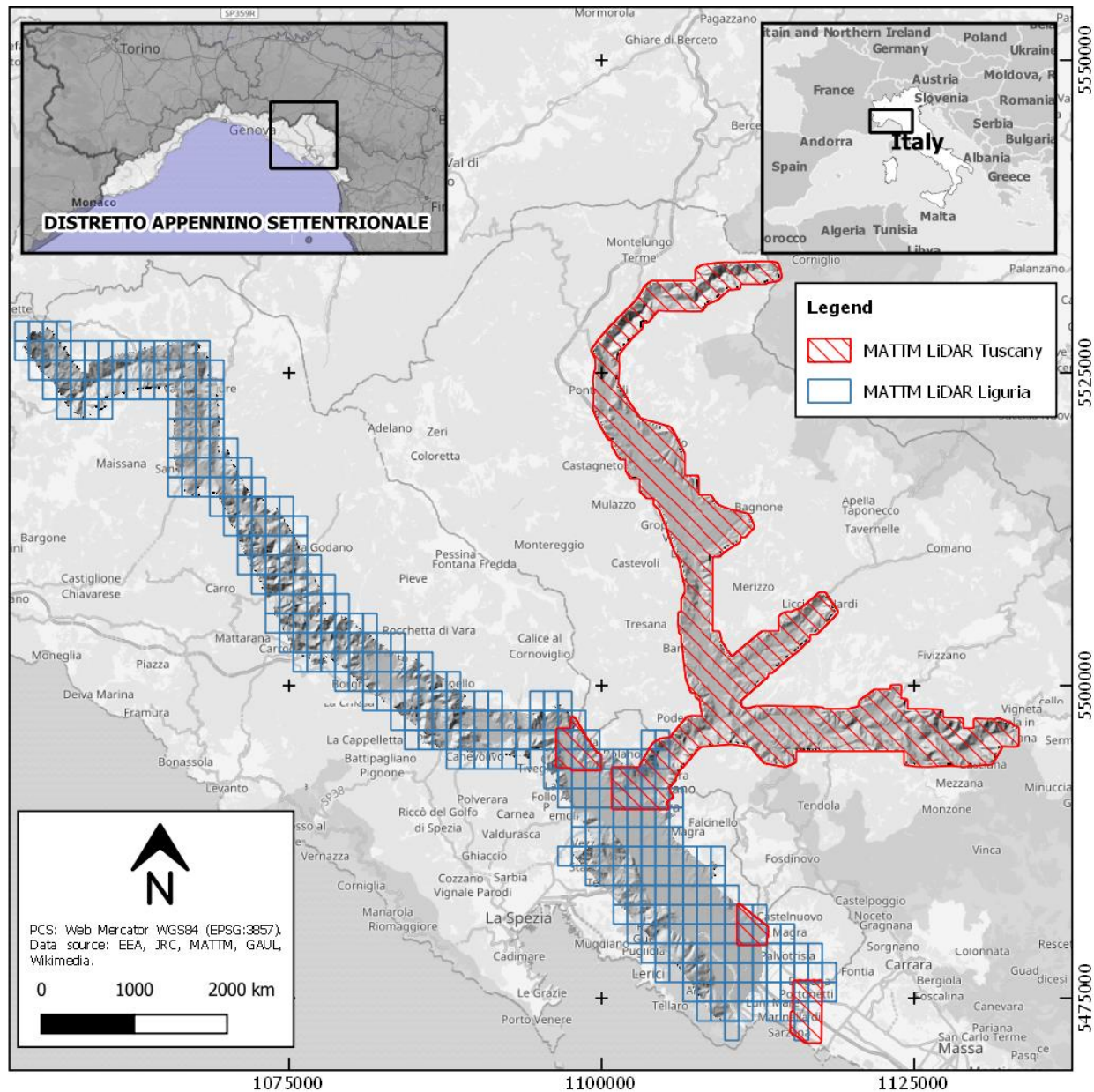


Figure 34 – Coverage of MATTM LiDAR data for the Magra river basin. Hill shaded DEM from mosaicking of all available tiles is shown in graded grayscale.

3.3.2.2 Flowlines

Input flowlines are assumed as streamlines in a vector file (shapefile) derived from the D8 drainage modeling of the Filled DEM through thresholding based on the drainage area (600000 cells for DEM at 10m resolution and 3000 cells for DEM at 90m resolution). Obtained streamlines are then manually edited in the lower Magra valley by following river and channel center lines derived from visual interpretation in GIS of Very High Resolution (VHR) optical imagery from Bing open layer base map.

3.3.2.3 Runoff peak discharge

Input runoff peak discharge estimations at different return periods are derived from drainage area empirical expressions retrieved from the table 2.9.3.1 of the “*Relazione generale variante al Piano Stralcio Assetto Idrogeologico del fiume Magra e del torrente Parmignola*” report made by the Magra interregional river authority (AdB Magra, 2016). Thus, input gross peak discharge values (Q_{RP}) for each branch of the Magra sub-basins are computed by using the following formula:

$$Q_{RP} = k_1 \cdot A^{k_2}, \quad (4.37)$$

where A is the drainage area in square kilometers and k_1, k_2 are the coefficients defined in the following tables.

Return period (RP)		30 years		
Coefficient	A	k1	k2	Q (mcs)
Vara	A<15skm	16	0.85	
Vara	A>=15skm	24	0.7	
Upper Magra	A<39skm	15	0.85	
Upper Magra	A>=39skm	26	0.7	
Confluence				4393
Lower Magra		12	0.9	

Table 10 - Discharge values for the Magra river basin at 30 years RP (AdB Magra, 2016).

Return period (RP)		200 years		
Coefficient	A	k1	k2	Q (mcs)
Vara	A<23skm	25	0.85	
Vara	A>=23skm	40	0.7	
Upper Magra	A<65skm	23	0.85	
Upper Magra	A>=65skm	43	0.7	
Confluence				6700
Lower Magra		18	0.9	

Table 11 - Discharge values for the Magra river basin at 200 years RP (AdB Magra, 2016).

Discharge values for a 30-year and 200-year return period (medium and high magnitude of flood hazard) derived from these drainage-area-based empirical formulas have been then distributed across the entire river network of the Magra basin within a grid (discharge raster files in GeoTIFF format) coherent with the input flowlines.

3.3.3 Modeling

Hereinafter it is explained how REFLEX has been used for the flood modeling of the Magra river basin by highlighting all the assumptions employed in this case study.

3.3.3.1 DEM conditioning

The conditioning of the DEM has been the first activity carried out in this case study. The DEM at 10 m obtained from data fusion of multiple sources elevation did not require noise filtering due to the nature of the input source datasets. The *DEM-DTM 10m* data from Tuscany Region is already a hydrologically

conditioned DEM, and the other two source elevation data, resampled at the 10-meter resolution, already presented a good level of smoothness due to the bilinear interpolation employed in this resampling. In addition to that, it is worth considering that the here employed LiDAR data are extracted from a filtered and conditioned DTM product at 1m resolution derived from the LiDAR DSM. Also, the DTM at 5m spatial resolution from the Liguria region is obtained from an interpolation of elevation contours.

For these reasons, the filtering of input raw elevation mosaic for the Magra basin has not been employed in the REFLEX DEM conditioning. However, the burning of the streams into the DEM has been necessary for the lower Magra valley to ensure a flow enforcement coherent to the real river network of the area. Thus, a subset of the input flowlines has been derived to represent only the complex network in this valley. For each of the branches, a representative depression in meters has been then assigned in GIS. Higher depression values to be used for the depression of DEM surface elevation are assigned along the main stem and the tributaries having riverbanks affected by elevation artifacts due to dense canopy still present in LiDAR DSM. All the values assigned for burning the streams into this portion of the Magra DEM are shown in Figure 35.

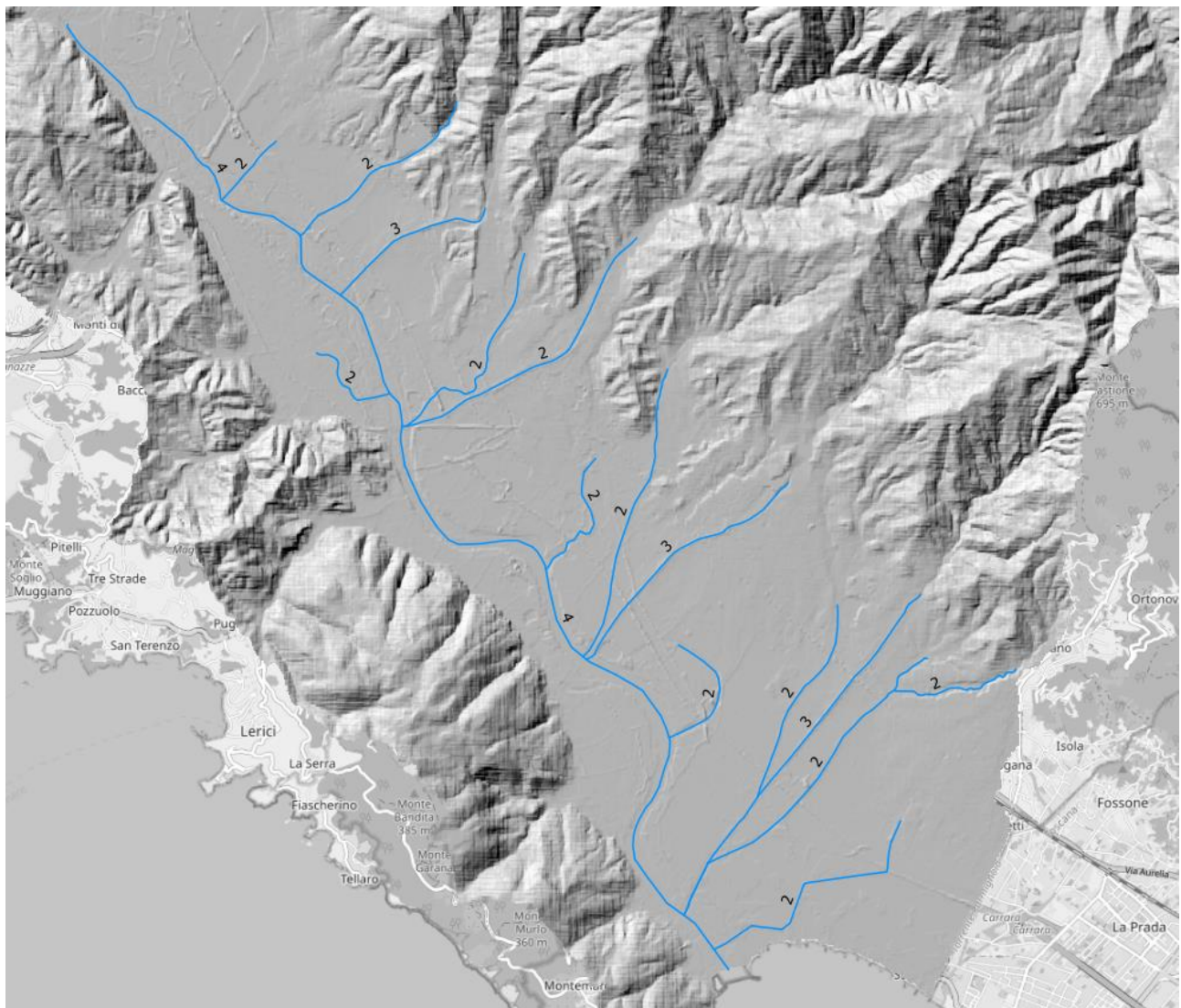


Figure 35 – Streamlines used in the stream burning of the 10m DEM in the Lower Magra valley. Labeled numbers indicate the artificial depression in meters used in the stream burning of the river branches.

Later, all these depression values have been defined as attributes into this vector file which has been then used as input for the DEM conditioning in the REFLEX Module 0.

After this manual pre-processing of input flowlines, Module 0 of the REFLEX model has been executed by giving as input the raw DEM at 10m resolution and the obtained flowlines with enriched metadata. This allowed the conditioning of the DEM in the whole basin. In REFLEX's Module 0 the DEM has been firstly filled using the epsilon filling algorithm of RichdDEM. The result of the filling of depressed areas is shown in Figure 36.

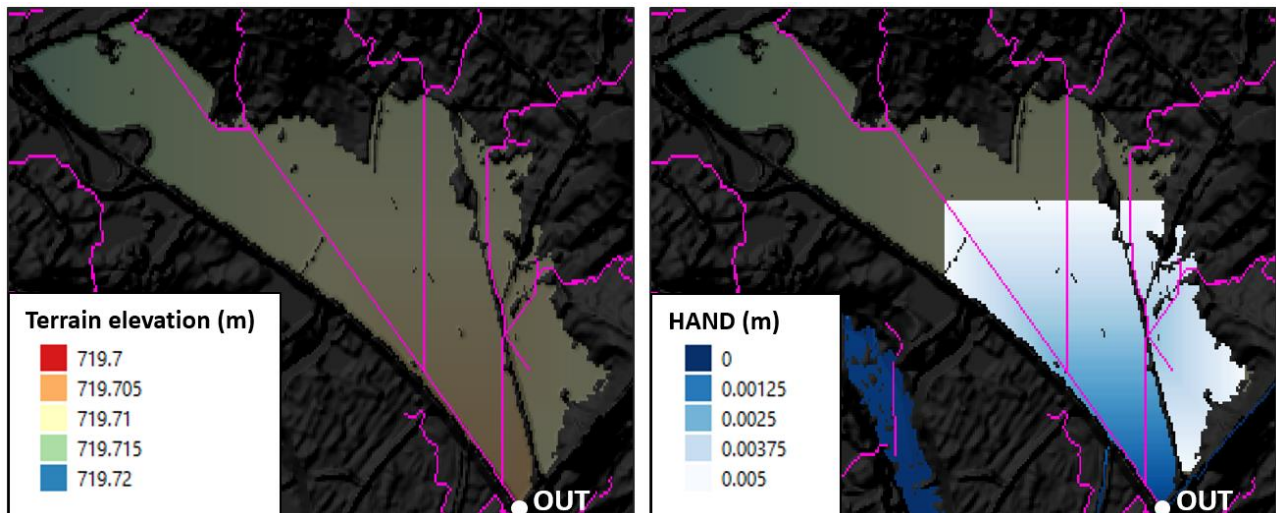


Figure 36 – Result of Epsilon filling over the lower Magra river basin. The Artificial gradient ensures a hydrologically consistent drainage of the area, also visually highlighted by estimated HAND contours only overfilled terrain elevation.

The epsilon filling is employed to do not affect the computation time required for the extraction of hydrological derivatives from both Holmgren's MFD and the D-Infinity flow directions algorithm in GRASS GIS and TauDEM software. As an example, while employing the TauDEM's D-infinity flow direction method (Tarboton, 1997) over LiDAR data, the implementation of the epsilon filling approach (Barnes, 2016) in REFLEX has shown a drastic reduction of the computation time required for TauDEM's D-Infinity Flow Direction model to resolve flats. This demonstrated the benefit of using the epsilon filling as the default method in the REFLEX DEM conditioning chain.

After the filling of the DEM, the burning of the streams into the filled DEM has been performed. As explained in Chapter 2 (see section 2.3.2), the DEM conditioning of REFLEX employs a different schema while deepening the DEM along the flowline with a certain value of SRD. Thus, in the river network shown in Figure 35, SRD is constant only for the connector branches while it is incremental for all the inlet branches.

Once the DEM conditioning of the REFLEX's Module 0 is accomplished, obtained outputs are:

1. a Filled DEM (only epsilon filling),
2. and a Conditioned DEM (epsilon filling and stream burning).

Figure 37 shows the hill-shaded digital elevations before and after the DEM conditioning of REFLEX. Resulted artificial depressions can be noticed in the Conditioned DEM along the input streamlines.

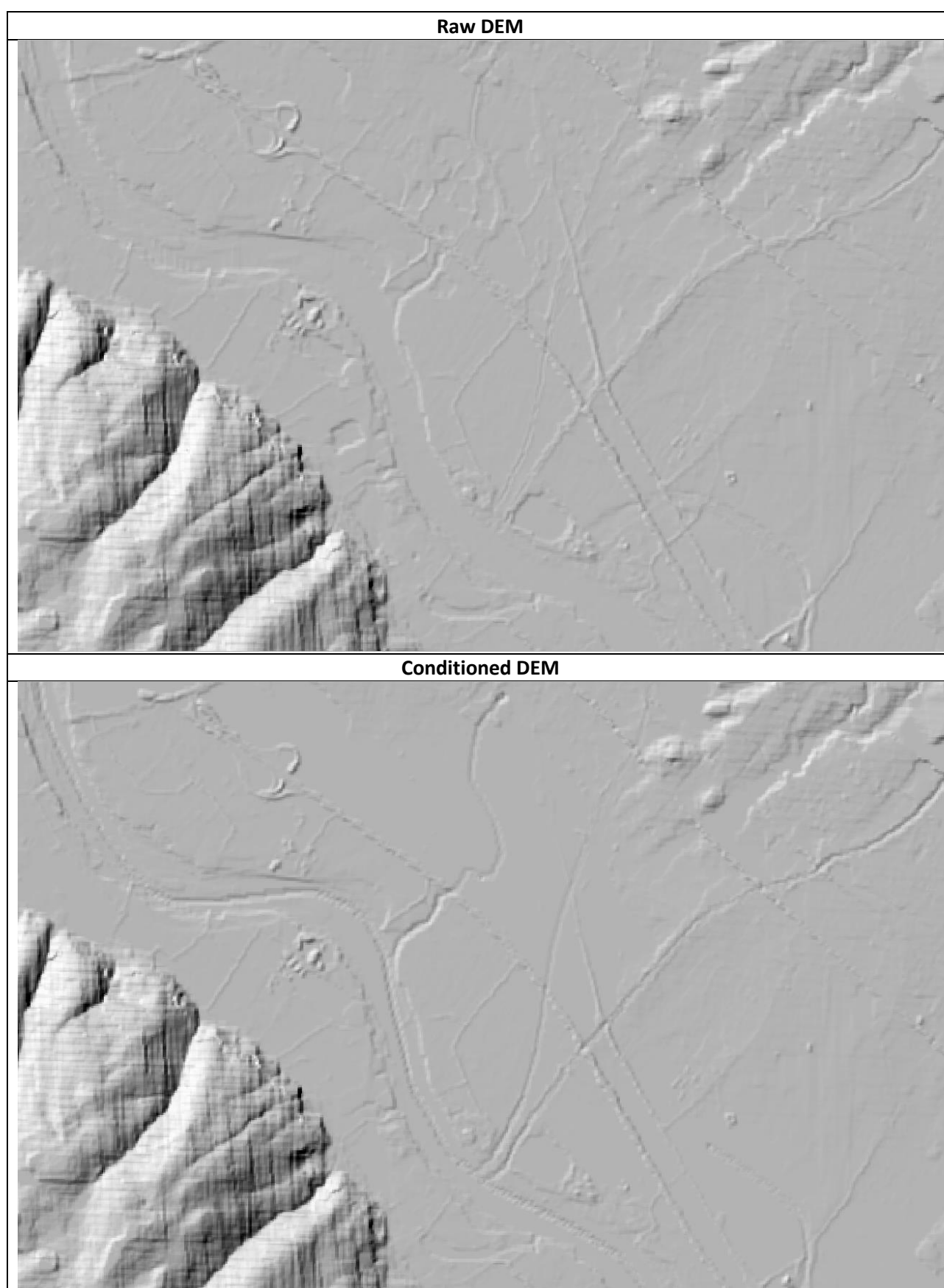


Figure 37 – Before and after the DEM Conditioning of the multi-source digital elevation model for Magra at 10m spatial resolution obtained with the REFLEX model.

An example of the elevation profiles for both raw and conditioned riverbed, obtained by using constant SRD values along a representative inlet river branch, is shown in Figure 38.

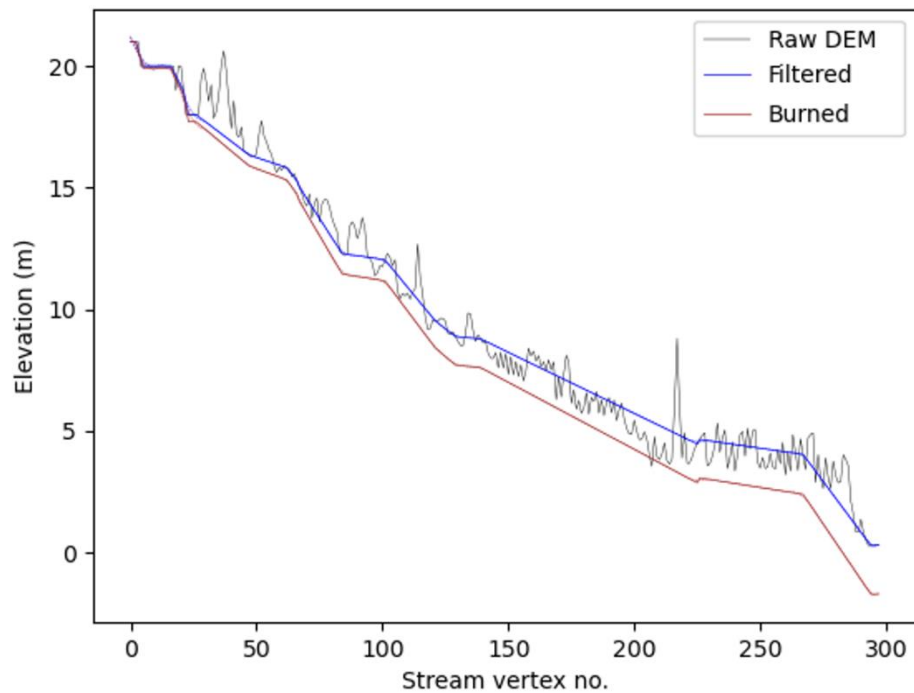


Figure 38 – A comparison of multiple elevation profiles for a river branch in the Magra river basin derived from resampled LiDAR high-resolution DEM. The dotted black line shows the input raw DEM, the blue line the filtered one, and the red line the burned one using incremental SRD values.

Instead, sample river profiles obtained by using incremental SRD value in a sample connector branch are shown in Figure 39.

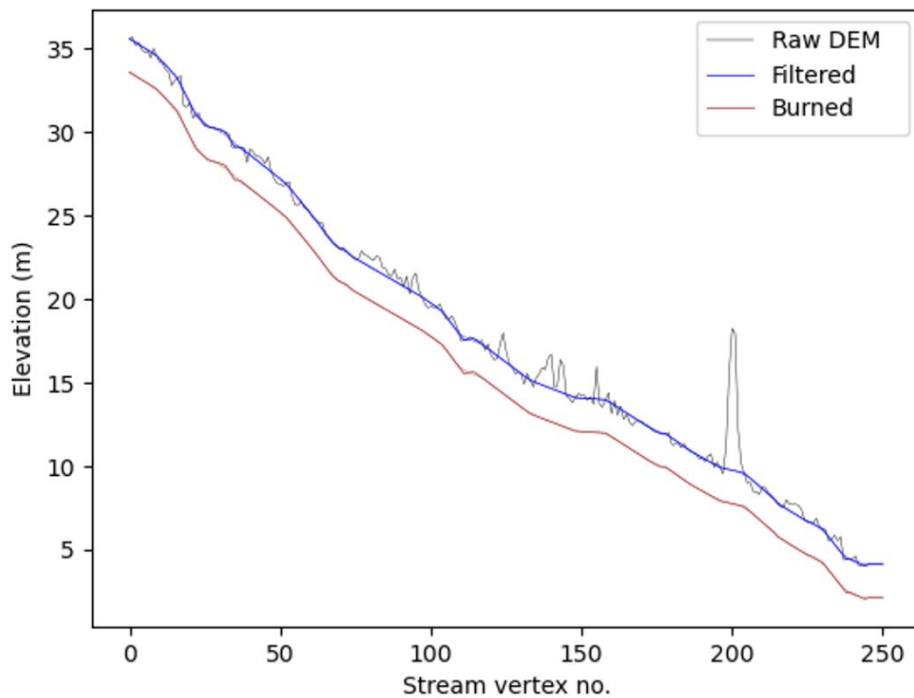


Figure 39 - A comparison of multiple elevation profiles for a river branch in the Magra river basin derived from resampled LiDAR high-resolution DEM. The dotted black line shows the input raw DEM, the blue line the filtered one, and the red line the burned one using constant SRD values.

In this case study, the magnitude of the filtering used for the stream burning (see scalar C in equation 1 of section 2.3.2.3) is assumed as unitary. The choice of $C=1$ represented, in fact, a fair balance in the filtering of filled DEM elevation along the streamlines. For this reason, this value has been defined as standard in the REFLEX configuration file.

Finally, to better assess the accuracy of the obtained Conditioned DEM, hydrological derivatives have been obtained in GIS from D8 by using both the Filled and the Conditioned DEM. Obtained flowlines derived from both these hydrologically conditioned DEMs are shown in Figure 40.

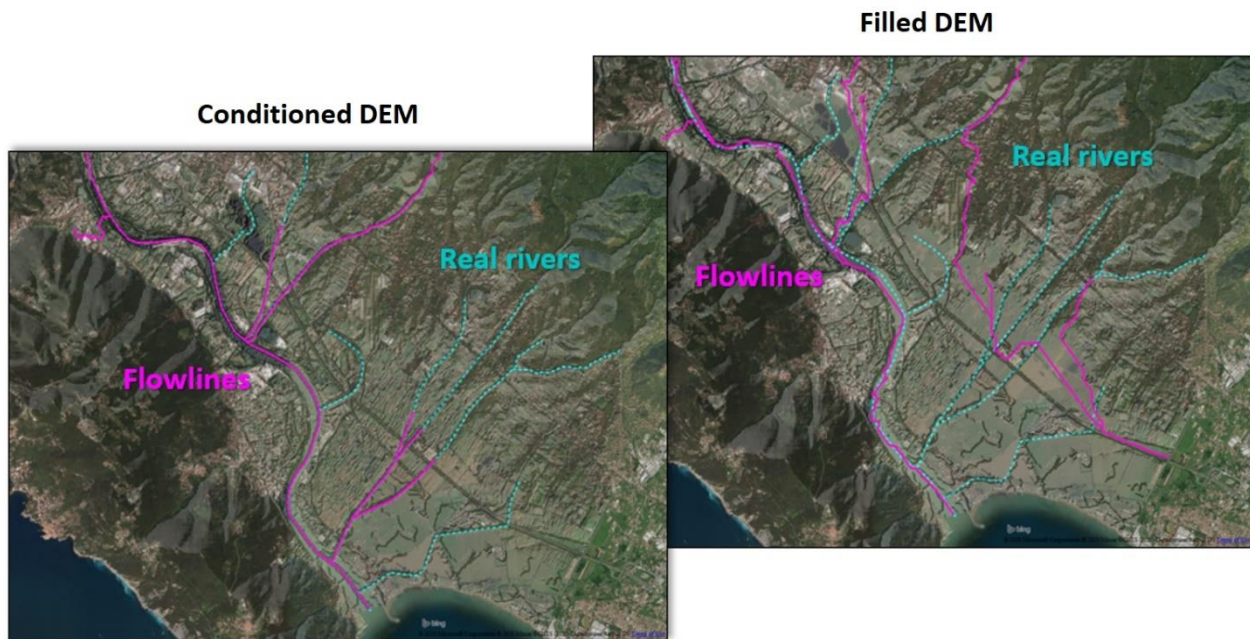


Figure 40 - A comparison between the DEM-based flowlines (lines in purple) derived from burned, on the left, and filled, on the right, LiDAR DEM over the Magra river basin. Artificial depressions introduced into the DEM along real river paths, allow the extraction of more realistic flowlines which are necessary as input for the REFLEX flood modeling.

As expected, flowlines derived from the only filled elevation data (output “Filled DEM” from REFLEX Module 0) cannot represent correct paths of the drainage from hillslope areas to the mouth of the river. Instead, stream vectors derived from the conditioned elevation data (output “Conditioned DEM” from REFLEX Module 0) truly represent the real path of the main stem and its tributaries in the lower Magra valley.

Results obtained in this analysis have demonstrated the advantages of burning the streams into the DEM over an urban river environment characterized by a complex river network. This application has shown the potential of the hydrologically conditioning method developed and integrated into the REFLEX chain.

3.3.3.2 Drainage modeling

The drainage modeling methodology implemented in REFLEX allows the employment of different HAND delineations from D8, Holmgren’s MFD, or D-infinity methods. All these drainage approaches have been evaluated in this case study over the Magra river basin. This preliminary assessment aimed to identify the most suitable drainage approach to be employed in REFLEX as the default drainage method for the creation of HAND maps.

The creation of HAND maps for a generic river branch requires a Hydrologically conditioned DEM and, ideally, the flowlines derived from it. As an example, to produce HAND maps by using the D8 drainage method the ideal approach is to compute heights above the nearest drainage by using channel cells over a flowline raster derived from the same D8 flow direction grid. The same applies to the MFD method. However, this is not always possible because input streamlines may be extracted from D8 flow direction (e.g. streamlines from WWF's HydroSHEDS) and HAND delineation may be derived by using a different flow drainage model (e.g. D-infinity) or even another pre-processed version of the same input DEM.

To simulate this potential configuration input, flowlines are not derived in REFLEX from the same flow direction grid employed in HAND contours delineation. This assumption is taken to decorrelate the relationship between flowlines and flow directions into the HAND extraction and to better evaluate the behavior of HAND delineation using multiple drainage methods.

Therefore, two different pre-processing levels of LiDAR filtered data, resampled at the 5-meter spatial resolution, are employed for this scope: an only filled DEM and another one in which the elevation has been also artificially depressed along the streamlines. The first one is obtained by only filling the source filtered LiDAR data while the second one is derived by burning the input stream vector, used in this case study, into the same input elevation data.

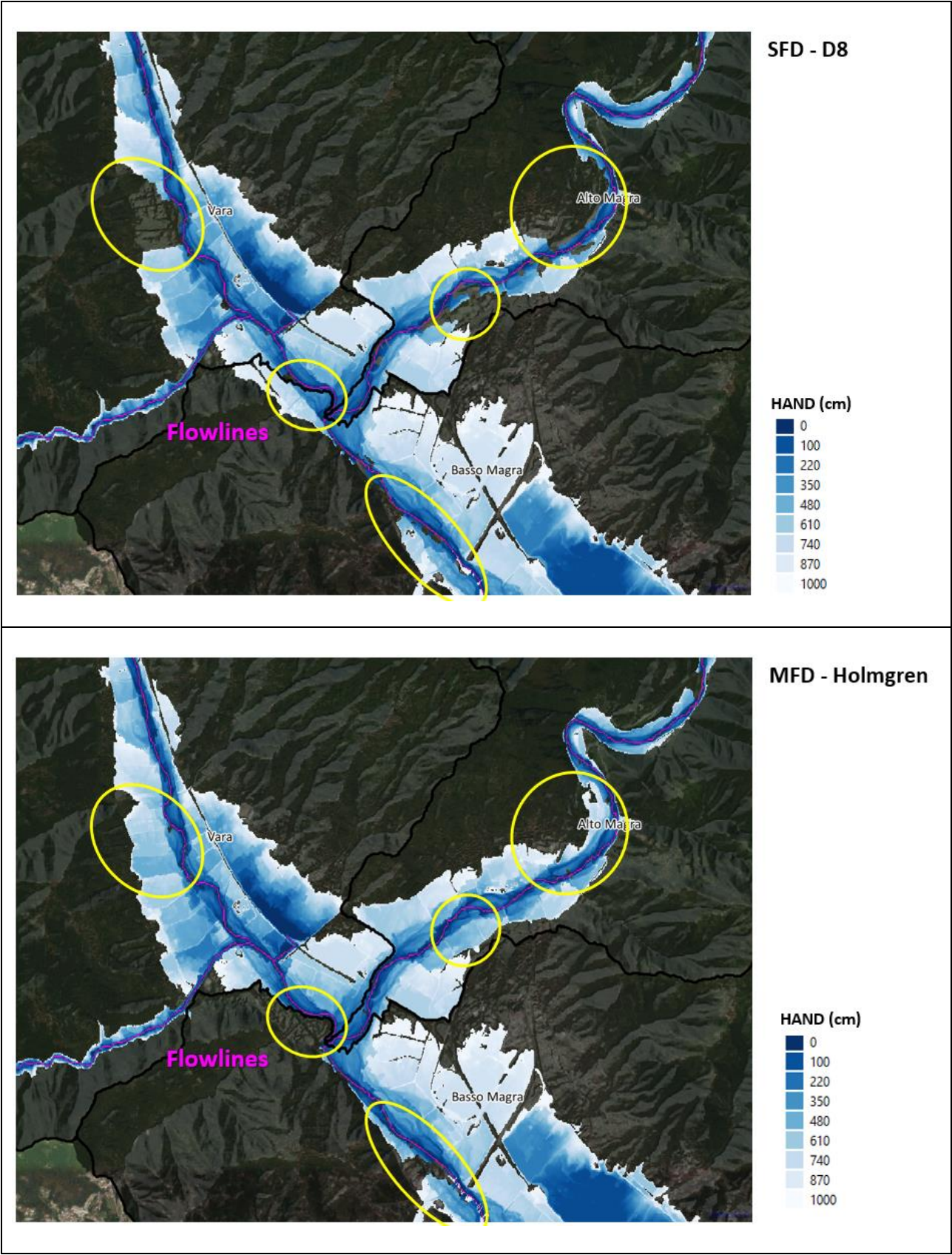
The first hydrologically conditioned DEM, the burned DEM, is used to extract high-fidelity flowlines which better represents the river centerline of lower Magra valley inland waters. As shown in Chapter 2 (see section 2.3.2), the D8 method is defined as the default drainage model in REFLEX for general basin delineation of hydrological features such as contributing Area, Streams, Sinks, Watersheds. Thus, channel cells in this HAND delineation (see section 2.6) are identified from flowlines derived from D8. Instead, the second one, the filled DEM, is used to derive flow direction grids for the D8, MFD, and D-infinity.

Flowlines derived from the burned DEM combined with D8, MFD, and D-infinity flow direction from filled DEM are then used to create three HAND maps dataset, one for each drainage method. Obtained results near the confluence between the Upper Magra and the Vara rivers are shown in Figure 41.

From an overall perspective, at basin scale, no major difference can be noted among the different methods. However, at small scales, differences in the three drainage methods can be recognized in terms of water extent and depth by looking at the HAND contours above 10m from the nearest drainage (see parts highlighted with yellow circles in Figure 41).

While the D8 method appears to do not effectively delineate flat areas due to the limitations of the 8-direction schema, both Holmgren's MFD and D-infinity drainage models have shown a better delineation over river surroundings areas with a gentle slope. Furthermore, the implementation of Holmgren's MFD in GRASS GIS has shown limitations near river junctions with zones of no data that were not present in the results obtained from the D-infinity algorithm of TauDEM.

Therefore, this analysis is confirming the on-paper advantage in using the D-infinity drainage models for the HAND delineation in REFLEX given its successful application also over complex LiDAR data of the lower Magra valley. As a result, the D-Infinity drainage model has been defined as the default method in the REFLEX configuration file.



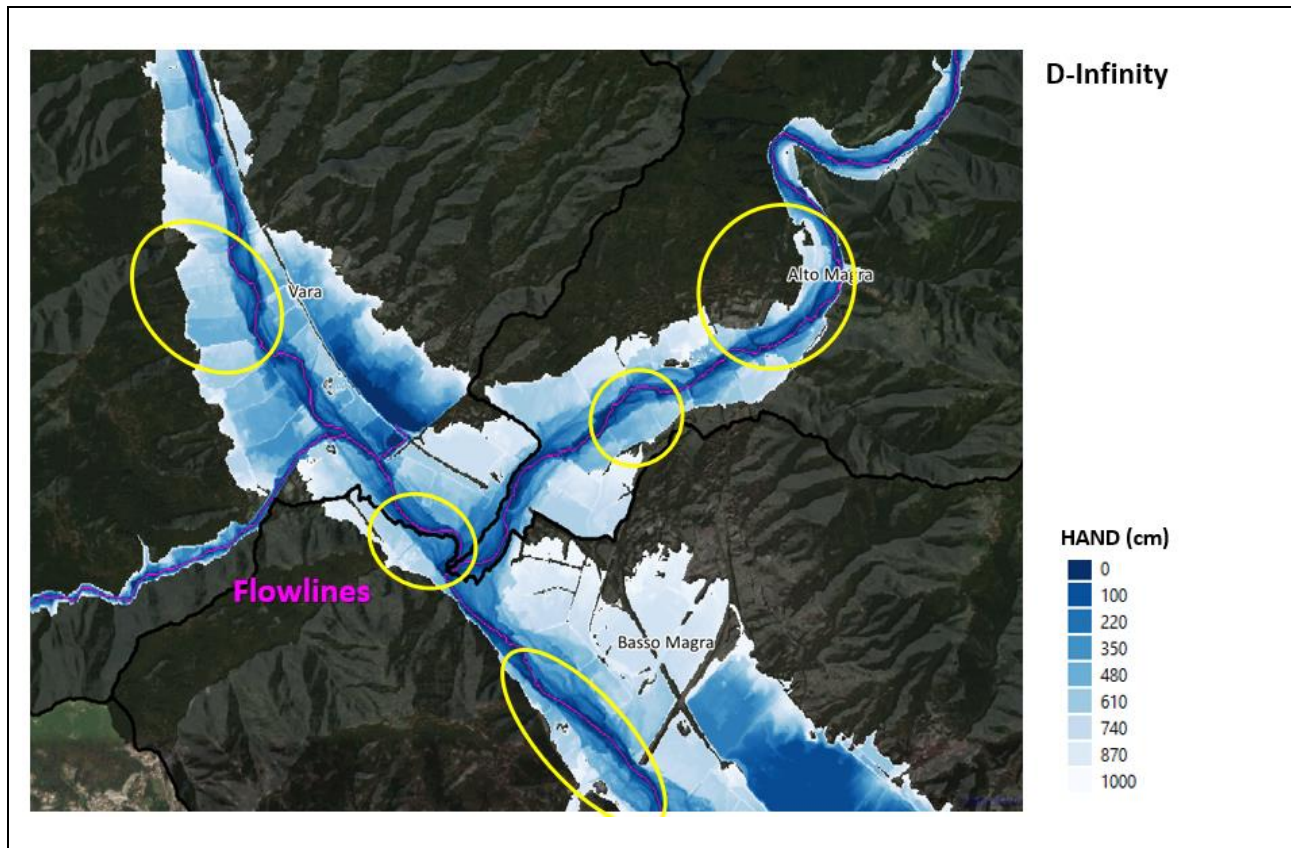


Figure 41 – Evaluation of HAND contours using multiple drainage algorithms for the Magra river basin, near the junction between Magra and Vara rivers. Only pixels having a height above the nearest drainage values below 10 m are considered. HAND contours are derived from the Filled resampled LIDAR data at 5m from MATTM. Input flowlines are derived from the burned DEM. The vertical distance from flowlines is shown in a blue graded color scale for D8, Holmgren's MFD, and D-infinity drainage methods. Input flowlines are shown in purple. HAND maps are derived from the Filled DEM and not from the burned one to avoid artifacts caused by the burning of streams into the DEM. From an overall perspective, the DINF method shows a continuous delineation of relative vertical distances. Areas of discontinuity encountered in the other methods are highlighted with circles in yellow.

3.3.3.3 REFLEX simulation and employed parameters

After the conditioning of the DEM in the REFLEX Module 0, epsilon filled and conditioned DEMs are obtained. The conditioned DEM is obtained by burning the streams into the DEM. Later, in the REFLEX Module 1, D8 flow direction and multiple hydrological derivatives are extracted from the Conditioned DEM obtained in the previous step. Based on the results of the analysis shown in the previous section, in REFLEX Module 1 the D-infinity drainage method is also used to derive from the Filled DEM a second flow direction grid, necessary for the estimation of HAND contours in REFLEX Module 3. Input discharge values, extracted at each sub outlet of all reaches, are then used in REFLEX Module 2 to derive ETUH shape flood hydrographs using the formulas (from 6 to 9) expressed in Chapter 2 (see section 2.5.4). In the estimation of the ETUH of each river branch, the time base t_b is computed by assuming as the time of concentration the centered mean of the values derived from the eight empirical formulas listed in Table 5. In this estimation, the centered mean is derived by excluding $t_{c, min}$ and $t_{c, max}$ of the series. This allowed the estimation of the surface runoff volumes V_{obj} at multiple return periods across the entire basin. Surface runoff volumes from the Module 2 and a library of 154 HAND maps obtained from the Module 3 are then used as input in the REFLEX Flood Inundation module for its Manning-based volume optimization over all the reaches. In this fourth module, a constant value of $0.06 \text{ [m}^{1/3} \cdot \text{s]}$ has been assumed for the roughness coefficient over all the basin, and therefore used in the flood modeling of all reaches. This representative value is obtained by averaging the three most

representative manning coefficients often employed in the hydraulic modeling of the Ligurian basins (Regione Liguria, 2020b):

- 0.035 for channel-bed roughness in low-medium stream flow,
- 0.05 for natural or scarcely urbanized floodplains,
- and 0.1 for densely urbanized floodplains.

This approach has been used for both the input DEM at 90m and 10m spatial resolution. The full list of the REFLEX parameters employed in the flood simulations at multiple return periods is reported in Table 12.

Parameter	Value
ACPX	APP_SETT
DOMAIN	magra
RRS_M	10
RRS_DD	0.0001 (0.0008333 for 90m DEM)
NANDEMVAL	-9999
EPSG_CRS	4326
EPSG_PRJ	32632
STR_BURNING_ENABLED	True
TARGET_EPSG	4326
DCOND_BUFFER_CELLS	20
DCOND_FILTERING_MAGNITUDE	1
REMOVE_SINK_ENABLED	False
PIT_REMOVAL_ENABLED	False
EPS_FILLING_ENABLED	True
SOLVE_FLATS_ENABLED	False
FD_METHOD_STREAMS	D8
FD_METHOD_HAND	DINF
DRAINAGE_THRSLD	3000 (600000 for 90m DEM)
BUFFER_DISTANCE_CELL	50
COASTEXP	1
HAND_TRSHLD_ELEV	2000
HAND_MASK_BUFF_DIST_M	300
GRADIENT_LIMIT	0.0003
STR_ELEV_PERCENTILE	25
HEAD_LOSS	20
VOLMIN	1000
WDMIN	0.1
WDMAX	15
ITERATIONS_MAX_VOL_OPT	5
ROUGHNESS_COEFF	0.06
TOLERANCE_VOL_OPT_M	0.1
RP	30 (200 for simulation at 200-year RP)

Table 12 – List of parameters used in the application of REFLEX in the Magra river basin at 30- and 200-year return periods.

3.3.4 Results

In this section are summarized major results obtained in the REFLEX case study for the Magra river basin. After a description of the benchmark flood maps, a validation of the flood extent is performed at different return periods using both the DEM at 10m and 90m resolutions.

3.3.4.1 Benchmark flood maps used for validation

In this case study, the benchmark flood maps to which the REFLEX model outputs are compared are the Flood Hazard Map retrieved from the *Piano di Gestione del Rischio Alluvioni - PGRA* dataset of the Northern Apennine Interregional River Basin Authority (AdB Distrettuale Appennino Settentrionale, 2021).

Figure 42, and Figure 43 show respectively the flood extent for a 30-year and a 200-year return period used as a reference in this analysis.

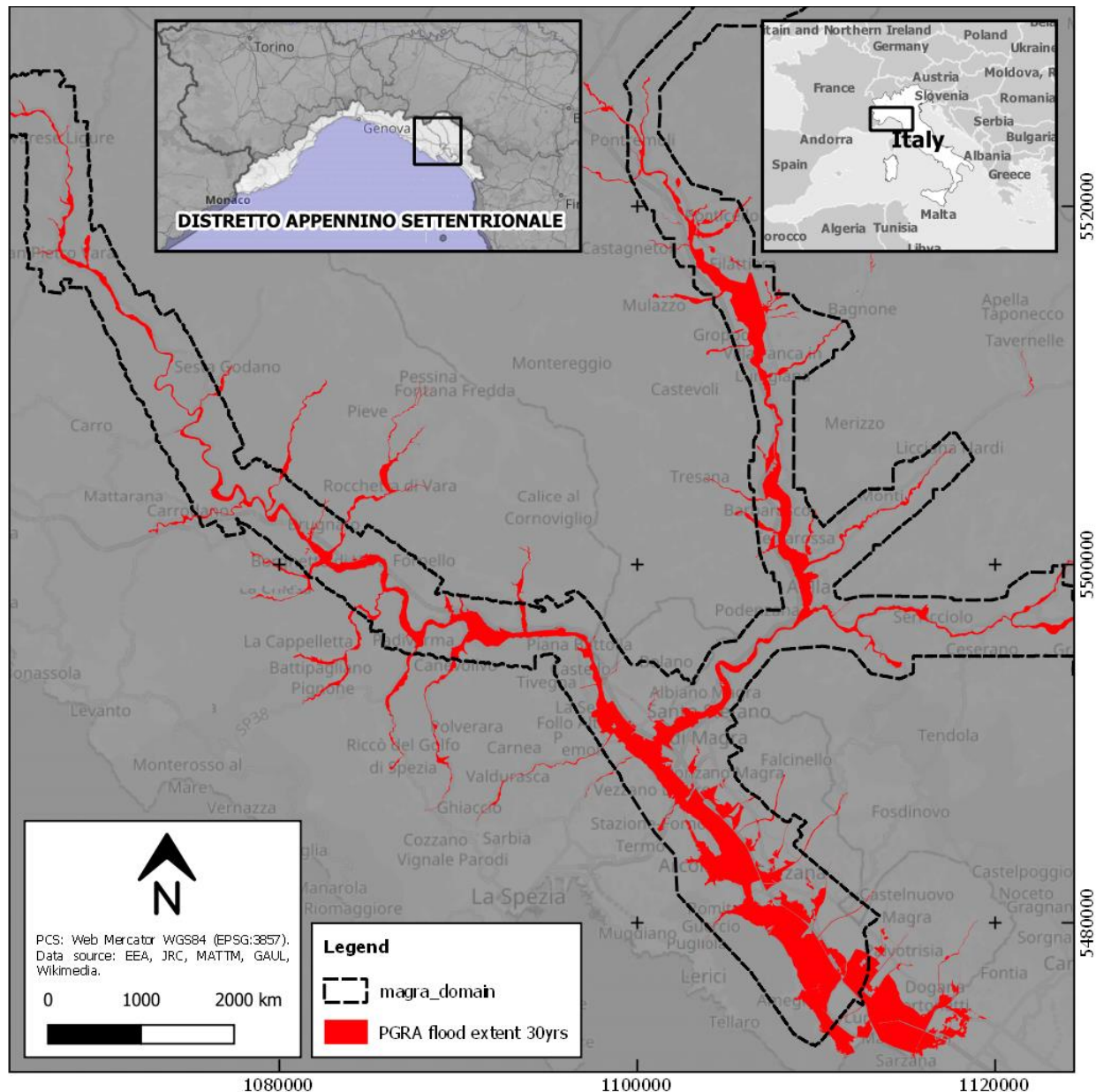


Figure 42 – Flood hazard map for the Magra river basin from “Piano di Gestione del Rischio Alluvioni” of the Northern Apennine Interregional River Basin Authority. Areas in red show flood extent at the 30-year return period used as a reference in this case study.

Flood extent obtained from REFLEX at multiple return periods and multiple resolutions are compared with the ones of the PGRA flood hazard maps by employing a confusion matrix as explained in section 2.7.4.

In this binary classification, statistics are calculated by considering only the areas contained within the coverage of LiDAR tiles, which is highlighted in Figure 42 with a dashed black line. The choice of this domain is here assumed for two main reasons:

- it includes all the floodplains of the Magra river basin,
- the input DEM has a higher vertical and spatial accuracy given from the source raw LiDAR data.

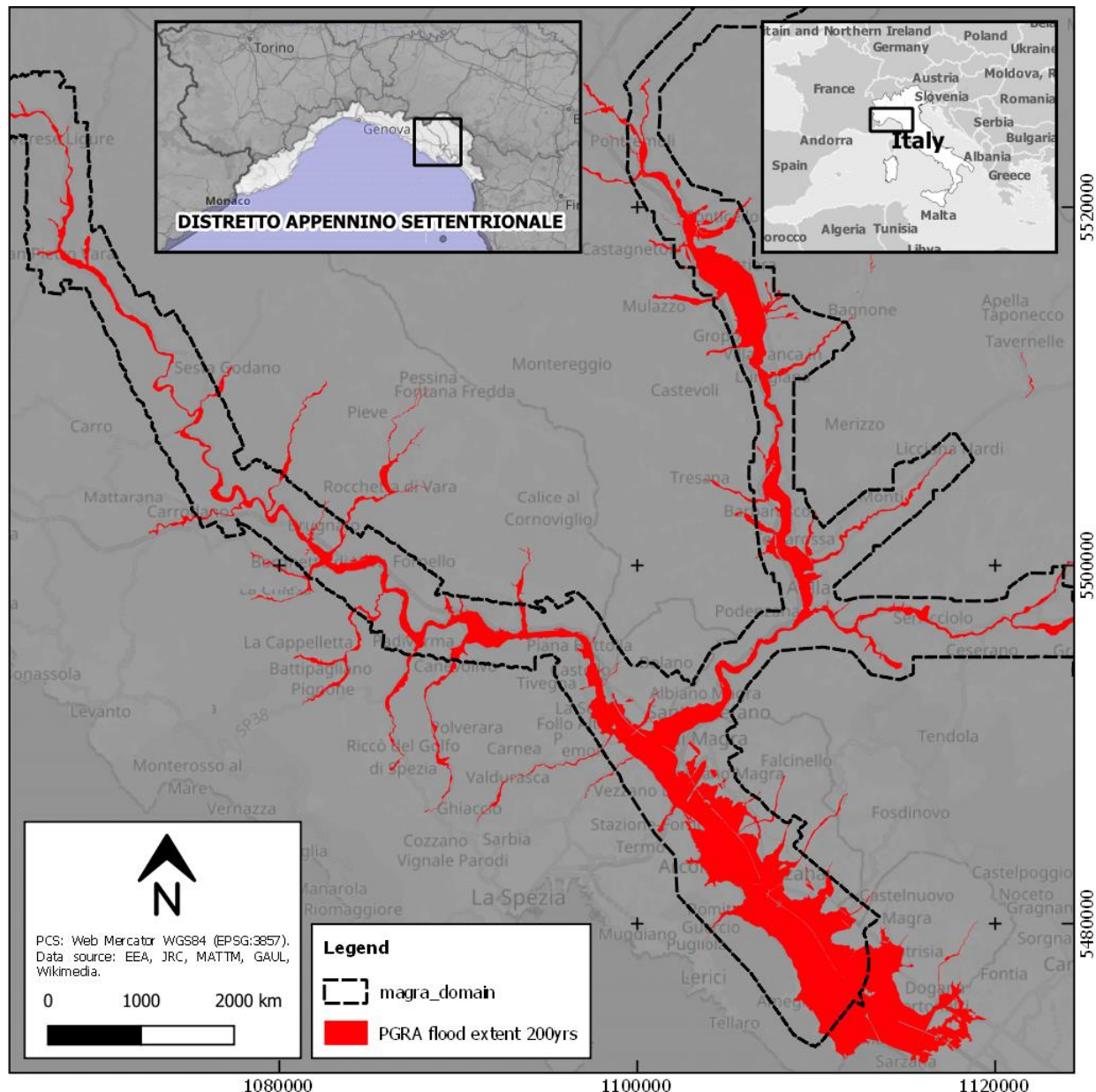


Figure 43 – Flood hazard map for the Magra river basin from “Piano di Gestione del Rischio Alluvioni” of the Northern Apennine Interregional River Basin Authority. Areas in red show flood extent at the 200-year return period used as a reference in this case study.

3.3.4.2 The importance of the Manning correction into REFLEX volume optimization

To better assess the role of the iterative Manning-based volume optimization described in Chapter 2, the REFLEX model has been deployed without and with this option. In the first configuration, the REFLEX Flood Module performs only a static volume optimization which is performed by computing flood extent at each reach by using the total surface runoff volume drained by the in the input hydrograph at the base time (parameter “*ITERATIONS_MAX_VOL_OPT=0*”). In the second configuration, instead REFLEX performs an iterative volume optimization (default method) in which flood maps are derived by using as surface runoff volume the one derived at the transit time.

To reduce computation time, the input DEM employed in this analysis is the one at 90m spatial resolution derived from the MERIT DEM dataset. Obtained results at a 30-year return period for both these configurations are shown in Figure 44, in which REFLEX extents are compared to the PGRA flood hazard maps.

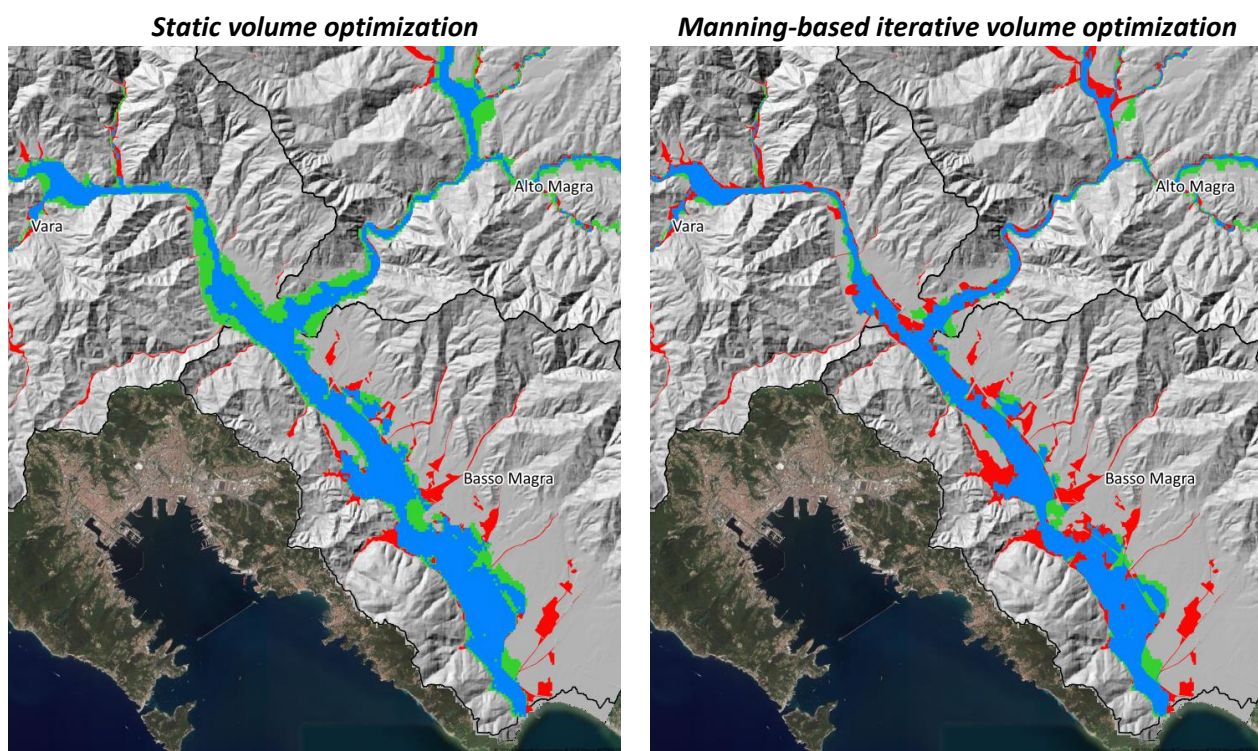


Figure 44 -A comparison between the validation of REFLEX flood extents against the reference flood hazard map (PGRA) for the same flood return period (RP 30 years) using MERIT DEM over the Magra river basin. Areas of exclusions are shown in red, areas of omissions in green, and the matched areas in blue. On the left and the right are shown REFLEX modeling results respectively without and with the volume optimization routine based on Manning’s formula.

From an overall perspective, flood extents derived from the static volume optimization are generally overestimated in the whole basin. On the contrary, a better agreement is depicted from REFLEX’s flood maps derived from the Manning-based iterative volume optimization.

This experiment demonstrates the on-paper advantages in using the iterative runoff volume optimization, based on the transit time and Manning’s formula, which seems to solve the over-estimation of flood extent of the REFLEX flood module that occurs when this option is disabled.

Furthermore, this analysis has also shown, on average, that five iterations are enough to reach the convergence of the Manning-based iterative volume optimization. As a result, the number of five iterations has been assumed as default in the REFLEX configuration file (parameter “*ITERATIONS_MAX_VOL_OPT*”).

3.3.4.3 Flood extent and water depth for the 30-year return period at 10m resolution

The water depth map at 10 m spatial resolution derived from the REFLEX model for the return period of 30 years is shown in Figure 45.

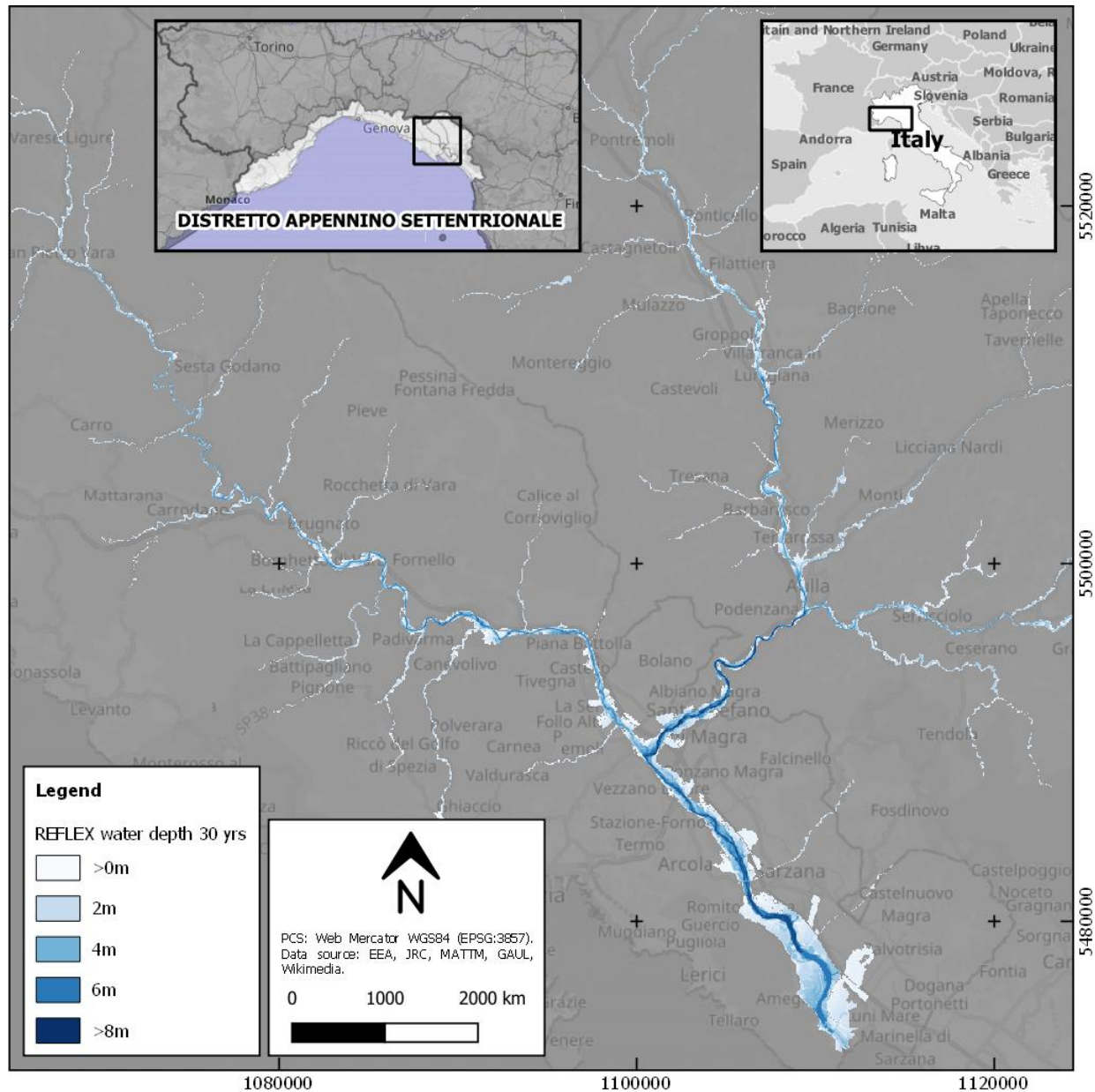


Figure 45 – Water depth at 10 spatial resolution from the REFLEX flood modeling at 30-year return period for the Magra basin.

3.3.4.4 Flood extent and water depth for the 200-year return period at 10m resolution

The water depth map at 10 m spatial resolution derived from the REFLEX model for the return period of 200 years is shown in Figure 46.

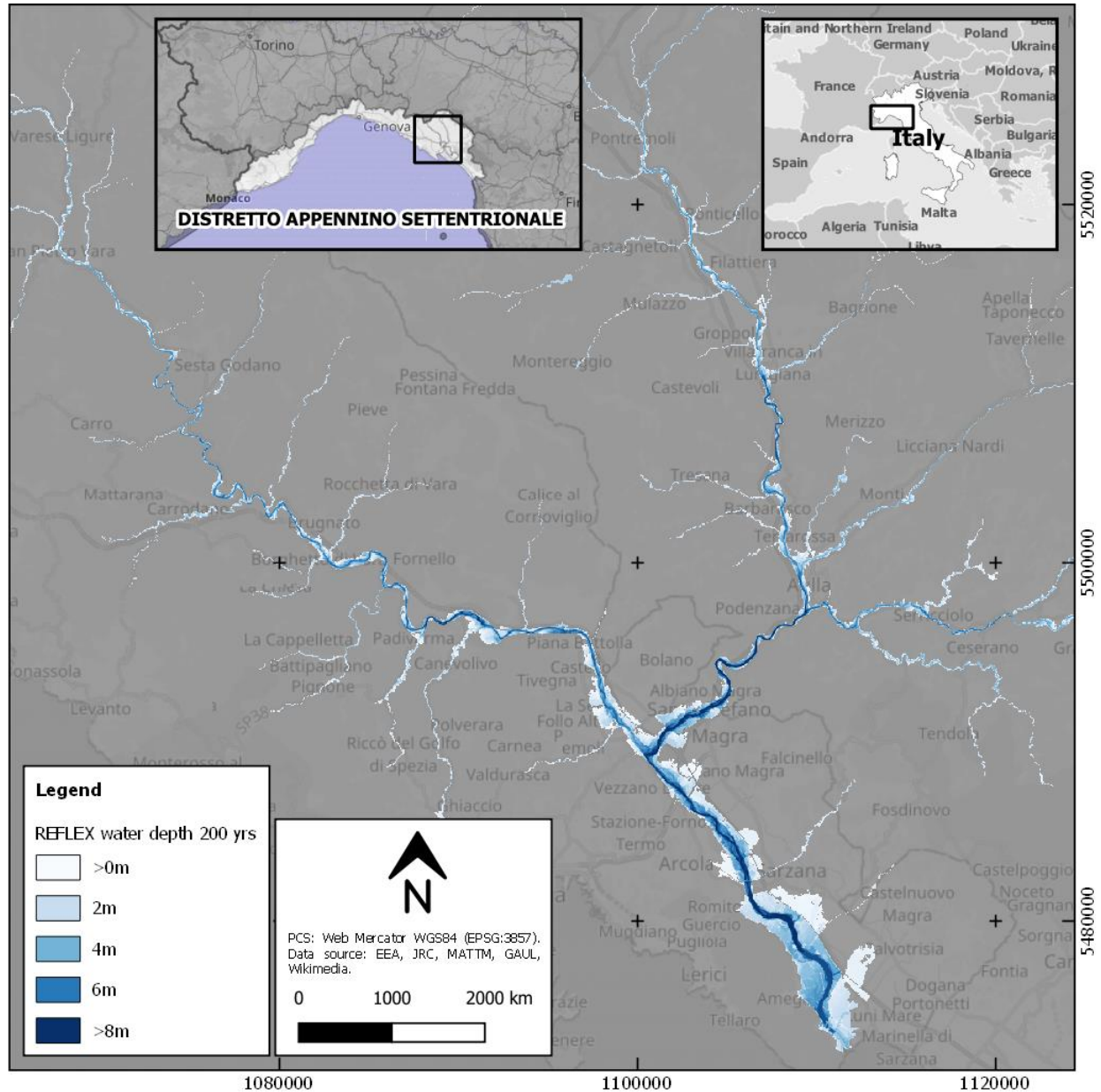


Figure 46 – Water depth at 10 spatial resolution from the REFLEX flood modeling at 200-year return period for the Magra basin.

3.3.4.5 Flood extent validation for the 30-year REFLEX map at 10m resolution

The output from the validation of REFLEX flood extent is depicted in Figure 47, which shows agreement, errors of exclusion, and inclusion of flood hazard at 30-year return period.

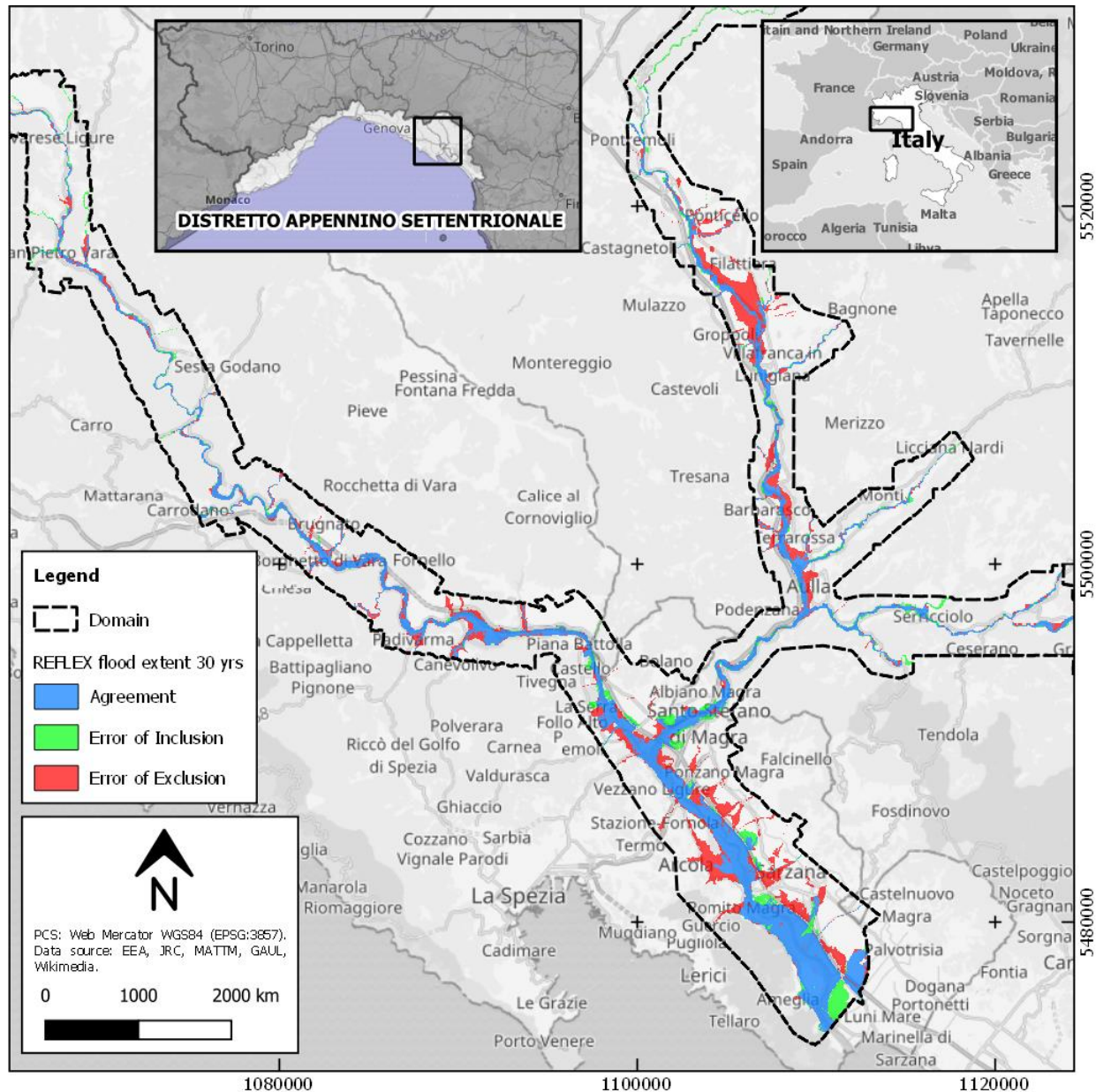


Figure 47 –The figure shows a comparison between the flood extent delineation from the REFLEX model at the 30-year return period and the PGRA Flood Hazard map at the same return period for the Magra river basin in Northern Italy. Areas in blue, green, and red show respectively agreement (TP), error of inclusion (FP), and error of exclusion (FN).

For a better visual interpretation of the obtained binary classification of pixels within the domain, a series of more detailed maps over multiple portions of the basins are also presented in the following pages. In such maps, areas in blue, green, red, and light yellow represent respectively True Positive (TP), False Positive (FP), False Negative (FN), and True Negative (TN) pixels.

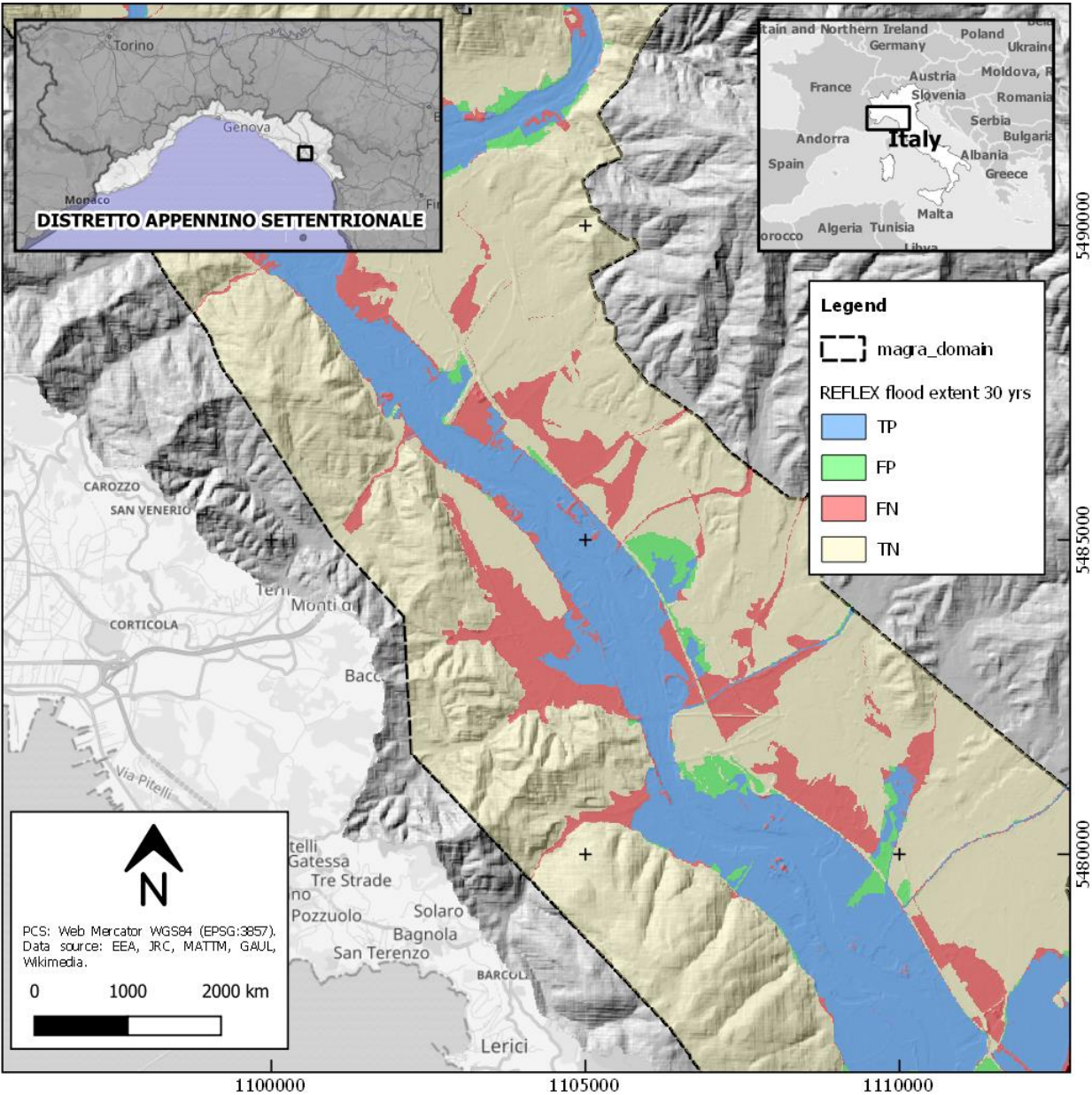


Figure 48 – Detail of binary classification at 30-year return period in the low Magra valley.

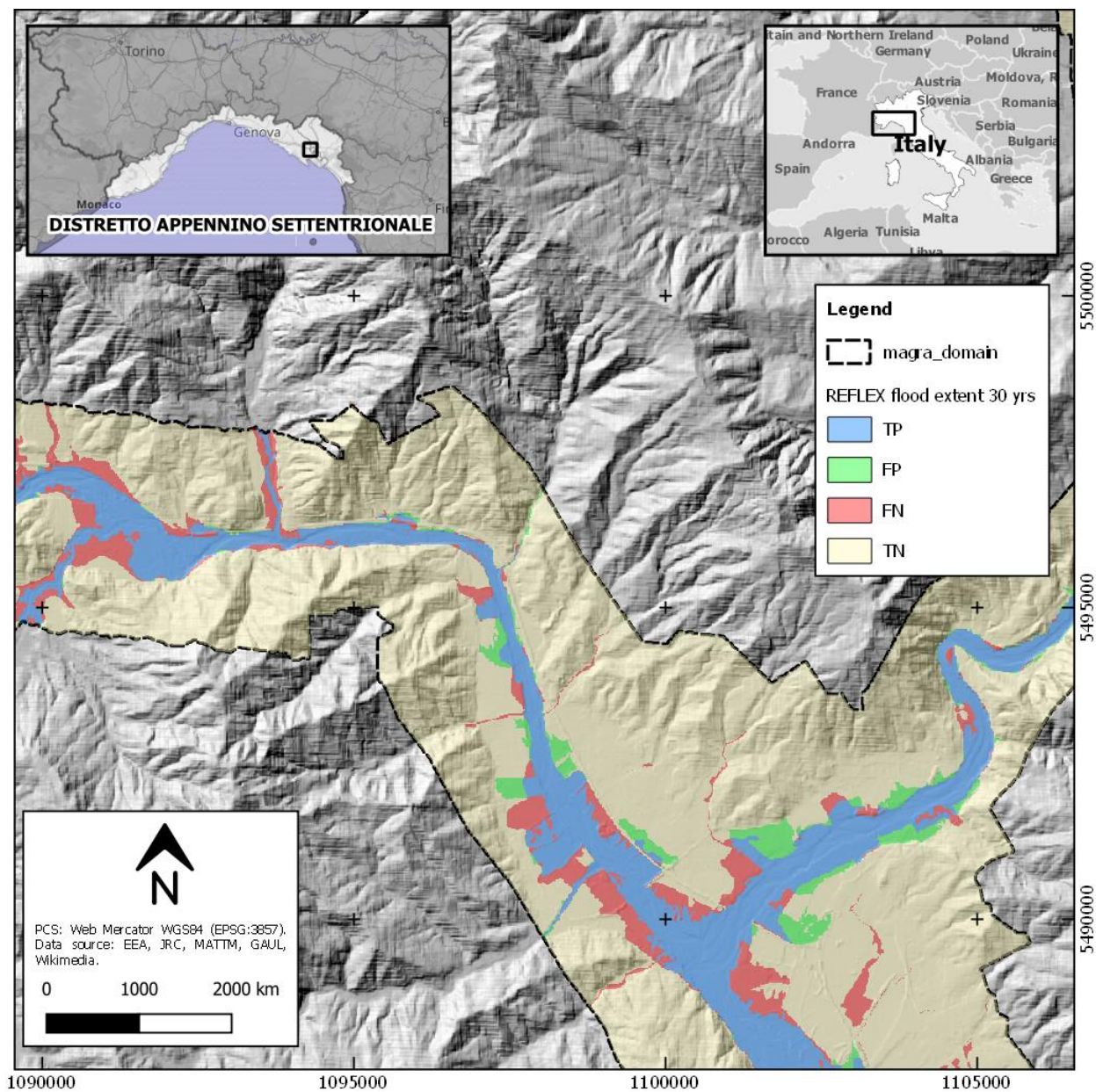


Figure 49 – Detail of binary classification at 30-year return period at the junction between Vara and Magra rivers.

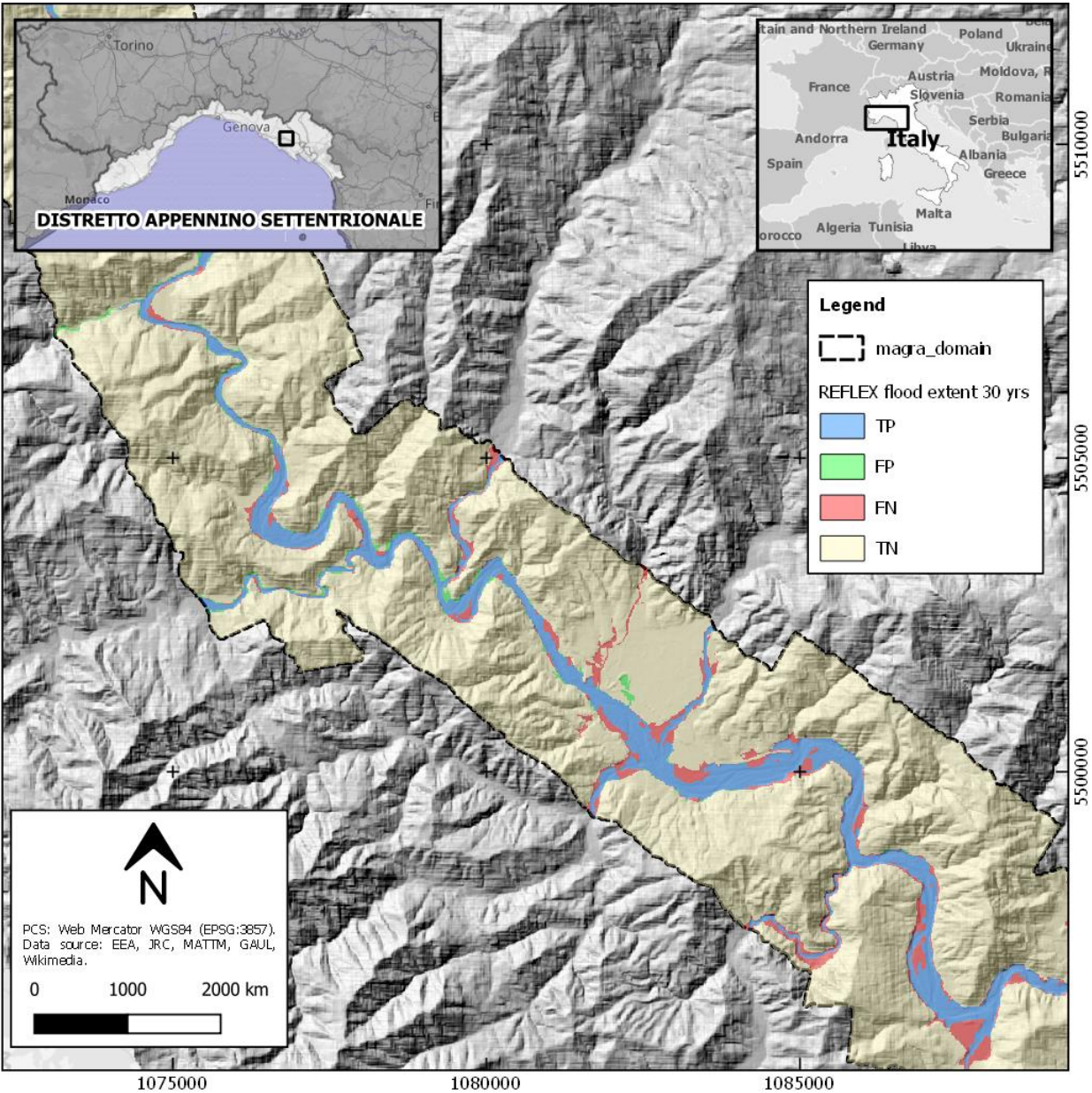


Figure 50 – Detail of binary classification at 30-year return period in the Vara Magra river.

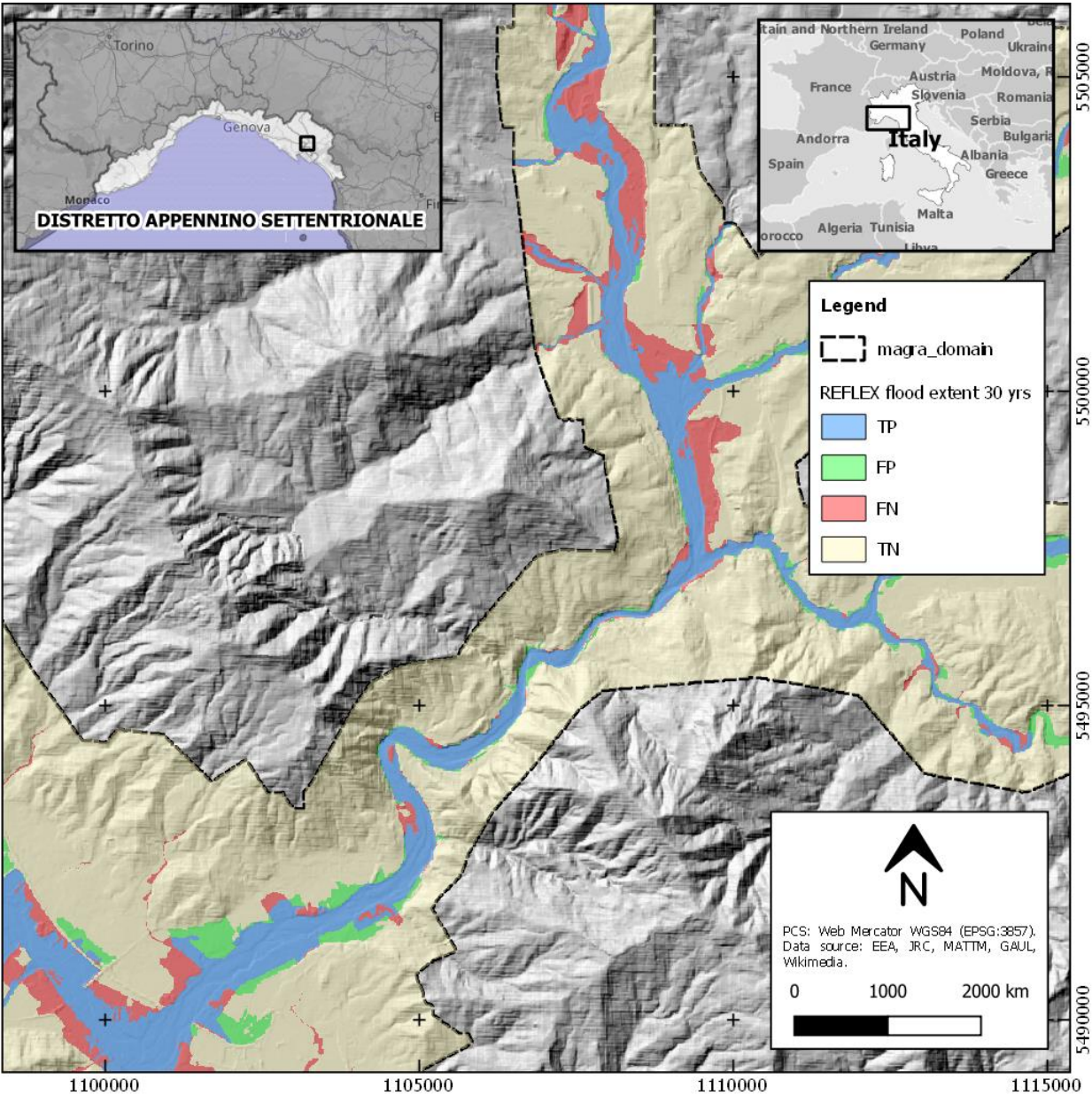


Figure 51 – Detail of binary classification at 30-year return period in the Lower Magra river.

This binary classification allowed the estimation of multiple indexes which are summarized in Table 13.

At the basin scale, the REFLEX model shows a very high overall accuracy of 0.93. However, the 0.66 of sensitivity, or true positive rate (TPR), highlights that a certain number of pixels classified as False Positive (FP) are present in the REFLEX flood extent. Significant FP pixels have been encountered mainly in both the Lower Magra valley and in the upstream part of the Higher Magra river basin. Despite that, it is worth highlighting that a precision value of 0.84 demonstrates that the REFLEX modeled flood extent includes a low number of false positives pixels.

From an overall perspective, these outcomes can also be effectively summarized by looking at both Cohen's Kappa and Matthews Correlation coefficients which show respectively a good K value of 0.7 and a moderate MCC value of 0.7 for all the Magra river basin.

Statistics	Description	RP 30 years			
		Magra	Vara	Lower Magra	Higher Magra
ACC	Overall accuracy	0.93	0.96	0.82	0.91
TPR	Sensitivity	0.66	0.69	0.63	0.58
PPV	Precision	0.84	0.86	0.80	0.87
K	Cohen's kappa coefficient	0.70	0.74	0.64	0.65
MCC	Matthews Correlation Coefficient	0.70	0.75	0.68	0.67

Table 13 – Results from the binary classification of flood extent at 30-year return period.

Instead, while looking at each of the three macro sub-basins the highest value of MCC (0.75) has been registered over the Vara river basin and the lowest (0.67) in the Higher Magra. This analysis highlighted a better performance of REFLEX in the Vara river basin, probably caused by the less urbanized nature of this river environment.

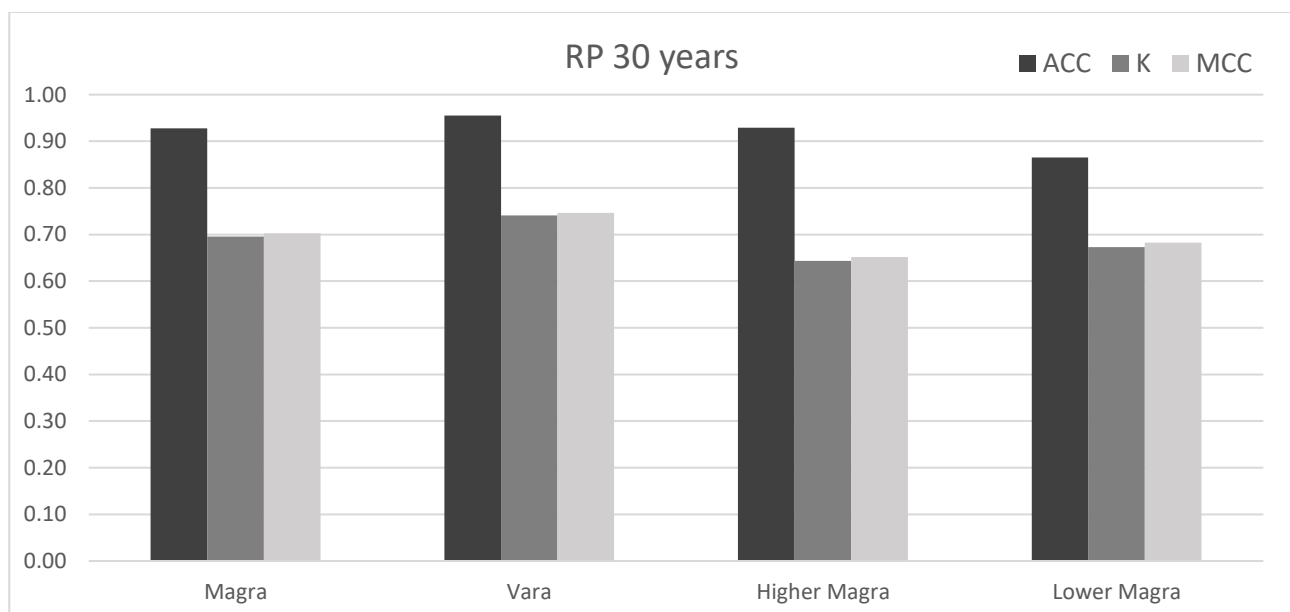


Figure 52 – Bar chart showing accuracy, Cohen's kappa coefficient, and index, and Matthews Correlation Coefficient of the binary classification of the 30-year return period flood map from REFLEX at different scales.

3.3.4.6 Flood extent validation for the 200-year REFLEX map at 10m resolution

The output from the validation of REFLEX flood extent is depicted in Figure 53, which shows agreement, errors of exclusion, and inclusion of flood hazard at the 200-year return period.

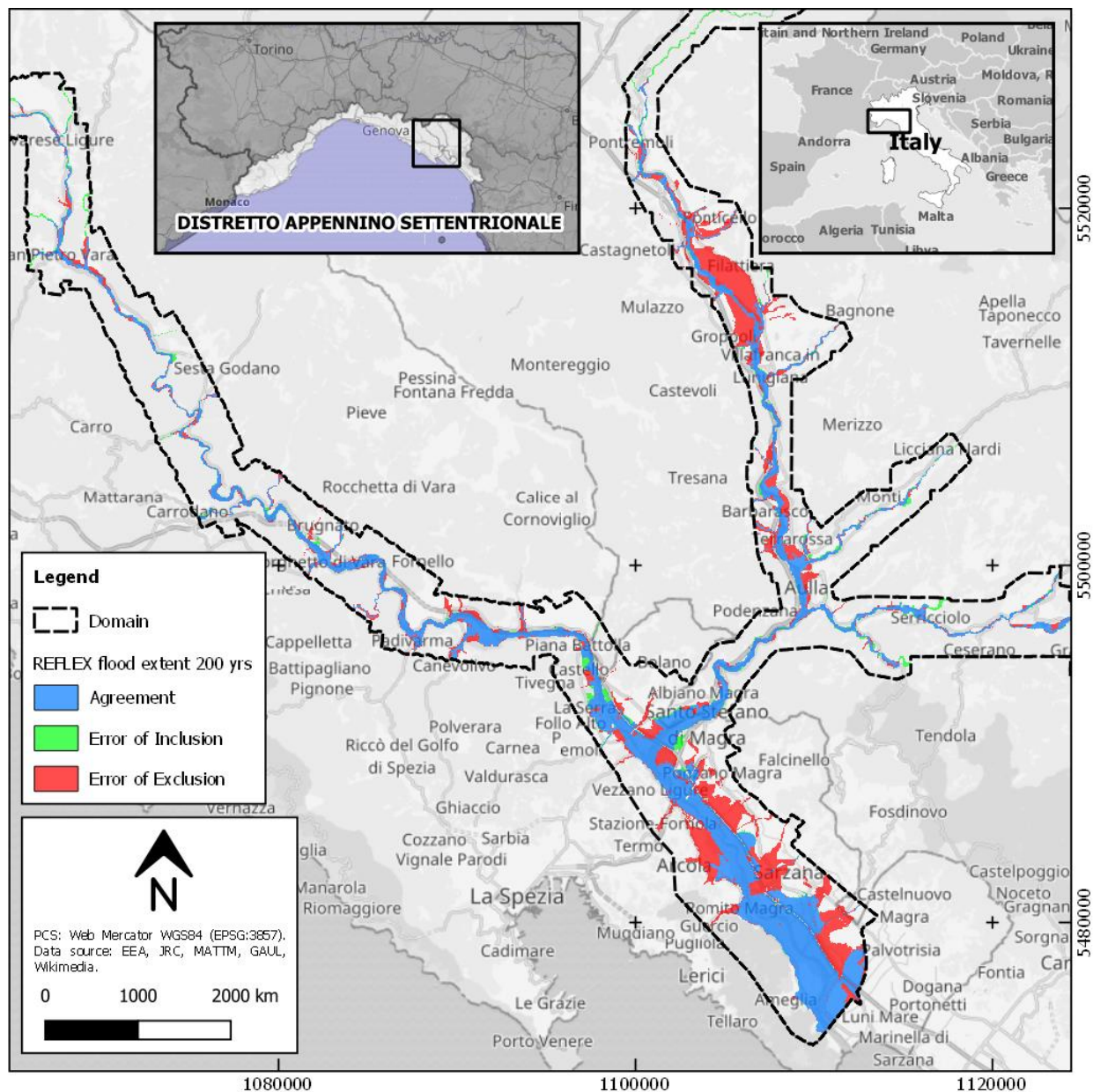
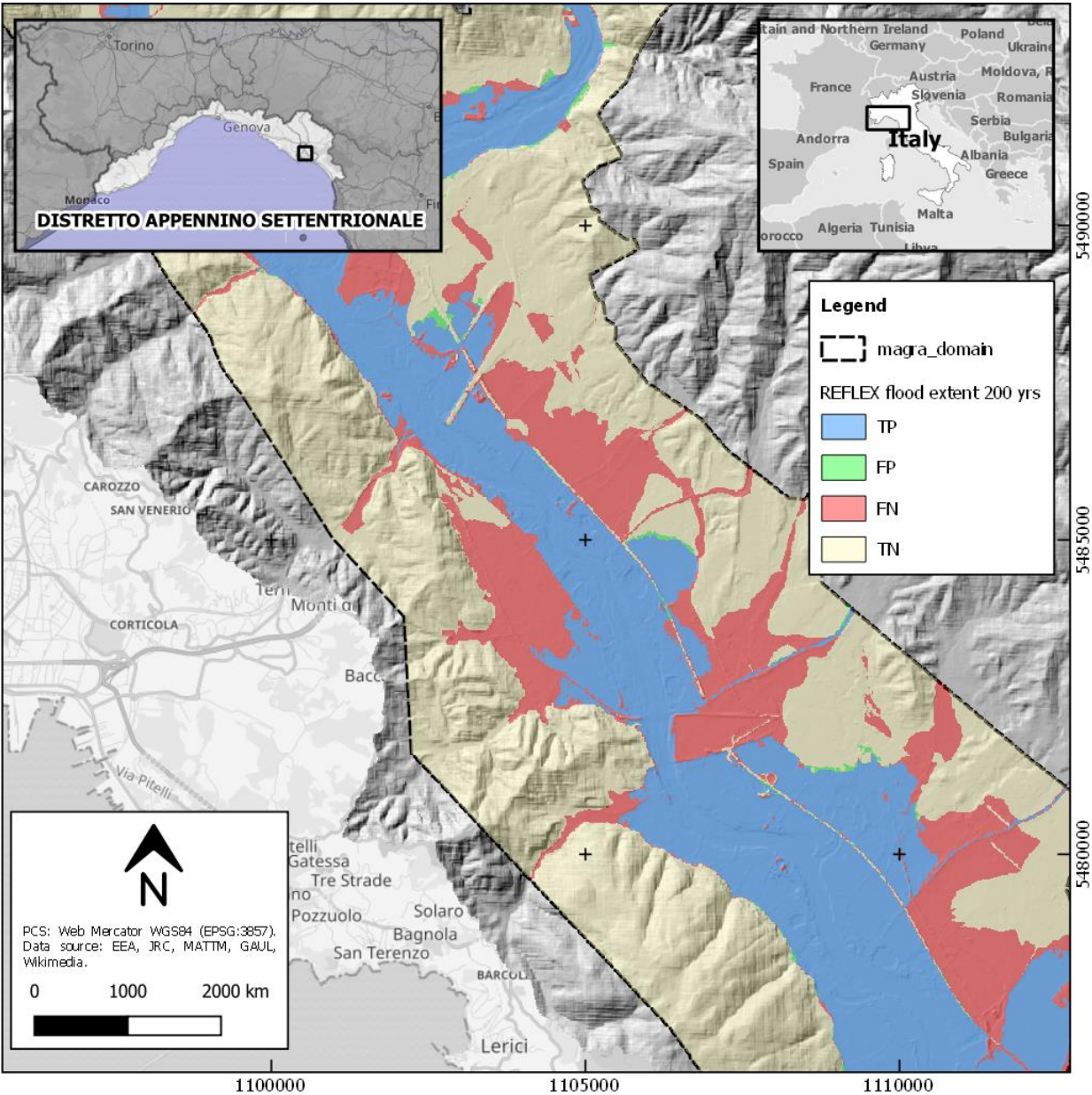


Figure 53 – The figure shows a comparison between the flood extent delineation from the REFLEX model at the 200-year return period and the PGRA Flood Hazard map at the same return period for the Magra river basin in Northern Italy. Areas in blue, green, and red show respectively agreement (TP), error of inclusion (FP), and error of exclusion (FN).

Again, for a better visual interpretation of the obtained binary classification of pixels within the domain, a series of more detailed maps over multiple portions of the basins are also presented in the following pages. In such maps, areas in blue, green, red, and light yellow represent respectively True Positive (TP), False Positive (FP), False Negative (FN), and True Negative (TN) pixels.



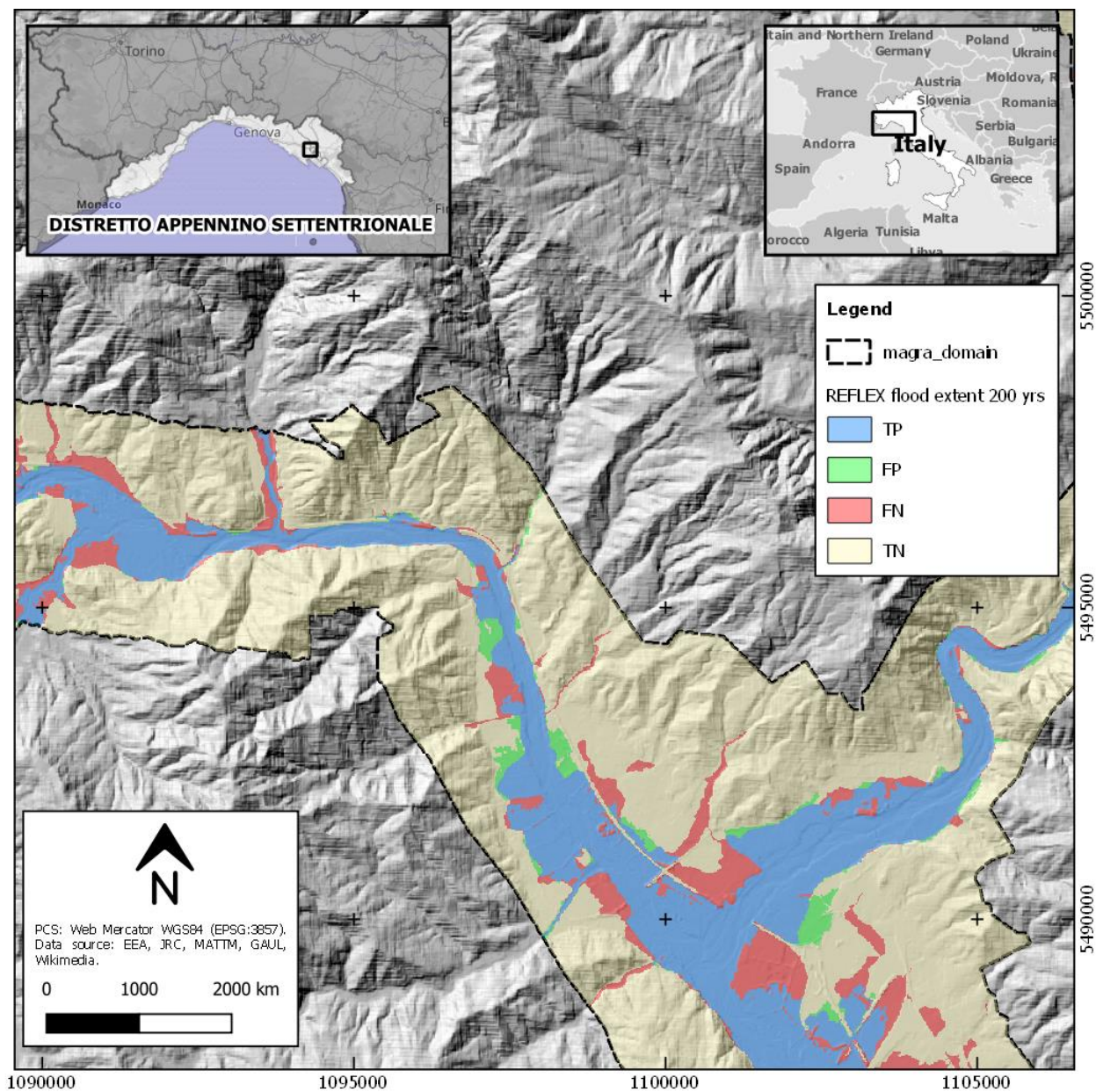


Figure 55 – Detail of binary classification at 200-year return period at the junction between Vara and Magra rivers.

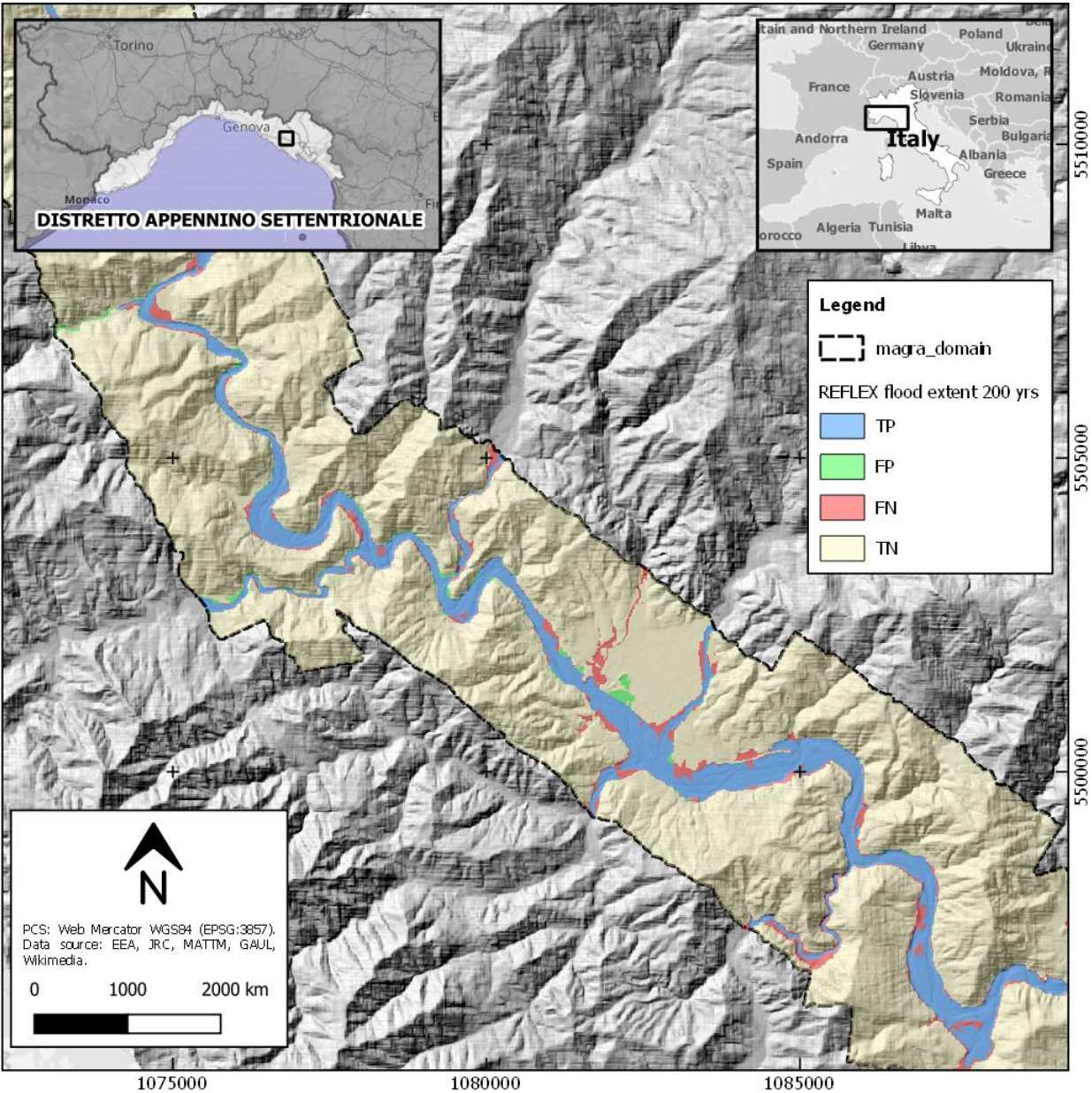


Figure 56 – Detail of binary classification at 200-year return period in the Vara Magra river.

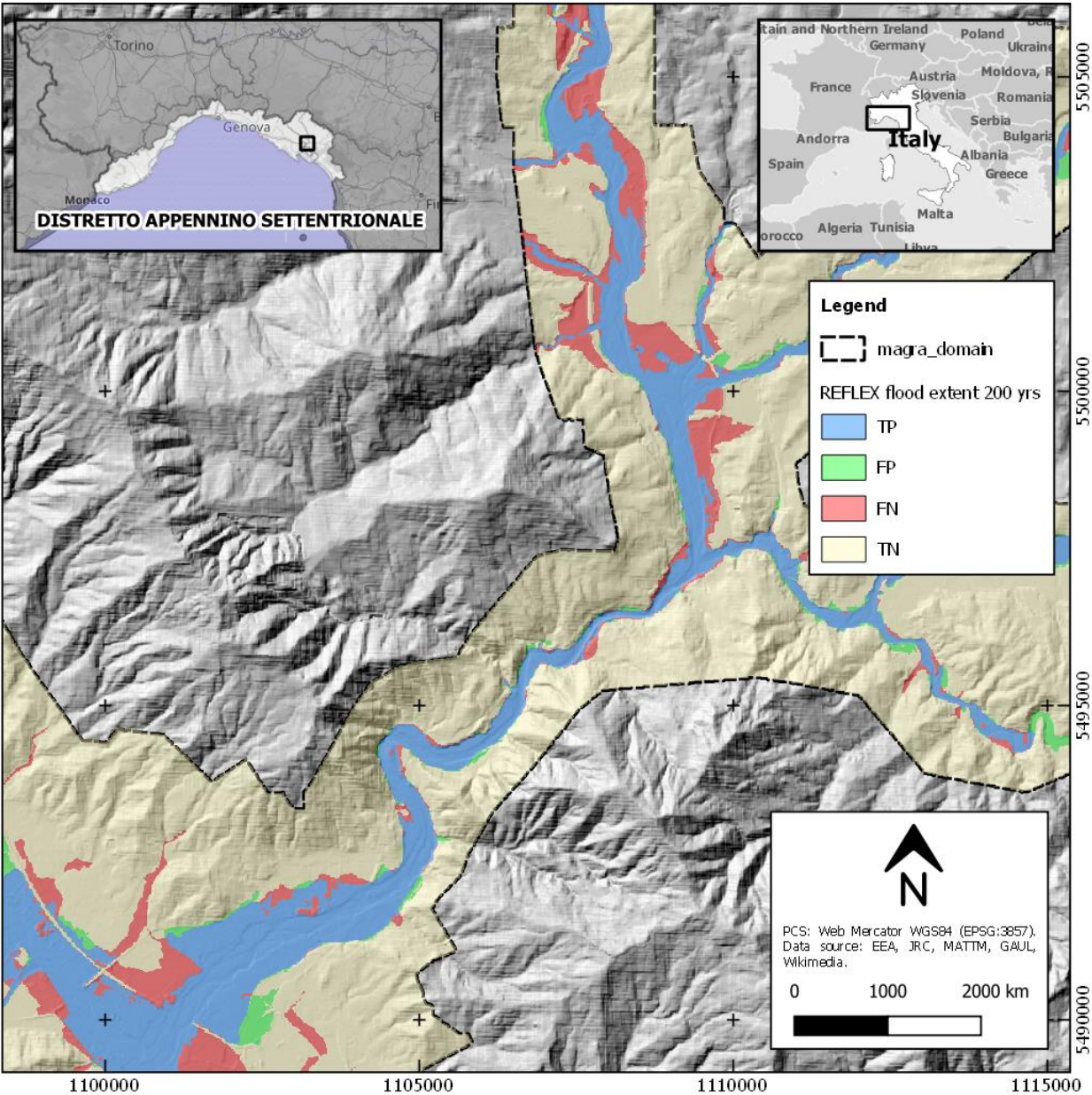


Figure 57 – Detail of binary classification at 200-year return period in the Lower Magra river.

This binary classification allowed the estimation of multiple indexes which are summarized in Table 14.

Statistics	Description	RP 200 years			
		Magra	Vara	Lower Magra	Higher Magra
ACC	Overall accuracy	0.91	0.95	0.87	0.93
TPR	Sensitivity	0.64	0.74	0.68	0.60
PPV	Precision	0.92	0.89	0.88	0.99
K	Cohen's kappa coefficient	0.70	0.78	0.67	0.64
MCC	Matthews Correlation Coefficient	0.72	0.78	0.68	0.65

Table 14 – Results from the binary classification of flood extent at 200-year return period.

Similar statistics to the one obtained in the REFLEX flood maps at 30-year return period have resulted also in the flood modeling at 200 years (Figure 58).

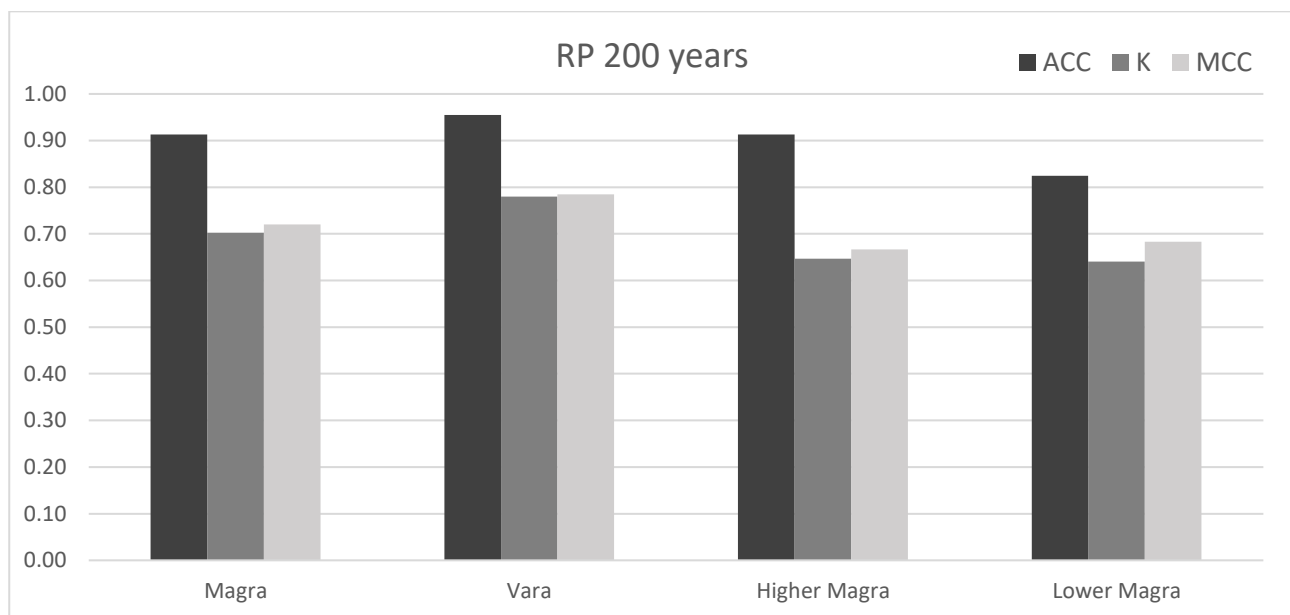


Figure 58 – Bar chart showing accuracy, Cohen's kappa coefficient, and index, and Matthews Correlation Coefficient of the binary classification of the 200-year return period flood map from REFLEX at different scales.

3.3.4.7 Discussion

Results obtained from this case study have first shown the importance of an accurate hydrologically conditioning of the source raw DEM, which is crucial in deploying REFLEX. Also, the advantages in using the D-infinity drainage model as the default schema to derive HAND contours from the conditioned elevation data have been proven useful in the REFLEX flood modeling. Furthermore, this case study has demonstrated the potential of the iterative runoff volume optimization based on the transit time derived from a simplified version of Manning's formula. This novel iterative approach dramatically reduces the overestimation of flood extent in REFLEX when the surface runoff volumes are derived from the time integral of the whole triangular hydrograph. As also explained in Chapter 2, obtained results confirmed that the estimation of the transit time is needed to encounter the streamflow average velocity into this hydro-geomorphological approach.

Input discharge values at multiple return periods allowed the estimation of flood hazard maps from REFLEX at 10m spatial resolutions. These maps have been validated in terms of the flood extent by using official reference flood hazard maps retrieved from local authorities. The binary classification over the basin has shown high values of the REFLEX overall accuracy, with moderate values of Kappa and Matthews Correlation coefficients due to the presence of false negatives over a certain portion of the basin. In particular, the presence of false-negative pixels in REFLEX hand maps has been registered mostly in defended floodplains of the Magra river basins where multiple secondary tributaries join the main stem. Instead, concerning the false positives, it is worth noticing that few pixels have been classified as FP in the REFLEX flood maps, as also demonstrated by high precision values registered in the whole basin.

Similar confusion matrices and then associate statistics have been derived from both REFLEX scenarios at 30 and 200 years return periods. Despite small differences at the basin scale, the performance of REFLEX is almost identical also while looking at the scales of Vara, Higher, and Lower Magra basins. This result highlights the coherence of the REFLEX method, which seems to provide flood modeled results independently from the magnitude of the flood event.

3.4 REFLEX Case study – The Entella river basin in Northern Italy

Hereinafter are shown results obtained from the application of REFLEX into a second basin in Northern Italy.

3.4.1 Case study description

The second case study where REFLEX has been applied is the Entella river basin, which is also part of the Northern Apennines District in northern Italy. The Entella river basin is located in the central east of this hydrological region, and it covers most of the eastern territory of the province of Genoa in the Liguria Region. The Entella river basin extends for about 375 square kilometers, has a maximum elevation of 1969 meters m above the mean sea level, and comprises multiple high relief areas belonging to Lavagna (east), Sturla (north), and Graveglia (west) tributaries (see map in Figure 59). Before reaching the mouth in the Ligurian Sea the Entella river intersects the alluvial coastal floodplain of Chiavari and Lavagna municipalities, located between the Rupinaro (north-west) and Fravega (south-east) small coastal catchments. This floodplain is densely urbanized and is frequently affected by flooding (Roccati et al., 2020).



Figure 59 – The Entella river basin in Northern Italy investigated in this REFLEX case study.

3.4.2 Input data

The initialization of REFLEX over the Entella river basin required a similar data collection activity to the one presented for the Magra river basin. All these inputs are described below.

3.4.2.1 Digital Elevation Model

The input digital elevation models employed in this case study are retrieved from two different conditioned elevation data at 90 and 1m spatial resolutions. The first DEM is derived from the MERIT DEM dataset (Yamazaki et al., 2017), while the second one is obtained from the LiDAR DTM of the Italian Ministry for the Environment Land and Sea (MATTM) and accessed via CIMA Research Foundation. The multiple LiDAR DTM tiles required to cover the area of interest have been processed in GIS before their use in REFLEX. This pre-processing required merging all the tiles and resampling the output mosaic into a 5m spatial resolution DEM.

3.4.2.2 Flowlines

Input flowlines are assumed as (shapefile) derived from the Filled DEM at 5m resolution with thresholding on the drainage area from the D8. The resulting stream network used in REFLEX is shown in Figure 60.

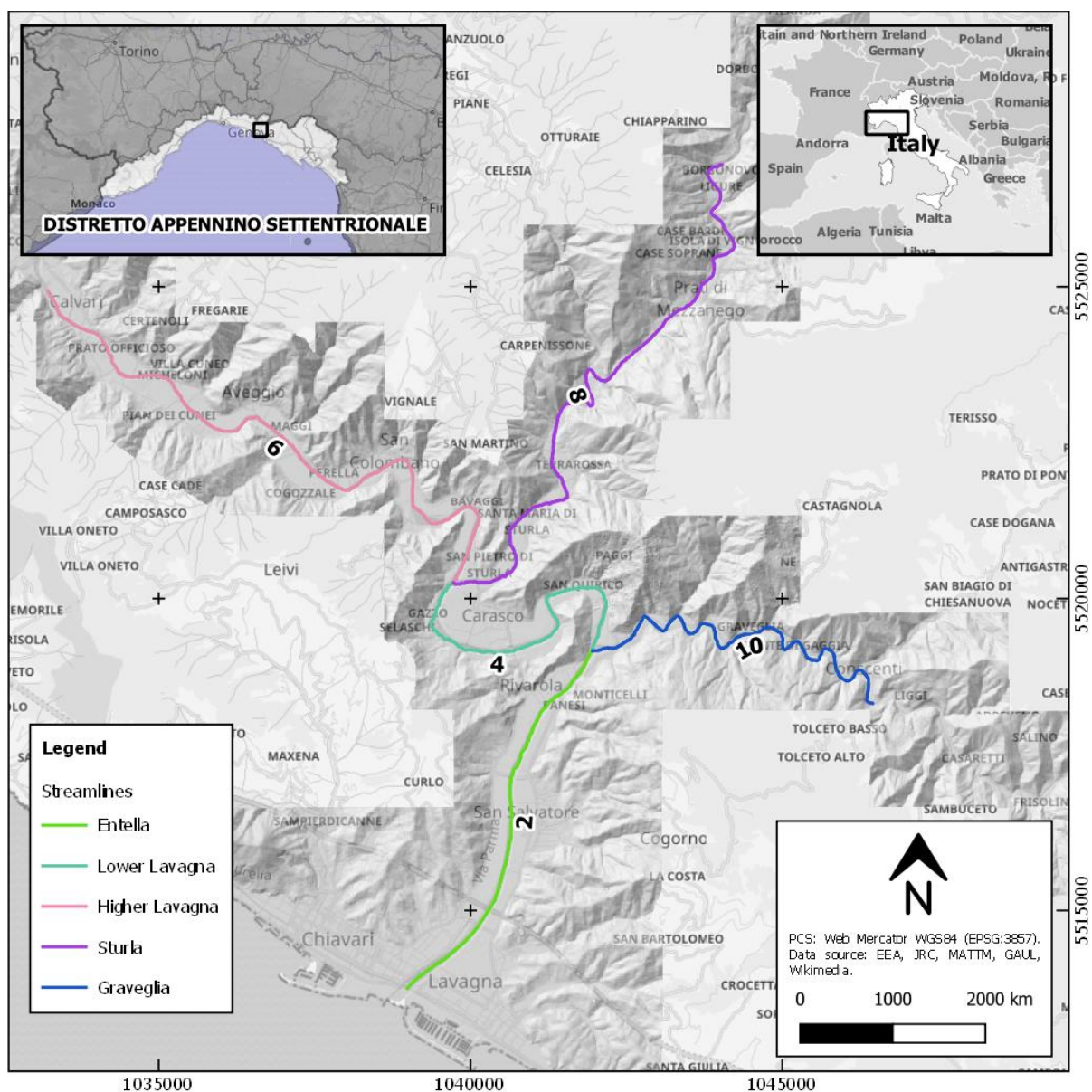


Figure 60 - streamlines employed in REFLEX modeling of the Entella river basin.

Obtained streamlines in a vector file have been then manually edited only in the final portion of the river network within the coastal floodplain (branch no.2). This vector editing in QGIS has been made by following the Entella river centerline derived from a visual interpretation of VHR optical imagery (Bing base map).

3.4.2.3 Runoff peak discharge

Input runoff peak discharge estimations at different return periods are derived from the “*Piano di Bacino Stralcio Sul Rischio Idrogeologico*” report of the Ligurian Region and the Northern Apennine Interregional River Authority (Regione Liguria, 2020b). The discharge values extracted from “Table 1.16” of the report published in May 2020 are included in Table 15 for all five branches of the input streamlines.

Stream ID	Entella river basin River branch	Runoff peak discharge		
		50 years	200 years	500 years
6	Higher Lavagna stream (near confluence with Sturla)	916	1614	2343
8	Sturla stream (near the junction with the Lavagna stream)	474	839	1223
4	Lower Lavagna stream (from the confluence with Sturla river to the junction with Graveglia river)	1307	2300	3337
10	Graveglia stream (near confluence with the Lavagna stream)	331	584	849
2	Entella river (from the confluence with Graveglia river to the sea mouth)	1559	2739	3971

Table 15 - Discharge values for the Entella river basin at 50-, 200-, and 500-year RP (Regione Liguria, 2020b).

The above listed discharge values for 50-, 200-, and 500-year return period (medium, high, and very high magnitude of flood hazard) derived from this report have been then distributed across the entire river network of the Entella basin within a grid (discharge raster files in GeoTIFF format) coherent with the input flowlines. Furthermore, values for the 150-year RP have been also derived from the rating curves given in the same report. Obtained values are the following: 1430 (branch 6), 745 (branch 8), 2044 (branch 4), 519 (branch 10), and 2436 (branch 2) cubic meters per seconds.

3.4.3 Modeling

Hereinafter is explained the flood modeling approach adopted for this second REFLEX case study over the Entella river basin.

3.4.3.1 DEM conditioning

As described in the first case study, a conditioning of the DEM has been carried out also in this second basin. Both the DEMs have not been filtered due to the low amount of noise in both MERIT DEM and LiDAR DTM source products. Input DEMs derived from either the MERIT dataset or the LiDAR data have been first filed in REFLEX Module 0 using the epsilon filling. Later, the stream burning has been performed only on the Entella river branch being the only one intersecting a dense urban floodplain.

3.4.3.2 Coastal expansion

The REFLEX coastal expansion of HAND maps has been particularly useful for this case study. As widely explained in Chapter 2, in REFLEX the HAND contours are expanded over a buffer zone of the catchment by using a GIS-based method. Such a method relies on an a priori hydraulic head loss and the Euclidean distance of hillslope pixels from the river centerline (see section 2.6.2.2). In such HAND expansion vertical distances

from nearest drainage are artificially constructed (see equation 16), for each riverbank pixel within a searching zone $D(r_n)$ by assuming the hydraulic head loss $-JL$ constant. The domain $D(r_n)$ used for the computation of this HAND expansion is built as a function of a maximum distance from the river d_{max} and a buffer b of the watershed. Thus, three parameters drive the coastal expansion of HAND in REFLEX Module 3 which are b , d_{max} , and JL .

The a priori buffer distance b depends on the pixel spacing of the DEM. In the flood modeling of the whole Entella river, this buffer has been defined as 50 cells to ensure a buffer of the watershed of at least 250m. Given the higher slopes of the other reaches, the HAND costal expansion is triggered in REFLEX only in the river branch number 2 of the Entella stream network. The application of equation 12 resulted into $d_{max} = 2739\text{ m}$. Therefore, as shown in Figure 61, the searching domain for the expansion of HAND in this river branch are made mostly on a 250 meters buffer zone of the sub-catchment being d_{max} particularly higher than b .

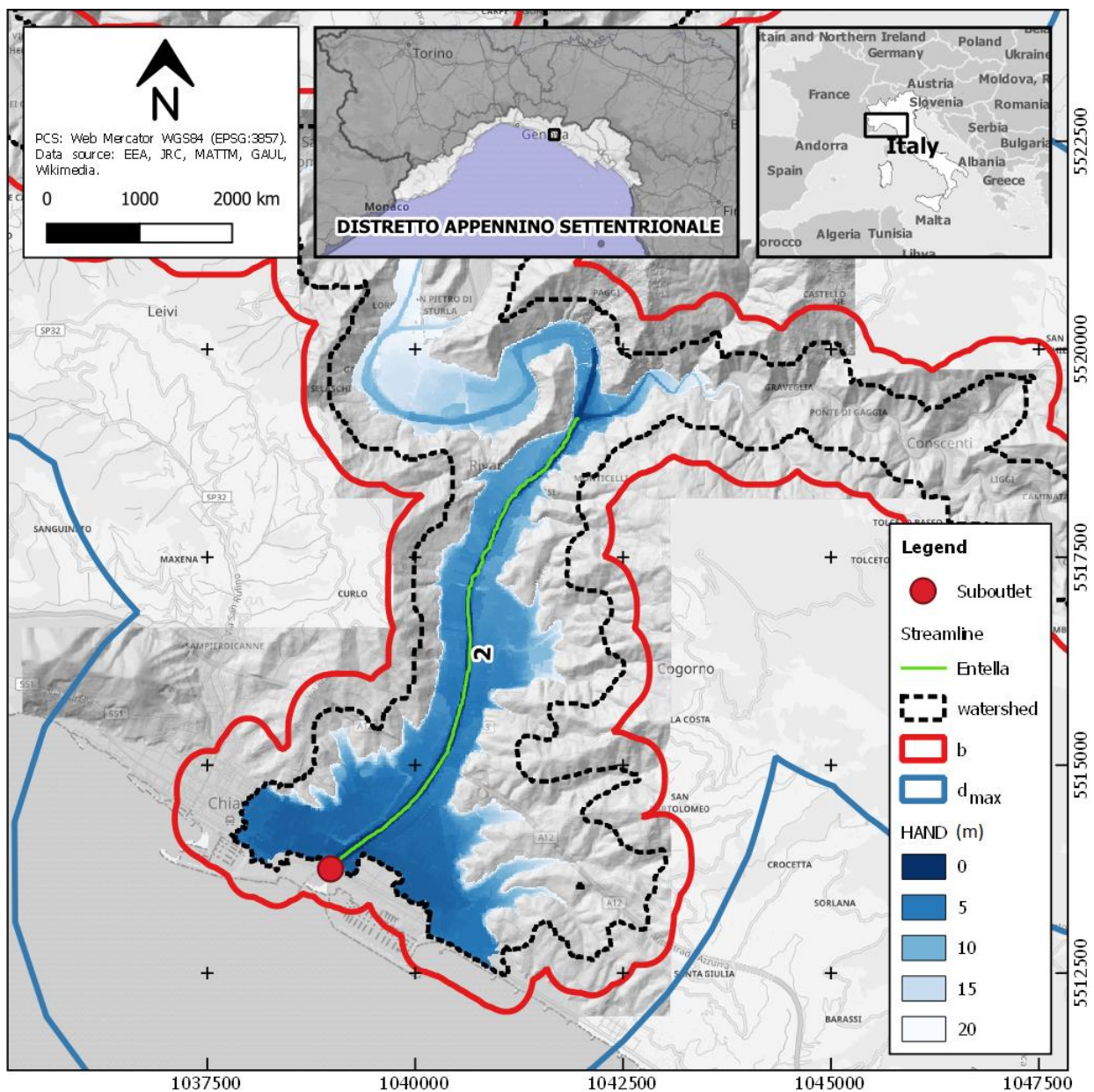


Figure 61 – Watershed, sub-outlet, not expanded HAND map, and search areas (b and d_{max}) for the Entella river branch.

After these assumptions on the distances, the remaining parameter to be defined before employing REFLEX is the head loss in meter per pixel JL . The role of this parameter has been evaluated by using multiple values. This has been first evaluated by using a $JL = 0.2 \text{ m}$. The planar view of the resulting expanded HAND map and the cross-section in the riverbank highlighted a strong discontinuity in the relative vertical elevation between the original HAND map and the expanded one. This expansion cannot ensure a proper delineation of water depth in the floodplain, as shown by the slope of HAND over the expansion (see the red curve shown in Figure 62). Therefore, the same evaluation has been then repeated using lower values of JL .

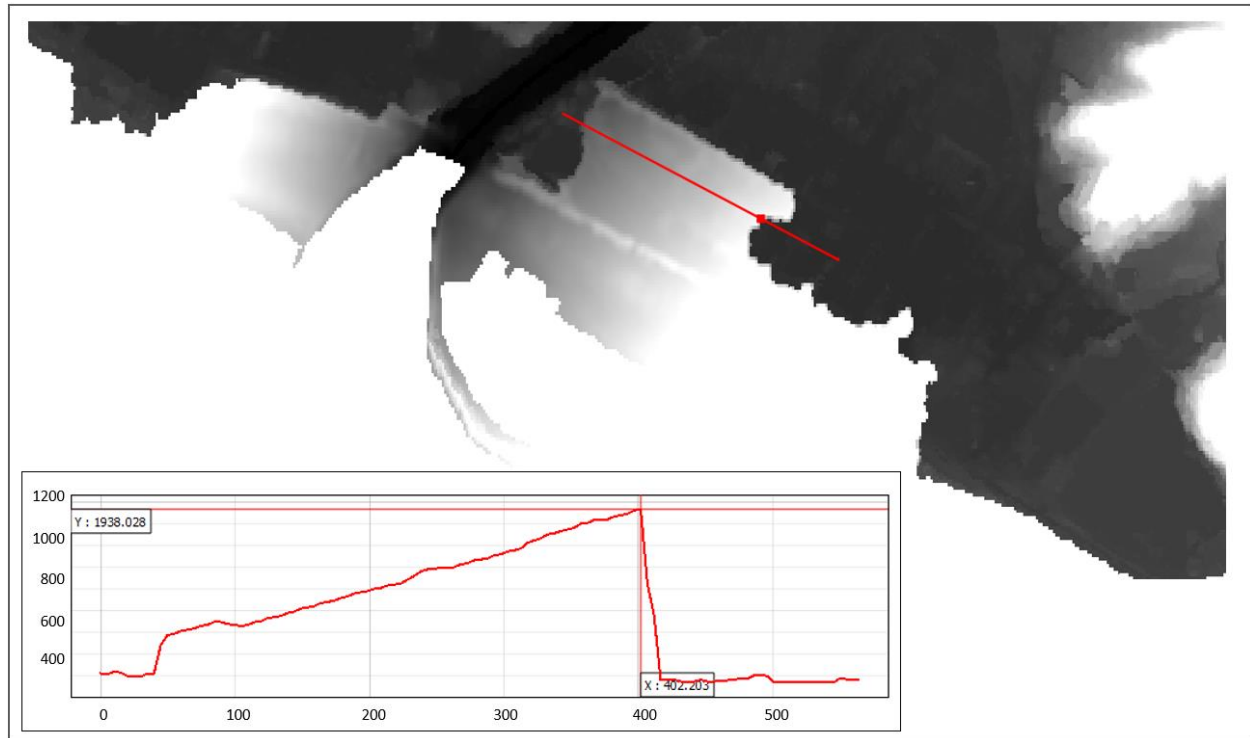


Figure 62 – Planar view in shaded gray and cross-section of expanded HAND in Entella's floodplain using a head loss of 20cm per pixel.

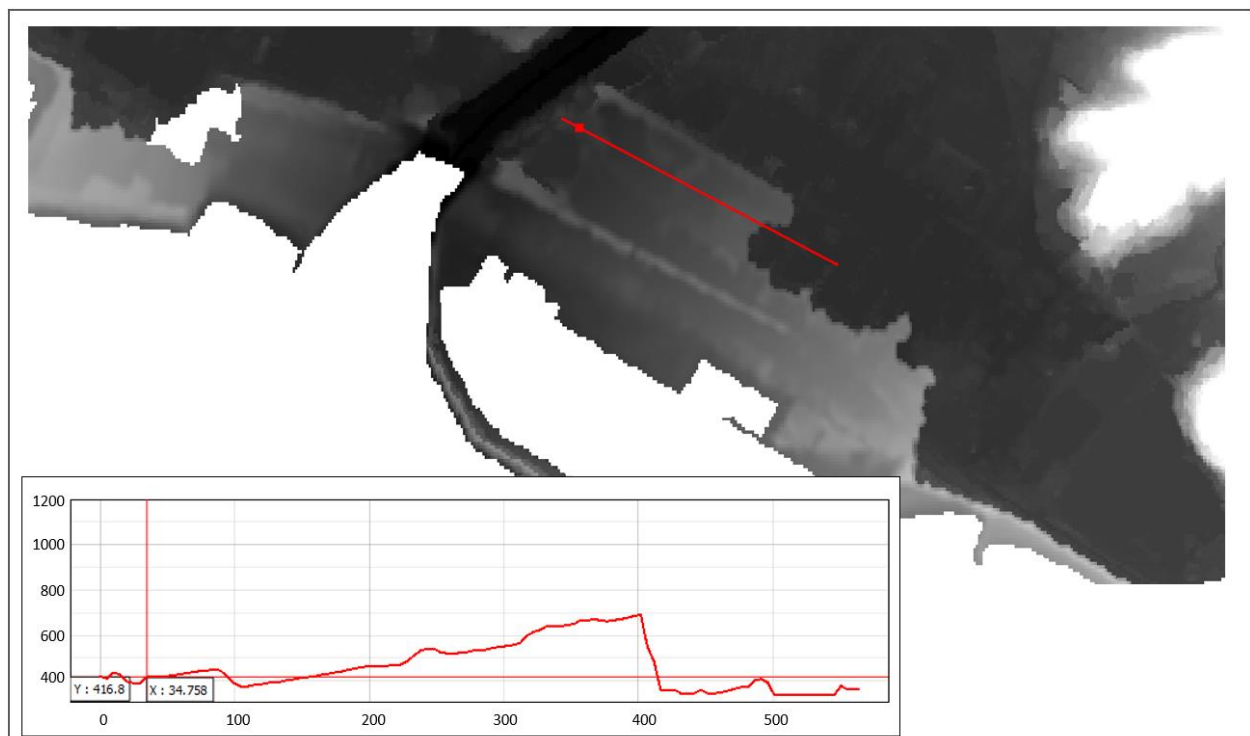


Figure 63 – Planar view in shaded gray and cross-section of expanded HAND in Entella's floodplain using a head loss of 5cm per pixel.

A head loss of 0.05 meters has sensitively reduced the discontinuity in the expansion of HAND (Figure 62). However, artifacts in relative elevation delineation are still persistent, particularly over pixels having a higher distance from the nearest drainage. After other iterations, the optimum value has been then found for JL equal to 0.01 meter, which essentially consists of a rising 0.2% elevation slope being the DEM pixel spacing equal to 5 meters. The obtained expanded HAND is shown in Figure 64, in which no significant artifacts in relative heights delineation are depictable.

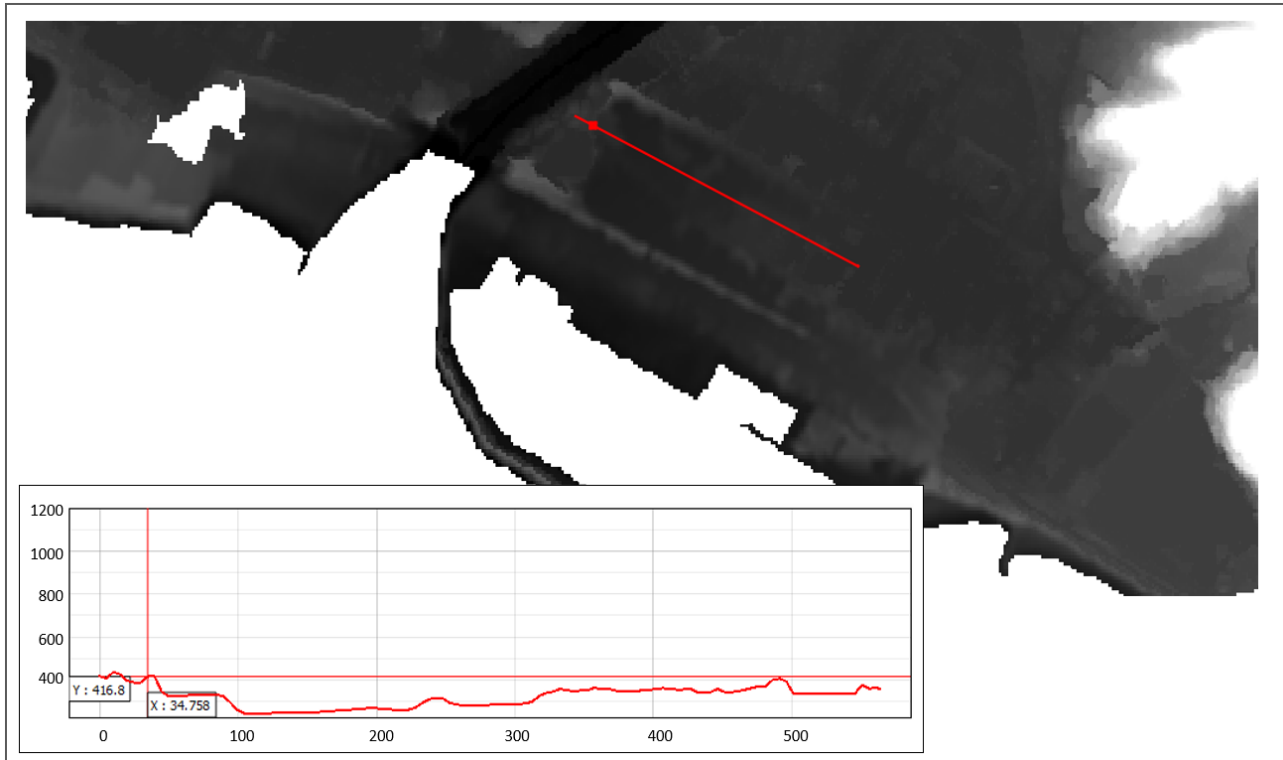


Figure 64 – Planar view in shaded gray and cross-section of expanded HAND in the Entella floodplain using a head loss of 1cm per pixel.

The here described assumptions allowed the definition of REFLEX coastal expansion parameters to be used for the flood modeling of the Entella river basin.

3.4.3.3 Manning-based iterative volume optimization

REFLEX has been deployed in the Entella river basin by using the same configuration of the one used in the Magra river basin, being both these basins similar and located in the same hydrological region. Concerning the parametrization of the Flood module, the experience acquired in the first case study led to assume five iterations also in the flood modeling with REFLEX over the Entella. This assumption is also taken to better assess whether the iterative volume optimization routine can similarly converge also into this second basin.

Figure 65 shows an evolution of the 200-year flood extent derived from this iterative process in the Entella river branch number 2. As already noticed in the Magra case study, the obtained flood extents converged after only 5 iterations with no significant differences in the results of the following iterations. Thus, the truncation at 5 iterations represents a good balance to both ensure good model accuracy and to minimize computation time. Similar behaviors have been registered in all other river branches.

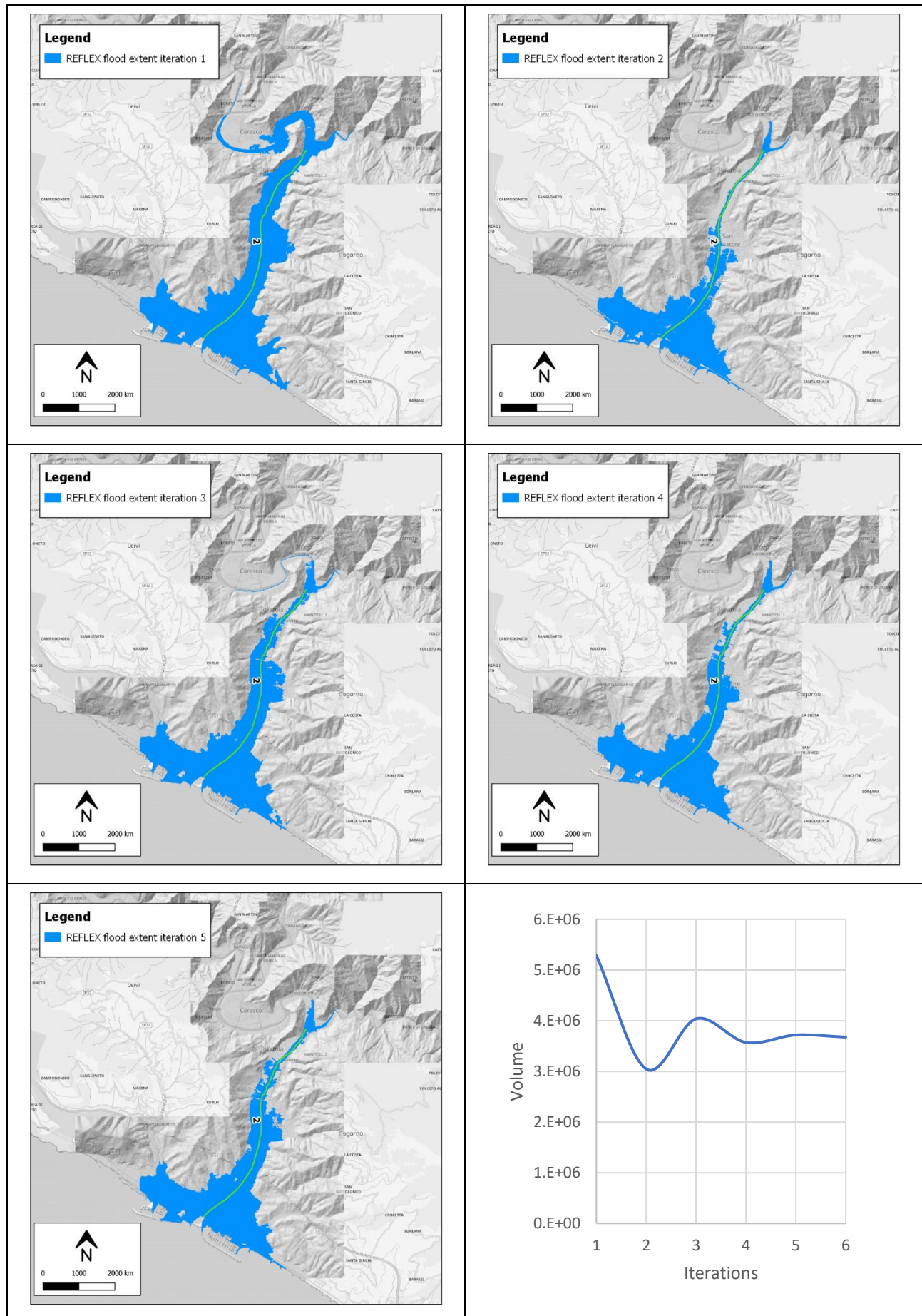


Figure 65 – Iterative Evolution of water extent for a sample Entella subbasin in the REFLEX Manning-based volume optimization.

3.4.3.4 REFLEX simulation and employed parameters

The full list of the REFLEX parameters employed in the flood simulations of the Entella at multiple return periods is reported in the table below.

Parameter	Value
ACPX	APP_SETT
DOMAIN	Entella
RRS_M	5
RRS_DD	0.00005 (0.0008333 for 90m DEM)
NANDEMVAL	-9999
EPSG_CRS	4326
EPSG_PRJ	32632
STR_BURNING_ENABLED	True
TARGET_EPSG	4326
DCOND_BUFFER_CELLS	20
DCOND_FILTERING_MAGNITUDE	1
REMOVE_SINK_ENABLED	False
PIT_REMOVAL_ENABLED	False
EPS_FILLING_ENABLED	True
SOLVE_FLATS_ENABLED	False
FD_METHOD_STREAMS	D8
FD_METHOD_HAND	DINF
DRAINAGE_THRSLD	60000 (for 5m DEM)
BUFFER_DISTANCE_CELL	50
COASTEXP	1
HAND_TRSHLD_ELEV	2000
HAND_MASK_BUFF_DIST_M	300
GRADIENT_LIMIT	0.0003
STR_ELEV_PERCENTILE	25
HEAD_LOSS	20
VOLMIN	1000
WDMIN	0.1
WDMAX	15
ITERATIONS_MAX_VOL_OPT	5
ROUGHNESS_COEFF	0.06
TOLERANCE_VOL_OPT_M	0.1
RP	50 (150, 200, 500)

Table 16 – List of parameters used in the application of REFLEX in the Magra river basin at 30- and 200-year return periods.

3.4.4 Results

Hereinafter are summarized major results obtained in this REFLEX case study over the Entella river basin. After a description of the benchmark flood maps, a validation of the flood extent derived using DEMs at multiple spatial resolutions is performed for different return periods.

3.4.4.1 Benchmark flood maps used for validation

In this case study, Flood Hazard Maps of the PGRA of the Northern Apennine Interregional River Basin Authority (AdB Distrettuale Appennino Settentrionale, 2021) are used to validate the REFLEX modeled flood extent. PGRA flood extents for 50-, 200- and 500-year return periods are shown in Figure 66.

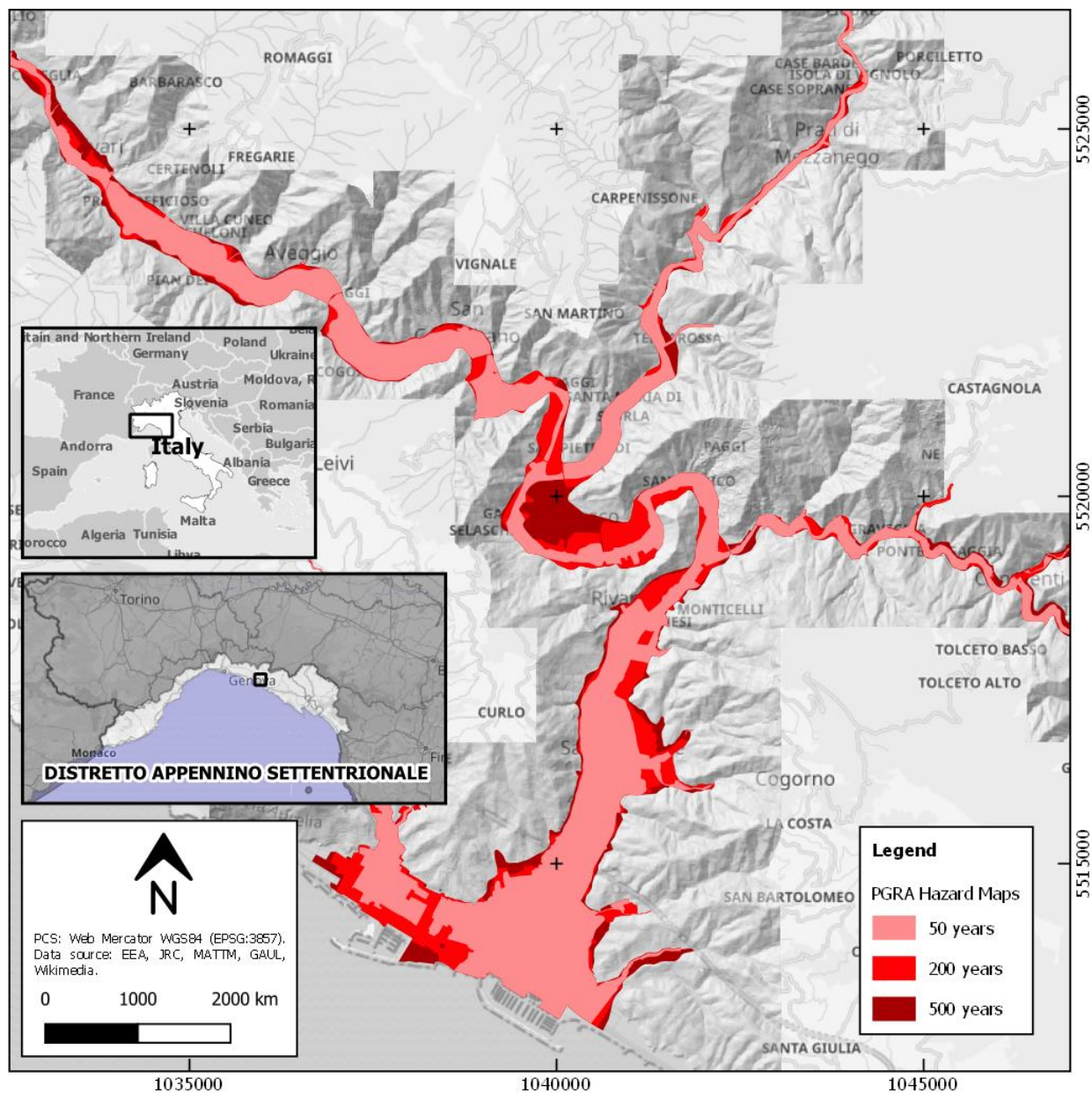


Figure 66 – Flood hazard map for the Entella river basin from “Piano di Gestione del Rischio Alluvioni” of the Northern Apennine Interregional River Basin Authority. Areas in light red, red, and dark red show flood extent at 50-, 200- and 500-year return periods, respectively.

In addition to the PGRA dataset, the flood hazard maps at 50-, 150-, and 500-years RP derived from the CIMA Research Foundation via 2D hydraulic modeling have been also used as a reference for this REFLEX case study. An example of the CIMA's hazard map obtained with the TELEMAC-2D hydraulic model at the 500-year return period is shown in Figure 67. CIMA's flood hazard maps have been derived using the same LiDAR DTM of the Italian Ministry for the Environment Land and Sea (MATTM) employed in this case study.

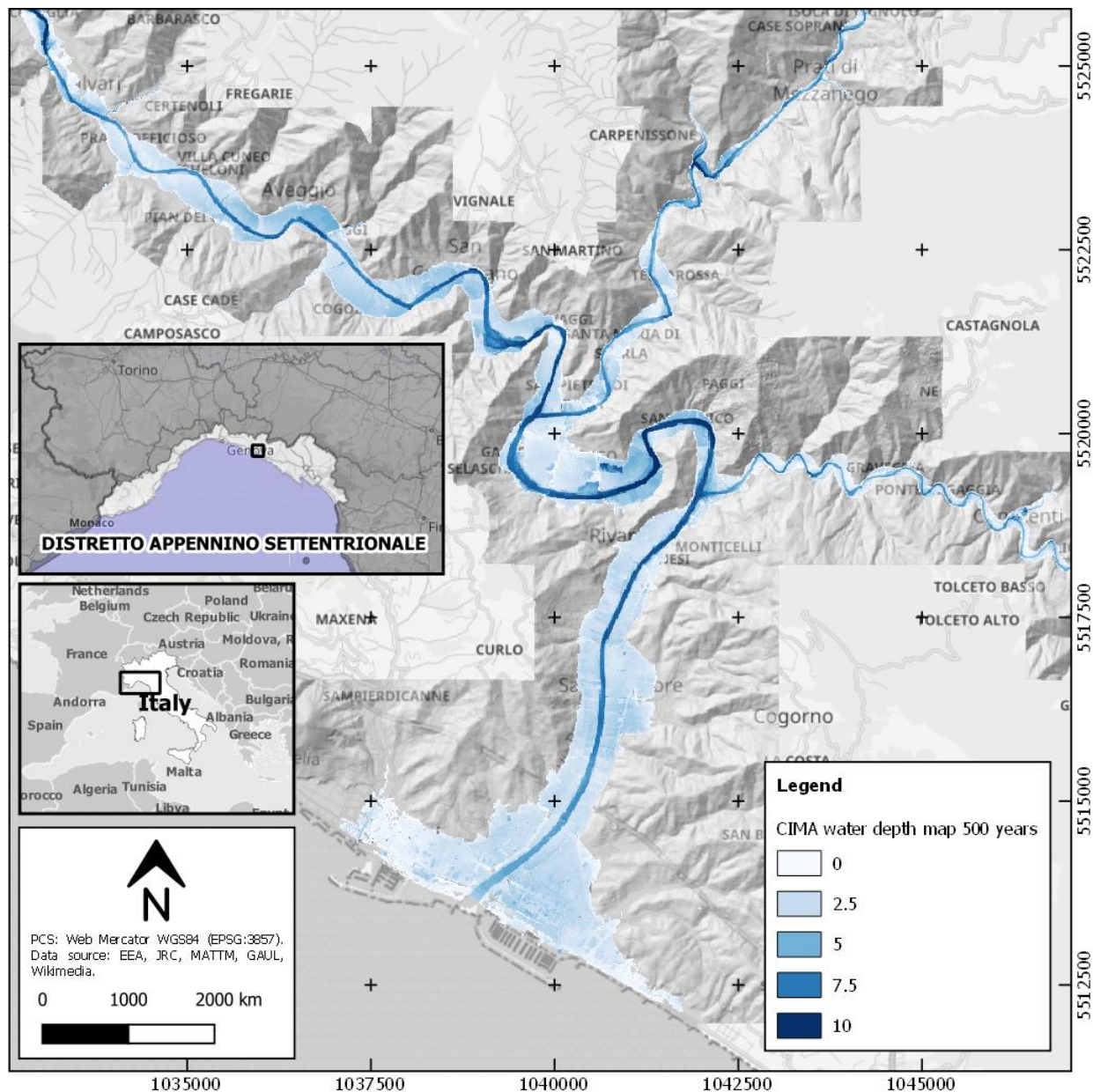


Figure 67 – Flood hazard map at 500-year return period for the Entella river basin from CIMA Research Foundation.

3.4.4.2 Flood extent and water depth for multiple-year return periods at 5m resolution

The floodwater extent maps at 5 m spatial resolution derived from the REFLEX model for return periods of 50, 200, and 500 years are shown in Figure 68.

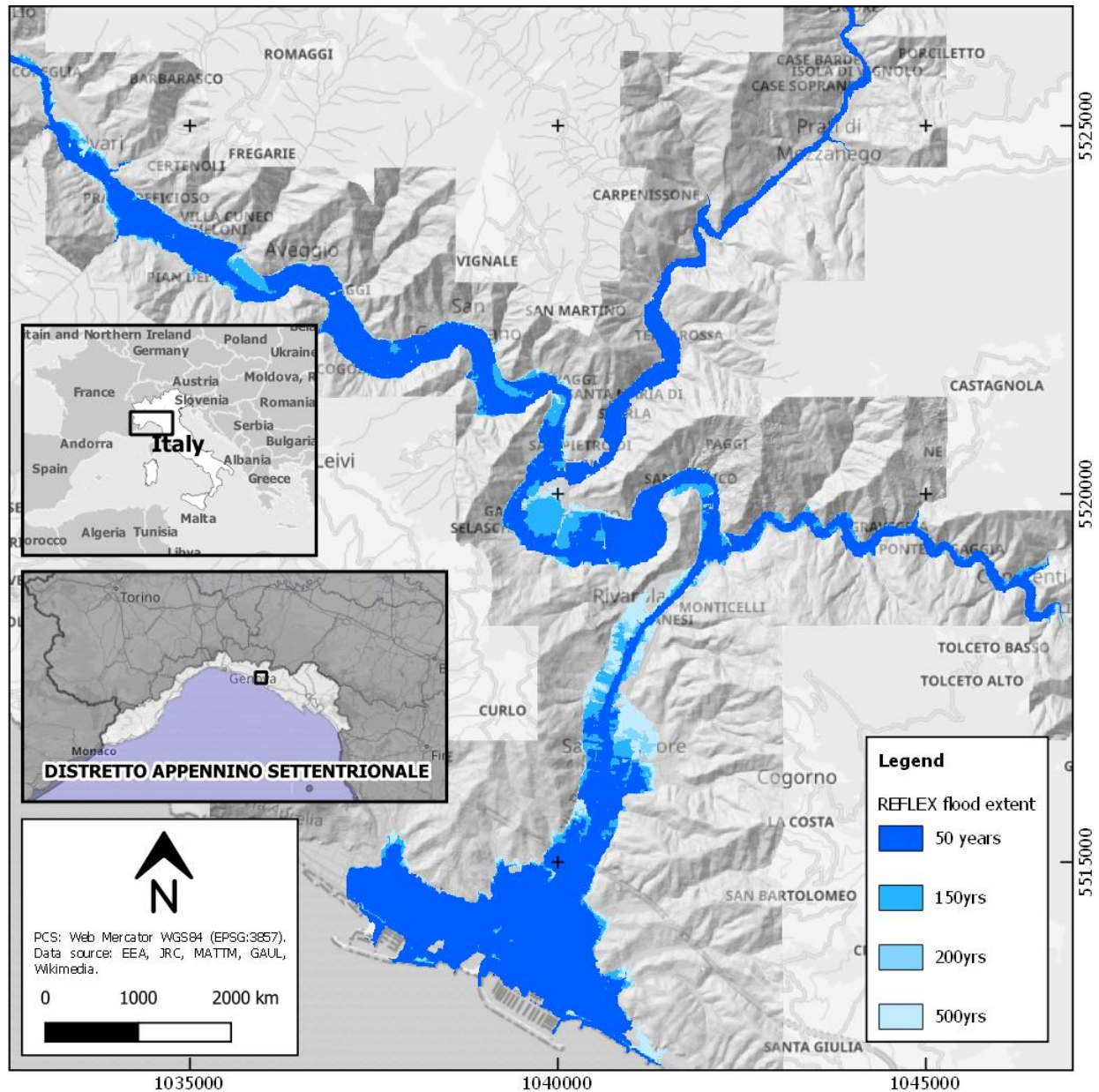


Figure 68 – Water extent over the Entella river basin derived from the REFLEX flood model at different flood magnitudes. Hill shaded LiDAR data from MATTM is shown in graded grayscale. Reflex flood extent at 5m resolution for 50, 150, 200, and 500 years return periods are shown in dark blue, blue, light blue, and very light blue respectively.

The water depth map at 5 m spatial resolution derived from the REFLEX model for a return period of 50 years is shown in Figure 69.

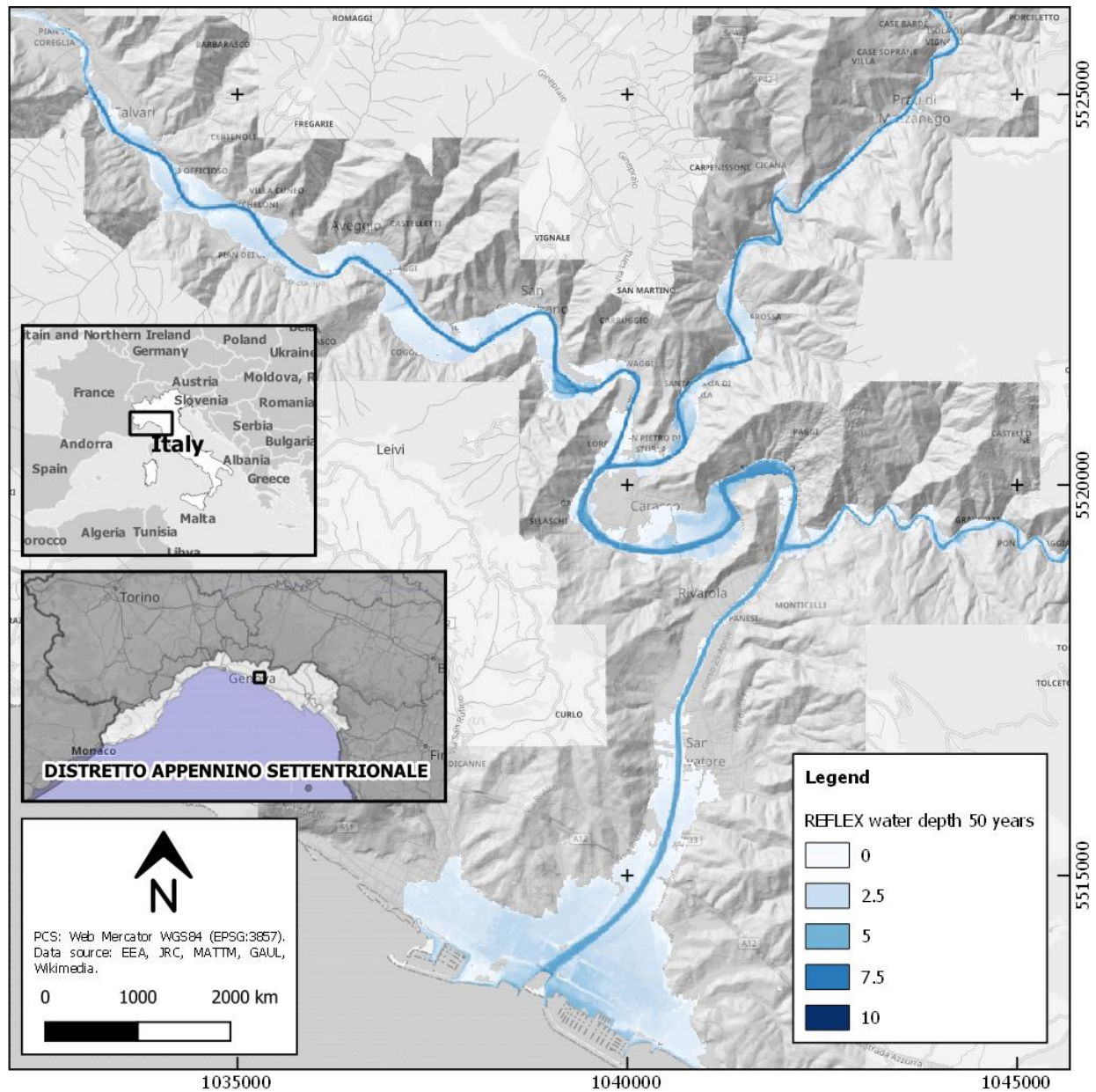


Figure 69 – Water depth over the Entella river basin derived from the REFLEX flood model at 50 years return periods. Water depths in meters are shown in a blue scale graded color bar.

The water depth map at 5 m spatial resolution derived from the REFLEX model for a return period of 150 years is shown in Figure 70.

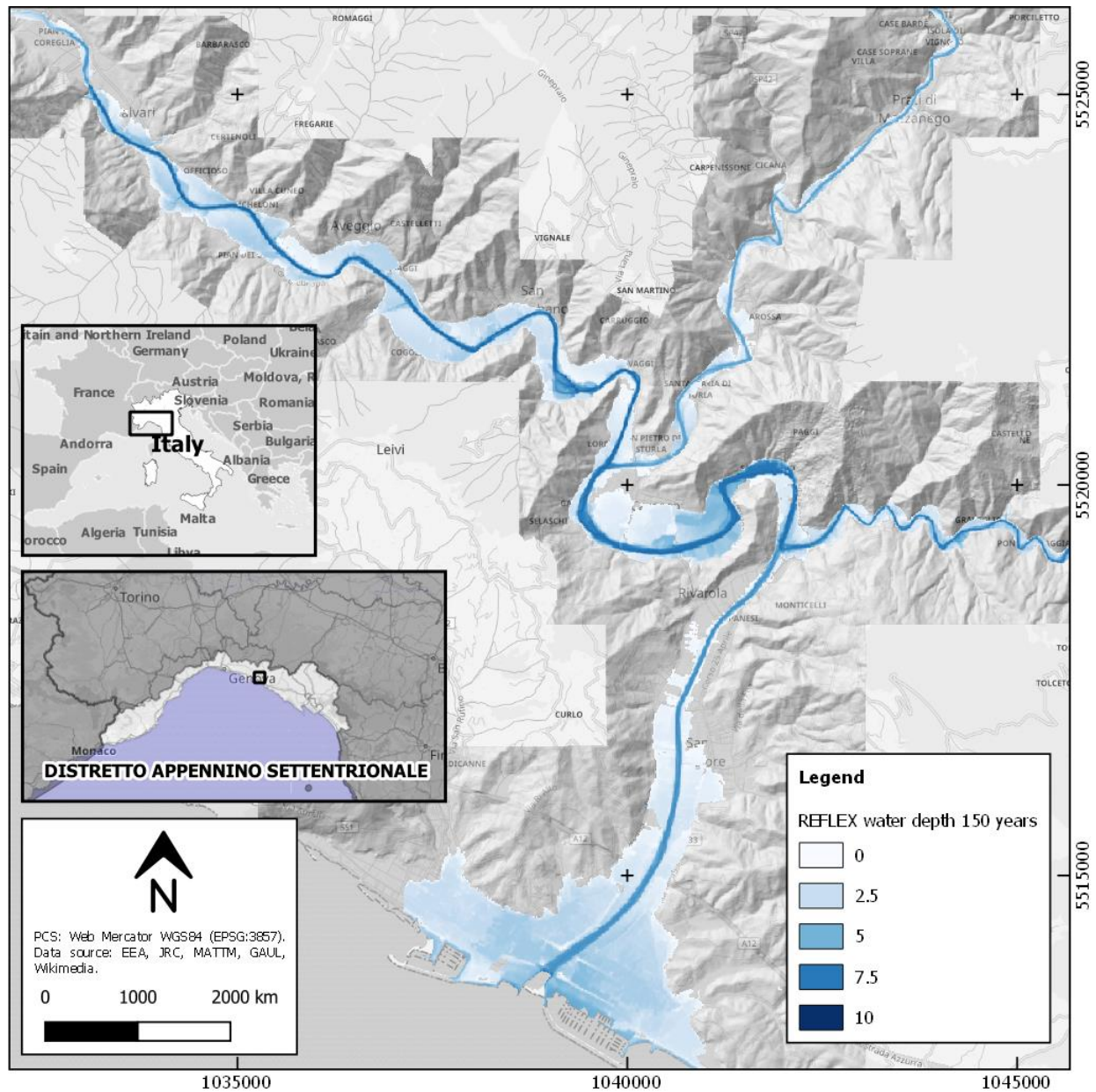


Figure 70 – Water depth over the Entella river basin derived from the REFLEX flood model at 150 years return periods. Water depths in meters are shown in a blue scale graded color bar.

The water depth map at 5 m spatial resolution derived from the REFLEX model for a return period of 200 years is shown in Figure 71.

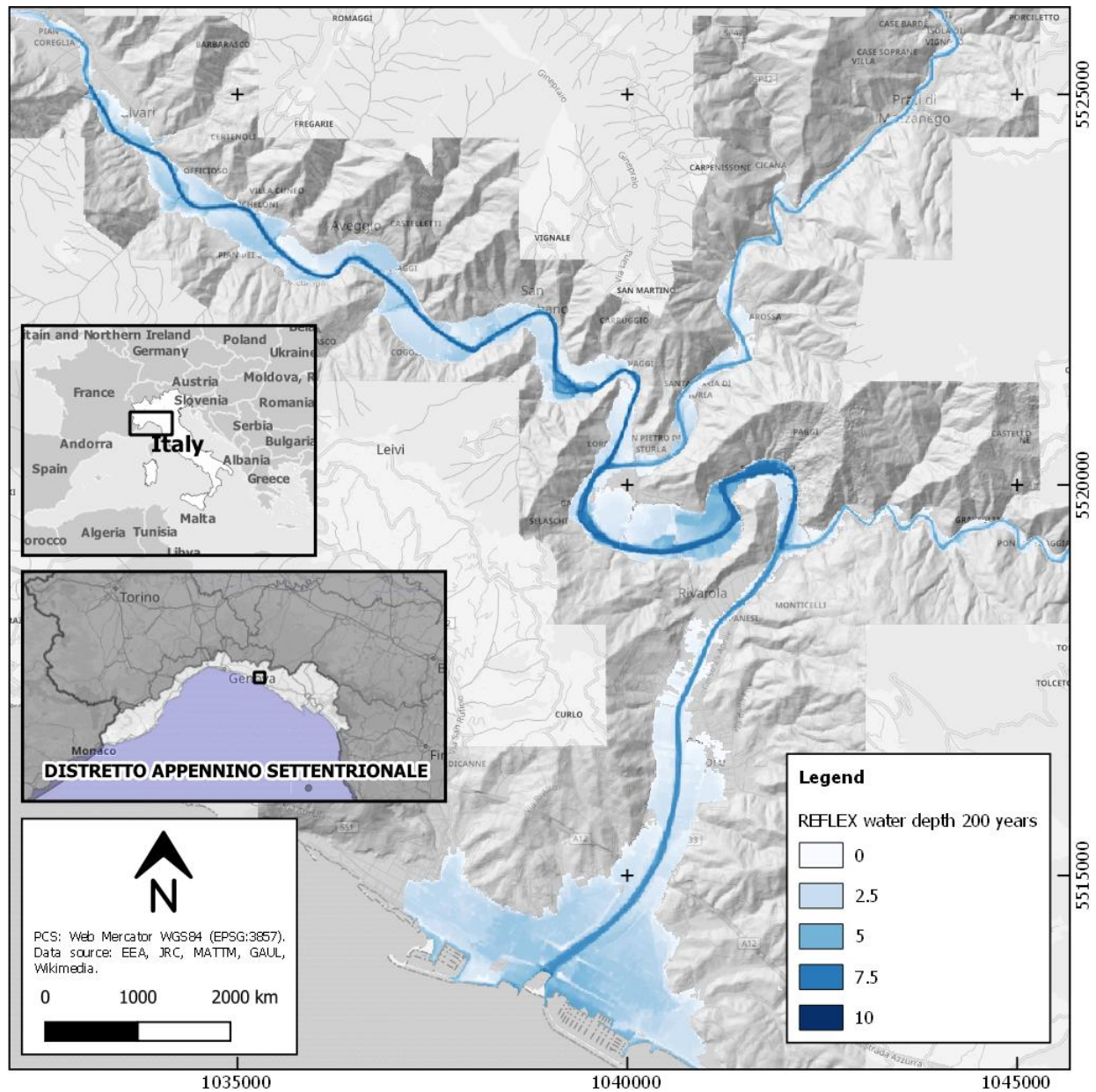


Figure 71 – Water depth over the Entella river basin derived from the REFLEX flood model at 200 years return periods. Water depths in meters are shown in a blue scale graded color bar.

The water depth map at 5 m spatial resolution derived from the REFLEX model for a return period of 500 years is shown in Figure 72.

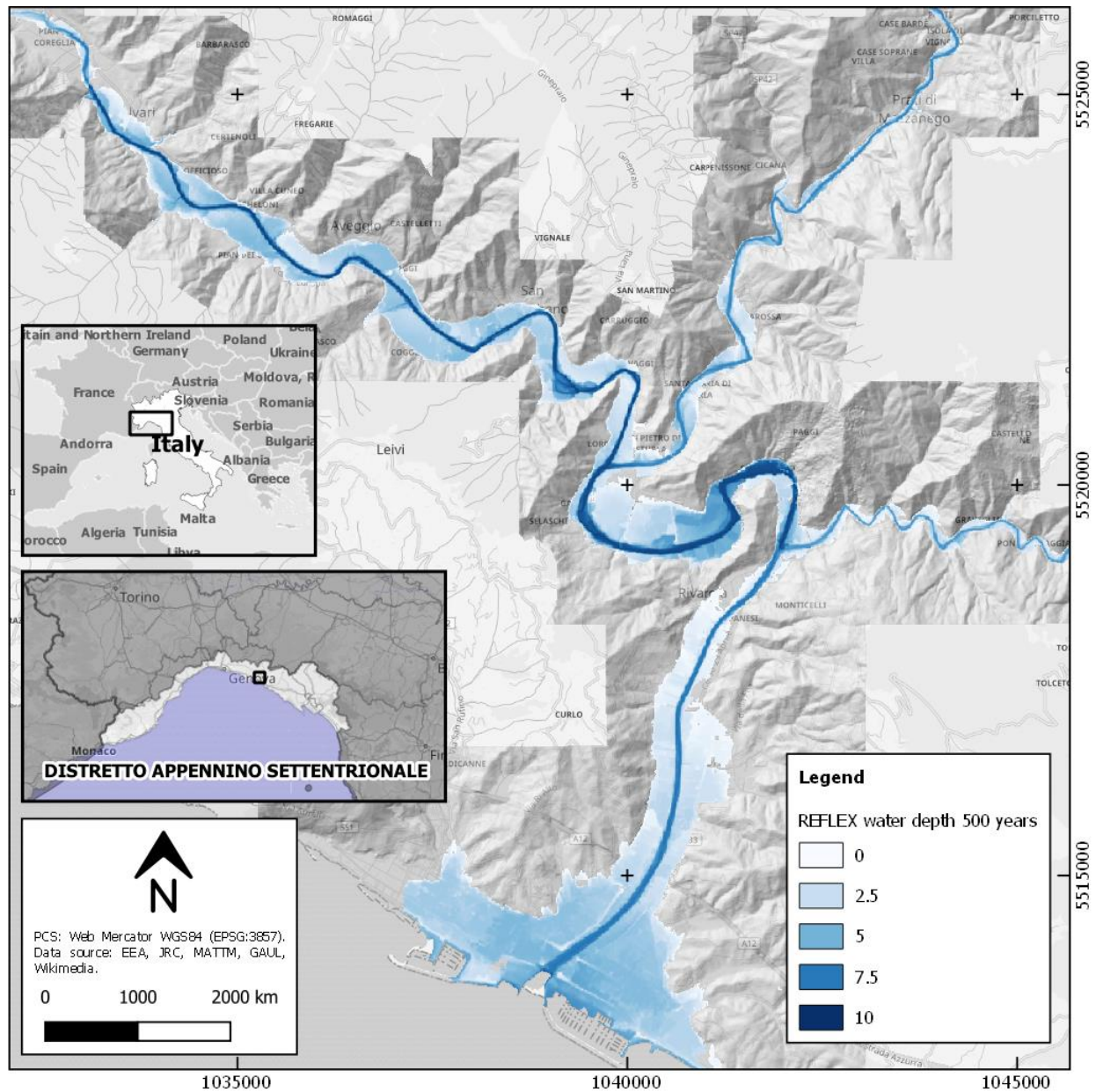


Figure 72 – Water depth over the Entella river basin derived from the REFLEX flood model at 500 years return periods. Water depths in meters are shown in a blue scale graded color bar.

3.4.4.3 Flood extent validation for the 50-year REFLEX map at 5m resolution

The output from the validation of REFLEX flood extent using the PGRA hazard maps is shown in Figure 73, which shows agreement, errors of exclusion, and inclusion of flood hazard at 50-year return period.

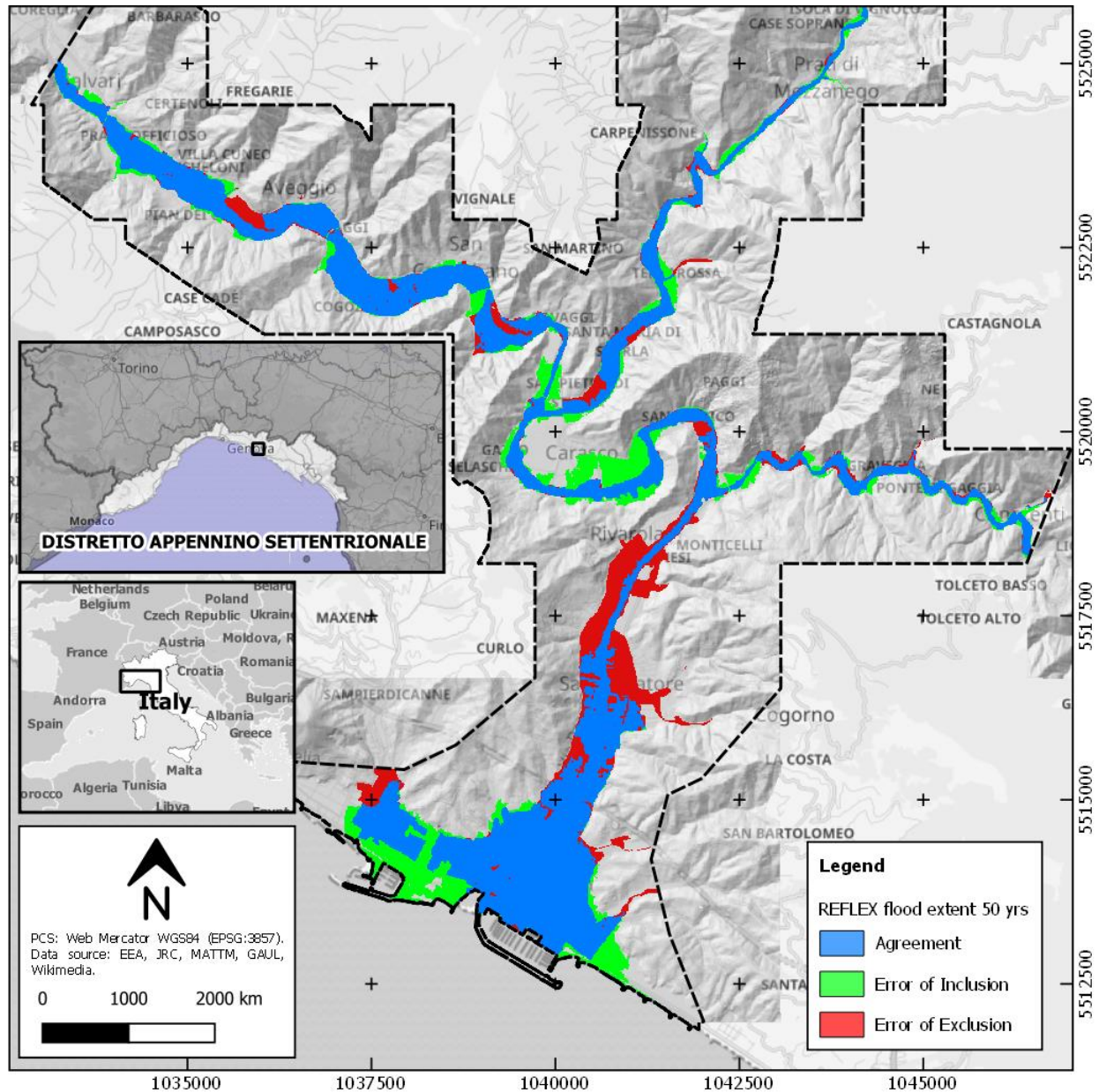


Figure 73 - Comparison between the flood extent delineation from the REFLEX model at the 50-year return period and the PGRA Flood Hazard map at the same return period for the Entella river basin in Northern Italy. Areas in blue, green, and red show respectively agreement (TP), error of inclusion (FP), and error of exclusion (FN).

3.4.4.4 Flood extent validation for the 200-year REFLEX map at 5m resolution

The output from the validation of REFLEX flood extent using the PGRA hazard maps is depicted in Figure 74, which shows agreement, errors of exclusion, and inclusion of flood hazard at 200-year return period.

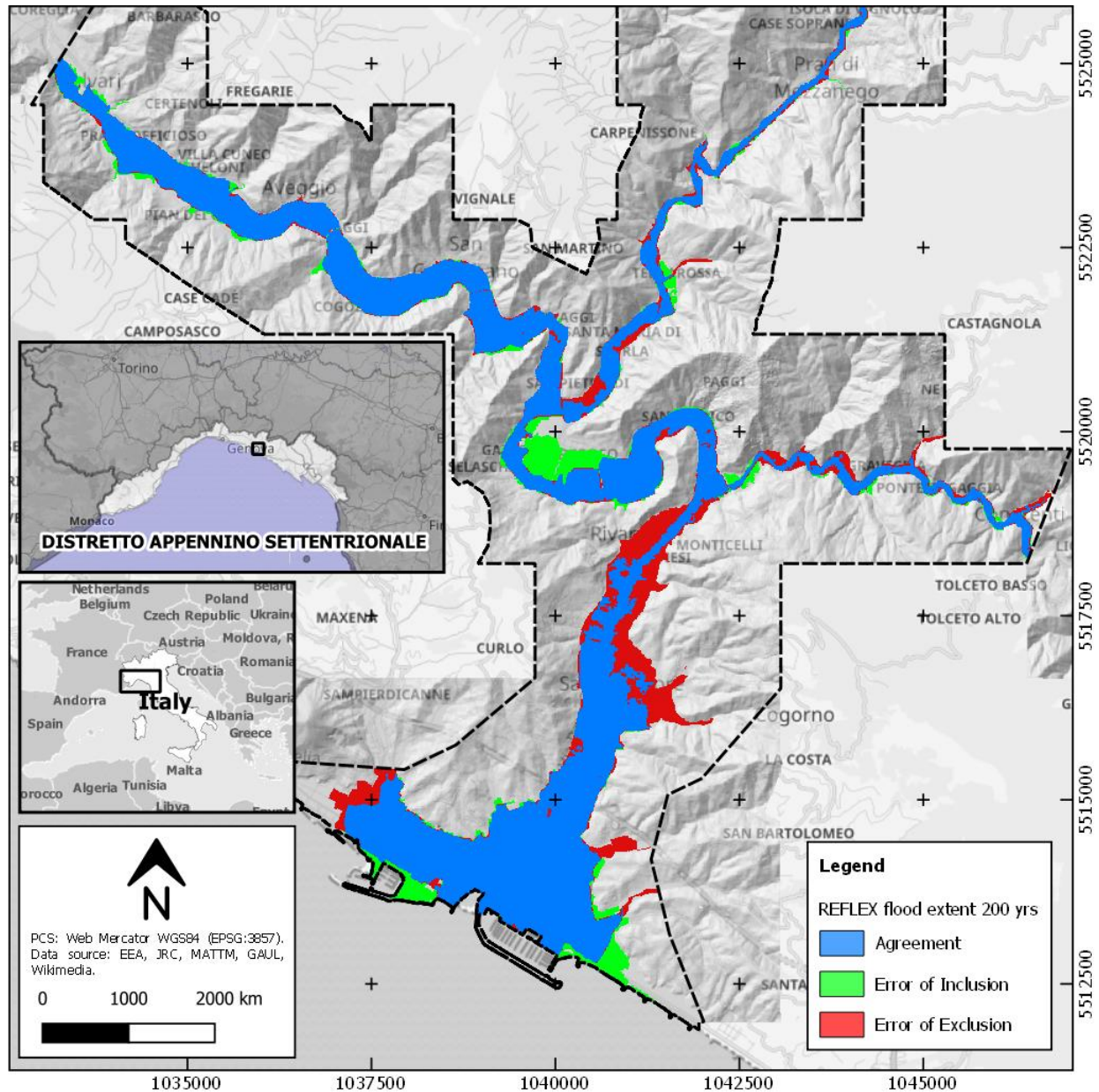


Figure 74 - Comparison between the flood extent delineation from the REFLEX model at the 200-year return period and the PGRA Flood Hazard map at the same return period for the Entella river basin in Northern Italy. Areas in blue, green, and red show respectively agreement (TP), error of inclusion (FP), and error of exclusion (FN).

3.4.4.5 Flood extent validation for the 500-year REFLEX map at 5m resolution

The output from the validation of REFLEX flood extent using the PGRA hazard maps is depicted in Figure 75, which shows agreement, errors of exclusion, and inclusion of flood hazard at 500-year return period.

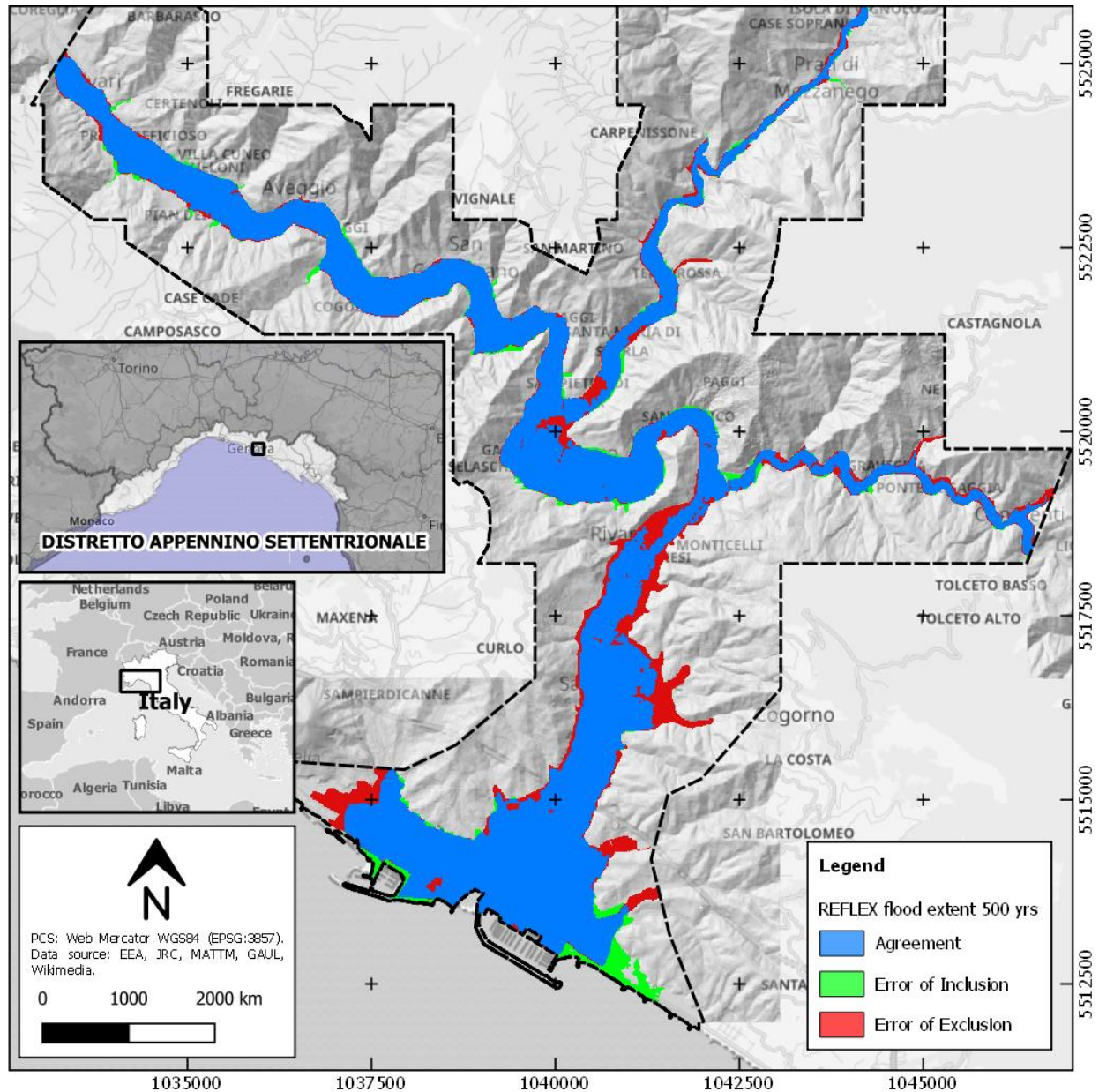


Figure 75 - Comparison between the flood extent delineation from the REFLEX model at the 500-year return period and the PGRA Flood Hazard map at the same return period for the Entella river basin in Northern Italy. Areas in blue, green, and red show respectively agreement (TP), error of inclusion (FP), and error of exclusion (FN).

3.4.4.6 Outcomes from flood extent validation using the PGRA flood hazard maps

This binary classification allowed the estimation of multiple indexes which are summarized in Table 17.

Statistics	Description	Return period		
		50 years	200 years	500 years
ACC	Overall accuracy	0.94	0.95	0.96
TPR	Sensitivity	0.82	0.85	0.87
PPV	Precision	0.78	0.89	0.94
K	Cohen's kappa coefficient	0.76	0.84	0.88
MCC	Matthews Correlation Coefficient	0.76	0.84	0.88

Table 17 - Results from the binary classification of flood extent in the Entella at 50-, 200-, and 500-year return periods using the PGRA flood hazard map as a benchmark.

At the basin scale, the REFLEX model shows very high accuracy (e.g., ACC=0.95 at 200-year return period), high precision (e.g., K=0.89 at 200-year return period), and strong agreement (e.g., MCC=K=0.84 at 200-year return period) in all three modeled flood magnitudes. Higher FN and FP pixels have been encountered mainly in the Lower Entella, where low relief topography does not simplify the flood delineation of this hydro geomorphological method. A complete overview of all obtained metrics obtained at multiple return periods over the Entella is shown in the bar chart of Figure 76.

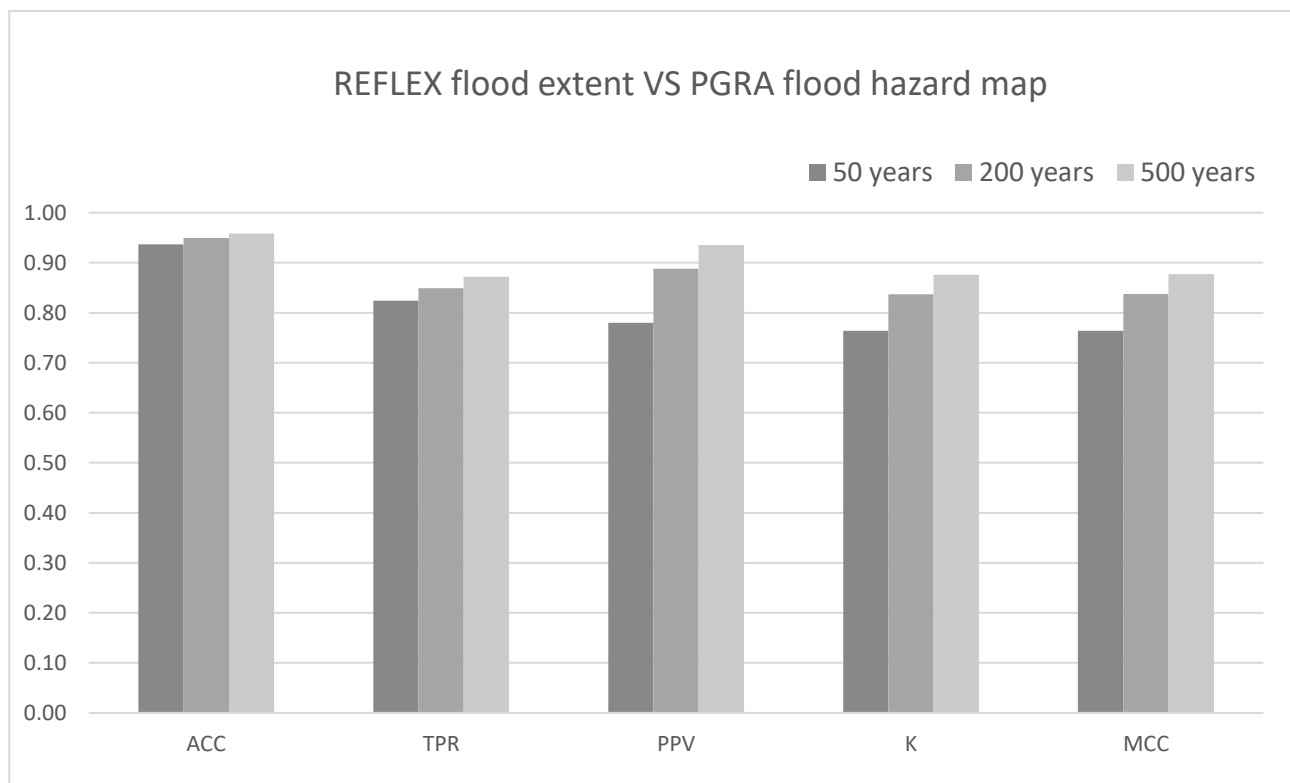


Figure 76 - Bar chart showing accuracy, Cohen's kappa coefficient, and index, and Matthews Correlation Coefficient of REFLEX binary classification in the Entella at multiple return periods using the PGRA flood hazard map as a benchmark.

It is evident from the above bar chart that, intuitively, the fit between predicted and reference flood extents increases while flood magnitude is also increasing. As expected, such metrics confirmed REFLEX's strengths in modeling events of medium-high flood magnitudes.

3.4.4.7 REFLEX water depth validation using CIMA flood hazard maps

The validation of the REFLEX model accuracy has been also accomplished by taking as second benchmark detailed flood hazard maps at multiple return periods derived from the TELEMAC-2D hydraulic model. This second reference flood hazard map represents, in fact, an accurate output from a 2D hydrodynamic model that allows to better highlight the strengths and limitations of the REFLEX model. Furthermore, being the CIMA's flood hazard map provided as a water depth map derived by using the same LiDAR data, it also allows an evaluation of the flood depth estimated by REFLEX. Figure 77 shows the output from this second validation of the REFLEX flood extent at the 500-year return period.

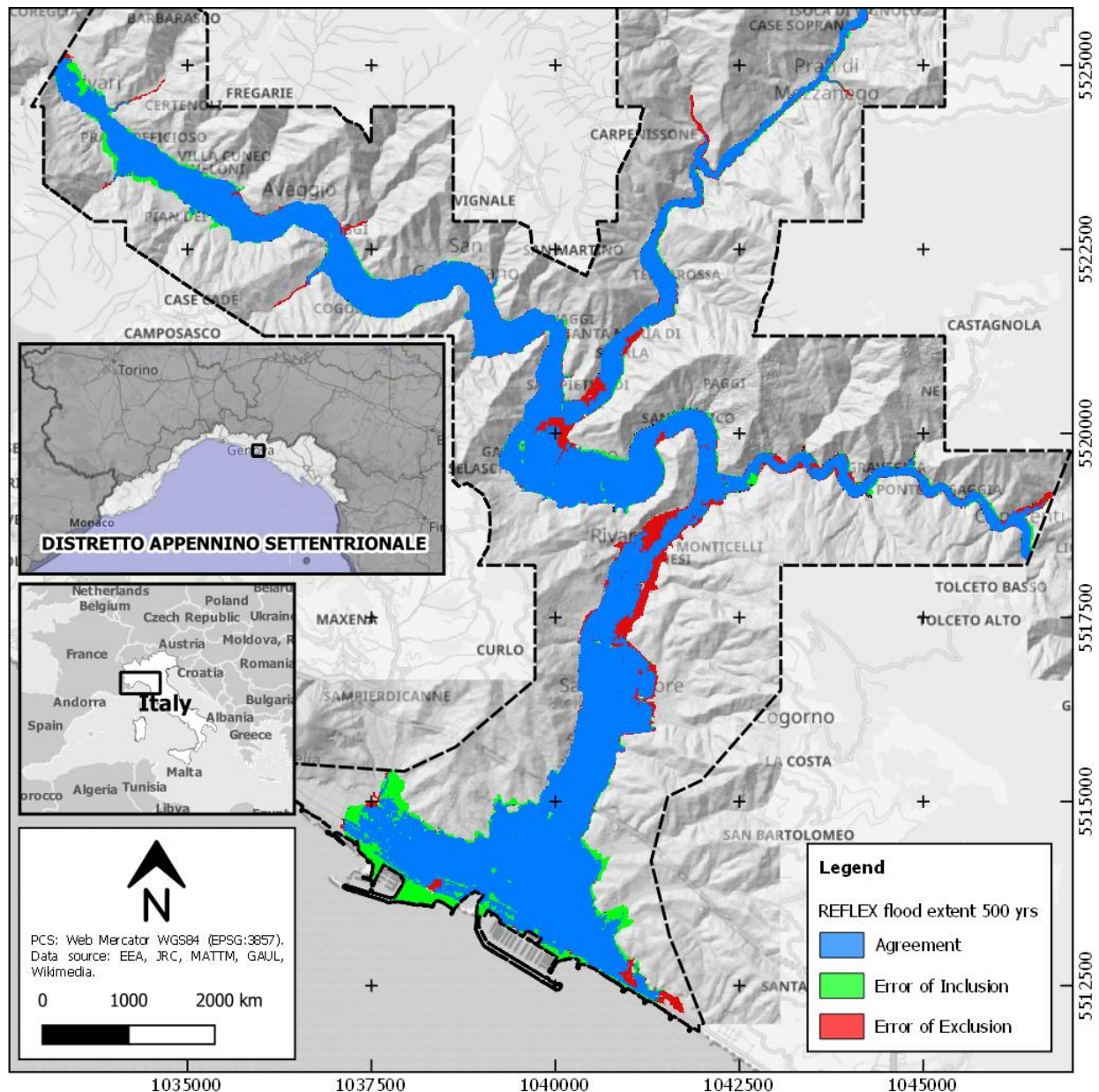


Figure 77 - Comparison between the flood extent delineation from the REFLEX model at the 500-year return period and the CIMA Flood Hazard map at the same return period for the Entella river basin in Northern Italy. Areas in blue, green, and red show respectively agreement (TP), error of inclusion (FP), and error of exclusion (FN).

This binary classification allowed the estimation of multiple indexes which are summarized in Table 18.

Statistics		Description	Return period 500 years
ACC	Overall accuracy		0.97
TPR	Sensitivity		0.93
PPV	Precision		0.92
K	Cohen's kappa coefficient		0.91
MCC	Matthews Correlation Coefficient		0.91

Table 18 – Metrics from the binary classification of flood extent in the Entella at 500-years using the CIMA flood hazard maps.

This very good match between REFLEX and TELEMATC flood extent at the same return period allowed a comprehensive comparison of water depth over the area of matching, which is shown in Figure 78. A water depth difference raster is derived as $WD_{\text{difference}} = WD_{\text{REFLEX}} - WD_{\text{reference}}$ over the area of agreement.

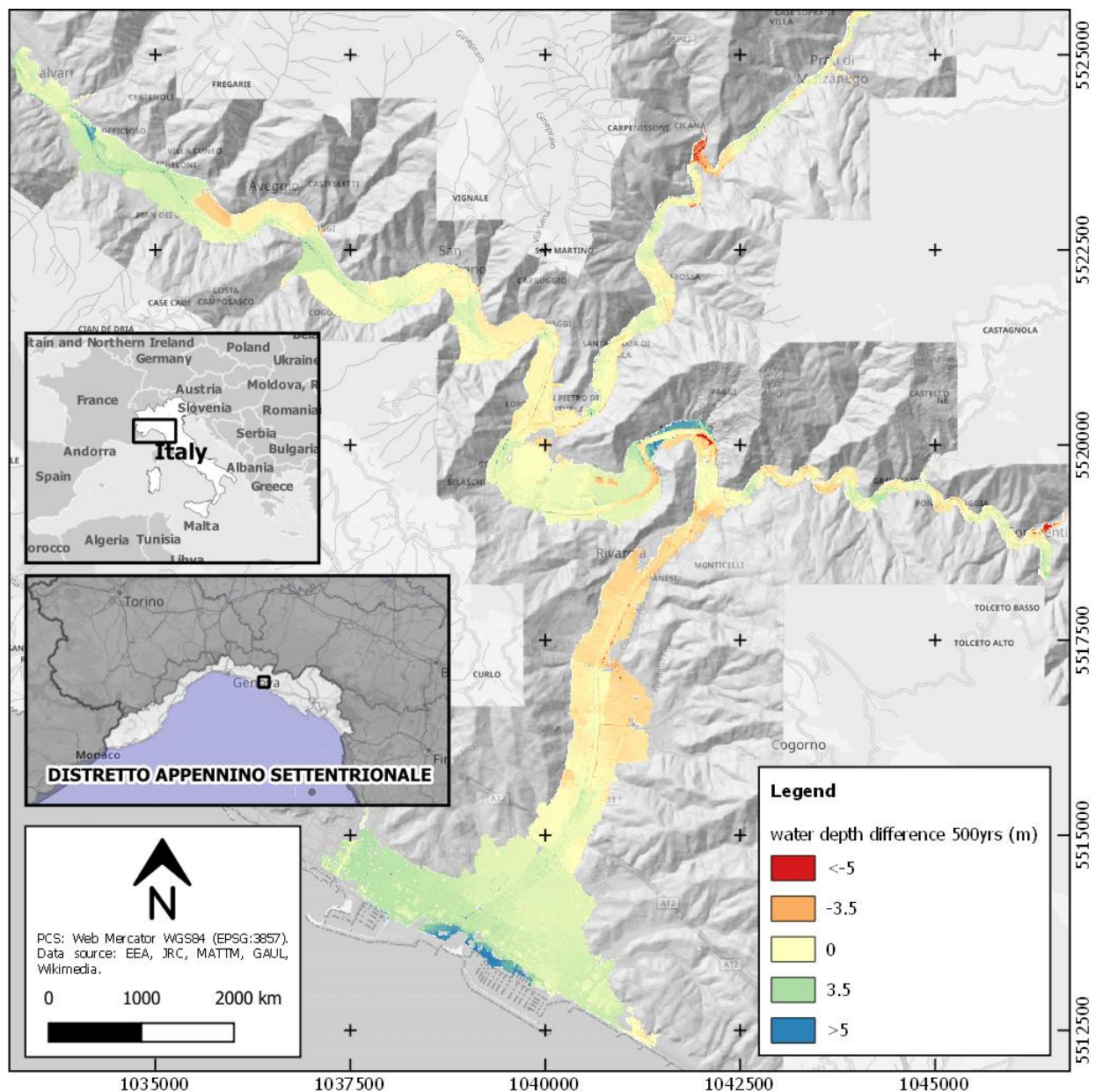


Figure 78 – Water depth difference in meters between the REFLEX water depth map at the 500-year return period and the one from the CIMA water depth map at the same return period for the Entella river basin in Northern Italy. Areas in red, yellow, and blue show respectively underestimate ($0 < WD_{\text{difference}} < -5$), match ($WD_{\text{difference}} = 0$), and overestimate ($5 < WD_{\text{difference}} < 0$).

From an overall perspective, the differences in water depth over the Entella floodplains ranges between a minimum of -6.26 meter to a maximum of 5.95 meters. Most of these values are comprised within a range of $|WD_{\text{difference}}| < 2$ m, as shown in the raster histogram in Figure 79.

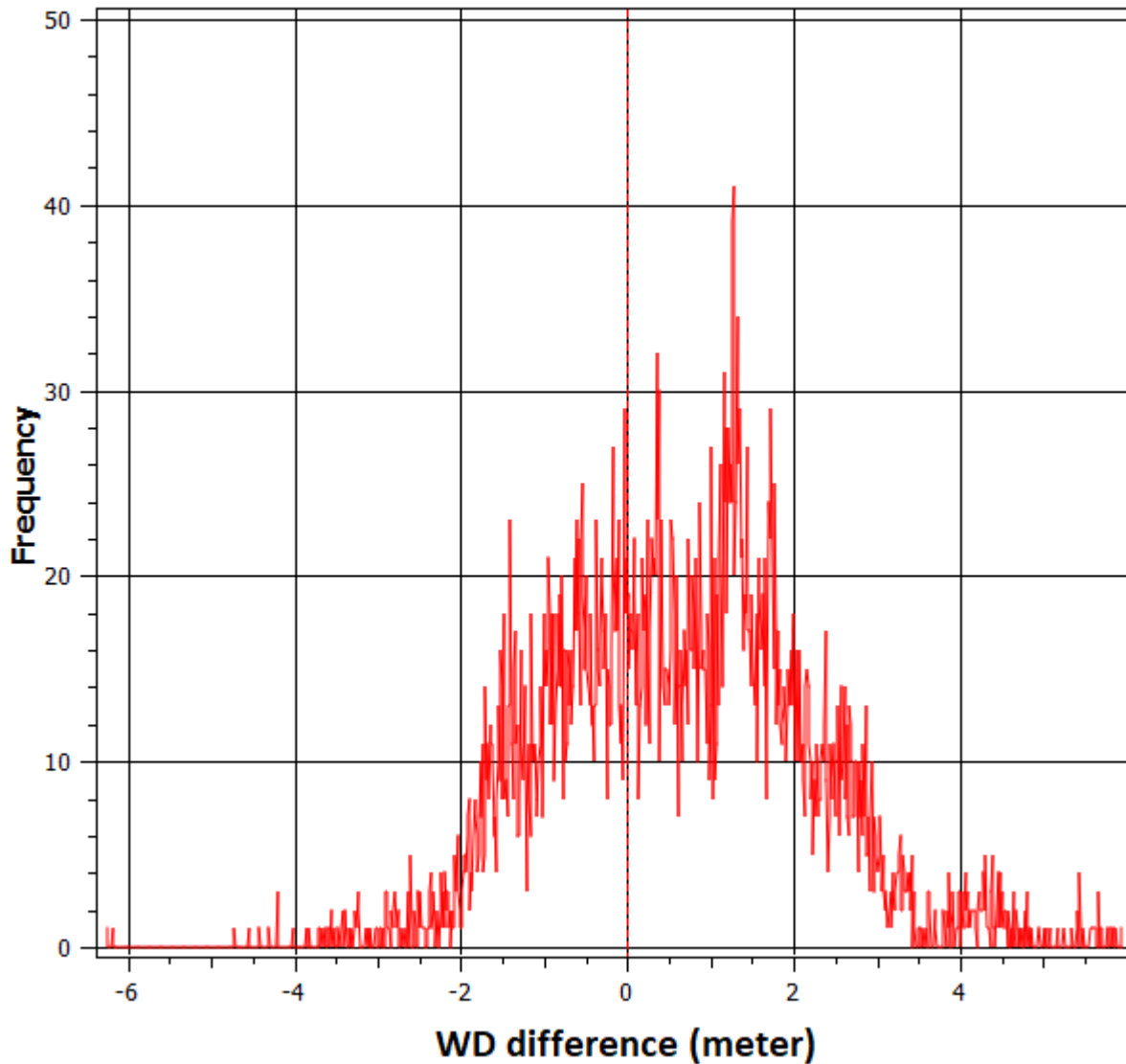


Figure 79 - Distribution of Water depth differences between the REFLEX water depth and the benchmark one derived by CIMA Foundation using TELEMAC 2D model.

Despite a satisfactory agreement between REFLEX and TELEMAC water depths, this quantitative analysis highlights an expected limitation of this hydro-geomorphological model in estimating flood depth.

3.4.4.8 Discussion

This second REFLEX case study confirmed the role of filtered and conditioned elevation data in the rapid flood modeling at medium-small scales. Resampled LiDAR elevations have shown their strengths in delineating flood extent also while comparing REFLEX results with detailed flood hazard maps at 1m spatial resolution from PGRA and CIMA Research Foundation.

The application of REFLEX in this second Ligurian river basin has been particularly useful to evaluate the strengths and limitations of the coastal expansion method developed for this hydro geomorphological model. In fact, HAND expansion has been necessary to effectively simulate floodwaters near the coast. The artificial extension of HAND contours from the watershed boundary to the neighbor coastal basins has ensured a coherent mapping of the flood. No significant gaps have been encountered in the REFLEX flood extent near the coast. This method allowed to solve the “water wall” effect in flooded areas constrained by the watershed, previously observed while employing not expanded HAND contours. However, when extending this method in different locations and at different scales, some of the parameters employed in this research may be redefined. A fine-tuning of these parameters may be undertaken by extensively employing REFLEX in multiple hydrological regions and by comparing modeled results with different flood records.

Furthermore, the Manning-based iterative volume optimization has shown a satisfactory application also within this application of REFLEX in the Entella. This routine, which is necessary to estimate surface runoff volume at transit time, allowed to effectively delineate flood hazard at multiple return periods in the main stem and its tributaries basins. Furthermore, this case study has also confirmed the suitable number of iterations to ensure the convergence of the Manning-based volume update. Five iterations represented a good balance to both ensure good model accuracy and minimize computation time.

Concerning the validation of modeling results at multiple return periods, the obtained REFLEX water extent and water depth maps have been validated by using multiple reference flood hazard maps. The validation of the extent has been first performed by using the same reference dataset employed in the Magra case study, the PGRA flood hazard maps. Obtained metrics have shown a very good agreement between predicted and reference flood extents, with a strong agreement demonstrated by values of the Kappa index and of the Matthews Correlation Coefficient above 0.75 in all return periods.

REFLEX flood maps have been validated by using also accurate flood modeled results from 2D hydraulic modeling shared from CIMA Research Foundation. In this second validation, water depth and extent differences to the reference CIMA’s hazard map in both inclusion and exclusion errors are more significant near the coastal floodplains. This is probably related to a single distribution of the runoff volume in the Entella river branch. In fact, the water stage along each stream branch is assumed as constant in REFLEX, while in the reference 2D hydraulic simulation the same variable changes along the river due to modeled local hydrodynamics (e.g., lower water level due to local rapid change in velocity). This limitation may be overcome in future REFLEX developments with the definition of different weights in Manning’s based volume optimization of multiple segments of the Entella streamline. Such segments may be identified by subdividing a river branch into sub-branches having similar averaged riverbed slopes.

3.5 REFLEX Case study – The Secchia river basin in Northern Italy

This section summarized the outcomes of the application of REFLEX over the Secchia river basin, in Northern Italy.

3.5.1 Case study description

This REFLEX case study aims to simulate a scenario event for levee breaking in the Secchia river basin in Emilia Romagna, Italy. This scenario is based on a real event that occurred on the 18th of January 2014 in a portion of the Secchia river basin in the north of Modena (Figure 80). After four days of intense rainfall over the area, a levee breach occurred along the Secchia which resulted in severe flooding in Albareto di Modena, Bastiglia, and Sorbara municipalities.

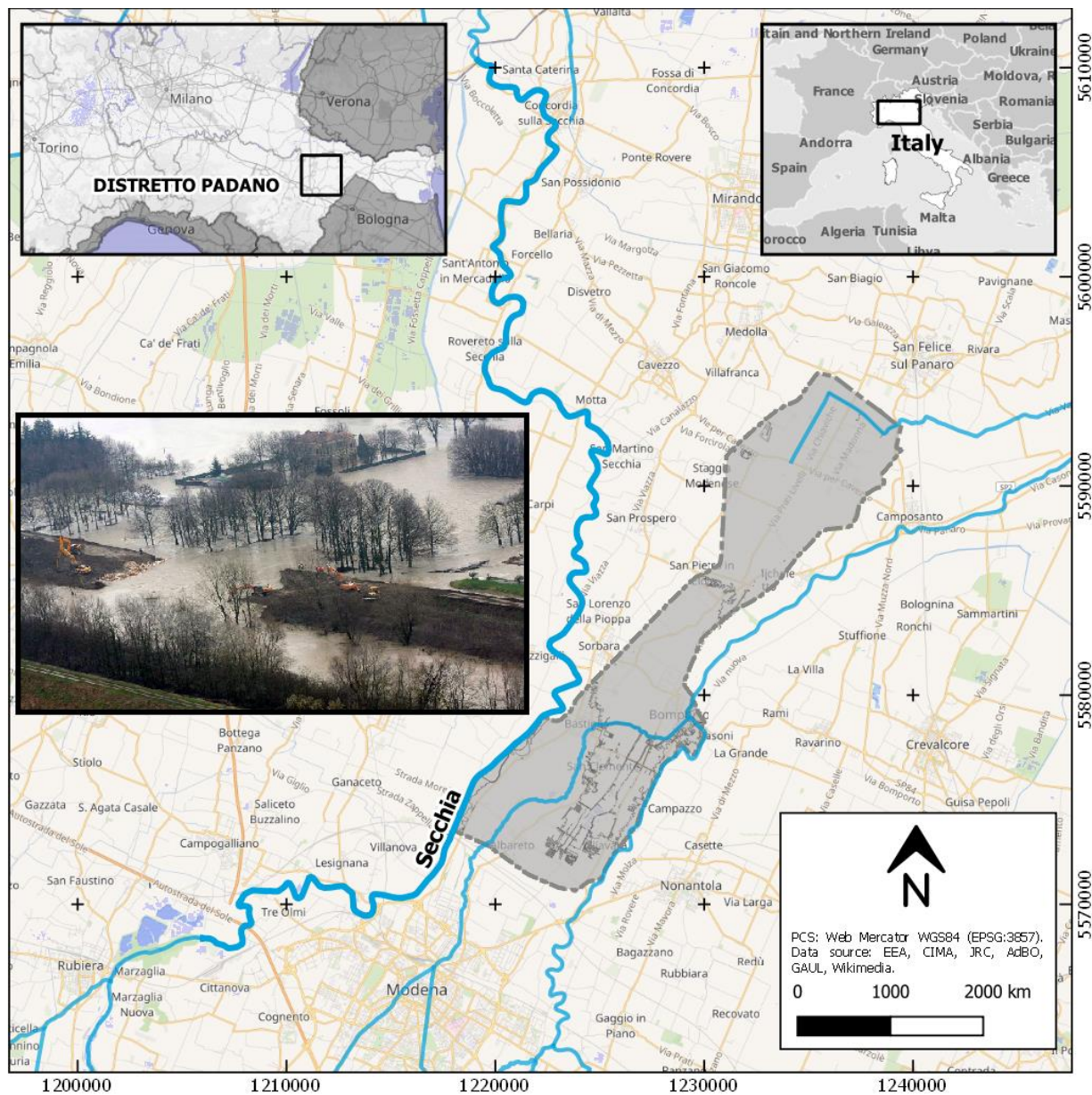


Figure 80 – A portion of the Secchia river basin in Northern Italy investigated in this REFLEX case study (Image credits: Ferrari, Protezione Civile Modena, Aeroclub Marzaglia).

3.5.2 Input data

The input high-resolution DEM at 1m spatial resolution and flood hydrograph at levee breaking have been derived from a hydraulic study performed by CIMA Research Foundation. Both these sources of information have been employed by CIMA to derive post-disaster flood delineation using an accurate 2D hydrodynamic modeling of the domain (Figure 81). In this study, the obtained flood extent has been also validated using satellite imagery.

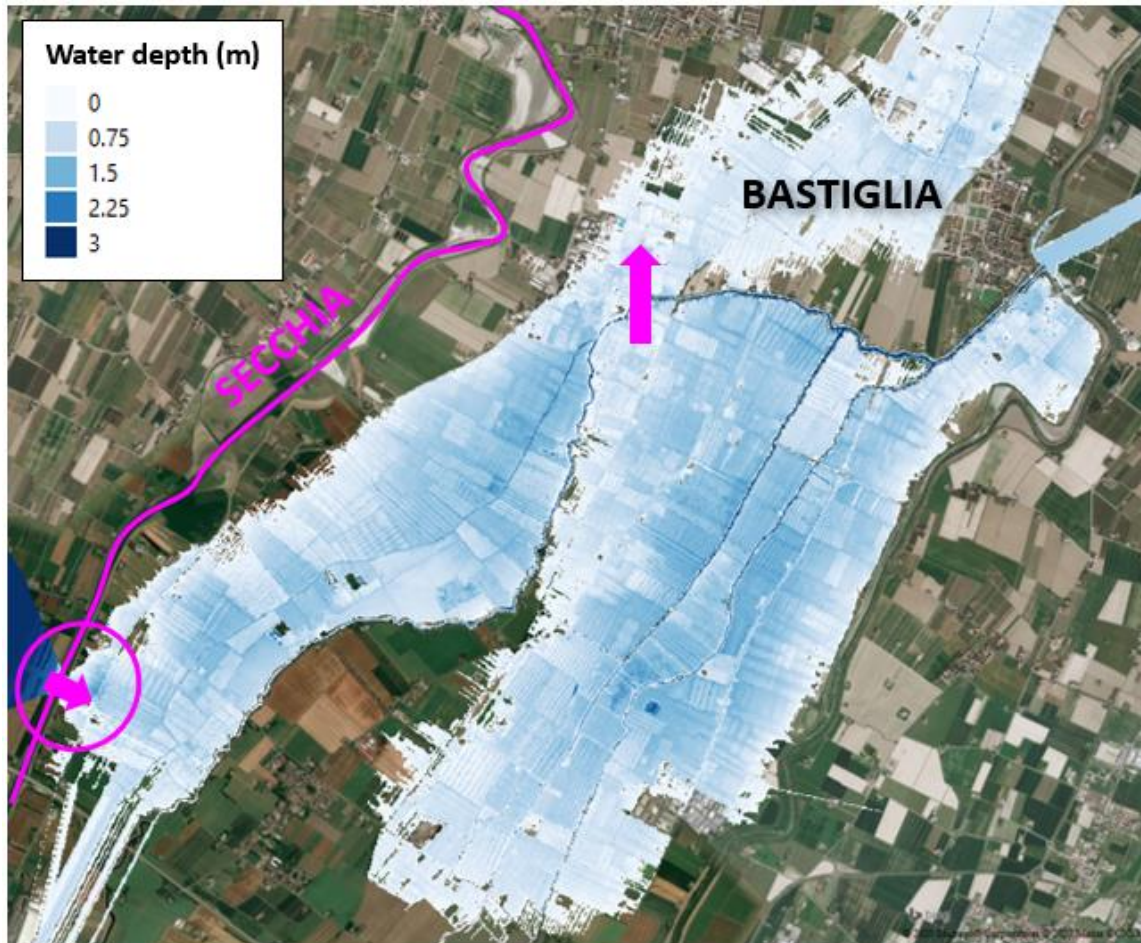


Figure 81 - Flood scenario from a 2D hydraulic model used as benchmarking (Source CIMA Foundation).

This modeled water depth map of the event has been used to assess the impact of the event over this portion of the Secchia river basin in the upstream and downstream areas near Bastiglia. Therefore, this CIMA's flood scenario represents the reference for this REFLEX case study.

3.5.3 Modeling and results

The REFLEX model has been applied over the entire domain of the area and, after the filling of input DEM, all hydrological derivatives have been obtained. The flowlines derived from the DEM, in the upstream part of the domain near the levee break, present a Y-shaped confluence that drains waters of the defended riverbanks of Secchia into another canal close to the Bastiglia municipality. Furthermore, by looking at the HAND maps derived from REFLEX (Figure 82), it is evident that the downstream part of the basin is not connected to the one directly interested by the levee break. Also, the portion of the domain in the north of Bastiglia belongs to another subbasin and thus the input hydrograph at the levee break is not sufficient for the REFLEX hydro-geomorphological approach. Discharge values need to be defined a priori in all the branches of the input streamlines and REFLEX cannot propagate the discharge into the river network of

neighbor watersheds. In this configuration, the REFLEX coastal expansion method is not sufficient to replace the flood modeling of another complete watershed.

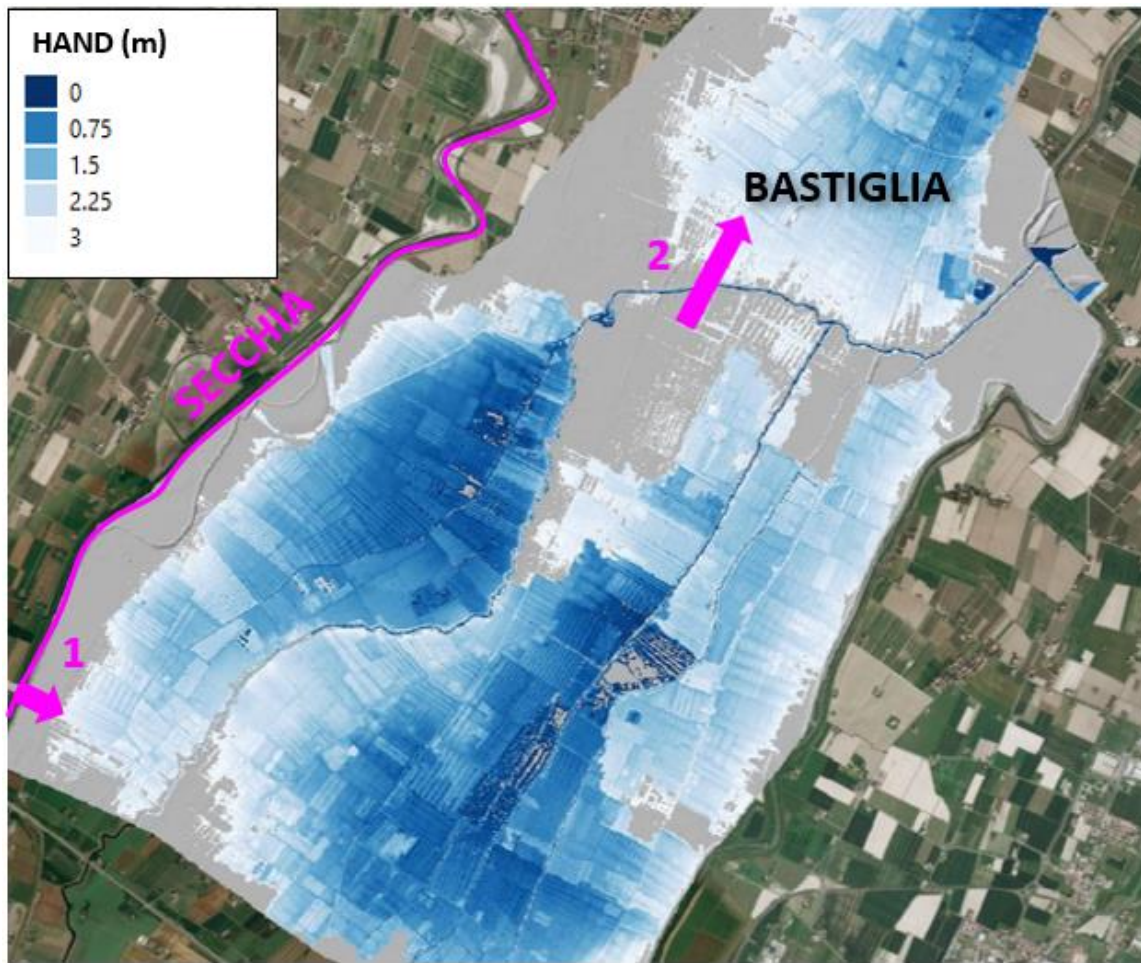


Figure 82 – HAND contours from REFLEX over the Secchia case study area.

3.5.4 Discussion

This third case study has highlighted an intrinsic limit of the REFLEX model. The failure of REFLEX in modeling the flooding due to a levee breaking in the Secchia river is driven by the geomorphological nature of the model. The REFLEX hydro geomorphological model is, in fact, developed for the rapid flood estimation of riverine flooding and therefore such a complex water hydrodynamic modeling becomes difficult to be simulated. Due to catchment boundary constraints, the simulation of this flooding scenario with REFLEX should require a priori distribution of surface runoff volumes which is difficult to assume. Furthermore, given the high values of vertical distances from the nearest drainage around the Secchia levee, the local flooding due to overtopping cannot be represented in REFLEX. Traditional fully 2D hydraulic models remain the only effective solutions for the numerical modeling of this type of flood event.

3.6 REFLEX Case study – Hazard Mapping in southern African countries

This section is about an extensive application of REFLEX in multiple southern African countries.

3.6.1 Case study description

The REFLEX model has been first tested and used in the context of a large-scale flood hazard assessment performed at CIMA research Foundation over multiple African Countries (e.g., Angola, Zambia) including also major islands of Western and Eastern Africa (e.g., Tanzania).

3.6.2 Input data

The input DEM employed in this case study was acquired from the USGS's HDMA dataset (Verdin, 2017). This was then conditioned according to the streams obtained from the flow direction included in the HDMA dataset.

Input flood discharge at multiple return periods was obtained from the modeled streamflow derived with the "Continuum" hydrological model (Silvestro et al., 2015). Continuum's simulations over the region have been forced with precipitation estimates from a global meteorological model and have been calibrated by using field streamflow observations at gauges when available.

3.6.3 Modeling

The discharge estimates obtained from Continuum have been used as input for REFLEX to estimate surface runoff volume across the entire river network. In the flood modeling of the southern African region, the REFLEX chain has been systematically employed over multiple basins across the Zambezi hydrological region, as well as its neighbor basins including the islands.

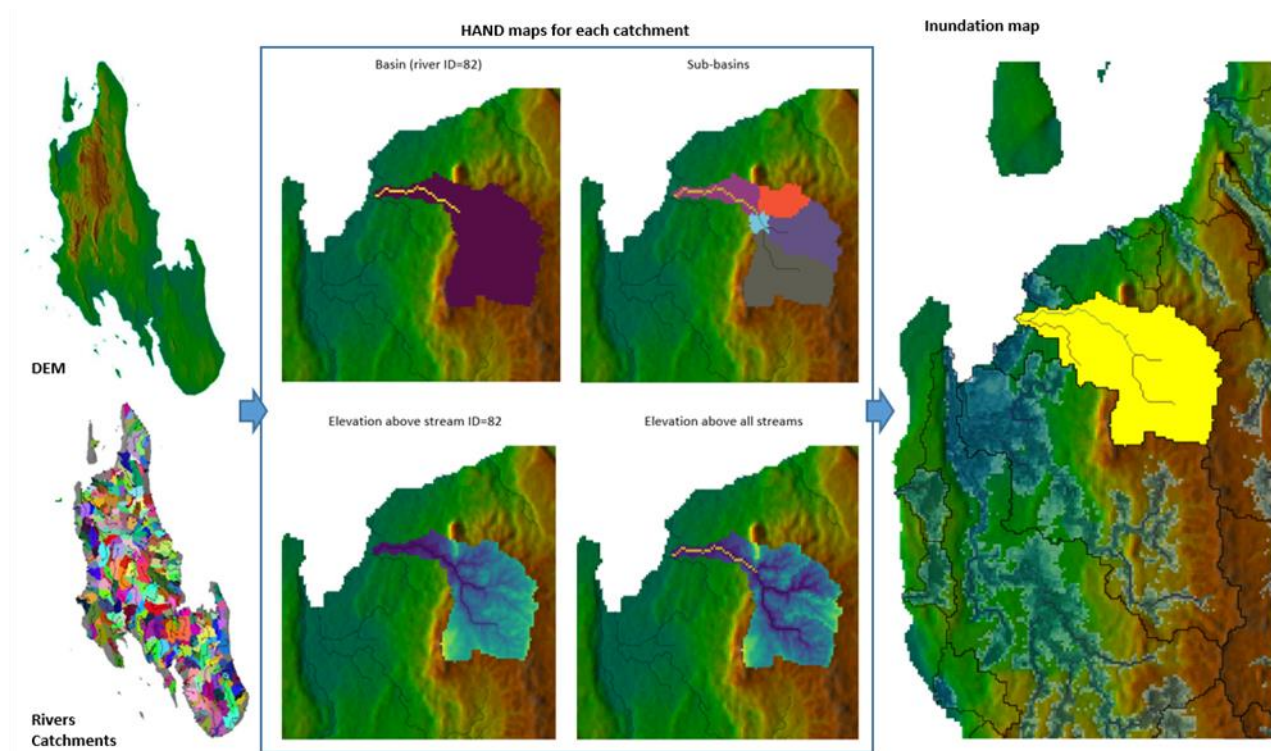


Figure 83 – An example of REFLEX flood mapping applied for the Zanzibar Island.

The resulting REFLEX flood maps results have been then merged to derive flood maps at 90m spatial resolution at different return periods over the entire region. This output dataset allowed to carry out multiple flood hazard assessments at the country level, for example for the entire Angola and Zambia administrative boundaries.

3.6.4 Results

The output results obtained from the application of REFLEX in Western and Eastern Africa are flood hazard maps at different return periods (e.g., from 5, 10, 15, 25, 50, 100, 250, and 500 years).

An example of a flood hazard map obtained in one of the Tanzania islands is shown in the figure below.

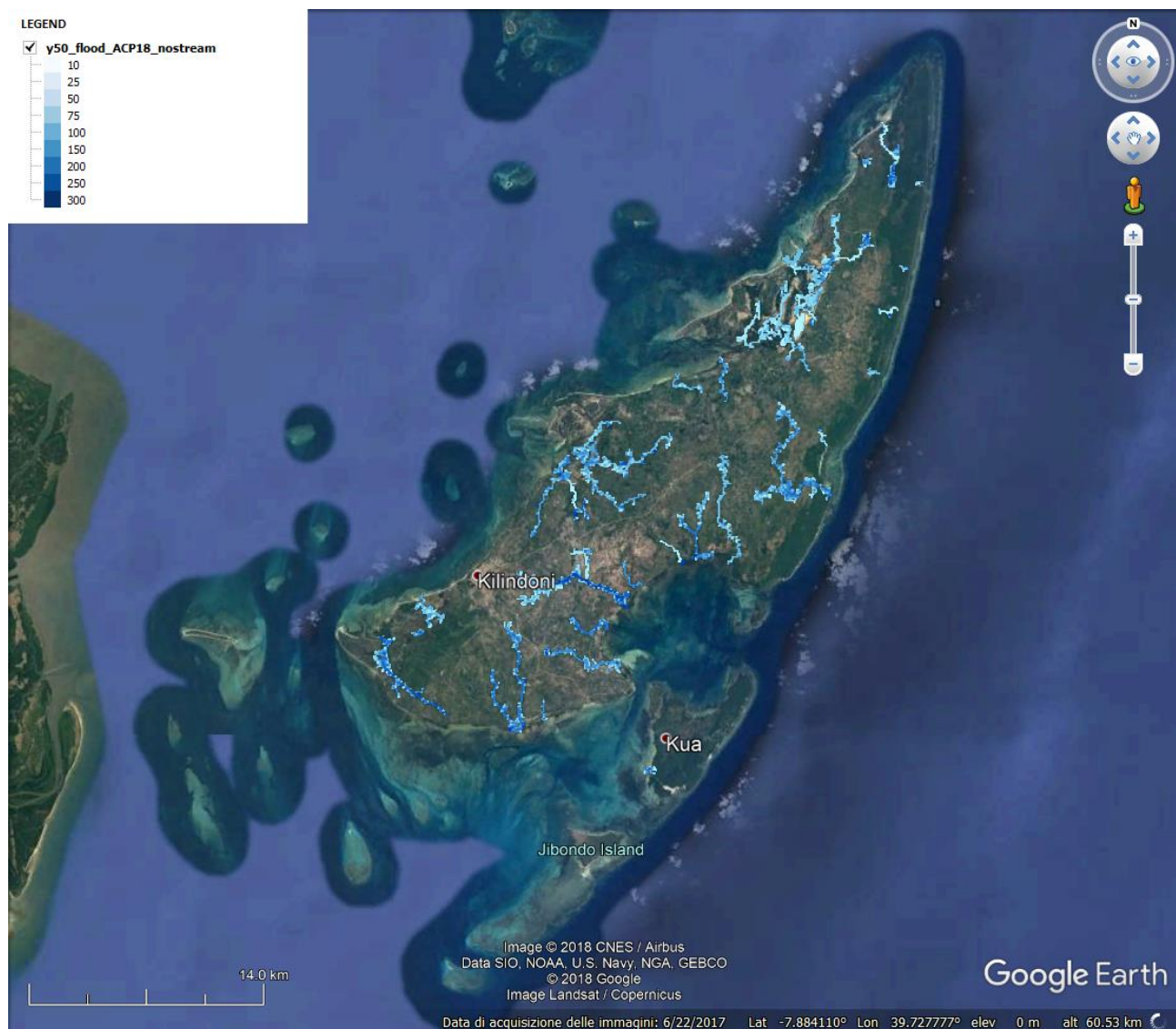


Figure 84 – Flood scenario 50 years Return Period derived from REFLEX over the Tanzania islands

An extraction of the large-scale flood mapping results obtained from REFLEX by CIMA over the entire Zambezi river basin is shown in the following hazard maps at the 50-year return period for Angola and Zambia.

As flood extent reference, the Maximum Water Extent derived from 37 years of Landsat observations by the JRC's GSW dataset (Pekel et al., 2016) are shown as an indication of similar flood magnitude.

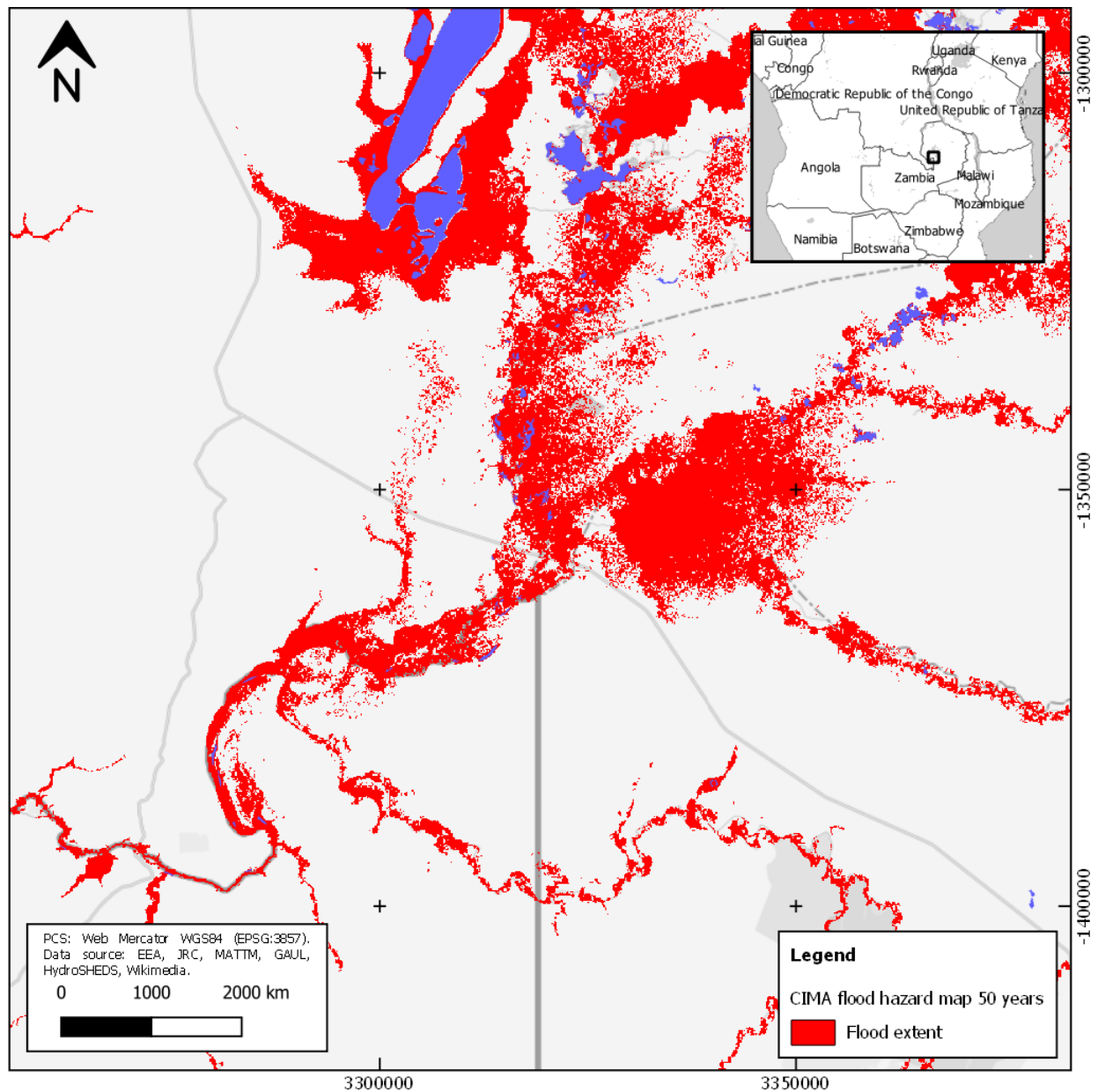


Figure 85 – Flood scenario 50 years Return Period derived from REFLEX in Northern Zambia near Lakes Kampolombo and Kangwena.

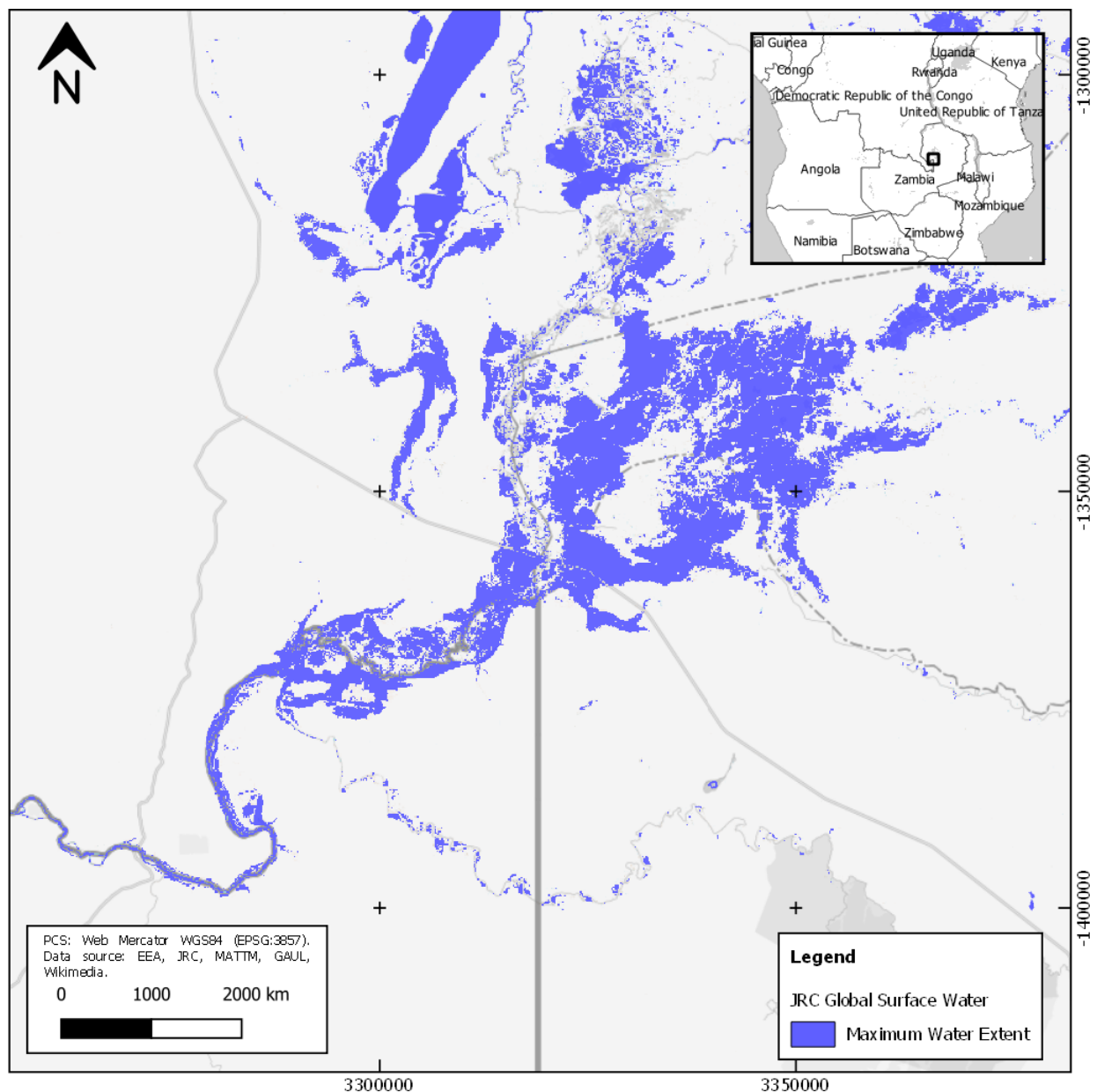


Figure 86 – Maximum Water Extent (1984-2020) from the Global Surface Water dataset (Pekel et al., 2016) in Northern Zambia near Lakes Kampilombo and Kangwena. This satellite-based water extent is derived from 37 years of Landsat observations (Source: EC JRC/Google).

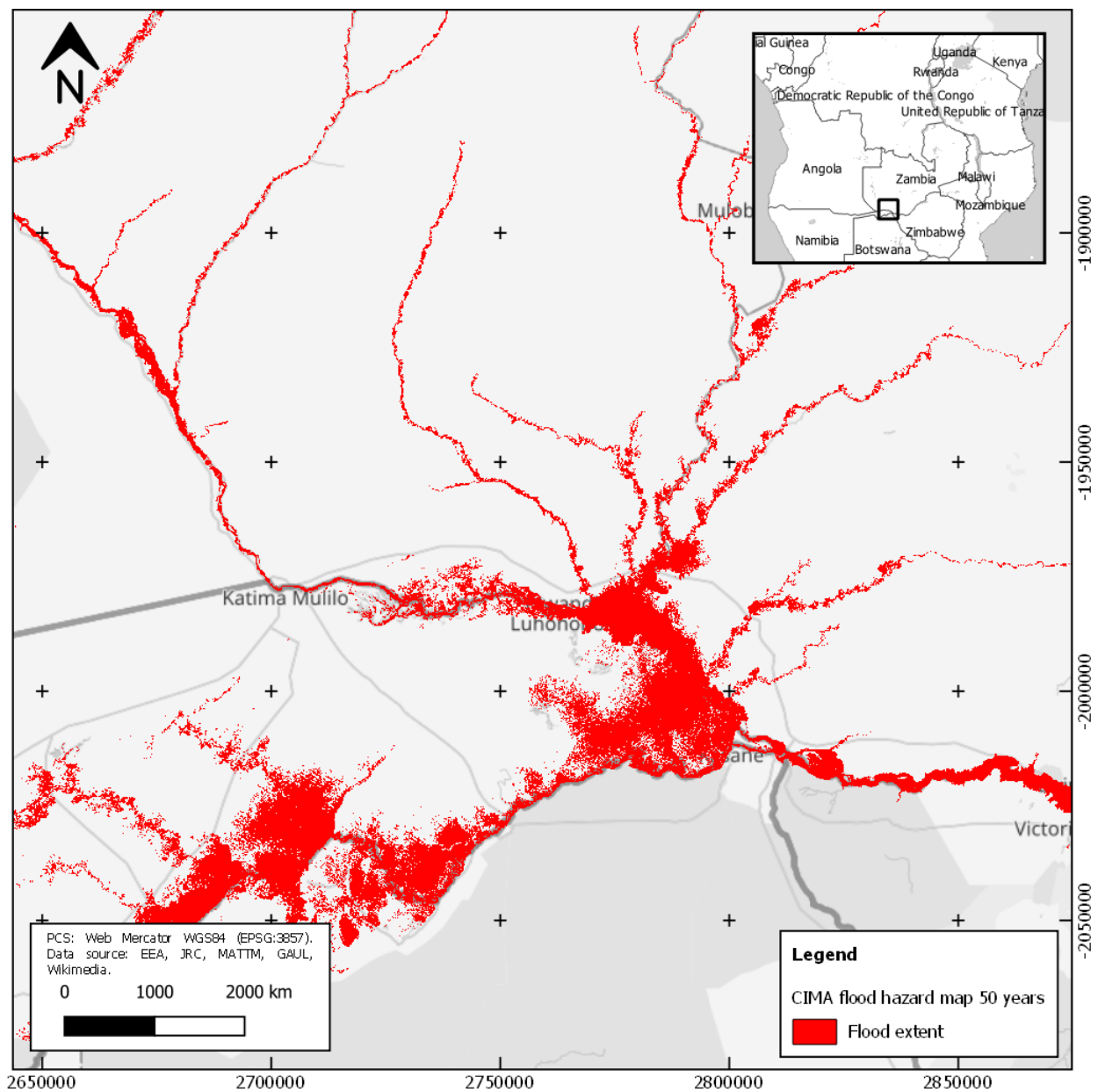


Figure 87 – Flood scenario 50 years Return Period derived from REFLEX in the south-west of Zambia along the Zambezi River in the Caprivi region near Katima Mulilo.

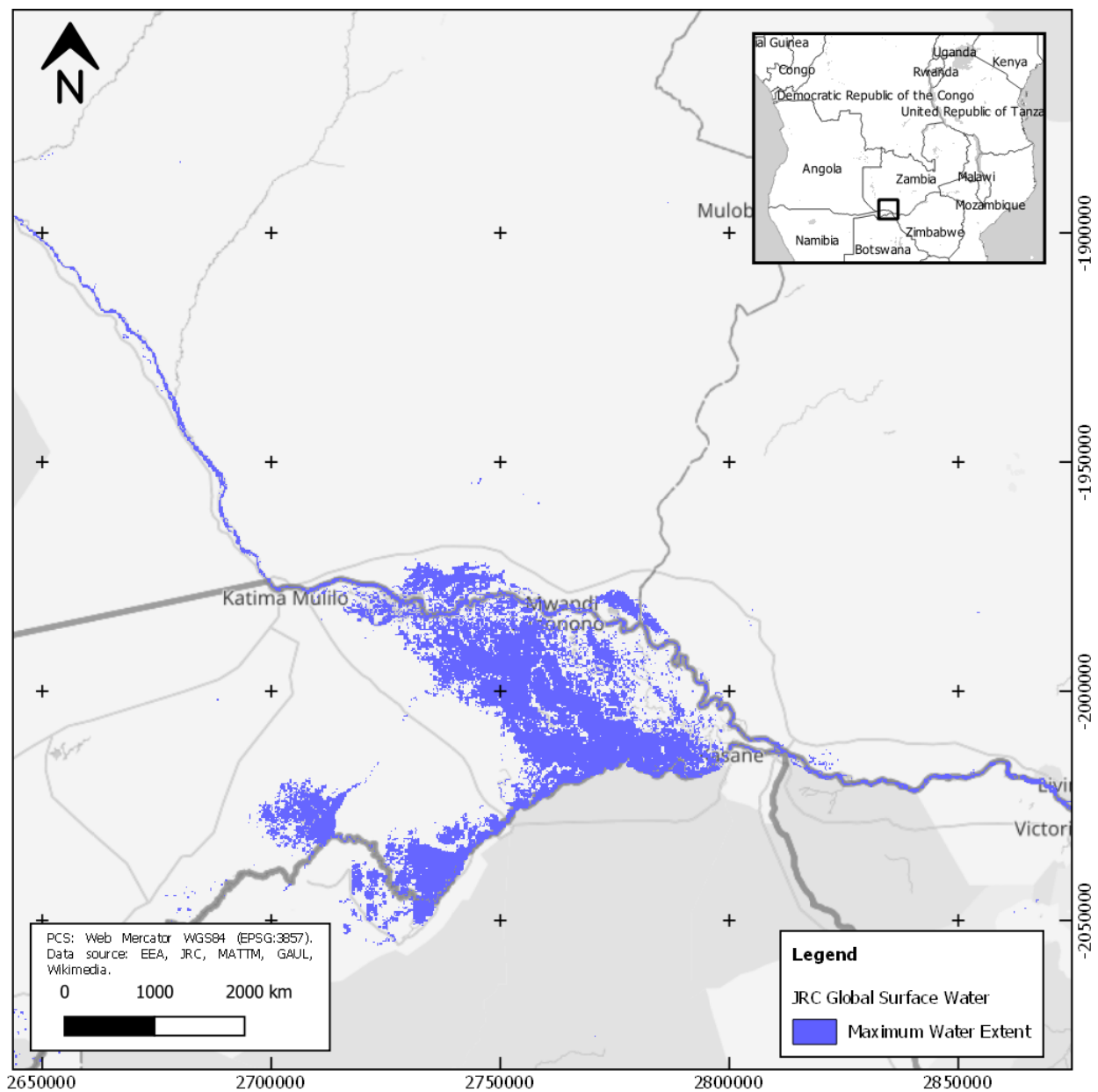


Figure 88 – Maximum Water Extent (1984-2020) from the Global Surface Water dataset (Pekel et al., 2016) in the southwest of Zambia along the Zambezi River in the Caprivi region near Katima Mulilo. This satellite-based water extent is derived from 37 years of Landsat observations (Source: EC JRC/Google).

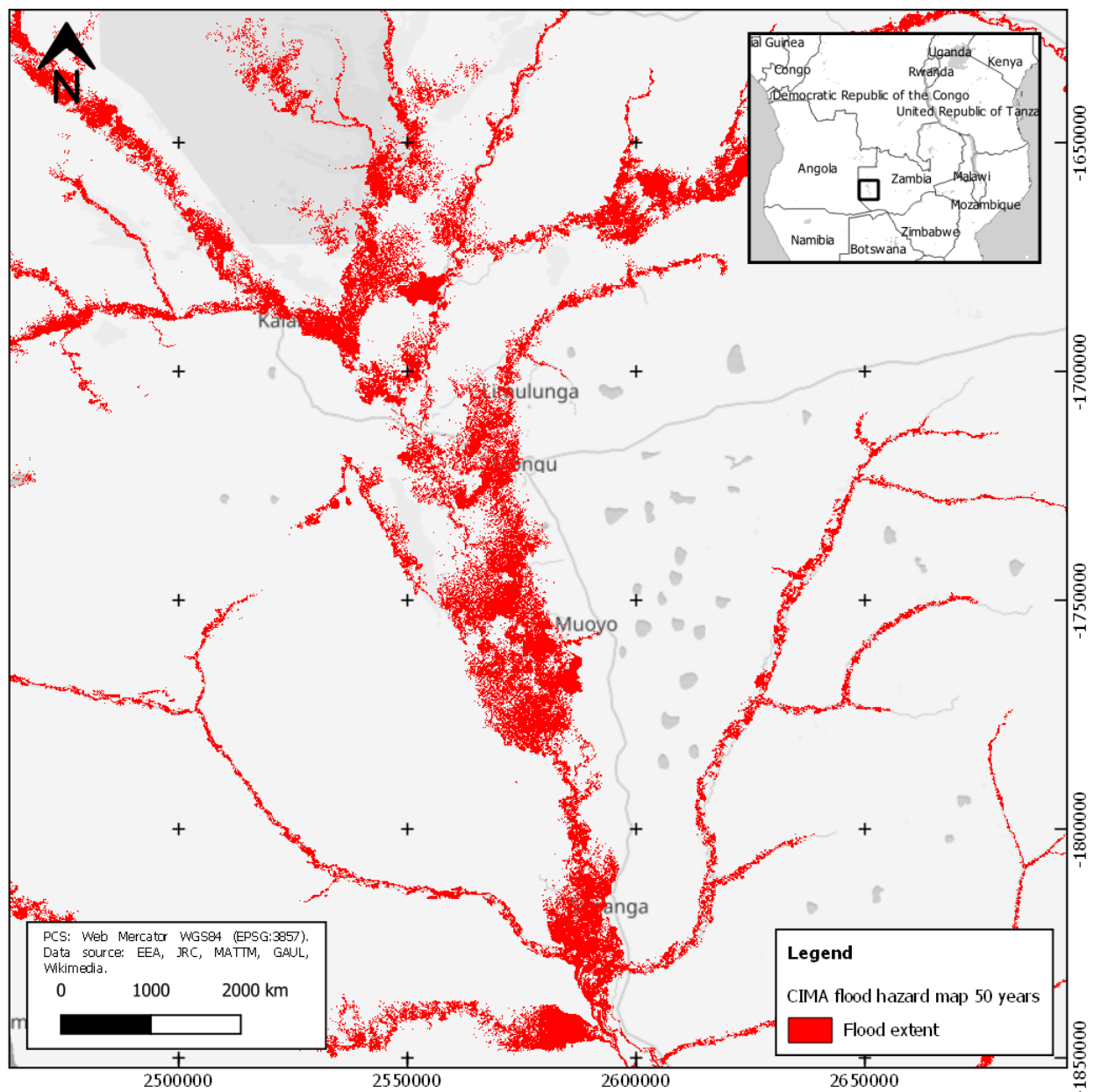


Figure 89 – Flood scenario 50 years Return Period derived from REFLEX in western Zambia along the Zambezi river in the Mongu region.

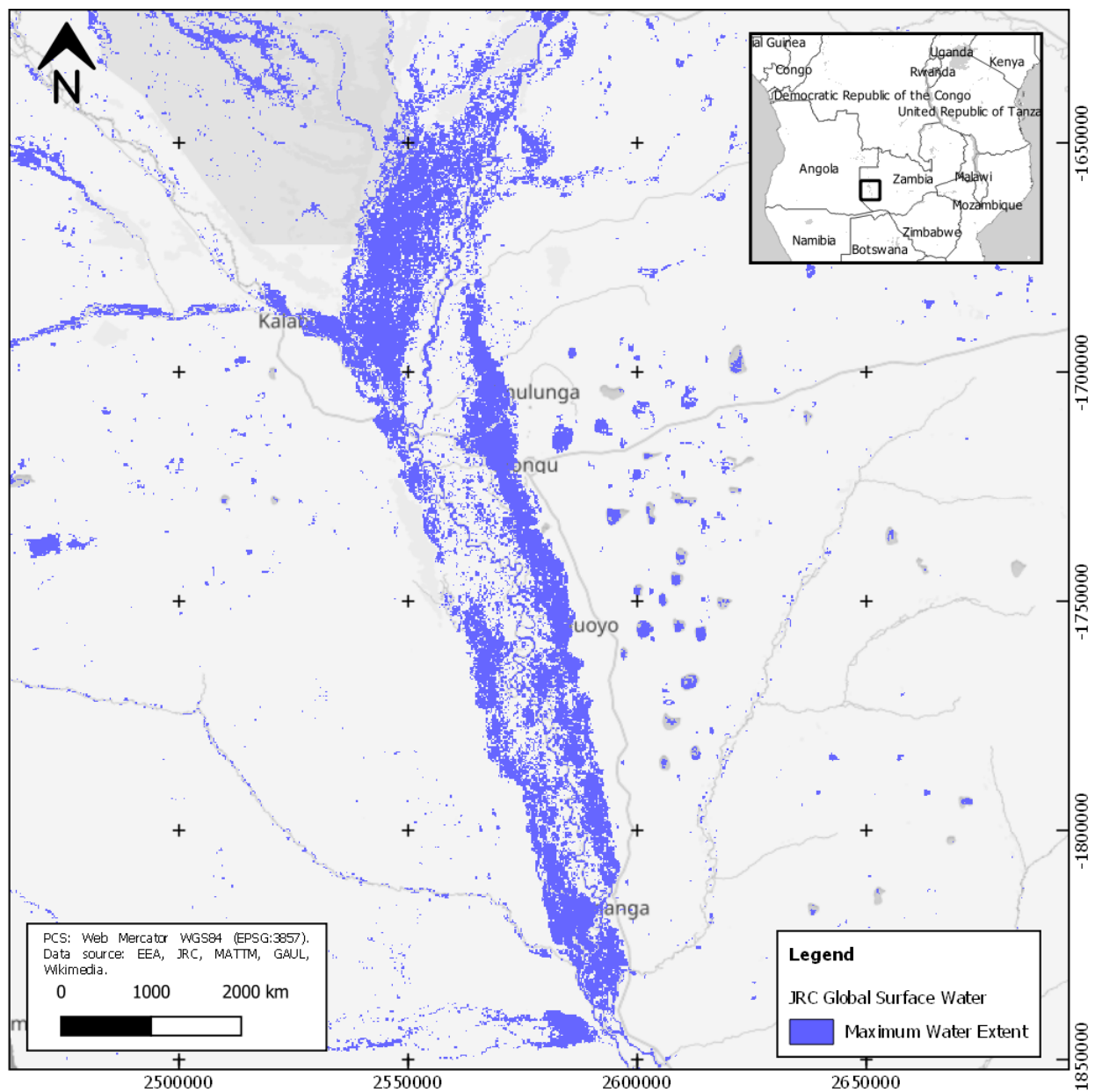


Figure 90 – Maximum Water Extent (1984-2020) from the Global Surface Water dataset (Pekel et al., 2016) in western Zambia along the Zambezi river in the Mongu region. This satellite-based water extent is derived from 37 years of Landsat observations (Source: EC JRC/Google).

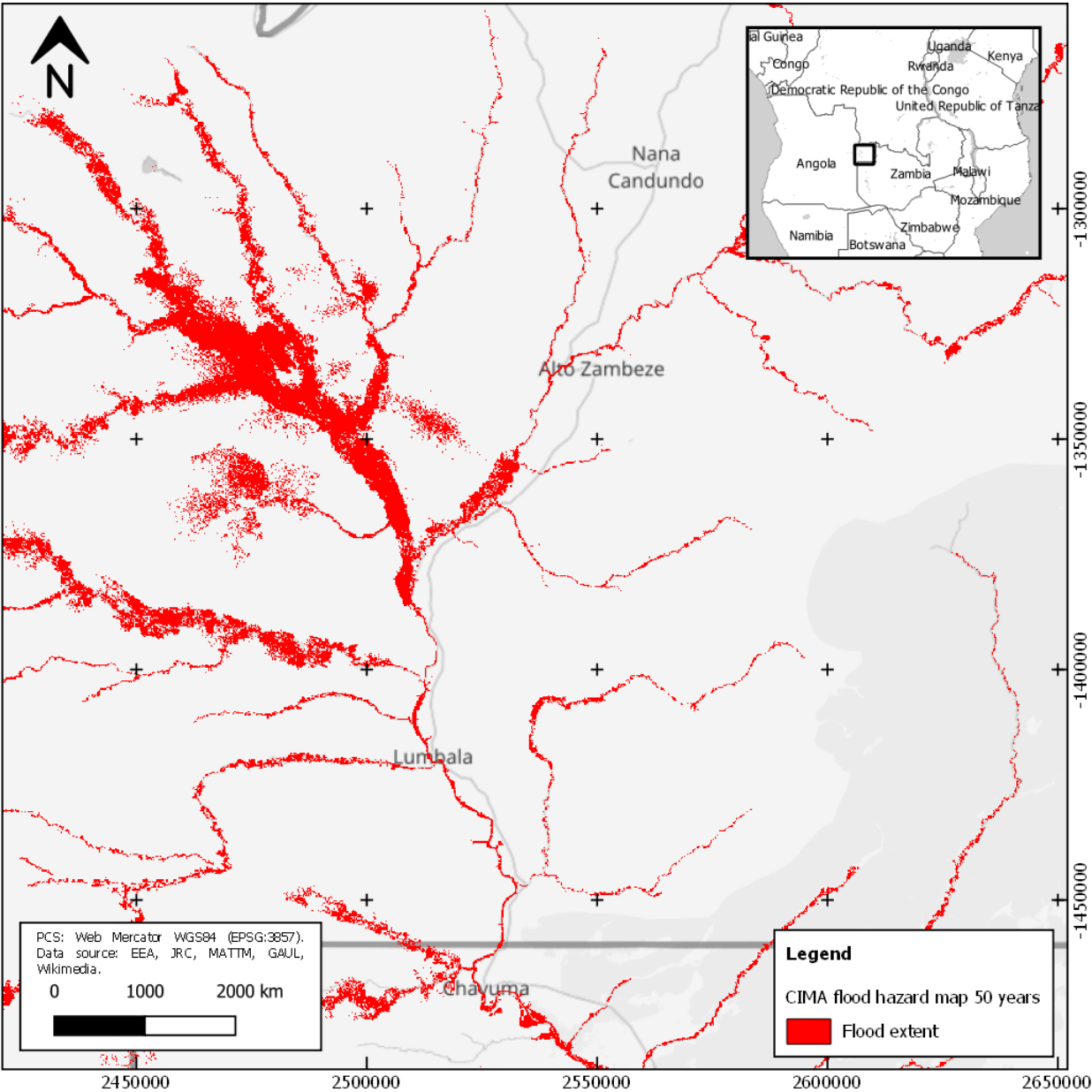


Figure 91 – Flood scenario 50 years Return Period derived from REFLEX in eastern Angola and north-west of Zambia in the Higher Zambezi.

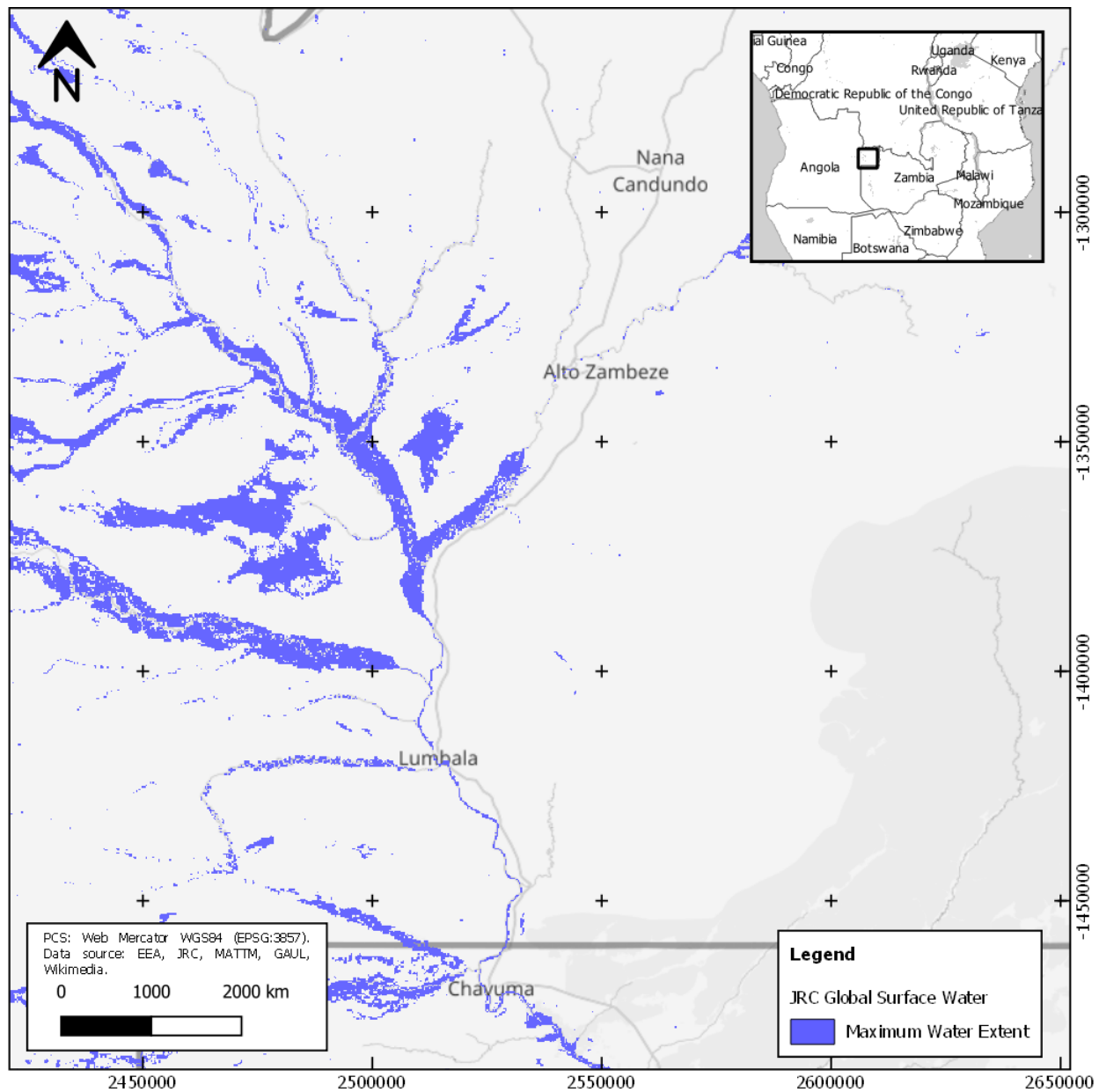


Figure 92 – Maximum Water Extent (1984-2020) from the Global Surface Water dataset (Pekel et al., 2016) in eastern Angola and north-west of Zambia in the Higher Zambezi. This satellite-based water extent is derived from 37 years of Landsat observations (Source: EC JRC/Google).

3.6.5 Discussion

The results obtained in this fourth case study illustrate a sample application of REFLEX at a large scale. Due to the hydro geomorphological nature of this model, the model developed in this Ph.D. research allows an extensive application of the method over multiple African basins without the definition of hydraulic boundary conditions and with a limited effort in terms of input data preparation.

A preliminary visual assessment of flood extent at 50-year return period to the Maximum Water Extent of the GSW dataset (Pekel et al., 2016) has shown a good overall agreement across multiple floodplains. The Maximum Water Extent is derived from JRC's Water Occurrence of satellite-detected water observed over 37 years (1984-2020) of observations from multiple Landsat missions (JRC, 2021). This reference is here employed to visually assess the performance of the REFLEX flood hazard maps due to the absence of a reference at this scale and for the same 50-year flood magnitude.

The first obtained results are showing good quality analysis in terms of floodwater delineation across the basin, however, further validation work is needed to better assess REFLEX model accuracy. This can be accomplished by comparing predicted and reference flood extent using local flood hazard maps over critical portions of the region or by employing SAR or optical satellite-based assessment of multiple historical events of the same magnitude.

Finally, it is worth highlighting that limitations in these flood hazard maps may be locally encountered due to poor calibration of modeled discharge values caused by the scarcity of streamflow observations from gauges.

3.7 Earth Observation data integration case studies

As collateral research, this Ph.D. has also investigated the exploitation of different types of Earth observation (EO) data to establish additional links with the REFLEX modeling chain.

This section includes preliminary results obtained in the estimation of water extent and surface height by using Copernicus's Sentinel-1 and Sentinel-3 data. Furthermore, the potential employment of this auxiliary data in this flood modeling method is presented.

3.7.1 An approach to detect water level from satellite altimetry

The second current major research activity consists of a hydrological application of a remote sensing technique to detect the height of large inland rivers by using information from satellite altimeter.

Over the last few years, radar altimetry data have been employed across different hydrological applications and the benefit of this Remote Sensing technique is becoming crucial over poor in situ data to derive critical information economically and sustainably.

In this case study, an application of a remote sensing technique is presented for height detection of large inland rivers by using Satellite SAR Altimetry data. This work is aimed at evaluating the use of the satellite altimeter to enable systematic ingestion of satellite-based river level estimations into hydrological modeling over poorly gauged river basins. An expected advantage of using such an approach is to better evaluate hydrological modeling outputs along the river network to improve the modeling of the discharge.

3.7.1.1 Case study description

The study area consists of the Chari river basin in the southern part of Chad. In this area, the Chari and the Logone rivers drain their surface waters to a confluence near the capital, N'Djamena, before reaching lake Chad (see Figure 93).

In this context, the benefits of exploiting satellite altimetry data for flood inundation purposes have been already demonstrated in previous studies through a combination of both gauge and radar altimetry data (Birkett, 2000; Crétau and Birkett, 2006). As an example, Coe and Birkett in 2005 have demonstrated that it is possible to predict river discharge at N'Djamena 10 days in advance by extracting water level estimations from altimetry data in the upstream part of the basin along Chari and Ouham rivers (Coe and Birkett, 2005).

Since 2015 UNITAR-UNOSAT and CIMA Foundation have been working together to support flood awareness and flood forecasting capacity in this portion of the country for humanitarian assistance purposes. For this scope, an integrated flood forecasting routine ('Flood Finder Chad') has been developed from these organizations to monitor the most vulnerable areas along the Chari and Logone rivers. The Flood Finder Chad modeling chain is essentially composed of a hydrological routine and a dedicated 1D flood model, which can cover the most vulnerable areas along the two rivers.

During 2016 and 2017 flood monitoring campaigns modeled discharges have been calibrated by using in situ river level measurements. However, in-situ data are often unavailable or available with limitations in acquisition frequency and spatial coverage. In this context and to increase the number of river level estimations along the Chari and Logone rivers, an extraction of height estimations by radar altimetry is investigated in this case study. Later, a validation of the obtained altimetry-based water level is performed through a comparison with gauge records collected in the field.

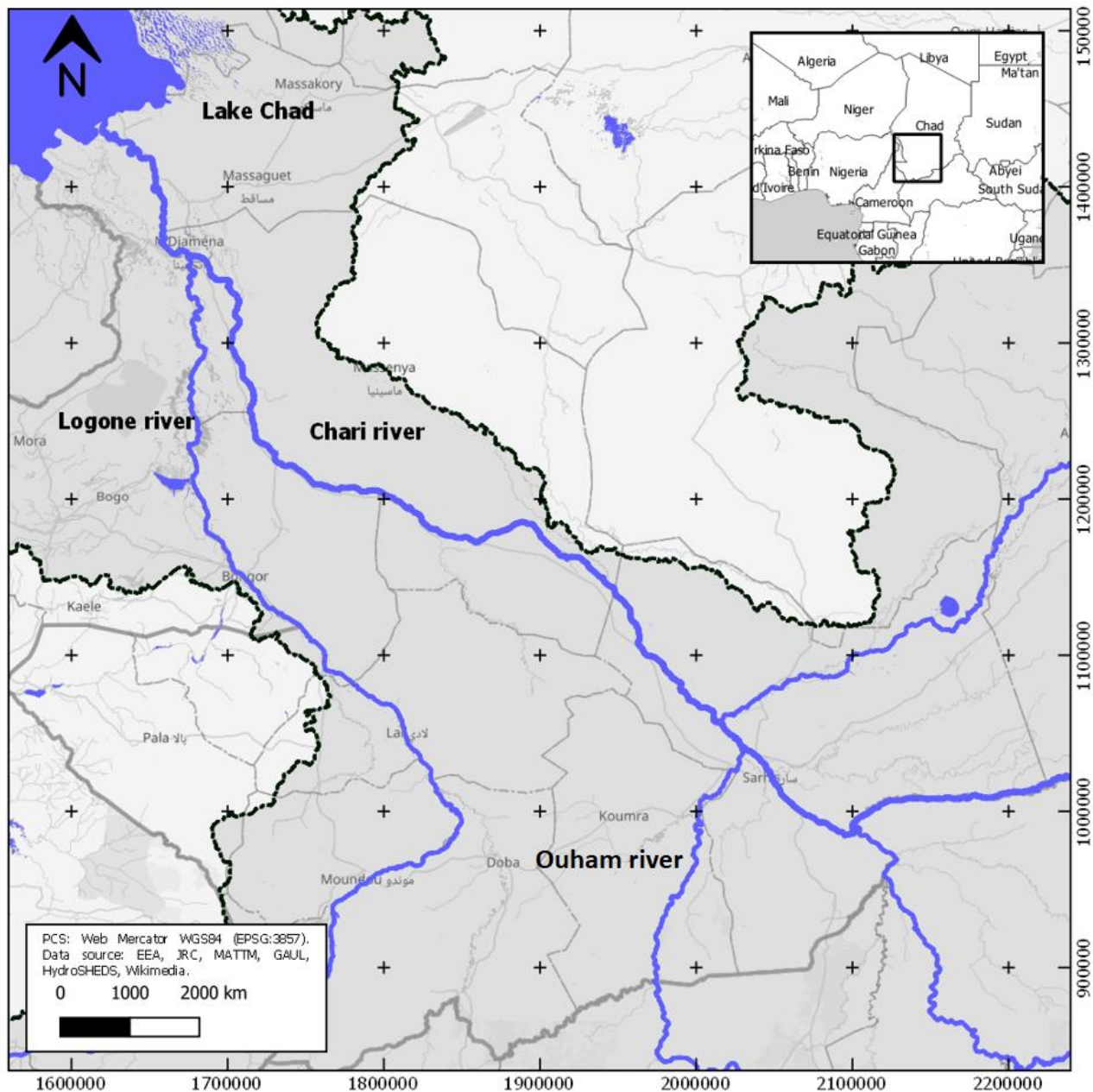


Figure 93 - The portion of the Chad basin in Southern Chad along the Logone and the Chari rivers investigated in this radar altimetry case study.

3.7.1.2 Input data

The first essential input for this research is field observation of water level to be used as a reference for the satellite-based estimation of water surface height. Water level records along the Chari and Logone rivers employed in this case study are the ones collected at multiple gauging stations and provided by the “Ministère de l’Eau et de l’Assainissement du Tchad”. This collection of water level field observations covers the 2016 and 2017 seasons, and it has been shared by UNOSAT for this research. Gauge records are available at the following gauging stations: N’Djamena, Bongor, Lai, Sarh, and Moundou (Figure 94).

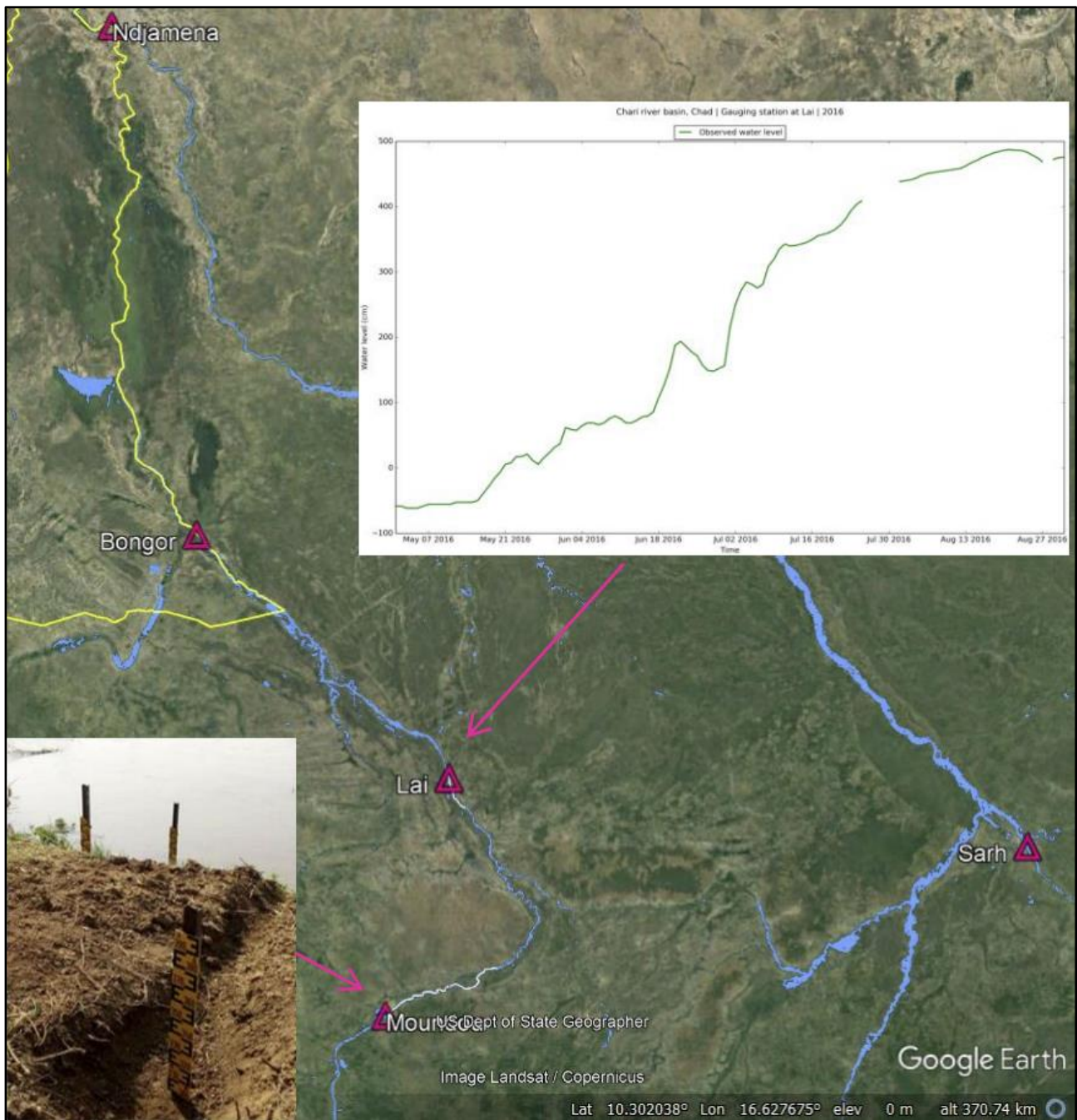


Figure 94 - Map of gauging station including an example of instrumentation and collected water level time series (Credits: Ministry of Environment, Water, and Fisheries Chad, Google).

After the collection of field data, the second necessary input dataset is composed of the retrieval of Copernicus Sentinel-3 altimetry products acquired in the basin over the same period 2016-2017.

This is accomplished starting from the identification, based on Sentinel-3A ground tracks, of “virtual stations” along the rivers. A virtual station is a representative point identified from the intersection between the satellite nominal track and the river centerline. Multiple virtual stations may be resulted by intersecting all Sentinel-3 tracks with the basin streamlines. In this case study, it has been considered only the virtual stations located near one of the five existing gauging stations. This data collection approach resulted in the creation of a collection of Sentinel-3 SRAL L1A data products in SAR mode (high-resolution) to be processed over only these targets.

3.7.1.3 Modeling

After the collection of all necessary inputs, the on-demand exploitation of Sentinel-3 SRAL L1A data products over the selected virtual stations is then achieved using the SARvatore for Sentinel-3 web processing service, provided within ESA's G-POD (Grid-Processing On-Demand) distributed computing platform (ESA, 2021b). The employment of the *SAR Versatile Altimetric Toolkit for Ocean Research and Exploitation - SARvatore* processor allowed the obtaining of Sentinel-3 SRAL L2 products at an 80Hz posting rate at each virtual station.

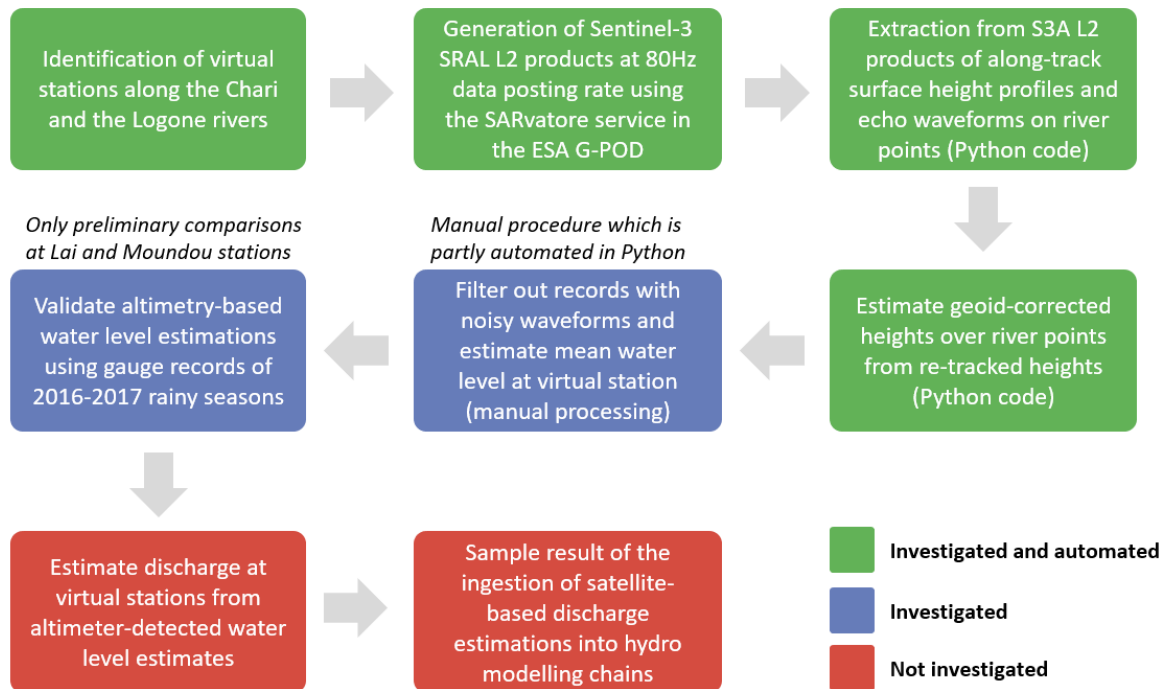


Figure 95 - The identified workflow to derive water level estimation from Sentinel-3 radar altimeter

Thanks to the SARvatore for Sentinel-3 software in G-POD, several S3 L2 products near the selected virtual stations for 2017 and 2016 have been obtained. Such L2 products have been then used to extract power echoes waveforms and along-track surface height profiles. After that, a semi-automated evaluation procedure of Altimeter SAR echoes has been developed in Python to derive consistent water surface elevation for the entire river and to avoid the inclusion of “polluted” estimations.

To do that, a python code has been developed to automatically read all obtained Sentinel-3 L2 products, extrapolate required information (e.g., Orbit, Range, Power Waveforms plots and statistics, etc.), and compute the height of water surface relative to EGM2008 geoid. This tool has allowed a coherent pre-processing of all the Sentinel-3 SRAL L1A data products retrieved over the two seasons in a virtual environment (ESA RSS Cloud Toolbox).

After that, a manual procedure has been adopted to filter noisy waveforms by visual inspection and to compute the absolute height of water surface height at virtual stations near Lai and Moundou stations. At this stage of development, a quick and dirty densification method based on water level slope has been used to interpolate the spatial distribution of S3A altimeter observations along the river. However linear regression methods should be explored. In principle, most of these manual steps should be automatized.

Finally, a first qualitative validation of altimetry-based water level has been performed by comparing satellite-based estimates to the river stage records from Logone and Chari gauges acquired during the 2016 and 2017 rainy seasons.

3.7.1.4 Results

Obtained satellite-based water surface height derived from the Sentinel-3 altimeter for Logone and Chari rivers have been compared with water levels observed in the 2016 and 2017 seasons.

In the satellite-based river stage estimation, heights of water surface are related to the EGM2008 geoid. Due to the lack of knowledge of the gauge height of zero flow, it has been considered as a reference minimum of surface heights on water points derived from the altimeter.

The resulting relative water level time series obtained at Lai station is shown in Figure 96.

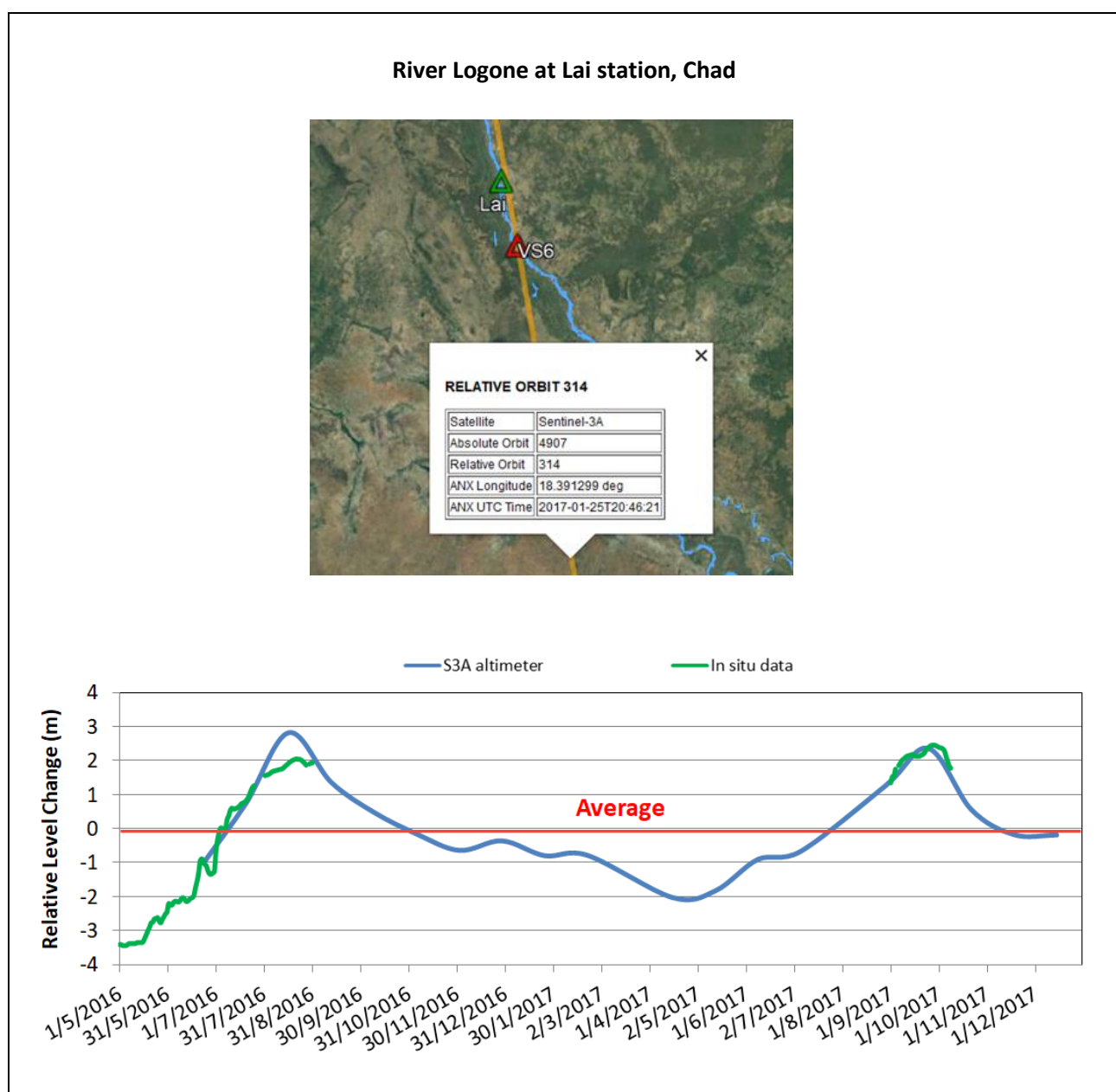


Figure 96 - Preliminary results about the validation of altimetry-based water estimations at Lai gauge, Logone River, Chad. Contains modified Copernicus sentinel-3 data (2016, 2017) accessed via the ESA G-POD. (Credits: ESA, Google).

The same results are also obtained for the Moundou station, as shown in Figure 97.

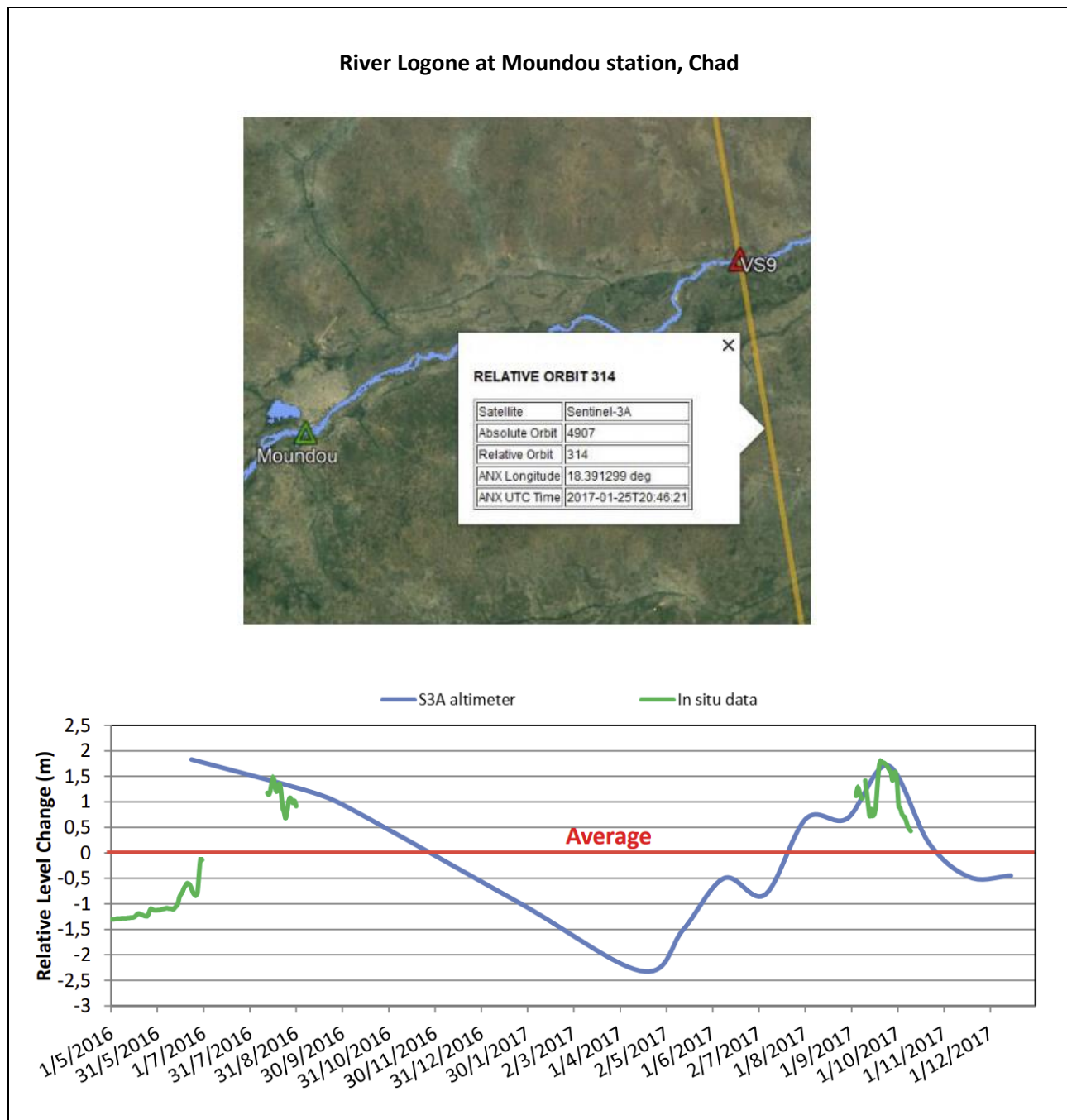


Figure 97 - Preliminary results about the validation of altimetry-based water estimations at Moundou gauge, Logone River, Chad. Contains modified Copernicus sentinel-3 data (2016, 2017) accessed via the ESA G-POD (Credits: ESA, Google).

3.7.1.5 Discussion

Despite these promising preliminary results about surface height comparisons at Lai and Moundou, further quantitative analysis (e.g., the performance of surface height measurement accuracy) is required.

In this case study, the exploitation of Sentinel-3 satellite altimetry data is not ideal due to the North-South extension of the Chad river basin. This orientation of the basin causes, in fact, a not-dense spatial distribution of virtual stations in the catchment. As a result, Se3A virtual stations are quite far from gauges Ndjamen, Moundou, and Logone.

Sarh gauges located nearby confluences, and are close enough to stream gauges only in few virtual stations (Lai and Moundou).

Furthermore, the intrinsic limitations of this EO data source also need to be considered. The Sentinel-3A revisit time of 27 days does not allow a detailed representation of water level evolution across the season. Also, in this case study, the first part of the 2016 season has not been evaluated because the S3 SRAL L1 products are available only since June 2016. Furthermore, it is still unknown what is a good bias to be added to the surface height measured by satellite to allow a direct comparison to the in-situ one.

Also, other limitations encountered in this analysis were due to the nature of water level records observed at gauges. These time series, in fact, are acquired with different frequencies in time and are not able to continuously represent water level across the entire season. Furthermore, this field data has not been fully exploited due to a lack of knowledge about the gage height of zero flow and control cross-section. As a result, only a comparison of a relative, and not absolute, level change has been possible while comparing water levels from altimetry and field observations.

The results obtained in this case study sets the ground for future work in this domain. However, further work is needed to obtain rating curves at gauges and convert satellite-derived water levels into discharge (assuming changes to the rating curves are small). In this processing, it may be useful to explore the use of different methods for densification such as linear regressions methods available in the literature.

Future research may also assess the assimilation of satellite-derived discharges to better calibrate hydrological models (e.g., CIMA's Continuum). In this case study, a hydrological routine may be employed to estimate again 2016-2017 modeled discharges (see Figure 98) and then to compare the results with the one released by UNITAR-UNOSAT within the 2016 and 2017 flood bulletins (UNOSAT, 2017).

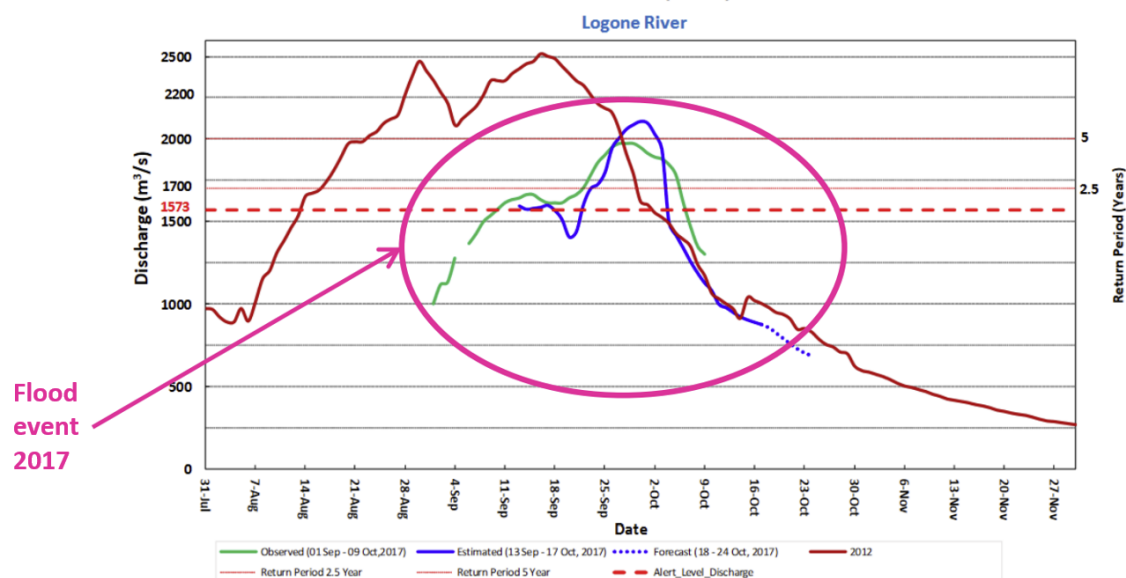


Figure 98 – Observed, estimated, and forecast discharge values at Lai station for 2017 in the Logone river (Credits: UNOSAT).

However, for this ambitious scope, the exploitation of other radar altimetry missions is foreseen to increase the amount of satellite-based water surface heights. In this regard, Sentinel-3 B data shall be also considered to further expand this analysis due to a better location of relative virtual stations across the basin (see Figure

99). As an example, by looking at Sentinel-3B ground tracks, new virtual stations may be located near Bongor Ndjameña gauges. Furthermore, the S3A virtual station downstream the station at Moundou can be complemented with two additional virtual stations upstream. This configuration near the Moundou stream gauge facilitates the validation of radar altimetry data and allows crossover analysis between ascending and descending passes.

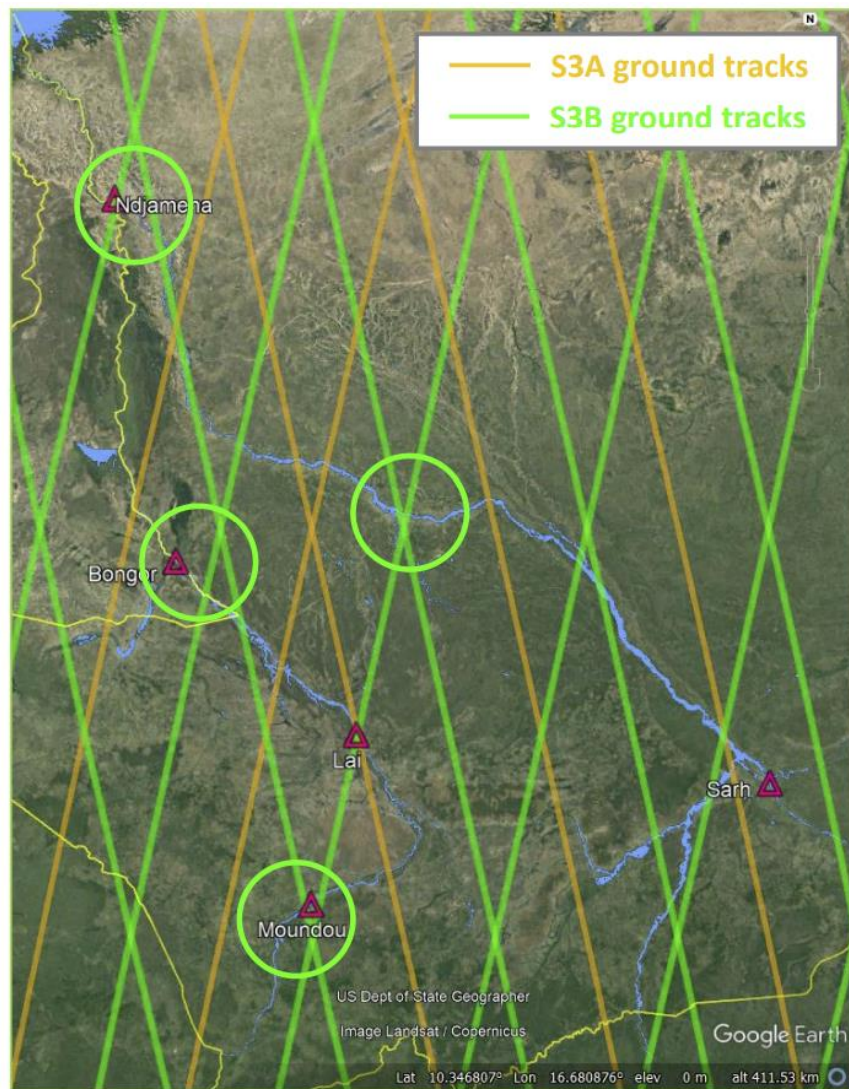


Figure 99 - Stream gauges, Sentinel-3 A and B ground tracks, and the identification of additional virtual stations, highlighted with circles in green, for the Chari and Logone river basins (Credits: ESA, Google).

Also, the water level estimations from the Sentinel-3 mission can be complemented by using the measurements from other radar altimeters, such as the ones from the Jason-3 mission. Having more is necessary to complement field observations and enhance hydrological modeling in the region.

3.7.2 HAND maps to reduce false alarms in SAR-based unsupervised flood mapping

Satellite images from both optical and SAR imagery are key assets to map inland waters. Thus, this EO data is widely employed to monitor disasters (e.g., International Charter Space Major Disaster, UNOSAT, Copernicus EMS, etc.). SAR missions are the reference for the satellite-based detection of water from space due to their advantages to detect standing water in all weather conditions.

In this case study, we evaluate the usage of a SAR flood mapping service to derive satellite-detected water extent. The chosen area of interest is located in the province of Khuzestan in Iran (Figure 100).

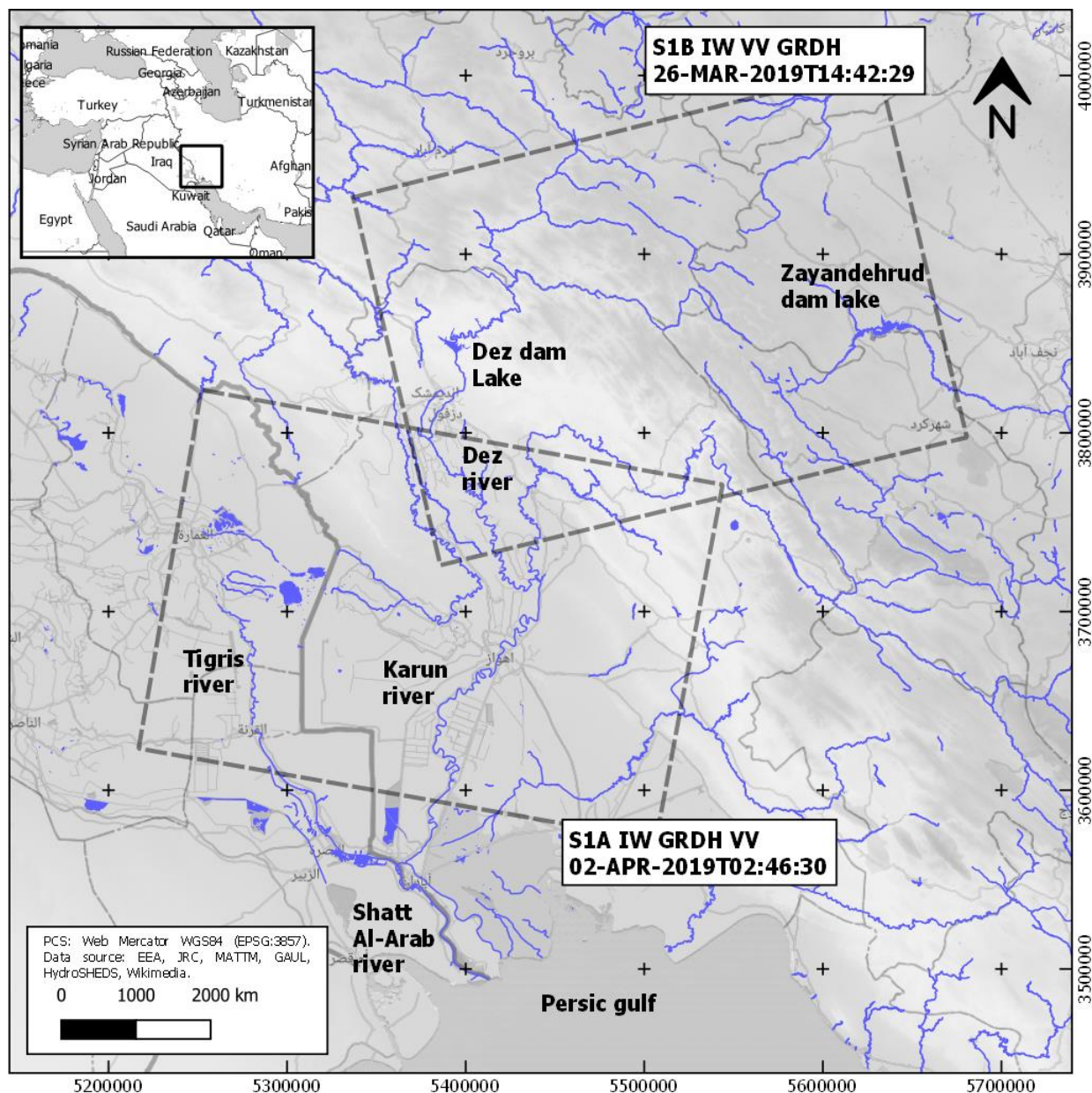


Figure 100 – A portion of the Karun river basin in the Khuzestan province in Iran investigated in this SAR flood mapping case study. Image footprints are also shown of SAR Ground Range Detected data acquired in March and April 2019 from Copernicus Sentinel-1 A and B satellites in Interferometric Wide mode and VV polarization.

In late March 2019, a state of emergency was declared in the South Western of this province which was affected by severe flood events due to heavy rainfall combined with the snow cover melting of the season. Different floodplains in the zones of the Higher and Lower Karun river basin were affected.

3.7.2.1 Input

Input SAR imagery is acquired from the Copernicus Sentinel-1 mission. Details are reported in Table 19.

Zone	Satellite	Product	Mode	Polarization	Acquisition date	Role
Higher Karun river	S1 B	GRDH	IW	VV	14-MAR-2019 T 14:42:29	Pre-event
Higher Karun river	S1 B	GRDH	IW	VV	26-MAR-2019 T14:42:29	Post-event
Lower Karun river	S1 A	GRDH	IW	VV	09-MAR-2019 T 02:46:29	Pre-event
Lower Karun river	S1 A	GRDH	IW	VV	02-APR-2019 T 02:46:30	Post-event

Table 19 - Input satellite imagery employed in this case study

The second input is the Water Occurrence from the GSW dataset (Pekel et al., 2016) derived from 37 years of optical imagery observations from the Landsat mission. The GSW Water Occurrence dataset indicates where surface water occurred between 1984 and 2020 (JRC, 2021).

3.7.2.2 Flood mapping

To obtain satellite-based water observations from Copernicus's Sentinel-1 data over this area, the HSBA change detection algorithm (Chini et al., 2017) available within the LIST's HASARD service in the ESA G-POD processing on-demand platform (ESA, 2021b) has been used. HASARD Flood map in the Higher Karun river basin from S1B SAR GRD data acquired on the 26th of March 2019 is reported in Figure 101

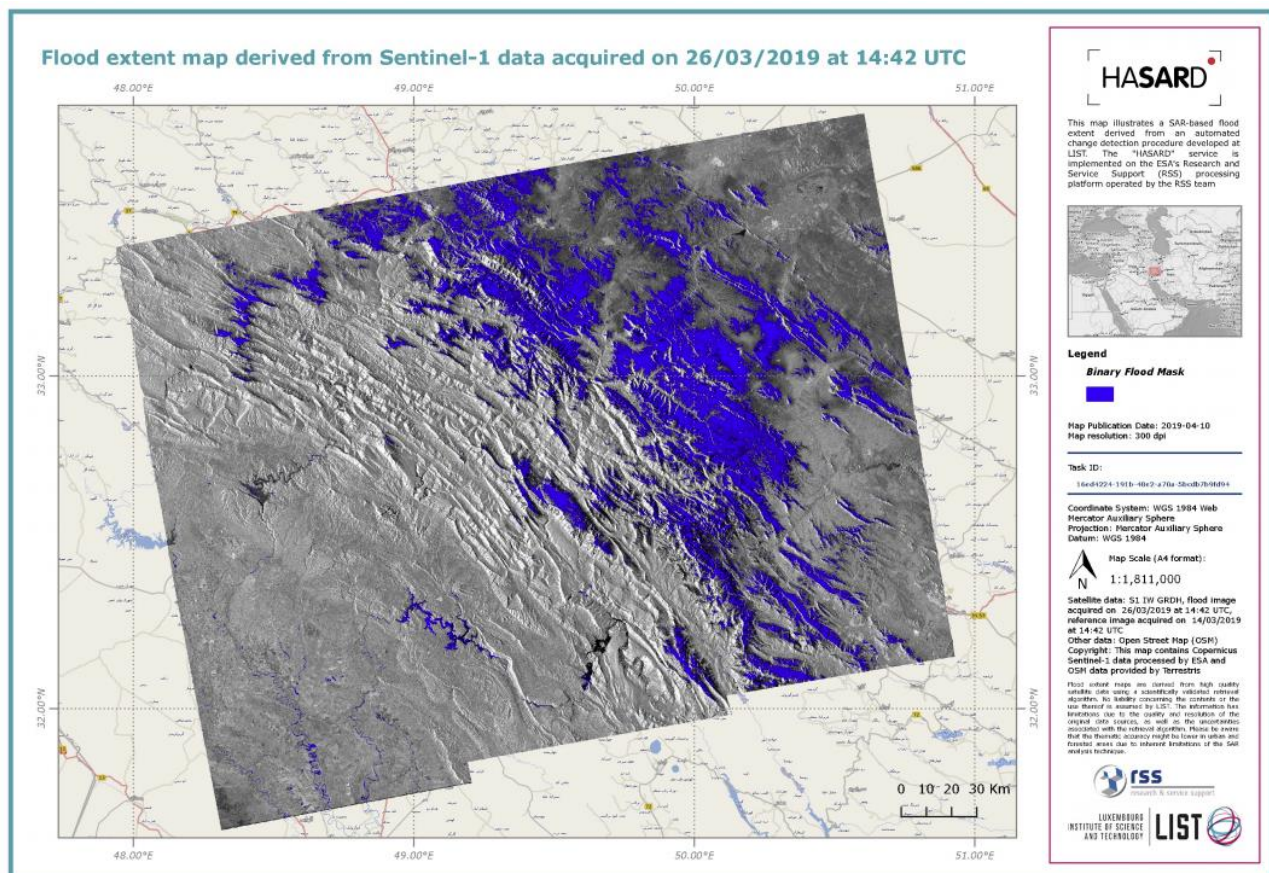


Figure 101 - HASARD flood map from Copernicus Sentinel-1B data acquired on 26 March 2019 over the southwest of the Khuzestan province, Iran. Contains modified Copernicus Sentinel-1 data (2019) accessed and processed in ESA G-POD (Credits: ESA, LIST).

Concerning the lower part of the Karun river basin, the Flood map for 2nd of April 2019 in Figure 102, derived again with the HASARD for Sentinel-1 service in G-POD, from S1A SAR GRD data, shows satellite-based flood-affected areas.

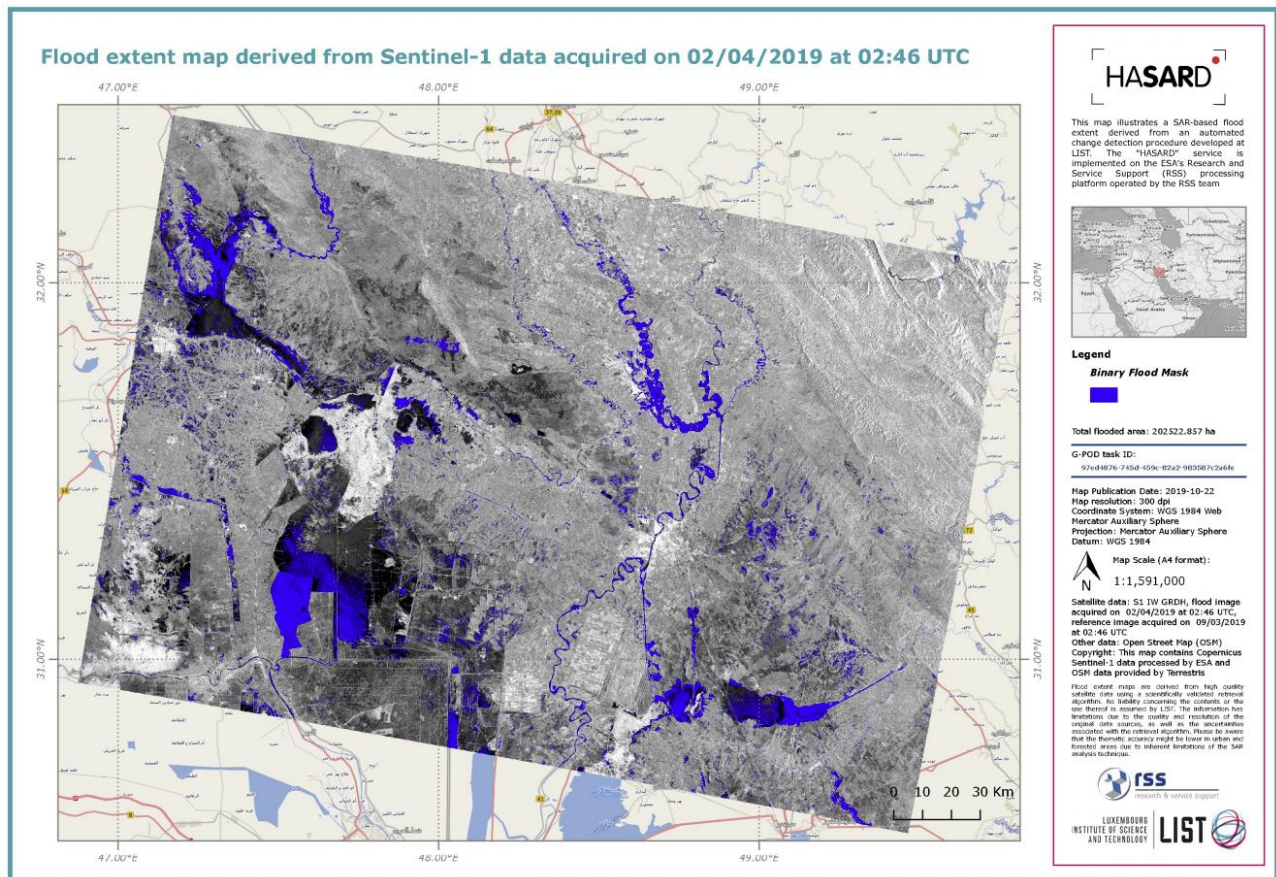


Figure 102 - HASARD flood map from Copernicus Sentinel-1 A data acquired on 2 April 2019 over the southwest of the Khuzestan province in Iran. Contains modified Copernicus Sentinel-1 data (2019) accessed and processed in ESA G-POD (Credits: ESA, LIST).

Binary flood masks are shown in blue in both these maps which highlights standing water along the higher and lower Karun river basin.

3.7.2.3 Results

A qualitative comparison between SAR-based flood estimates with the water occurrence (1984-2020) and the JRC's GSW dataset has been firstly done in the Sentinel-1 acquisitions in the lower Karun river (Figure 102). The binary flood mask from the HASARD service is shown in purple in Figure 103.

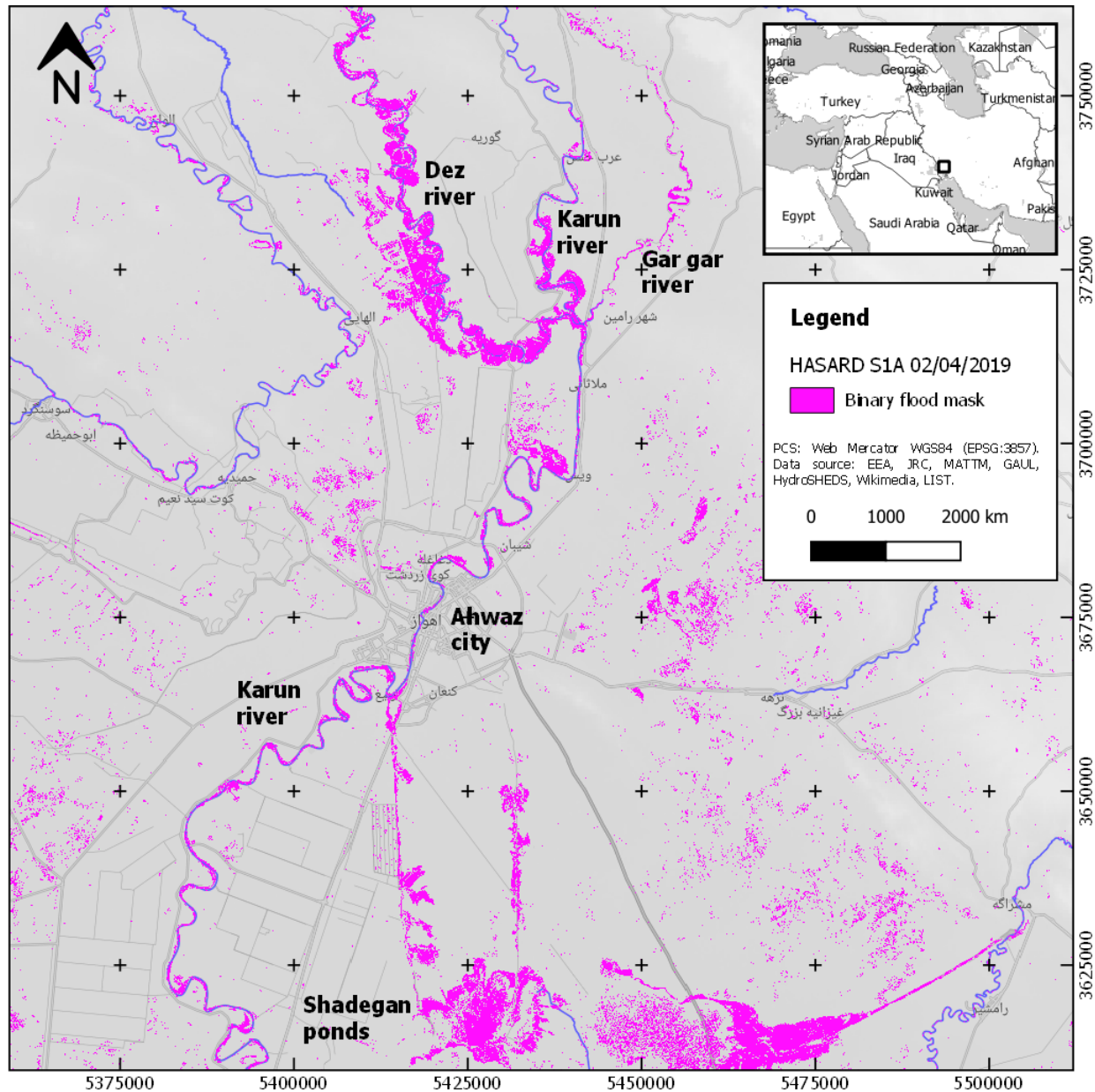


Figure 103 - HASARD Flood binary mask from Sentinel-1 data for the 2nd of April 2019 in the lower Karun river basin in Iran.

Permanent water surfaces with 100% occurrence appear in blue while not permanent waters with values minor than 100% occurrence (e.g., floods) are shown in graded colors from purple to white. The comparison of these sources of information allows a better interpretation of the event that occurred in April 2019. Floodwaters derived from HASARD along the Dez river before the junction with the Karun river are significant. However few areas along the lower Dez river have been classified as water in the 37 years of observations from the Landsat missions. This highlights a low occurrence of this event at the beginning of April over the Dez river. These first analyses are crucial in the post-assessment of the flood event because allow to focus the attention on singular events of interest across the basin and interpret the magnitude of the flooding through more in-depth studies on the area.

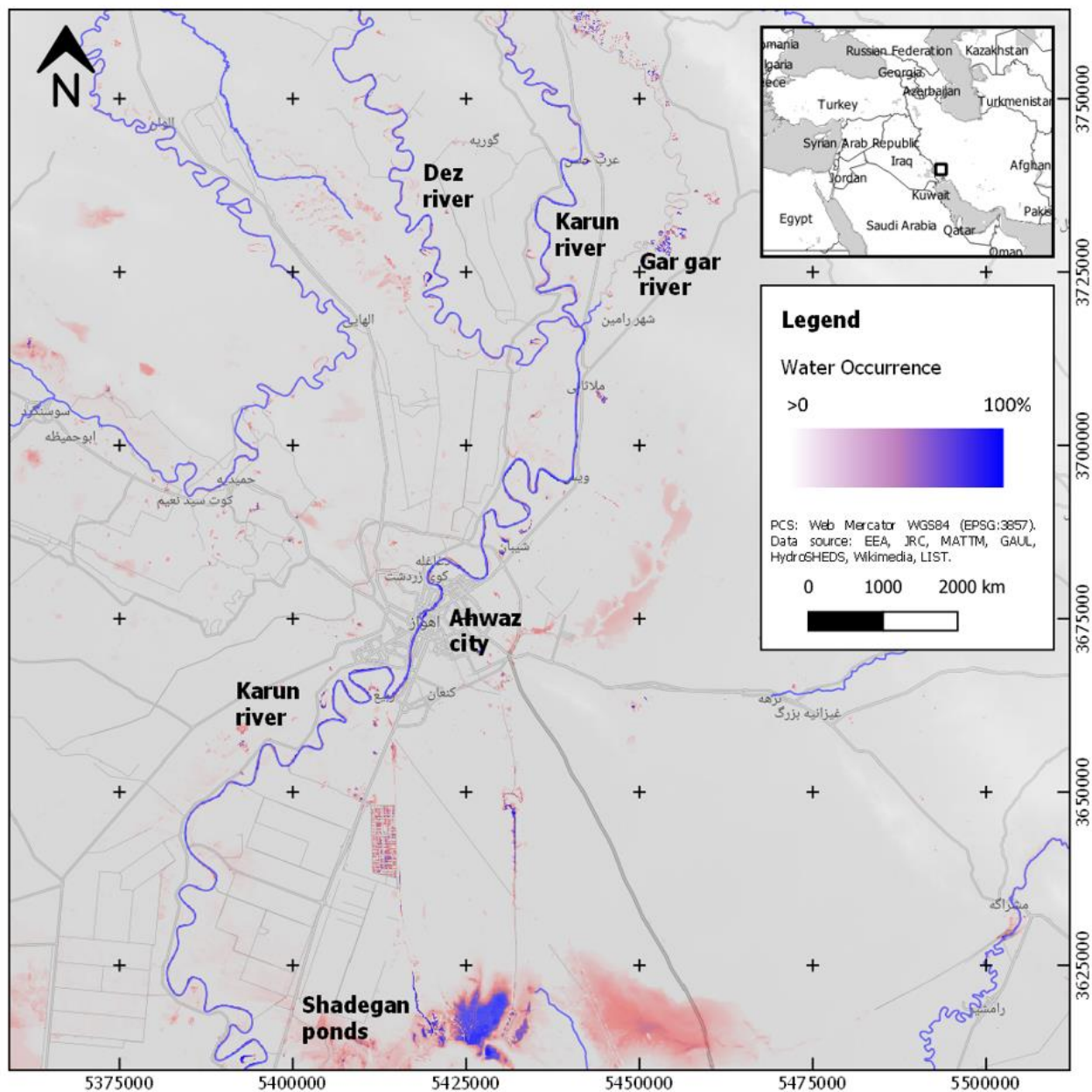


Figure 104 - Water Occurrence (1984-2020) from the Global Surface Water dataset (Pekel et al., 2016) over the lower Karun river basin in Iran. This satellite-based water extent is derived from 37 years of Landsat observations (Source: EC JRC/Google).

HASARD flood binary masks have also been analyzed in the higher Karun river basin. As shown in Figure 101, apart from the small flooding in the valley downstream of the Dez dam lake, most of the areas which are mapped as flood are located near the mountains. In these zones, false alarms are present due to the interpretation of radar backscatter from ground snow coverage which has been wrongly interpreted as water by the HSBA algorithm. Therefore, false alarms due to snow coverage need to be removed from this Sentinel-1 record before employing it in further analysis. To reduce the false positive on HASARD maps due to snow coverage in this region, the HAND model has been used. For this purpose, multiple HAND maps at 90m derived from the *MERIT Hydro* dataset (Yamazaki et al., 2019) have been extracted over this area. The thresholding of relative vertical distances with HAND minor than 10 m from the nearest drainage allowed to quickly classify potential floodplains over the entire Sentinel-1 scene. This classification has been then used to filter out false positives from the HASARD flood binary mask and maintain only the pixel classified as water from Sentinel-1. The result of before and after the HAND-based filtering of the SAR flood mapping output is shown in Figure 105. This provides evidence for the post-processing of these records to reduce false alarms.

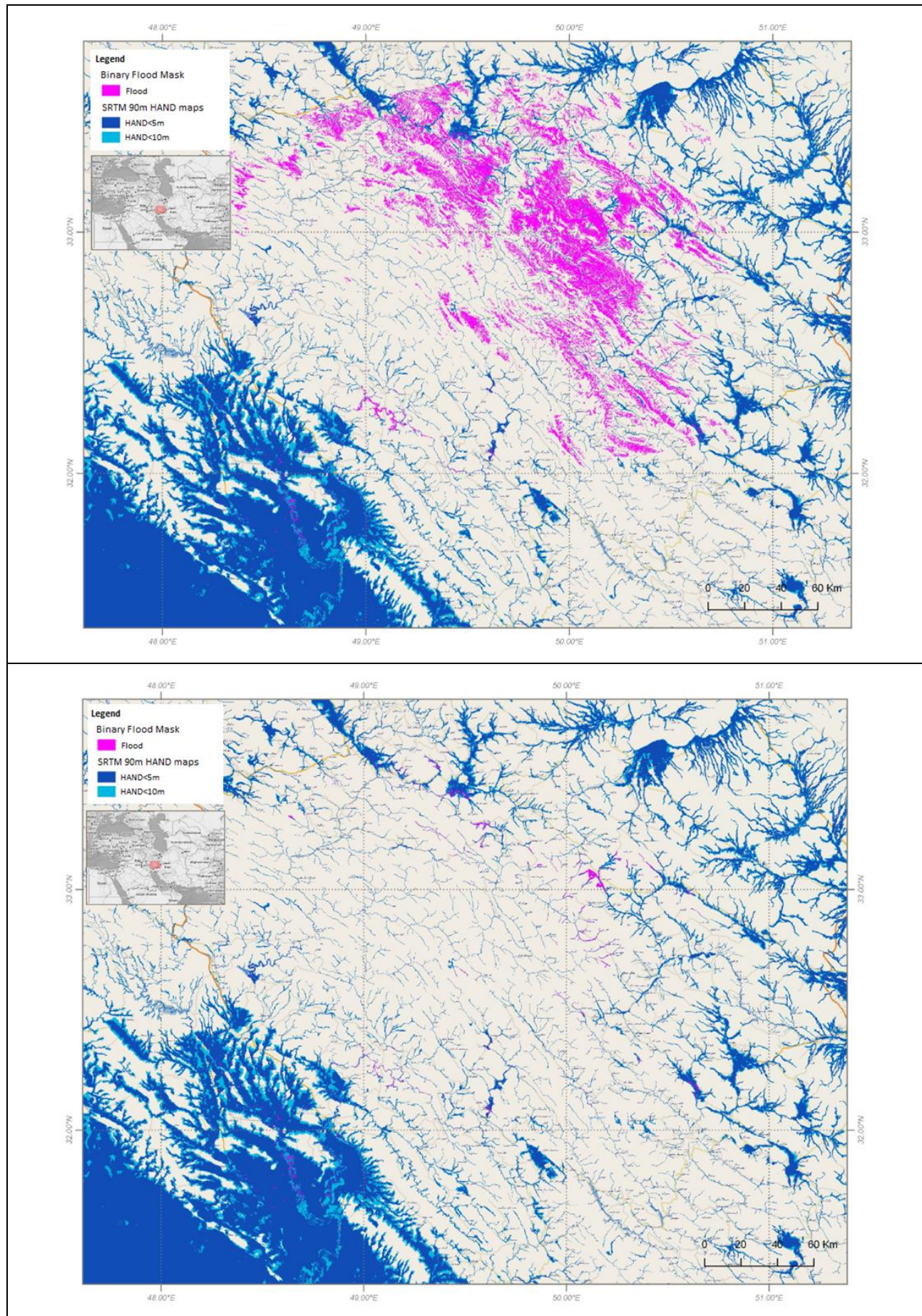


Figure 105 – Before (top) and after (bottom) the HAND-based filtering of HASARD flood binary mask with HAND from MERIT Hydro.

3.7.3 Discussion

This case study highlighted the potential of the LIST's HASARD flood mapping service to obtain on-demand SAR-based flood maps via a web platform within an area of the world. Obtained flood maps from HASARD can be used to collect flood records in areas not previously monitored and to enrich existing flood record repositories.

A collection of satellite-based flood records is crucial for the calibration and validation of flood models. Thus, HASARD SAR-based flood inundation extents may be used in future research to further validate existing or future REFLEX case studies. This satellite-based validation will be particularly useful over a scarce data environment such as the one investigated in the Southern Africa case study.

The preliminary analysis shown in this case study has also highlighted the potential in enhancing some limitations of the HSBA SAR-based flood detection algorithm (Chini et al., 2017) implemented into the HASARD service. It has been proven that the integration of SRTM-based HAND maps before/after the flood detection algorithm can remove some of the false alarms of this flood mapping service existing over land (e.g., snow coverage).

In this framework, the REFLEX modeling chain can be partially linked with the HASARD service to derive on the fly HAND maps from the D-infinity model using streamlines derived from the conditioned DEM. However, if streams are derived from an unsupervised extraction from the DEM, a post-processing of this hydrological derivative may be considered to remove some unrepresentative branches by extracting a permanent water mask from the GSW dataset (Pekel et al., 2016).

Conclusions

Low complexity flood models represent a new frontier in large-scale flood modeling. This is evident while considering the recent advances in hardware resources and cloud computing, the maturity of multiple open geospatial and hydrological software as well as the availability of a wide range of freely available terrain elevation at medium and high resolution. This trend is demonstrated by the number of hydro geomorphological models recently published in the literature (Verdin et al., 2016; Afshari et al., 2017; Liu et al., 2018; Zheng et al., 2018b; Johnson et al., 2019; Manfreda and Samela, 2019) which denotes the degree of innovation of this topic (Hocini et al., 2020).

An in-depth review of the state of the art of flood modeling performed in this thesis highlighted some of the limitations of existing numerical models. Traditional 1D/2D hydraulic models are still not suitable for flood modeling at medium-large scales. Despite the recent computation boost due to the enabling of GPU processing (Crossley et al., 2010) in some commercial software, 2D hydraulic models still require a significant modeling effort for extensive uses over multiple river basins. Moreover, the implementation of such models demands a high number of initial water heights and inflow boundary conditions which are not easy to determine in data-scarce environments. This explains the importance of low complexity flood models and why multiple of these models are still currently under development.

The review of this category of flood models has shown both their huge potential but also some limits.

Those currently available in the literature do not often satisfy some of the basic principles of fluid mechanics. Some of them are not able to simulate flood wave propagation (Manfreda and Samela, 2019). In others, the employment of shallow water equations depends on the arbitrary placement of single (Verdin et al., 2016) or multiple (Follum et al., 2017) cross-sections per stream, or synthetic rate curves derived from an a-priori segmentation of the river (Zheng et al., 2018a), with intrinsic limitations in coastal zones due to infinitely thin cross-sectional areas.

Similar limitations have been encountered also in the research and development activities carried out by institutions that employed similar approaches in operational chains for rapid estimation of extreme events and large-scale flood hazard modeling (see e.g., Arcorace et al., 2015, 2016; Herold and Rudari, 2013).

The outcomes from these studies as well as the review of the state of the art highlighted that there is still room for improvement in low complexity flood modeling chains, particularly for flood hazard mapping and early warning applications. In this context, new methodologies of low complexity flood modeling chains need to be developed by also considering the modeling connections between hydrological and hydraulic models. For this purpose, a novel low complexity flood model, named *Rapid Estimation of Flood EXtent – REFLEX*, has been proposed in this Ph.D. thesis as a robust and slim low tool to be used in operational hydro-modeling chains for applications at different scales (Arcorace et al., 2019).

REFLEX is a 2D hydro-morphological model which combines the advantages of geomorphological models with the ones of traditional hydraulic modeling. Its geomorphological nature allows in fact to sensitively reduce the computation time required for the flood modeling of an entire river basin. In addition to that, four simple hydraulic considerations are introduced in the method to ensure a simplified steady flow computation of flooding in open channels.

Firstly, assuming that input discharge is properly assigned in the river network (e.g., from stream gauges or a hydrological model), the choice in the REFLEX flood modeling of using the surface runoff volume to fill Height Above the Nearest Drainage contours (Nobre et al., 2015) allows fulfilling the conservation of mass at nodes. This volume-driven approach also reduces the propagation of error since it does not rely on a derived quantity, such as the river water stage, to simulate floods but directly on the input discharge. Therefore, scale effects in modeled water depth and extent are expected to be reduced at nodes, as shown in REFLEX flood modeling results in the Ligurian case studies.

Secondly, the introduction of Manning's equation (Manning R., 1891) allows a fast estimation of the transit time, coherently with flood wave propagation across all river branches, which is crucial in the estimation of the inundation flood volume in each sub-basin. Instead, in case the time integration of the input flood hydrograph is done by using the time of concentration (e.g., the longest runoff traveling time to the basin outlet), a general overestimation in water extent is foreseen over the entire basin. As demonstrated in detail in the Magra and Entella case studies (see sections 3.3 and 3.4 in Chapter 3), the travel time is a simple and reliable quantity to encounter the effect of flood wave propagation in low complexity flood models, particularly in short river branches having limited water storage capacity. This highlights the potential in flood modeling of the REFLEX's iterative runoff volume optimization based on simplified Manning's formula.

Thirdly, in REFLEX the backwater effect in a generic river branch is simulated by deriving HAND from the DEM also outside the sub-basin boundaries. Elevation data is extracted within a mask obtained by merging the watershed of a generic river branch with the ones from its tributaries identified from the Pfafstetter stream hierarchy (Pfafstetter, 1989). As a result, terrain elevations from upstream areas (e.g., in the six upstream watersheds) are considered as hillslope cells of the inlet channel pixel of the generic branch. This allows a static filling of water upstream, which is driven by the water depth of the branch and by the DEM slope of upstream areas. This simple estimation of the backwater effect has been particularly useful in the flood modeling of flat areas in large river basins such as the one encountered in the REFLEX case study in the Southern African countries.

Last but not the least, another innovative element is the artificial expansion of HAND contours across the divide into neighbor watersheds. Such expansion allows REFLEX to overcome the typical "water wall" effects along the divides that often happen in the lower parts of watersheds having shapes like a long bottom of a funnel. This GIS-based method based on both the a priori hydraulic head loss and the Euclidean distance from the stream has been proven useful in the flood modeling near the coast, as widely demonstrated in the Entella coastal floodplain (see section 3.4 in Chapter 3).

These four aspects highlight the principal hydraulic modeling features of this low complexity flood model which aspires to introduce a degree of novelty in the domain of hydro-geomorphology.

After the design of the whole method, a huge effort has been reserved into the development of the REFLEX tool, to harmonize the chain by linking multiple open-source software, to develop the code under modules for facilitating future modifications, and to contain computation time by using parallelized routines (e.g., the D-Infinity drainage algorithm in TauDEM as described in Tarboton, 1997 and Tesfa et al., 2011). In this process, it is worth highlighting that the REFLEX automated chain has been built by relying only on open software to simplify the sharing and the adoption of the method under different contexts.

After the release of a stable repository of the code, the REFLEX model has been applied to multiple case studies under different configurations and parametrizations.

First, the performance of REFLEX has been assessed over well-known river contexts, in different surveyed river basins in northern Italy. The first three case studies investigated the application of REFLEX within the Magra and the Entella river basins, in the Liguria region, and the Secchia river basin, in Emilia Romagna. These three locations have been selected due to the access of multiple discharges and flood hazard maps from detailed hydrological studies as well as very detailed DEM, having high spatial and vertical accuracy.

In the Magra case study, the extent of REFLEX flood maps at multiple return periods, from resampled LiDAR data of the Italian Ministry of the Environment and Protection of Land and Sea, has been validated by using official PGRA flood hazard maps from the Northern Apennine Interregional River Basin Authority. The binary classification over the whole basin has registered moderate values of Kappa and Matthews Correlation coefficients ($K=MCC=0.7$), mostly affected by false negatives in defended floodplains where the Magra river is intersected by multiple secondary tributaries, which are difficult to model with simplified hydraulics. The low percentage of false positives in REFLEX flood maps indicated the precision, or Positive Predictive Value, of the model ($PPV=0.9$). Results obtained from this first case study in the Magra basin also highlighted the advantages of using the D-infinity drainage model and demonstrated the potential in employing the developed DEM conditioning approach which relies on novel slope-based filtering of elevation data.

In the second case study in the Entella river basin, REFLEX has shown an overall better accuracy with respect to the one obtained in the Magra floodplains. Water extent and depth maps at multiple return periods have been validated by using multiple reference flood hazard maps. Obtained results highlighted a strong agreement between predicted and reference flood extents, as demonstrated by the K and MCC values above 0.75 for all return periods. Very good performance in the validation of REFLEX water extent is justified, first, by the effectiveness of the REFLEX coastal expansion which allowed a more realistic flood extent delineation near the sea. Secondly, a better performance can also be explained by the lower complexity of the Entella river network having fewer intersections along the major stem in flat areas.

This case study in the Entella river also allowed the validation of modeled water depths. In the comparison of REFLEX flood depths to the ones of the hazard map produced by the CIMA Research Foundation (see section 3.6 in Chapter 3), the water level differences have shown a satisfactory agreement between REFLEX and TELEMAT-2D (Hervouet, 2000), despite the intrinsic limitation of this hydro-geomorphological model. However, this water depth validation highlighted the limits in assuming the water stage constant along each river branch, which can significantly change along the branch due to local hydrodynamics.

This second case study not only allowed to assess the usage of the artificial coastal expansion in REFLEX with real data, but it also provided further evidence about the usefulness of the Manning-based iterative volume optimization as well as the convergence of this method.

The third REFLEX case study has focused the attention on a flat area of the Po valley along the Secchia river. Obtained results highlighted an intrinsic limit of the REFLEX model which cannot simulate the complex hydrodynamics of local flooding due to levee breaking. Even if this hydro geomorphological model is, in fact, developed for the rapid flood estimation of riverine flooding, such a complex flood scenario has been chosen to evaluate the performance of REFLEX by pushing it also in a scenario out of its scope. Expected outcomes have been helpful to better recognize and confirm the on-paper limitations of this model which are crucial in guiding the usage of this tool for other users.

After the experience acquired over these three case studies, the application of REFLEX has also been extended to data-scarce environments. Further case studies were needed to assess the feasibility of deploying REFLEX also at larger scales for extensive flood hazard mapping across multiple river basins.

Therefore, the method has been applied for a large-scale flood hazard mapping over multiple African Countries in Western and Eastern Africa. Flood hazard maps obtained for Angola, Zambia, and Tanzania demonstrated a valuable and reliable application of REFLEX at a large scale. In such applications, the hydro geomorphological nature of the method developed in this Ph.D. allowed an extensive application of this flood model with a limited effort in terms of input data preparation and the definition of hydraulic boundary conditions. Despite the calibration limits due to a scarcity of streamflow observations from gauges, a qualitative evaluation of these flood hazard maps obtained from REFLEX has shown a good overall agreement with the water extent records observed from 37 years (1984-2020) of Landsat observations across multiple floodplains. A further CAL/VAL work in this REFLEX modeling at a large scale can be extended with additional exploitation of remotely sensed estimations.

In this regard, this Ph.D. research has also proposed additional methods for the pre-processing of REFLEX inputs as well as for gathering additional observations which are particularly useful in situations where no field observations are available. As collateral research, some preliminary analysis has indicated and evaluated multi-source satellite-based methodologies to improve and calibrate/validate REFLEX flood modeling results over data-scarce environments.

The results obtained in the case study in Chad along the Logone and Chari rivers have shown how to estimate river water level estimations from the Sentinel-3 radar altimeter using the ESA's SARvatore processor in G-POD (Dinardo, 2020; ESA 2021b) across multiple locations of this African endorheic basin (see section 3.7.1 in Chapter 3). This preliminary work sets the ground for the following conversion of water surface heights into discharge estimates. Altimetry-based discharge estimations would be extremely useful if combined with existing observations at Lai, Moundou, and N'djamena stream gauges to obtain a more continuous time series of water levels.

Furthermore, the case study of the Karun river basin in southwestern Iran demonstrated the potential of the LIST's HASARD on-demand flood mapping service in G-POD (ESA 2021a) to map inland waters extent. This processor, based on the HSBA SAR-based flood detection algorithm (Chini et al., 2017), allowed to easily derive multiple satellite-detected water extent from Sentinel-1 SAR images over this basin. This case study highlighted how HASARD flood binary masks can be combined with HAND maps and the Water Occurrence from 35-years of Landsat observations (Pekel et al., 2016; JRC, 2021) to reduce false alarms and to better interpret flood records (see section 3.7.2 in Chapter 3). A collection of reliable satellite-based flood estimates is in fact crucial in the calibration and validation of REFLEX, particularly over data-scarce environments.

The lesson learned from these case studies highlighted the pro and cons of the usage of the hydro geomorphological method implemented in this Ph.D. research.

The REFLEX flood model requires few inputs to simulate flooding: the DEM and the surface runoff volumes over pre-defined flow lines. This low complexity flood model is not only a geomorphologic model but also integrates simplified numerical implementation of flow mechanics. The modeling chain is scalable as demonstrated in the successful employment of REFLEX in both local flood hazard applications, using high-resolution LiDAR data, and regional/continental scale flood modeling, using global mid resolution DEM. Also, the modeling of the flood extent is coherent to the given amount of surface runoff volume, and thus it can simulate flood modeled results under different magnitudes of the events, as demonstrated in the flood hazard maps for Magra, Entella, and multiple Southern African countries.

The last implementation of the code is stable and allows the employment of the whole processing chain without supervision under multiple basins with different model parameterizations. Concerning the

performance of this model, REFLEX allows a fast delineation of the flood extent. To have an estimation of REFLEX computation time, 29 minutes have been necessary for a complete REFLEX simulation of the whole Entella basin using a DEM at 5m spatial resolution (7.5k X 3.5k pixels) in a machine with Linux OS (Ubuntu), 8 CPU, and 32 GB of RAM. A similar simulation using a traditional 2D hydraulic model can require many hours of simulation. All these features become significantly important while considering that REFLEX is meant to be employed in regional-scale flood modeling and deployed in a cluster processing environment to allow a scale-up of resources for massive processing. Finally, the REFLEX code is easy to share because it relies only on freely accessible and open-source software.

Concerning the application of REFLEX, this low complexity flood model is particularly useful over a riverine environment given the simplified hydraulics available in the method. Being its morphological nature, REFLEX relies mostly on the DEM. As a result, a better performance of this model has been shown overall while validating REFLEX in hilly topography and by using high-resolution DEMs having high vertical and spatial accuracy (e.g., LiDAR data). Furthermore, the assumption of a constant water stage along each branch of the river represents a limit of this model. In addition to that, this model does not allow to simulate flood overtopping with overflow across multiple watersheds, as seen in the case study in the Secchia river.

Future works after this Ph.D. research may further explore the application over ungauged river basins.

When applying REFLEX in different locations and at different scales, some of the parameters employed in this thesis may be revisited. Future research may provide a fine-tuning of REFLEX coastal expansion parameters through the extensive employment of REFLEX in multiple hydrological regions of the world. Also, in the application of the current DEM conditioning chain over large areas, good quality input flow lines may not be always available. Therefore, in case REFLEX input streamlines are derived from an unsupervised extraction from the DEM, a post-processing of this hydrological derivative may be considered to remove some not representative branches. As an example, the 100% Water Occurrence of the Global Surface Water dataset (Pekel et al., 2016; JRC, 2021) can be used to identify suitable flow accumulation threshold by feature matching with permanent waters or to exclude dry stream branches from the source dataset.

Furthermore, in the application of REFLEX over multiple data-scarce environments, the model validation is often possible only by comparing modeled extents to available flood records derived from EO data. As an example, this is possible by exploiting SAR-based flood inundation extents, which have not been fully employed in the validation work of present case studies. In this domain, SAR missions are a key source of information given their advantages in detecting standing water in all weather conditions. Thus, flood binary masks from the Sentinel-1 mission, like the ones derivable from the LIST's HASARD flood mapping service, can be effectively employed to extend, as an example, available flood records from UNOSAT, or the Dartmouth Flood Observatory.

Preliminary results by using Copernicus's Sentinel-3 radar altimetry data in Chad have shown a potential usage of this data in this flood modeling method, mainly for streamflow calibration purposes. Future research may also assess the assimilation of satellite-derived discharges to better calibrate hydrological models. In the Chadian case study, the Continuum (Silvestro et al., 2013, 2015) hydrological routine may be employed, for example, to estimate again 2016-2017 modeled discharges and successively compare the results with the one released by UNITAR-UNOSAT within the 2016 and 2017 flood bulletins (UNOSAT, 2017). However, for this ambitious scope, the exploitation of also other radar altimetry missions in the Chad basin is foreseen to increase the amount of satellite-based water surface heights (e.g., Sentinel-3 B data due to a better location of relative virtual stations across the basin, Jason-3, etc.). Having more satellite overpasses along the river is necessary to complement field observations and enhance hydrological modeling in the region.

Finally, concerning the status of REFLEX's code, it is also advisable to further enhance the performance of the existing version of the whole chain developed in this Ph.D. This can be carried out by parallelizing some of its steps, such as the REFLEX Module 2, and by doing an advanced optimization of the most time-consuming processes, as the iterative volume optimization routine in the fourth module. Also, it is advisable to develop software portability as well as to ensure a continuous development of each REFLEX module, also from external contributors. Being this chain built on only open source or freely accessible software the REFLEX model is suitable to be shared among the user community via a GIT repository.

Acknowledgments

I wish to thank Luca Dell’Oro and Dr. Einar Bjorgo of UNITAR-UNOSAT, as well as Dr. Roberto Rudari of CIMA Research Foundation. With their passion for this topic, they inspired my research path (SRTM-FM, Flood-FINDER, etc.) since my participation at the Global Flood Partnership, back in 2014.

Then I wish to thank Prof. Giorgio Boni from the University of Genoa and Dr. Simone Gabellani of CIMA for their patience and guidance throughout this Ph.D. work. I am glad to have had them as tutors of this Ph.D. given their wide experience in this domain. They have always been helpful, supportive, and proactive. Also, I would like to thank all the colleagues and friends at CIMA Research Foundation (Francesco Silvestro, Alessandro Masoero, Valerio Basso, Lorenzo Campo, Alessia Matano, Lorenzo Alfieri, Andrea Libertino, and all the others). Without them, this research work would not have been possible. Being part of the CIMA Research Foundation family has been constructive and fun. I enjoyed being part of this collaborative environment within my daily work on this research.

I would also like to thank Dr. Jerome Benveniste of ESA who advised me multiple times with ideas and knowledge in the application of satellite altimetry for inland waters. A big thank also to the whole ESRIN Altimetry team, particularly to Dr. Marco Restano who gave me multiple hints in the usage of the SARVatore processor. I also wish to thank Olivier Senegas of UNOSAT, for helping me to access in situ water level observation in Chad as well as Dr. Stefano Vignudelli of CNR for his assistance in the interpretation of inland water results. A big thank goes to Dr. Marco Chini, Dr. Ramona Pelich, and Dr. Patrick Matgen of LIST for giving me access and support in the usage of the HASARD flood mapping service.

Last but not the least, I would also like to thank Dr. Giancarlo Rivolta Dr. Giovanni Sabatino, and all my former colleagues (Roberto Cuccu, Jose Manuel Delgado Blasco, Massimo Orlandi, and all the others) of ESA Research and Service Support (RSS) who gave me continuous and valuable support in boosting the computing resources of this research with the provision of two Cloud Toolboxes as well as the access to the HASARD and the SARVatore services in G-POD.

Bibliography

- Abileah R.**, Scozzari A., and Vignudelli S. (2017), "Envisat RA-2 Individual Echoes: A Unique Dataset for a Better Understanding of Inland Water Altimetry Potentialities", *Remote Sens.* 2017, 9, 605. DOI: [10.3390/rs9060605](https://doi.org/10.3390/rs9060605).
- AdB Distrettuale Appennino Settentrionale (2021)**, "Pericolosità da alluvione nel Distretto Appennino Settentrionale (PGRA) - dominio fluviale [2839]", Open data, flood hazard maps in Shapefile format. Accessed 05/05/2021 at: <http://www.adbarno.it/opendata/>.
- AdB Magra (2016)**, "Relazione generale variante al Piano Stralcio Assetto Idrogeologico del fiume Magra e del torrente Parmignola", Report, modified with D.C.I. n. 3 of 29/06/2016, Sarzana, Italy. Accessed 05/05/2021 at: http://www.appenninosettentrionale.it/rep/magra/NdA_variante_CI_20160629.pdf.
- Afshari S.**, Ahmad A. Tavakoly A. A., Rajib M.A., Zheng X., Follum M. L., Omranian E., and Fekete B. M. (2017), "Comparison of new generation low-complexity flood inundation mapping tools with a hydrodynamic model", *Journal of Hydrology*, Volume 556, Pages 539-556, ISSN 0022-1694. DOI: [10.1016/j.jhydrol.2017.11.036](https://doi.org/10.1016/j.jhydrol.2017.11.036).
- Albano R.**, Samela C., Crăciun I., Manfreda S., Adamowski J., Sole A., Sivertun A., and Ozunu A. (2020), "A. Large Scale Flood Risk Mapping in Data Scarce Environments: An Application for Romania", *Water* 2020, 12, 1834. DOI: [10.3390/w12061834](https://doi.org/10.3390/w12061834).
- Alfieri L.**, Burek P., Dutra E., Krzeminski B., Muraro D., Thielen J., and Pappenberger F. (2013), "GloFAS – global ensemble streamflow forecasting and flood early warning", *Hydrol. Earth Syst. Sci.*, 17, 1161-1175. DOI: [10.5194/hess-17-1161-2013](https://doi.org/10.5194/hess-17-1161-2013).
- Alfieri L.**, Pappenberger F., and Wetterhall F. (2014a), "The extreme runoff index for flood early warning in Europe", *Natural Hazards and Earth System Sciences*, 14(6), 1505–1515. DOI: [10.5194/nhess-14-1505-2014](https://doi.org/10.5194/nhess-14-1505-2014).
- Alfieri L.**, Salamon P., Bianchi A., Neal J., Bates P., and Feyen L. (2014b), "Advances in pan-European flood hazard mapping", *Hydrol. Process.*, 28: 4067-4077. DOI: [10.1002/hyp.9947](https://doi.org/10.1002/hyp.9947)
- Almeida I. K.**, Almeida A. K., Steffen J. L. et al. (2016), "Model for Estimating the Time of Concentration in Watersheds", *Water Res. Manag.* 30, 4083–4096. DOI: [10.1007/s11269-016-1383-x](https://doi.org/10.1007/s11269-016-1383-x)
- Andreadis K.**, Schumann G., and Pavelsky T. (2013), "A simple global river bankfull width and depth database", *Water Resources Research*. 49. DOI: [10.1002/wrcr.20440](https://doi.org/10.1002/wrcr.20440).
- Arcorace M.**, Dell'Oro L., Piemontese L., Bjorgo E., and Dave R. (2015), "SRTM-FM – A Hydrologically Conditioned SRTM Dataset for Flood Mapping A Case Study over the Zambezi River Basin, Mozambique and Malawi", UNISDR Scientific and Technical Advisory Group (STAG), Online Case Studies: Using Science for DRR, Case Studies 2015, PreventionWeb. Accessed 05/05/2021 at: https://www.preventionweb.net/files/workspace/7935_arcoracezambeziriverbasin.pdf.

- Arcorace M.**, Silvestro F., Rudari R., Boni G., Dell’Oro L., and Bjorgo E. (2016), “Forecast-based Integrated Flood Detection System for Emergency Response and Disaster Risk Reduction (Flood-FINDER)”, Geophysical Research Abstracts, Vol. 18, EGU2016-8770, EGU General Assembly 2016. Accessed 05/05/2021 at: <https://meetingorganizer.copernicus.org/EGU2016/EGU2016-8770.pdf>.
- Arcorace M.**, Masoero A., Gabellani S., Boni G., and Basso V. (2019), “Evaluating a novel 2D hydro-morphological modelling approach for a rapid estimation of flood extent and water depth: the REFLEX model”, Geophysical Research Abstracts EGU General Assembly, 21, 17456. Accessed 05/05/2021 at: <https://meetingorganizer.copernicus.org/EGU2019/EGU2019-17456.pdf>.
- Barnes R.**, Lehman C., and Mulla D. (2014a), “An efficient assignment of drainage direction over flat surfaces in raster digital elevation models”, Computers and Geosciences 62, 128–135, DOI: [10.1016/j.cageo.2013.01.009](https://doi.org/10.1016/j.cageo.2013.01.009).
- Barnes R.**, Lehman C., and Mulla D. (2014b), “Priority-flood: An optimal depression-filling and watershed-labeling algorithm for digital elevation models”, Computers and Geosciences, Volume 62, Pages 117-127, ISSN 0098-3004. DOI: [10.1016/j.cageo.2013.04.024](https://doi.org/10.1016/j.cageo.2013.04.024).
- Barnes R.** (2016), “Parallel priority-flood depression filling for trillion cell digital elevation models on desktops or clusters”, Computers and Geosciences, Volume 96, 2016, Pages 56-68, ISSN 0098-3004. DOI: [10.1016/j.cageo.2016.07.001](https://doi.org/10.1016/j.cageo.2016.07.001).
- Barnes R.**, (2020), “RichDEM Terrain Analysis Software”. Accessed 05/05/2021 at: <http://github.com/r-barnes/richdem>.
- Bates P. D.** and De Roo A. P. J. (2000), “A Simple Raster-Based Model for Flood Inundation Simulation”, Journal of Hydrology. 236. 54-77. DOI: [10.1016/S0022-1694\(00\)00278-X](https://doi.org/10.1016/S0022-1694(00)00278-X).
- Beven K. J.** and Kirkby M. J. (1979), “A physically based, variable contributing area model of basin hydrology”, Hydrological Sciences Journal, 24:1, 43-69, DOI: [10.1080/02626667909491834](https://doi.org/10.1080/02626667909491834).
- Birkett C. M.** (2000), “Synergistic remote sensing of lake Chad: variability of basin inundation”, Remote Sens. Environ., 72, pp. 218-236. DOI: [10.1016/S0034-4257\(99\)00105-4](https://doi.org/10.1016/S0034-4257(99)00105-4)
- Chen C.**, Gao Y., and Li Y. (2019), “A feature-preserving point cloud denoising algorithm for LiDAR-derived DEM construction”, Survey Review, 53:377, 146-157, DOI: [10.1080/00396265.2019.1704562](https://doi.org/10.1080/00396265.2019.1704562).
- Chini M.**, Hostache R., Giustarini L., and Matgen P. (2017), “A Hierarchical Split-Based Approach (HSBA) for automatically mapping flooded areas using SAR images of variable size and resolution”, IEEE Transactions on Geoscience and Remote Sensing, Vol. 55, No. 12, December 2017. DOI: [10.1109/TGRS.2017.2737664](https://doi.org/10.1109/TGRS.2017.2737664).
- Coe M. T.**, and Birkett C. M. (2005), “Water Resources in the Lake Chad Basin: Prediction of river discharge and lake height from satellite radar altimetry”, Water Resour. Res., 40 (10), DOI: [10.1029/2003WR002543](https://doi.org/10.1029/2003WR002543).
- Cohen J.** (1960), “A Coefficient of Agreement for Nominal Scales”, Educational and Psychological Measurement, 20(1), 37-46. DOI: [10.1177/001316446002000104](https://doi.org/10.1177/001316446002000104).

- Costa-Cabral M. C.**, and Burges S. J. (1994), "Digital Elevation Model Networks (DEMON): A model of flow over hillslopes for computation of contributing and dispersal areas", *Water Resources Research*, 30(6), 1681–1692. DOI: [10.1029/93WR03512](https://doi.org/10.1029/93WR03512).
- CRED and UNISDR (2018)**, "Economic Losses, Poverty and Disasters (1998 - 2017)". Accessed 05/05/2021 at: <https://www.undrr.org/publication/economic-losses-poverty-disasters-1998-2017>.
- Crétau J. -F.** and Birkett C.M. (2006), "Lake studies from satellite altimetry", *Comptes Rendus Geoscience*, Volume 338, Issues 14–15, Pages 1098-1112. DOI: [10.1016/j.crte.2006.08.002](https://doi.org/10.1016/j.crte.2006.08.002).
- Crétau J. -F.**, Nielsen K., Frappart F., Papa F., Calmant S., and Benveniste J. (2017), "Hydrological applications of satellite altimetry: Rivers, lakes, man-made reservoirs, inundated areas" In *Satellite Altimetry over Oceans and Land Surfaces*; Stammer D., Cazenave A. Eds.; Earth Observation of Global Changes; CRC Press, FL, USA, 2017; pp. 459–504. DOI: [10.1201/9781315151779](https://doi.org/10.1201/9781315151779).
- Crossley A.**, Lamb R., Waller S., and Dunning P. (2010), "Fast 2D flood modelling using GPU technology - recent applications and new developments". Accessed 05/05/2021 at: <http://www.jflow.co.uk/sites/default/files/Crossley%20Lamb%20Waller%20-%20BHS%202010.pdf>
- Danielson J. J.**, and Gesch D. B. (2011), "Global multi-resolution terrain elevation data 2010 (GMTED2010)", U.S. Geological Survey Open-File Report 2011–1073, 26 p. Accessed 05/05/2021 at: <https://pubs.er.usgs.gov/publication/ofr20111073>.
- Dinardo S.** (2020), "Techniques and Applications for Satellite SAR Altimetry over water, land and ice", 56, Darmstadt, Technische Universität, ISBN 978-3-935631-45-7. DOI: [10.25534/tuprints-00011343](https://doi.org/10.25534/tuprints-00011343).
- Dodov B.**, and Foufoula-Georgiou E. (2004), "Generalized hydraulic geometry: Derivation based on a multiscaling formalism", *Water Resour. Res.*, 40, W06302. DOI: [10.1029/2003WR002082](https://doi.org/10.1029/2003WR002082).
- Bogning S.**, Frappart F., Blarel F., Niño F., Mahé G., Bricquet J.-P., Seyler F., Onguéné R., Etamé J., Paiz M.-C., and Braun J.-J. (2018), "Monitoring Water Levels and Discharges Using Radar Altimetry in an Ungauged River Basin: The Case of the Ogooué", *Remote Sensing*. DOI: [10.3390/rs10020350](https://doi.org/10.3390/rs10020350).
- Ehlschlaeger C.** (1989), "Using the AT Search Algorithm to Develop Hydrologic Models from Digital Elevation Data", *Proceedings of International Geographic Information Systems (IGIS) Symposium '89*, pp 275-281 (Baltimore, MD, 18-19 March 1989).
- ESA (2015)**, "Satellite Earth Observations In Support Of Disaster Risk Reduction", CEOS Earth Observation Handbook For WCDRR, Special 2015 WCDRR Edition. Accessed 05/05/2021 at: http://www.eohandbook.com/eohb2015/files/CEOS_EOHB_2015_WCDRR.pdf
- ESA (2021a)**, "HASARD Service in G-POD - User Manual and Terms and Conditions", ESA Research and Service Support. Accessed 05/05/2021 at: <https://wiki.services.eoportal.org/tiki-index.php?page=HASARD+Service+in+G-POD+-+User+Manual+and+Terms+and+Conditions>
- ESA (2021b)**, GPOD SENTINEL-3 SARvatore Software Prototype User Manual, ESA Research and Service Support. Accessed 05/05/2021 at: <https://wiki.services.eoportal.org/tiki-index.php?page=GPOD+SENTINEL-3+SARvatore+Software+Prototype+User+Manual>

- Esfandiari M.**, Abdi G., Jabari S., McGrath H., Coleman D. (2020), "Flood Hazard Risk Mapping Using a Pseudo Supervised Random Forest", *Remote Sens.* 2020, 12, 3206. DOI: [10.3390/rs12193206](https://doi.org/10.3390/rs12193206).
- ESRI (2021a)**, "ArcGIS Pro overview". Accessed 05/05/2021 at: <https://www.esri.com/en-us/arcgis/products/arcgis-pro/overview>
- ESRI (2021b)**, "ArcGIS Pro Tool Reference for Flow Direction (Spatial Analyst)". Accessed 05/05/2021 at: <https://pro.arcgis.com/en/pro-app/tool-reference/spatial-analyst/flow-direction.htm>
- Fairfield J.**, and Leymarie P. (1991), "Drainage networks from grid digital elevation models", *Water resources research* 27, 709–717. DOI: [10.1029/90WR02658](https://doi.org/10.1029/90WR02658).
- Follum M. L. (2012)**, "AutoRoute Rapid Flood Inundation Model", Coastal and Hydraulics Engineering Technical Note ERDC/CHL CHETN-IV-88, U.S. Army Engineer Research and Development Center, Coastal and Hydraulics Laboratory, Vicksburg, Mississippi. Accessed 05/05/2021 at: <https://usace.contentdm.oclc.org/digital/collection/p266001coll1/id/4330/>
- Follum M. L.**, Tavakoly A. A., Niemann J. D., and Snow A. D. (2017), "AutoRAPID: A Model for Prompt Streamflow Estimation and Flood Inundation Mapping over Regional to Continental Extents", *J. Am. Water Resour. Assoc.*, 53, 280–299, DOI: [10.1111/1752-1688.12476](https://doi.org/10.1111/1752-1688.12476).
- Follum M. L.**, Vera R., Tavakoly A. A., and Gutenson, J. L. (2020), "Improved accuracy and efficiency of flood inundation mapping of low-, medium-, and high-flow events using the AutoRoute model", *Nat. Hazards Earth Syst. Sci.*, 20, 625–641. DOI: [10.5194/nhess-20-625-2020](https://doi.org/10.5194/nhess-20-625-2020).
- Freeman T. G. (1991)**, "Calculating catchment area with divergent flow based on a regular grid", *Comput. Geosci.*, 17(3), 413–422. DOI: [10.1016/0098-3004\(91\)90048-I](https://doi.org/10.1016/0098-3004(91)90048-I).
- Gallant J. (2011)**, "Adaptive smoothing for noisy DEMs", In *Proceedings of the Geomorphometry 2011*, Redlands, CA, USA, 7–8 September 2011. Accessed 05/05/2021 at: https://gis-lab.info/docs/gallant2011_adaptive_smoothing_for_noisy_dems.pdf
- Garbrecht J.**, and Martz L. (1997), "The assignment of drainage direction over flat surfaces in raster digital elevation models", *Journal of hydrology* 193 (1-4), 204–213. DOI: [10.1016/S0022-1694\(96\)03138-1](https://doi.org/10.1016/S0022-1694(96)03138-1)
- Geoscience Australia (2021)**, "The Smoothed Digital Elevation Model (DEM-S)". Accessed 05/05/2021 at: <http://www.ga.gov.au/scientific-topics/national-location-information/digital-elevation-data>
- GRASS Development Team (2021a)**, "GRASS 7.8 Reference Manual". Accessed 05/05/2021 at: <https://grass.osgeo.org/grass78/manuals/index.html>
- GRASS Development Team (2021b)**, "GRASS User Manual: r.watershed". Accessed 05/05/2021 at: <https://grass.osgeo.org/grass78/manuals/r.watershed.html>
- GRASS Development Team (2021c)**, "GRASS User Manual: r.terraflow". Accessed 05/05/2021 at: <https://grass.osgeo.org/grass78/manuals/r.terraflow.html>
- GRASS Development Team (2021d)**, "GRASS User Manual: r.flow". Accessed 05/05/2021 at: <https://grass.osgeo.org/grass78/manuals/r.flow.html>

- GRASS Development Team (2021e)**, "GRASS User Manual: r.stream.distance". Accessed 05/05/2021 at: <https://grass.osgeo.org/grass78/manuals/addons/r.stream.distance.html>
- GRASS Development Team (2021f)**, "GRASS User Manual: r.accumulate". Accessed 05/05/2021 at: <https://grass.osgeo.org/grass78/manuals/addons/r.accumulate.html>
- GRASS Development Team (2021g)**, "GRASS User Manual: r.stream.basins". Accessed 05/05/2021 at: <https://grass.osgeo.org/grass78/manuals/addons/r.stream.basins.html>
- GRASS Development Team (2021h)**, "GRASS User Manual: r.stream.order". Accessed 05/05/2021 at: <https://grass.osgeo.org/grass78/manuals/addons/r.stream.order.html>
- GRASS Development Team (2021i)**, "GRASS User Manual: r.cost". Accessed 05/05/2021 at: <https://grass.osgeo.org/grass78/manuals/r.cost.html>
- GRASS Development Team (2021j)**, "GRASS User Manual: r.hydrodem". Accessed 05/05/2021 at: <https://grass.osgeo.org/grass78/manuals/addons/r.hydrodem.html>
- Greenlee D. D. (1987)**, "Raster and Vector Processing for Scanned Linework", Photogrammetric Engineering and Remote Sensing 53 (10): 1383–1387. Accessed 05/05/2021 at: https://www.asprs.org/wp-content/uploads/pers/1987journal/oct/1987_oct_1383-1387.pdf
- Hack J. T. (1957)**, "Studies of longitudinal profiles in Virginia and Maryland", U.S. Geological Survey Professional Paper, 294–B. DOI: [10.3133/pp294B](https://doi.org/10.3133/pp294B).
- Herold C. and Rudari R. (2013)**, "The Global Flood Model: Improvement of the Global Flood Model for the GAR 2013 and 2015", Background Paper prepared for the Global Assessment Report on Disaster Risk Reduction 2013, Geneva, Switzerland. Accessed 05/05/2021 at: <http://www.preventionweb.net/english/hyogo/gar/2013/en/bgddocs/Herold%20and%20Rudari,%202013%20CIMA.pdf>
- Hervouet J.-M. (2000)**, "TELEMAC modelling system: an overview", Hydrol. Process., 14: 2209-2210. DOI: [10.1002/1099-1085\(200009\)14:13<2209::AID-HYP23>3.0.CO;2-6](https://doi.org/10.1002/1099-1085(200009)14:13<2209::AID-HYP23>3.0.CO;2-6).
- Hocini N., Payrastre O., Bourgin F., Gaume E., Davy P., Lague D., Poinsignon L., and Pons F. (2020)** "Performance of automated flood inundation mapping methods in a context of flash floods: a comparison of three methods based either on the Height Above Nearest Drainage (HAND) concept, or on 1D/2D shallow water equations", Hydrol. Earth Syst. Sci. Discuss. DOI [preprint]: [10.5194/hess-2020-597](https://doi.org/10.5194/hess-2020-597), in review.
- Holmgren P. (1994)** "Multiple flow direction algorithms for runoff modelling in grid based elevation models: An empirical evaluation", Hydrological Processes. 8. 327 – 334, DOI: [10.1002/hyp.3360080405](https://doi.org/10.1002/hyp.3360080405).
- Horritt M. S. and Bates P. D. (2001)**, "Predicting floodplain inundation: Raster-based modelling versus the finite-element approach", Hydrological Processes. 15. 825 - 842. DOI: [10.1002/hyp.188](https://doi.org/10.1002/hyp.188).
- Hutchinson M. F. (1989)**, "A new method for gridding elevation and streamline data with automatic removal of pits", Journal of Hydrology, vol. 106, p. 211-232. DOI: [10.1016/0022-1694\(89\)90073-5](https://doi.org/10.1016/0022-1694(89)90073-5).

- Hutchinson M. F. (2011)**, "ANUDEM VERSION 5.3 User Guide", The Australian National University Fenner School of Environment and Society, Canberra, Australia. Accessed 05/05/2021 at: https://fennerschool.anu.edu.au/files/usedem53_pdf_16552.pdf
- Kebede M. G.**, Wang L., Li X., and Hu Z. (2020) "Remote sensing-based river discharge estimation for a small river flowing over the high mountain regions of the Tibetan Plateau", *Int. J. Remote Sens.*, 41, 3322–3345. DOI: [10.1080/01431161.2019.1701213](https://doi.org/10.1080/01431161.2019.1701213).
- CIAT-CSI (2004)**, "Void-filled seamless SRTM data", Cali, Colombia. Accessed 05/05/2021 at: <http://srtm.csi.cgiar.org>
- Jarvis A.**, Reuter H. I., Nelson A., and Guevara E. (2008), "Hole-filled SRTM for the globe Version 4, the CGIAR-CSI SRTM 90m database". Accessed 05/05/2021 at: <http://www.cgiar-csi.org/data/srtm-90m-digital-elevation-database-v4-1>
- Jenson S. K.**, and Domingue J. O. (1988), "Extracting Topographic Structure from Digital Elevation Data for Geographic Information System Analysis." *Photogrammetric Engineering and Remote Sensing* 54 (11): 1593–1600. Accessed 05/05/2021 at: <https://pubs.er.usgs.gov/publication/70142175>.
- JRC (2021)**, "Global Surface Water Explorer". Accessed 05/05/2021 at: <https://global-surface-water.appspot.com>.
- Lea N. L. (1992)**, "An aspect driven kinematic routing algorithm, in *Overland Flow: Hydraulics and Erosion Mechanics*", edited by A. J. Parsons and A.D. Abrahams, Chapman and Hall, New York.
- Lehner B.**, Verdin K.L., and Jarvis A. (2008), "New global hydrography derived from spaceborne elevation data", *Eos, Transactions American Geophysical Union*, v. 89, no. 10, p. 93–94. DOI: [10.1029/2008EO100001](https://doi.org/10.1029/2008EO100001).
- Leopold L. B.**, and Maddock T. (1953), "The hydraulic geometry of stream channels and some physiographic implications", *U.S. Geol. Surv. Prof. Paper*, 252, 57 pp. DOI: [10.3133/pp252](https://doi.org/10.3133/pp252)
- Lindsay J. B.**, and Creed I. F. (2005), "Removal of artifact depressions from digital elevation models: towards a minimum impact approach", *Hydrol. Process.*, 19: 3113-3126. DOI: [10.1002/hyp.5835](https://doi.org/10.1002/hyp.5835).
- Lindsay J. B. (2016)**, "Efficient hybrid breaching-filling sink removal methods for flow path enforcement in digital elevation models", *Hydrol. Process.*, 30: 846– 857. DOI: [10.1002/hyp.10648](https://doi.org/10.1002/hyp.10648).
- Lindsay J. B.**, Francioni A., and Cockburn J. (2019), "LiDAR DEM Smoothing and the Preservation of Drainage Features", *Remote Sensing*. 11. 1926. DOI: [10.3390/rs11161926](https://doi.org/10.3390/rs11161926).
- Liu Y. Y.**, Maidment D. R., Tarboton D. G., Zheng X., Yildirim A., Sazib N. S., and Wang S. (2016) "A CyberGIS Approach to Generating High-resolution Height Above Nearest Drainage (HAND) Raster for National Flood Mapping", *The Third International Conference on CyberGIS and Geospatial Data Science*, July 26–28, 2016, Urbana, Illinois. DOI: [10.13140/RG.2.2.24234.41925/1](https://doi.org/10.13140/RG.2.2.24234.41925/1).
- Liu Y. Y.**, Maidment D. R., Tarboton D. G., Zheng X., and Wang S. (2018) "A CyberGIS Integration and Computation Framework for High-Resolution Continental-Scale Flood Inundation Mapping", *Journal of the American Water Resources Association (JAWRA)*. DOI: [10.1111/1752-1688.12660](https://doi.org/10.1111/1752-1688.12660).

- Manning R. (1891)**. "On the flow of water in open channels and pipes". Transactions of the Institution of Civil Engineers of Ireland. 20: 161–207
- Manfreda S.**, and Samela C. **(2019)** "A DEM-based method for a rapid estimation of flood inundation depth", Journal of Flood Risk Management, 12 (Suppl. 1):e12541, DOI: [10.1111/jfr3.12541](https://doi.org/10.1111/jfr3.12541).
- Mark D. M. (1984)**, "Automatic Detection of Drainage Networks from Digital Elevation Models", Cartographica, 21(2/3): 168-178. DOI: [10.3138/10LM-4435-6310-251R](https://doi.org/10.3138/10LM-4435-6310-251R).
- Martz L. W.**, and Garbrecht J. **(1992)**, "Numerical Definition of Drainage Network and Subcatchment Areas from Digital Elevation Models", Computers and Geosciences, Vol. 18, No. 6, pp. 747-761. DOI: [10.1016/0098-3004\(92\)90007-E](https://doi.org/10.1016/0098-3004(92)90007-E).
- Matthews B. W. (1975)**, "Comparison of the predicted and observed secondary structure of T4 phage lysozyme", Biochimica et Biophysica Acta (BBA) - Protein Structure, Volume 405, Issue 2, 1975, Pages 442-451, ISSN 0005-2795. DOI: [10.1016/0005-2795\(75\)90109-9](https://doi.org/10.1016/0005-2795(75)90109-9).
- Meng X.**, Currit N., and Zhao K. **(2010)**, "Ground Filtering Algorithms for Airborne LiDAR Data: A Review of Critical Issues", Remote Sensing, 2, 833-860, DOI: [10.3390/rs2030833](https://doi.org/10.3390/rs2030833).
- Metz M.**, Mitasova H., and Harmon R. **(2011)**, "Efficient extraction of drainage networks from massive, radar-based elevation models with least cost path search", Hydrol. Earth Syst. Sci. Vol 15, 667-678, DOI: [10.5194/hess-15-667-2011](https://doi.org/10.5194/hess-15-667-2011).
- Mitasova H.**, Mitas L., Brown W. M., Gerdes D. P., Kosinovsky I., and Baker T. **(1995)**, "Modeling spatially and temporally distributed phenomena: New methods and tools for GRASS GIS", International Journal of Geographical Information Systems 9(4), 433-446. DOI: [10.1080/02693799508902048](https://doi.org/10.1080/02693799508902048).
- Mockus V. (1972)**, National Engineering Handbook, Section 4, Hydrology, Chapter 21, Notice 4-102. Accessed 05/05/2021 at: <https://directives.sc.egov.usda.gov/OpenNonWebContent.aspx?content=18393.wba>.
- Nardi F.**, Vivoni E. R., and Grimaldi S. **(2006)**, "Investigating a floodplain scaling relation using a hydrogeomorphic delineation method", Water Resour. Res., 42, W09409, DOI: [10.1029/2005WR004155](https://doi.org/10.1029/2005WR004155).
- Neal J.**, Schumann G., and Bates P. D. **(2012)**, "A simple model for simulating river hydraulics and floodplain inundation over large and data sparse areas", Water Resources Research. 48. 11506. DOI: [10.1029/2012WR012514](https://doi.org/10.1029/2012WR012514).
- Nobre A.**, Cuartas L., Hodnett M, Rennó C., Medeiros G., Silveira A., Waterloo M.J., and Saleska S. **(2011)**, "Height Above the Nearest Drainage - a hydrologically relevant new terrain model", Journal of Hydrology. 404. 13-29. 10.1016/j.jhydrol.2011.03.051. DOI: [10.1016/j.jhydrol.2011.03.051](https://doi.org/10.1016/j.jhydrol.2011.03.051).
- Nobre A.**, Cuartas L., Momo M., Severo D. L., Pinheiro A. and Nobre C. **(2015)**, "HAND contour: A new proxy predictor of inundation extent", Hydrological Processes. DOI: [10.1002/hyp.10581](https://doi.org/10.1002/hyp.10581).
- O'Callaghan J. F.**, and Mark D. M. **(1984)**, "The extraction of drainage networks from digital elevation data", Comput. Vision Graphics Image Process., 28, 323–344. DOI: [10.1016/S0734-189X\(84\)80011-0](https://doi.org/10.1016/S0734-189X(84)80011-0).

- Orlandini S.**, Moretti G., Franchini M., Aldighieri B., and Testa B. (2003), "Path-based methods for the determination of nondispersive drainage directions in grid-based digital elevation models", *Water Resour. Res.*, 39(6), 1144. DOI: [10.1029/2002WR001639](https://doi.org/10.1029/2002WR001639).
- Orlandini S.**, and Moretti G. (2009), "Determination of surface flow paths from gridded elevation data", *Water Resour. Res.*, 45, W03417. DOI: [10.1029/2008WR007099](https://doi.org/10.1029/2008WR007099).
- Pekel J. F.**, Cottam A., Gorelick N., and Belward A. S. (2016), "High-resolution mapping of global surface water and its long-term changes", *Nature*, 540(7633), 418–422. DOI: [10.1038/nature20584](https://doi.org/10.1038/nature20584).
- Pilesjö P.**, and Zhou Q. (1996), "A multiple flow direction algorithm and its use for hydrological modelling", *Proceedings of Geoinformatics'96 Conference*, 366–376. DOI: [10.1002/hyp.3360080405](https://doi.org/10.1002/hyp.3360080405).
- Pingel T.**, Clarke K., and McBride W. (2013), "An Improved Simple Morphological Filter for the Terrain Classification of Airborne LIDAR Data", *ISPRS Journal of Photogrammetry and Remote Sensing*, 77, 21-30. DOI: [10.1016/j.isprsjprs.2012.12.002](https://doi.org/10.1016/j.isprsjprs.2012.12.002).
- Pfafstetter O.** (1989), "Classification of hydrographic basins: coding methodology", unpublished manuscript, Departamento Nacional de Obras de Saneamento, August 18, 1989, Rio de Janeiro; available from J.P. Verdin, U.S. Geological Survey, EROS Data Center, Sioux Falls, South Dakota, USA.
- Planchon O.**, and Darboux F. (2002) "A fast, simple and versatile algorithm to fill the depressions of digital elevation models", *Catena*. 46. 159-176. DOI: [10.1016/S0341-8162\(01\)00164-3](https://doi.org/10.1016/S0341-8162(01)00164-3).
- QGIS Development Team** (2021), "QGIS (Version 3.4-Madeira)", Open-Source Geospatial Foundation Project. Accessed 05/05/2021 at: <https://qgis.org>.
- Qin C.**, Zhu A. X., Pei T., Li B., Zhou C., and Yang L. (2007), "An adaptive approach to selecting a flow partition exponent for a multiple flow direction algorithm", *International Journal of Geographical Information Science*, 21(4): 443-458. DOI: [10.1080/13658810601073240](https://doi.org/10.1080/13658810601073240).
- Quinn P.**, Beven K., Chevallier P., and Planchon O. (1991), "The prediction of hillslope flow paths for distributed hydrological modelling using digital terrain models", *Hydrol. Processes*, 5, 59–79. DOI: [10.1002/hyp.3360050106](https://doi.org/10.1002/hyp.3360050106).
- R Core Team** (2021a), "R: A language and environment for statistical computing", R Foundation for Statistical Computing, Vienna, Austria. Accessed 05/05/2021 at: <http://www.R-project.org/>.
- R Core Team** (2021b), "The R Package optimize: One Dimensional Optimization". Accessed 05/05/2021 at: <https://stat.ethz.ch/R-manual/R-devel/library/stats/html/optimize.html>.
- Rahmati O.**, Darabi H., Panahi M. et al. (2020), "Development of novel hybridized models for urban flood susceptibility mapping", *Sci Rep* 10, 12937. DOI: [10.1038/s41598-020-69703-7](https://doi.org/10.1038/s41598-020-69703-7).
- Regione Liguria** (2020a), "Geoportale Regione Liguria". Accessed 05/05/2021 at: <https://geoportal.regione.liguria.it/>.
- Regione Liguria** (2020b), "Piano Di Bacino Stralcio Sul Rischio Idrogeologico", Ambito Regionale Di Bacino 16, Report, Genoa, Italy. Accessed 05/05/2021 at: http://www.pianidibacino.ambienteinliguria.it/GE/ambito16/documenti/GE_Amb16_RelGen_rev09.pdf.

Regione Toscana (2021), "The GEOscopio geoportal", webgis. Accessed 05/05/2021 at:
www502.regione.toscana.it/geoscopio/cartoteca.html

Rennó C. D., Nobre A. D., Cuartas L. A., Soares J. V., Hodnett M. G., Tomasella J., and Waterloo M. J. (2008), "HAND, a new terrain descriptor using SRTM-DEM: Mapping terra-firme rainforest environments in Amazonia", *Remote Sens. Environ.*, 112, 3469–3481. DOI: [10.1016/j.rse.2008.03.018](https://doi.org/10.1016/j.rse.2008.03.018).

Reuter H. I., Nelson A., and Jarvis A. (2007), "An evaluation of void filling interpolation methods for SRTM data", *International Journal of Geographic Information Science*, 21:9, 983-1008. DOI: [10.1080/13658810601169899](https://doi.org/10.1080/13658810601169899).

Roccati A., Mandarino A., Perasso L., Robbiano A., Luino F., and Faccini F. (2020), "Large-scale geomorphology of the Entella River floodplain (Italy) for coastal urban areas management", *Journal of Maps*. DOI: [10.1080/17445647.2020.1738281](https://doi.org/10.1080/17445647.2020.1738281).

Roggero M. (2001), "Airborne laser scanning: clustering in raw data", *Int. Arch. Photogramm. Remote Sens. Spatial Inf. Sci.*, Vol. XXXIV Part 3/W4, 227–232. Accessed 05/05/2021 at: <http://www.isprs.org/proceedings/XXXIV/3-W4/pdf/Roggero.pdf>.

Salimi E. T., Nohegar A., Malekian A. et al. (2017), "Estimating time of concentration in large watersheds", *Paddy Water Environ* 15, 123–132. DOI: [10.1007/s10333-016-0534-2](https://doi.org/10.1007/s10333-016-0534-2).

Samela C., Troy T. J., and Manfreda S. (2017), "Geomorphic classifiers for flood-prone areas delineation for data-scarce environments", *Advances in Water Resources*, Volume 102, 2017, Pages 13-28, ISSN 0309-1708, DOI: [10.1016/j.advwatres.2017.01.007](https://doi.org/10.1016/j.advwatres.2017.01.007).

Samela C., Albano R., Sole A., and Manfreda S. (2018), "A GIS tool for cost-effective delineation of flood-prone areas", *Computers, Environment and Urban Systems*, Volume 70, 2018, pages 43-52, ISSN 0198-9715. DOI: [10.1016/j.compenvurbsys.2018.01.013](https://doi.org/10.1016/j.compenvurbsys.2018.01.013).

Santos P., Reis E., Pereira S., and Santos M. (2019) "A flood susceptibility model at the national scale based on multicriteria analysis", *Science of The Total Environment*. 667. 325-337. DOI: [10.1016/j.scitotenv.2019.02.328](https://doi.org/10.1016/j.scitotenv.2019.02.328).

Schumann G., Neal J., Voisin N., Andreadis K., Pappenberger F., Phanthuwongpakdee N., Hall A., and Bates, P. D. (2013), "A first large-scale flood inundation forecasting model", *Water Resources Research*. 49. 6248-6257. DOI: [10.1002/wrcr.20521](https://doi.org/10.1002/wrcr.20521).

Seibert J., and McGlynn B. L. (2007), "A new triangular multiple flow direction algorithm for computing upslope areas from gridded digital elevation models", *Water Resour. Res.*, 43, W04501, DOI: [10.1029/2006WR005128](https://doi.org/10.1029/2006WR005128).

Silvestro F., Gabellani S., Delogu F., Rudari R., and Boni G. (2013), "Exploiting remote sensing land surface temperature in distributed hydrological modelling: The example of the Continuum model", *Hydrology and Earth System Sciences*, 17, 39-62. DOI: [10.5194/hess-17-39-2013](https://doi.org/10.5194/hess-17-39-2013).

Silvestro F., Gabellani S., Rudari R., Delogu F., Laiolo P., and Boni G. (2015), "Uncertainty reduction and parameters estimation of a distributed hydrological model with ground and remote sensing data", *Hydrology and Earth System Sciences*, 19, 1727–1751, 2015. DOI: [10.5194/hess-19-1727-2015](https://doi.org/10.5194/hess-19-1727-2015).

- Sithole G.** and Vosselman G. (2003), "Comparison of filtering algorithms," in Proceedings of the ISPRS Working Group III/3 Workshop: 3-D Reconstruction from Airborne Laserscanner and InSAR data., Dresden, Germany, pp. 8-10. Accessed 05/05/2021 at: <https://research.tudelft.nl/en/publications/comparison-of-filtering-algorithms>.
- Soille P.**, Vogt J., and Colombo R. (2003), "Carving and adaptive drainage enforcement of grid digital elevation models", *Water Resour. Res.*, 39, 1366-1372, DOI: [10.1029/2002WR001879](https://doi.org/10.1029/2002WR001879).
- Soille P.** (2004), "Optimal Removal of Spurious Pits in Grid Digital Elevation Models." *Water Resources Research* 40: 229–244. DOI: [10.1029/2004WR003060](https://doi.org/10.1029/2004WR003060).
- Stein J. L.** (2018), "An enhanced Pfafstetter catchment reference system", *Water Resources Research*, 54, 9951–9963. DOI: [10.1029/2018WR023218](https://doi.org/10.1029/2018WR023218).
- Stevenson J. A.**, Sun X., and Mitchell N. C. (2010), "Despeckling SRTM and other topographic data with a denoising algorithm", *Geomorphology*, 144:238-252. DOI: [10.1016/j.geomorph.2009.07.006](https://doi.org/10.1016/j.geomorph.2009.07.006).
- Strahler A. N.** (1957), "Quantitative analysis of watershed geomorphology", *Eos Trans. AGU*, 38 (6), 913–920. DOI: [10.1029/TR038i006p00913](https://doi.org/10.1029/TR038i006p00913).
- Sun X.**, Rosin P.L., Martin R.R., and Langbein F.C. (2007), "Fast and Effective Feature-Preserving Mesh Denoising". *IEEE Transactions on Visualization and Computer Graphics*, 13(5):925-938. DOI: [10.1109/TVCG.2007.1065](https://doi.org/10.1109/TVCG.2007.1065).
- Tarboton D. G.** (1997), "A new method for the determination of flow directions and upslope areas in grid digital elevation models", *Water Resour. Res.*, 33(2), 309–319, DOI: [10.1029/96WR03137](https://doi.org/10.1029/96WR03137).
- Tarboton D. G.**, and Baker M. E. (2008) "Towards an algebra for terrain-based flow analysis", *Representing, modeling and visualizing the natural environment: innovations in GIS* 13, 167–194. DOI: [10.1201/9781420055504](https://doi.org/10.1201/9781420055504).
- Tarboton D. G.** (2021), "Terrain Analysis Using Digital Elevation Models - TauDEM", Version 5, Utah State University, Logan. Accessed 05/05/2021 at: <https://hydrology.usu.edu/taudem/taudem5/index.html>
- Tarpanelli A.**, Barbetta S., Brocca L., and Moramarco T. (2013), "River Discharge Estimation by Using Altimetry Data and Simplified Flood Routing Modeling", *Remote Sensing*. 5. 4145-4162. DOI: [10.3390/rs5094145](https://doi.org/10.3390/rs5094145).
- Tarpanelli A.**, Camici S., Nielsen K., Brocca L., Moramarco T., and Benveniste J. (2019), "Potentials and limitations of Sentinel-3 for river discharge assessment", *Adv. Space Res.* DOI: [10.1016/j.asr.2019.08.005](https://doi.org/10.1016/j.asr.2019.08.005).
- Tesfa T. K.**, Tarboton D. G., Watson D. W., Schreuders K. A., Baker M. E., and Wallace R. M. (2011), "Extraction of hydrological proximity measures from DEMs using parallel processing", *Environ. Model. Softw.*, 26, 1696–1709. DOI: [10.1016/j.envsoft.2011.07.018](https://doi.org/10.1016/j.envsoft.2011.07.018).
- Toma L.**, Wickremesinghe R., Arge L., Chase J. S., Scott Vitter J., Halpin P.N., and Urban D. (2001), "Flow computation on massive grids", In *Proc. of the 9th ACM international symposium on Advances in geographic information systems*, Pages 82–87. DOI: [10.1145/512161.512180](https://doi.org/10.1145/512161.512180).

- UNISDR (2015a)**, “Sendai Framework for Disaster Risk Reduction 2015 – 2030”, UNISDR, Geneva, 2015 - ICLUX EN5000 1st edition. Accessed 05/05/2021 at: http://www.preventionweb.net/files/43291_sendaiframeworkfordrren.pdf
- UNISDR (2015b)**, “Earth observations in support of national strategies for disaster-risk management - A Synergy Framework for the integration of Earth Observation technologies into Disaster Risk Reduction”, UN World Conference on Disaster Risk Reduction, Sendai, 25/02/2015. Accessed 05/05/2021 at: https://www.un-spider.org/sites/default/files/White_paper_Earth%20observations%20for%20DRR.pdf
- UNOSAT (2011)**, “Time Series Analysis of Thailand Flood 2011”. Accessed 05/05/2021 at: <http://www.unitar.org/unosat/node/44/1615>.
- UNOSAT (2017)**, “Flood Finder Chad 2017, Bulletin N°9, 27 September 2017”. Accessed 05/05/2021 at: https://www.humanitarianresponse.info/system/files/documents/files/unosat_flood-finder-chad-2017_eng_bulletin-n9_chad_2017.pdf.
- USGS (2008)**, “HydroSHEDS Data Set Development”. Accessed 05/05/2021 at: <https://www.hydrosheds.org/page/development>
- Verdin J., Verdin K. L., Mathis M., Magadzire T., Kabuchanga E., Woodbury M., and Gadain H. (2016)**, “A software tool for rapid flood inundation mapping”, U.S. Geological Survey Open-File Report 2016–1038, 26 p. DOI: [10.3133/ofr20161038](https://doi.org/10.3133/ofr20161038).
- Verdin K. L., and Jenson S. K. (1996)**, “Development of continental scale DEMs and extraction of hydrographic features”, in Third International Conference on Integrating GIS and Environmental Modelling. Accessed 05/05/2021 at: http://www.ncgia.ucsb.edu/SANTA_FE_CD-ROM/sf_papers/verdin_kristine/santafe2.html.
- Verdin K. L., and Verdin J. (1999)**, “A topological system for delineation and codification of the Earth’s river basins, Journal of Hydrology”, 218 (1-2), 1–12. DOI: [10.1016/S0022-1694\(99\)00011-6](https://doi.org/10.1016/S0022-1694(99)00011-6).
- Verdin K. L. (2017)**, “Hydrologic Derivatives for Modeling and Analysis—A new global high-resolution database”, In USGS report. DOI: [10.3133/ds1053](https://doi.org/10.3133/ds1053).
- Vignudelli S., De Basio F., Scozzari A., Zecchetto S., and Papa A. (2019)**, “Sea level trends and variability in the Adriatic Sea and around Venice”, Proceedings of international association of geodesy symposia—international review workshop on satellite altimetry Cal/Val activities and applications, 23–26 April 2018, Crete, Greece, 1–10, Springer, Berlin. DOI: [10.1007/1345_2018_51](https://doi.org/10.1007/1345_2018_51).
- Vosselman G. (2000)**, “Slope based filtering of laser altimetry data”. IAPRS, Vol XXXIII, Part B3, Amsterdam, The Netherlands. pp. 935-942. Accessed 05/05/2021 at: https://www.researchgate.net/publication/228719860_Slope_based_filtering_of_laser_altimetry_data
- Wang L., and Liu H. (2006)**, “An efficient method for identifying and filling surface depressions in digital elevation models for hydrologic analysis and modelling”, International Journal of Geographical Information Science, Vol. 20, No. 2: 193-213. DOI: [10.1080/13658810500433453](https://doi.org/10.1080/13658810500433453).

- Wang C. K.**, and Tseng Y. H. (2010) "DEM generation from airborne lidar data by an adaptive dualdirectional slope filter", *International Archives of the Photogrammetry, Remote Sensing and Spatial Information Sciences - ISPRS Archives*, 38, 628-632. Accessed 05/05/2021 at: https://www.isprs.org/PROCEEDINGS/XXXVIII/part7/b/pdf/628_XXXVIII-part7B.pdf
- Wang J.**, Yang H., Li L., Gourley J. J., Sadiq I. K., Yilmaz K. K., Adler R. F., Policelli F. S., Habib S., Irwn D., Limaye A. S., Korme T., and Okello L. (2011), "The coupled routing and excess storage (CREST) distributed hydrological model". *Hydrol. Sci. J.* 56(1), 84–98. DOI: [10.1080/02626667.2010.543087](https://doi.org/10.1080/02626667.2010.543087).
- Wang Y.**, Qin C., and Zhu A. (2019), "Review on algorithms of dealing with depressions in grid DEM", *Annals of GIS*, 25:2, 83-97, DOI: [10.1080/19475683.2019.1604571](https://doi.org/10.1080/19475683.2019.1604571).
- Wolock D. M.**, and McCabe G. J. (1995), "Comparison of Single and Multiple Flow Direction Algorithms for Computing Topographic Parameters in TOPMODEL", *Water Resour. Res.*, 31 (5), 1315– 1324, DOI: [10.1029/95WR00471](https://doi.org/10.1029/95WR00471).
- Wright N.** (2013), "Small Island Developing States, disaster risk management, disaster risk reduction, climate change adaptation and tourism", Background Paper, GAR 2013. Accessed 05/05/2021 at: <http://www.preventionweb.net/english/hyogo/gar/2013/en/bgdocs/Wright,%20N.,%202013.pdf>
- Wu H.**, Adler R. F., Tian Y., Huffman G. J., Li H., and Wang J. (2014), "Real-time global flood estimation using satellite-based precipitation and a coupled land surface and routing model", *Water Resour. Res.*, 50, 2693–2717. DOI: [10.1002/2013WR014710](https://doi.org/10.1002/2013WR014710).
- Yamazaki D.**, Ikeshima D., Tawatari R., Yamaguchi T., O'Loughlin F., Neal J. C., Sampson C. C., Kanae S., and Bates P. D. (2017), "A high-accuracy map of global terrain elevations", *Geophys. Res. Lett.*, 44, 5844–5853. DOI: [10.1002/2017GL072874](https://doi.org/10.1002/2017GL072874).
- Yamazaki D.**, Ikeshima D., Sosa J., Bates P. D., Allen G. H., and Pavelsky T. M. (2019), "MERIT Hydro: A high-resolution global hydrography map based on latest topography datasets", *Water Resources Research*, vol.55, pp.5053-5073. DOI: [10.1029/2019WR024873](https://doi.org/10.1029/2019WR024873).
- Zhang K.**, Chen S., Whitman D., Shyu M., Yan J., and Zhang C., (2003), "A progressive morphological filter for removing nonground measurements from airborne LIDAR data", *IEEE Transactions on Geoscience and Remote Sensing* 41 (4), 872–882. DOI: [10.1109/TGRS.2003.810682](https://doi.org/10.1109/TGRS.2003.810682).
- Zheng X.**, Tarboton D. G., Maidment D. R., Liu Y. Y., and Passalacqua P. (2018a), "River channel geometry and rating curve estimation using height above the nearest drainage", *J. Am. Water Resour. Assoc.*, 54, 785–806, 2018a. DOI: [10.1111/1752-1688.12661](https://doi.org/10.1111/1752-1688.12661).
- Zheng X.**, Maidment D. R., Tarboton D. G., Liu Y. Y., and Passalacqua P. (2018b), "GeoFlood: Large-scale flood inundation mapping based on high-resolution terrain analysis", *Water Resources Research*, 54, 10,013– 10,033. DOI: [10.1029/2018WR023457](https://doi.org/10.1029/2018WR023457).
- Zhou Q.**, Pilesjö P., and Chen Y. (2011), "Estimating surface flow paths on a digital elevation model using a triangular facet network", *Water Resources Research*, 47(7), 1–12. DOI: [10.1029/2010WR009961](https://doi.org/10.1029/2010WR009961).
- Zhou G.**, Sun Z., and Fu S. (2016), "An efficient variant of the Priority-Flood algorithm for filling depressions in raster digital elevation models", *Computers and Geosciences* 90, Part A, 87 – 96. DOI: [10.1016/j.cageo.2016.02.021](https://doi.org/10.1016/j.cageo.2016.02.021).